Numerical Studies on the Motion of Particles in Current-Carrying Liquid Metals and its Application to LiMCA Systems

by

Mei Li
Department of Mining and Metallurgical Engineering
McGill University
Montreal, Quebec, Canada

October 1999

A Thesis submitted to the
Faculty of Graduate Studies and Research
in partial fulfillment of the requirements for the degree of
Doctor of Philosophy

0-612-70187-5

To Jun

ABSTRACT

A numerical model is developed concerning the motion of particles in current-carrying liquid metals in a cylindrical coordinate system. The fluid flow is obtained by solving Navier-Stokes equations, and particle trajectories by equations for the motion of particles which incorporate the drag, added mass, history, fluid acceleration and electromagnetic force, with correction factors for particle shape and orientation. Wall effects and the flow conditions in the entrance region are considered. Dimensionless numbers Re, R_H, γ, and k are introduced to represent the fluid velocity, electric current, particle density and particle size, respectively. Electromagnetic force squeezes non-conducting particles away from, while pushes more conductive particles towards the symmetric axis. In a cylindrical pipe or ESZ orifice, particles follow the fluid flow closely in the axial direction. In the radial direction, at low current, non-conductive particles move towards the central axis first and then to the sidewall, while at high current, directly to the wall because of the competition between the fluid acceleration and the electromagnetic force which increases with particle size, electric current, and distance from the central axis. Lighter and larger particles move faster towards the wall. The dominating increase in added mass over electromagnetic force on oblates than on prolates, the smaller drag force and the lower added mass on prolates, with their symmetric axes perpendicular to the transverse axis of the ESZ, move prolates faster towards the wall. In parabolic ESZ orifice, bubbles lead and heavier particles lag behind the fluid flow in the axial direction, and the transient time difference makes particle discrimination realizable. The conditioning effect is attributed to the dramatic increase in fluid velocity near the parabolic orifice wall upon current surge. Designs are proposed for improving the conditioning effect in steel LiMCA, for reducing the background noise and avoiding orifice blockage for magnesium LiMCA, and for lowering the detection limits in magnesium and steel LiMCA.

RÉSUMÉ

Un modèle numérique a été développé pour simuler le mouvement des particules dans courant-porter les métaux liquides dans un système de coordonnées cylindriques. Le flux de fluide est obtenu en résolvant des équations de Navier-Stokes, et la trajectoire des particules par des équations pour le mouvement des particules qui incorporent la traîner, la masse ajoutée, l'histoire, l'accélération liquide et la force électromagnétique, avec des facteurs de correction pour la forme et l'orientation de particules. Des effets de mur et les conditions d'écoulement dans la région d'entrée sont considérés. Des nombres sans dimensions Re, R_H, γ et k sont présentés pour représenter la vitesse liquide, le courant électrique, la densité de particules et la dimension particulaire, respectivement. La force électromagnétique éloigné les particules non-conductrices, alors quelle poussé les particules plus conductrices vers l'axe symétrique. Dans un tube cylindrique ou l'orifice d'ESZ, les particules suivent le flux de fluide étroitement dans la direction axiale. Dans la direction radiale, pour un bas courant, les particules non-conductrices se déplacent d'abord vers l'axe central, puis ensuite vers la paroi latérale, tandis que pour un courant élevé, elles vont directement au mur en raison de la concurrence entre l'accélération liquide et la force électromagnétique qui augmente avec la dimension particulaire, le courant électrique, et la distance de l'axe central. Les particules plus légères et plus grandes se déplacent plus rapidement vers le mur. L'augmentation dominante de la masse ajoutée au-dessus de la force électromagnétique sur des oblates que sur des prolates, de la force de résistance à l'avancement plus petite et de la masse ajoutée inférieure sur des prolates, avec leurs axes symétriques perpendiculaires à l'axe transversal de l'ESZ, déplacent les prolates plus rapidement vers le mur. Dans l'orifice parabolique d'ESZ, les bulles mènent et les particules plus lourdes derrière trainent le flux de fluide dans la direction axiale, et la différence passagère de temps rend la discrimination de particules possible. L'effet de traitement est attribué à l'augmentation excessive de la vitesse liquide près du mur parabolique d'orifice sur la montée subite actuelle. On propose des conceptions pour améliorer l'effet de traitement en acier LiMCA, pour réduire le bruit de fond et éviter le colmatage d'orifice pour le magnésium LiMCA, et pour abaisser les limites de détection en magnésium et acier LiMCA.

Acknowledgements

I would like to thank my supervisor, Professor Roderick I. L. Guthrie, for his guidance and support. Throughout the course of the research he has been a fertile source of ideas and helpful advice, and has inspired me to achieve more than I thought possible.

I sincerely thank Dr. Ramani Sankanaraynan and Chris Carozza for teaching me how to use the molten metal and water based LiMCA systems.

Special thanks go to Dr. Jiyoung Byun, for sharing his knowledge and experience on molten magnesium. I also wish to thank Qi Xia for providing me some important literatures at the beginning of this work.

I am thankful to Dr. Robert Paquette and Dr. Pedro Netto for helpful discussion on METFLO program, Dr. Hussein Albuluwefa, Hyoungbae Kim and Jinsoo Kim for delightful collaboration on magnesium LiMCA and water modeling experiments.

I am extremely grateful to Harold Ward, Csaba Szalacsi and Martin Knoepfel for their help in machine shop.

I wish also to thank Florence Paray for translating the abstract of this thesis to French, Musbah Mahfoud, Dave and Claudia Gloria, Vicki Pedicelli, Dr. Mihaiela Isac, Ning Jin, Guohui Zheng, Yongqin Zhang, Jie Xiao for helping make my stay at McGill enjoyable.

I can never thank enough my family for their love and constant support.

Table of Contents

Abstract iii

Resume iv

Acknowledgements vi

Table of Contents vii

List of Figures xii

List of Tables xvi

List of Symbols xvii

Chapter 1 **Introduction and Background** 1

1.1 Electromagnetic Phenomena in Materials Processing Operations 1

1.1.1 Application of Rotational EMVF 3

1.1.2 Application of Irrotational EMVF 4

1.1.3 Application of Both Rotational and Irrotational EMVF 6

1.1.4 Unintentionally Applied EMVF Involved in High-Current Processes 7

1.2 Review of Mathematical and Physical Modeling in Electromagnetic Materials Processing 11

1.2.1 Theory 11

1.2.1.1 Fluid flow and electromagnetic fields 11

1.2.1.2 Particle motions 16

1.2.2 Mathematical. Physical Modeling and Experimentation 22

1.2.2.1 Mathematical modeling 22

1.2.2.1.1 Fluid flow 22

1.2.2.1.2 Particle motions 25

1.2.2.2 Physical modeling and experimentation 27

1.3 Objectives and Outline of This Thesis 30

References 33

Chapter 2 **Numerical Studies of the Motion of Particles in Current-Carrying Liquid Metals Flowing in a Circular Pipe** 45

2.1 Introduction 45

2.2 Mathematical Model and Numerical Methods 47

2.2.1 The Flow Field in the Pipe 47

2.2.2 The Equation of Motion of the Particles 51

2.2.3 Wall Effects 53

2.2.4 Numerical Methods 54

2.3 Results and Discussion 56

2.3.1 The Effect of R_H 57

2.3.2 The Effect of Re 60

2.3.3 The Effect of γ 61

2.3.4 The Effect of Blockage Ratio k 61

2.3.5 The Effect of Entry Point to the Pipe 62

2.3.6 The Application of the Model to LiMCA System 62

2.4 Conclusions 65

References 66

Chapter 3 **Numerical Studies of the Motion of Spheroidal Particles Flowing with Liquid Metals through an Electric Sensing Zone (ESZ)** 69

3.1 Introduction 69

3.2 Mathematical Model and Numerical Methods 73

3.2.1 The Flow Field in the ESZ 75

3.2.2 The Equation of Motion for Spheroidal Particles 75

3.2.3 Wall Effects 81

3.2.4 Numerical Methods 81

3.3 Results and Discussion 81

3.3.1 The Effect of R_H 83

3.3.2 The Effect of Re 92

3.3.3 The Effect of γ 95

3.3.4 The Effect of Blockage Ratio k 98

3.3.5 The Effect of Entry Point to the ESZ 100
3.3.6 The Application of the Model to LiMCA System in Aluminum Industries 103
3.4 Conclusions 106
References 107

Chapter 4 **Particle Discrimination in Water Based LiMCA System** 110
4.1 Introduction 110
4.2 Theory 113
4.2.1 The Flow Field in the ESZ 114
4.2.2 The Equation of Motion of Particles 116
4.2.3 Ohmic Model of ESZ 117
4.2.4 Numerical Methods 119
4.3 Experiment 120
4.3.1 Water Based LiMCA System — APS II System 120
4.3.2 Particle Discrimination Test 121
4.4 Results and Discussion 123
4.4.1 Fluid Flow 123
4.4.2 Particle Motion 128
4.4.2.1 Effect of particle density 128
4.4.2.2 Effect of particle size 130
4.4.2.3 Effect of entry point 133
4.4.3 Particle Discrimination in APS II System 134
4.5 Conclusions 142
References 143

Chapter 5 **LiMCA in Molten Aluminum, Magnesium and Steel** 145
5.1 LiMCA in Molten Aluminum 145
5.1.1 Introduction 145
5.1.2 Mathematical Model and Numerical Methods 148
5.1.2.1 Electric Sensing Zone (ESZ) principle 150

5.1.2.1.1 Non-conductive particle ($\rho_{e_p} >> \rho_e$) 151
5.1.2.1.2 Perfect conductive particle ($\rho_{e_p} << \rho_e$) 152
5.1.2.1.3 TiB_2 particle in molten aluminum 153
5.1.2.2 The flow field in the ESZ 153
5.1.2.3 The equation of motion of particles 154
5.1.2.4 Ohmic model of ESZ 156
5.1.2.5 Numerical methods 157
5.1.3 Results and Discussion 158
5.1.3.1 Fluid flow and electromagnetic fields 158
5.1.3.2 Particle motion 161
5.1.3.2.1 Effect of particle conductivity 161
5.1.3.2.2 Effect of particle density 166
5.1.3.2.3 Effect of particle size 169
5.1.3.2.4 Effect of electric current 170
5.1.3.2.5 Effect of fluid velocity within the ESZ 171
5.1.3.2.6 Effect of entry point 172
5.1.3.2.7 Effect of orifice shape 173
5.1.3.3 Conditioning operation 174
5.1.3.4 Particle discrimination 175
5.1.3.4.1 Discrimination of conductive and non-conductive particles . . . 175
5.1.3.4.2 Discrimination of non-conductive particles of different density . 176
5.2 LiMCA in Molten Magnesium 179
5.2.1 Introduction 179
5.2.2 Fluid Flow and Particle Motions within an ESZ of the CSTP . . 182
5.2.3 A New Design of the ESZ for CSTP 186
5.3 LiMCA in Molten Steel 186
5.3.1 Introduction 186
5.3.2 Flow Field 188
5.4 Conclusions 190
References 191

Chapter 6 **On the Detection, and Selective Separation of Inclusions in LiMCA System** 194
6.1 Introduction 194
6.2 Basis for the Development of a Smart-Probe 197
6.3 Mathematical Model and Numerical Methods 199
6.3.1 The Flow Field 199
6.3.2 The Equation of Motion for Particles 200
6.3.3 Wall Effects 200
6.3.4 Numerical Methods 200
6.4 Results and Discussion 201
6.4.1 Particle Separation via Smart-Probe 201
6.4.1.1 Fluid flow and electromagnetic fields 202
6.4.1.2 Trajectories of particles of different sizes and densities 206
6.4.2 Design Parameters for Smart-Probe 209
6.4.2.1 Electric current I / orifice size D arrangement 209
6.4.2.2 Orifice length $L_{orifice}$ 212
6.4.2.3 Orifice shape S 213
6.4.2.4 Extension radius H 213
6.4.2.5 Extension length L_e 216
6.4.2.6 Mean fluid velocity u_m flowing through the orifice 216
6.4.3 Smart-Probe for Magnesium and Steel LiMCA 218
6.5 Conclusions 221
References 222

Chapter 7 **Conclusions** 224

Statement of Originality 228

Appendix 229

List of Figures

2 — 1 The schematic representation of a particle flowing in a current-carrying liquid in a circular pipe 48

2 — 2 The effect of R_H on the particle trajectory 57

2 — 3 Force terms in the axial direction 58

2 — 4 Force terms in the radial direction 59

2 — 5 The effect of Re on the particle trajectory 60

2 — 6 The effect of γ on the particle trajectory 63

2 — 7 The effect of k on the particle axial distance upon reaching the wall for different density particles 63

2 — 8 The effect of entry point y_0 on particle trajectory 64

2 — 9 The predicted pass-through fraction for particles 65

3 — 1 Schematic representation of electric sensing zone principle 70

3 — 2 Schematic representation of the system used in the computation 74

3 — 3 The effect of R_H on the trajectories of spheroidal particles 85

3 — 4 Force terms in the radial direction on spheroidal particles 87

3 — 5 Comparison of the trajectories of spheroidal particles 88

3 — 6 The effect of particle shape and orientation on the correction factors 91

3 — 7 The effect of Re on the trajectories of spheroidal particles 94

3 — 8 The effect of γ on the trajectories of spheroidal particles 98

3 — 9 The effect of k on the axial distance traversed by spheroidal particles 99

3 — 10 The effect of entry point y_0 on the trajectories of spheroidal particles 102

3 — 11 The predicted pass-through fraction for spheroidal particles 104

4 — 1 Schematic representation of ESZ principle for particle size measurement . . . 111

4 — 2 The employed computational domain 115

4 — 3 The employed non-orthogonal, boundary-fitted grid 119

4 — 4 Schematic experimental set up of APS II system 120
4 — 5 The peak parameters generated by DSP in LiMCA system 122
4 — 6 Velocity vectors and the axial and radial velocity profiles
in an ESZ of $270\mu m$ with $u_m = 5.63 m/s$ 126
4 — 7 Velocity vectors and the axial and radial velocity profiles
in an ESZ of $320\mu m$ with $u_m = 7.5 m/s$ 127
4 — 8 Effect of particle density on the motion of particles 128
4 — 9 Effect of particle density on the axial velocity and relative axial velocity ... 129
4 — 10 Effect of particle size on the motion of particles 131
4 — 11 Effect of particle size on the axial velocity and relative axial velocity 132
4 — 12 Comparison of the relative velocity obtained by Brenen's theory
and numerical simulation 133
4 — 13 Axial and radial components of velocity and relative velocity 135
4 — 14 Electrical potential distribution 136
4 — 15 ESZ resistance change with the position of particles 137
4 — 16 Comparison of experimentally measured and numerically predicted
transient time versus particle size 140
4 — 17 Comparison of experimentally observed and numerically predicted
particle signal shapes 142

5 — 1 The employed computational domain in aluminum LiMCA 149
5 — 2 The employed non-orthogonal, boundary-fitted grid 157
5 — 3 Distribution of electrical potential, electric current density, self-induced
magnetic flux density, and specific electromagnetic force 160
5 — 4 Velocity vectors and the axial and radial velocity profiles 163
5 — 5 Effect of particle conductivity on the motion of particles 164
5 — 6 Electromagnetic force on particles of different conductivity 165
5 — 7 Effect of particle density on the motion of particles 166
5 — 8 Effect of particle density on the velocity and relative velocity 167
5 — 9 Effect of particle size on the motion of particles 170
5 — 10 Effect of electric current on the motion of particles 171

5 — 11 Effect of mean fluid velocity on the motion of particles 172
5 — 12 Effect of entry point on the motion of particles 173
5 — 13 Velocity vectors in the conditioning operation 175
5 — 14 The voltage pulse as a function of particle diameter 176
5 — 15 ESZ resistance change with the position of non-conductive particles 178
5 — 16 Numerically predicted transient time versus particle size 178
5 — 17 Numerically predicted voltage pulse in aluminum LiMCA system 180
5 — 18 Schematic of the CSTP for magnesium LiMCA 182
5 — 19 Cross-section view of an ESZ built inside the BN disc for CSTP 183
5 — 20 Predicted streamlines in magnesium LiMCA 184
5 — 21 Trajectory of a non-conductive particle in magnesium LiMCA 185
5 — 22 Proposed new design of ESZ for magnesium LiMCA 186
5 — 23 Schematic of the quartz tube arrangement for steel LiMCA 188
5 — 24 Velocity vectors at typical operating condition and conditioning operation in steel LiMCA 190

6 — 1 Schematic representation of "smart-probe" and its separation principle 198
6 — 2 Schematic representation of the domain and non-orthogonal, boundary-fitted grid used in the computation. 201
6 — 3 Distribution of the electrical potential, electric current density, self-induced magnetic flux density, and specific electromagnetic force for a "smart-probe". 205
6 — 4 Predicted velocity vectors and streamlines for a "smart-probe" 206
6 — 5 The effect of particle size and density on the particle trajectories in a "smart-probe" 208
6 — 6 The effect of electric current I (ampere) / orifice size D (μm) arrangement on the pass-through fraction of particles for a "smart-probe". 211
6 — 7 The effect of orifice length $L_{orifice}$ on the pass-through fractions of particles for a "smart-probe" 212
6 — 8 The streamlines for a "smart probe" with cylindrical orifice, the effect of orifice shape on the pass-through fraction of particles for a "smart-probe". 214

6 — 9 The effect of extension radius H on the pass-through fraction of particles for a "smart-probe" 215

6 — 10 The effect of extension length L_e on the pass-through fraction of particles for a "smart-probe" 216

6 — 11 The predicted velocity vectors and streamlines for a "smart-probe" of $u_m = 0.5 m/s$ 217

6 — 12 The effect of mean fluid velocity u_m on the pass-through fraction of particles for a "smart-probe" 219

6 — 13 The predicted pass-through fraction in "smart-probe" for magnesium and steel 220

B — 1 The 2D control volume and the notion 232

B — 2 Non-orthogonal, boundary-fitted grid used in lid-driven cavity flow 237

B — 3 Predicted streamlines for 300x300 CV at Re=100 237

B — 4 Variation of (a) minimum and (b) maximum stream function values at Re=100 as a function of control volume number 238

B — 5 Non-orthogonal, boundary-fitted grid used in laminar flow around a circular cylinder in a channel 239

B — 6 Drag coefficient for the 2D flow around a cylinder in a channel as a function of control volume number 240

B — 7 Trajectory of a steel ball in air 242

B — 8 Predicted particle trajectory inside an electric dust precipitator 243

List of Tables

1 — 1 Electromagnetic phenomena in materials processing operations 2

4 — 1 Physical properties of water and particles used in the particle discrimination study 115

4 — 2 Discharge coefficient for the probes used in particle discrimination study . . 124

5 — 1 Physical properties of liquid aluminum and particles as well as typical operating conditions of LiMCA in molten aluminum 149

5 — 2 Physical properties of liquid magnesium and typical operating conditions of LiMCA in molten magnesium 184

5 — 3 Physical properties of liquid steel and typical operating conditions of LiMCA in molten steel 189

6 — 1 Operating conditions and detection limit in molten metals 196

6 — 2 Probe dimensions, operating conditions and physical properties of molten magnesium 203

List of Symbols

a	radius of a spherical particle or equatorial radius of a spheroidal particle (m)
A	equipotential surface area inside orifice (m^2)
b	half symmetric axis of a spheroidal particle (m)
B	correction factor for history force
$\vec{B}$	magnetic flux density vector (weber/m^2)
C_D	drag coefficient
D	electric sensing zone diameter (m)
E	aspect ratio of a spheroidal particle
$\vec{E}$	electric field vector (volts/m)
E^M	correction factor for electromagnetic force
$\vec{F}$	Lorentz force per unit volume (N/m^3)
$\vec{F}_b$	body force term in Navier-Stokes equation (N/m^3)
Fr	Froud number
$\vec{g}$	gravitational acceleration vector (N/kg)
$\vec{H}$	magnetic field vector (amperes/m)
H	radius of extension in smart-probe (m)
I	electric current (amperes)
$\vec{J}$	electric current density vector (amperes/m^2)
J_0	electric current density at inlet (amperes/m^2)
J_x	axial component of the electric current density vector (amperes/m^2)
J_r	radial component of the electric current density vector (amperes/m^2)
k	blockage ratio
L	electric sensing zone length (m)
L_e	length of extension in smart-probe (m)
$L_{orifice}$	length of the orifice (m)
M^A	correction factor for added mass force

m_p	particle mass (kg)
m_f	fluid mass displaced by the particle (kg)
p	pressure (N/m^2)
R	electric sensing zone radius (m)
R^D	correction factor for drag force
Re	Reynolds number
Re_m	magnetic Reynolds number
Re_p	particle Reynolds number
R_H	magnetic pressure number
S	shape factor of a parabolic orifice
S_p	shape factor of a spheroidal particle
$\mathrm{S_h}$	source term for joule heating (W/m^3)
t	time (s)
$\vec{u}$	fluid velocity vector (m/s)
u	axial fluid velocity (m/s)
u_m	mean fluid velocity at the throat of a parabolic orifice (m/s)
$\vec{u}_p$	particle velocity vector (m/s)
u_p	axial particle velocity (m/s)
v	radial fluid velocity (m/s)
v_p	radial particle velocity (m/s)
V_p	particle volume (m^3)
y_0	entry point of particle flowing into an orifice (m)
μ_0	magnetic permeability of free space (Heneries/m)
μ_f	fluid dynamic viscosity (kg/m• s)
μ_m	magnetic permeability (Heneries/m)
ρ_{eff}	effective electrical resistivity of a compound media (ohm•m)
ρ_f	fluid density (kg/m^3)

ρ_p particle density (kg/m^3)

ρ_e electrical resistivity of fluid (ohm•m)

ρ_{e_p} electrical resistivity of particle (ohm•m)

ν_f fluid kinematic viscosity (m^2/s)

δ electromagnetic skin depth (m)

σ_e electrical conductivity (ohm^{-1}•m^{-1})

σ_f electrical conductivity of fluid (ohm^{-1}•m^{-1})

σ_p electrical conductivity of particle (ohm^{-1}•m^{-1})

φ electrical potential (volts)

ω angular frequency (s^{-1})

ψ magnetic scalar potential (amperes)

η_m magnetic diffusivity (m^2/s)

CHAPTER 1

Introduction and Background

Electromagnetic phenomena are involved in a wide variety of materials processing operations.[1] In most cases, the motion of particles is a major concern. For example, in the induction melting of steels, melts are gently agitated in order to promote the floatation of lighter, non-metallic inclusion particles. In the preparation of dispersion-hardened composite materials, agitation has to be supplied in order to keep buoyant or heavier particles in suspension. In electromagnetic separation of non-metallic inclusions, equipment is designed to move the inclusions to the wall of the pipes, through which a liquid metal is passed. In contrast, in LiMCA (Liquid Metal Cleanliness Analyzer) systems, special attention is paid to the design of the electric sensing zone (ESZ), so that the inclusions that need to be measured pass through, instead of depositing onto the wall of the ESZ.

In this chapter, firstly, a broad overview of the electromagnetic phenomena in materials processing operations is given, then the theory and the development of physical and mathematical modeling of these operations are reviewed, and finally the objectives of this research and outline of the thesis are described.

1.1 Electromagnetic Phenomena in Materials Processing Operations

Electromagnetic phenomena exist in many materials processing operations, where either an electric current, or a magnetic field, or both, are applied. A general overview of these processes is listed in Table 1.1.[1] In any event, an electromagnetic volume force (EMVF), $\bar{F} = \bar{J} \times \bar{B}$ ($\bar{F}$ is the electromagnetic force density, $\bar{J}$ current density, and $\bar{B}$ magnetic flux density), is excited within the liquid metals as a result of the interaction

Table 1.1 Electromagnetic phenomena in materials processing operations[1]

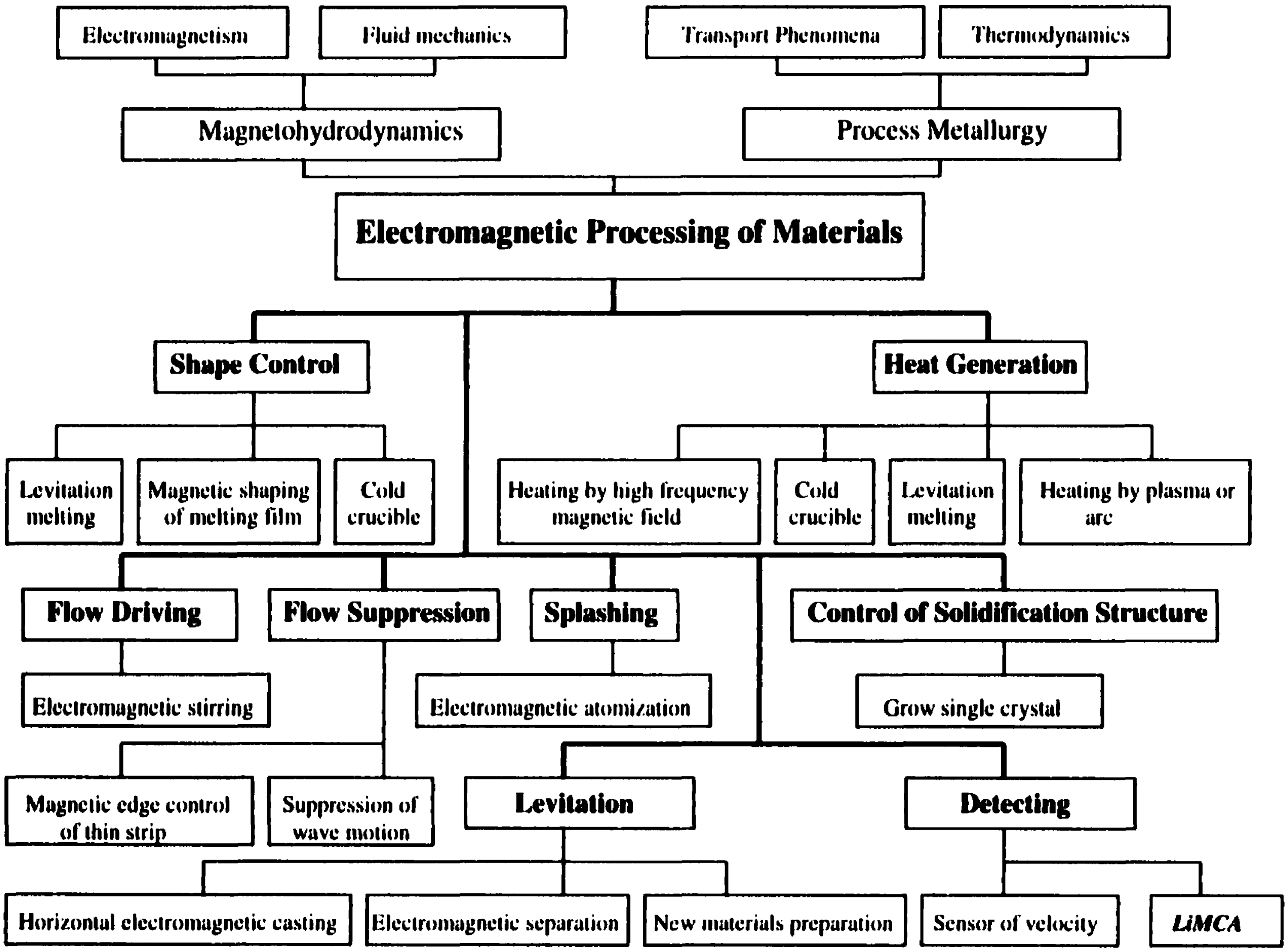

between the electric current and the magnetic field. EMVF may be resolved into two components:

$$\vec{F} = \vec{J} \times \vec{B} = (\vec{\nabla} \times \vec{H}) \times \vec{B} = -\vec{\nabla}(\frac{B^2}{2\mu_m}) + \frac{1}{\mu_m}(\vec{B} \bullet \vec{\nabla})\vec{B} \qquad (1.1)$$

where $\vec{H}$ is the magnetic field and μ_m is the magnetic permeability. The first term on the right of Equation (1.1) is the irrotational or potential part (magnetic pressure) of the body force, and the second term the rotational part. If the EMVF is potential ($\vec{\nabla} \times \vec{F} = 0$), it does not change the existing flow vorticity, and the effect can be balanced by a pressure gradient. However, if the EMVF is rotational ($\vec{\nabla} \times \vec{F} \neq 0$), additional motion will be induced in the liquid metals, where the initial velocity pattern may be changed dramatically.

1.1.1 Application of Rotational EMVF

Rotational EMVF is used widely in materials processing operations to stir or mix liquid metals. The purposes are to accelerate homogenization, or reaction and removal of inclusions, or to influence casting structure.[2-10]

Electromagnetic induction stirrers experienced their breakthrough in combination with electric arc furnaces(EAF) for steel making,[2,3] and resulted in a more uniform distribution of temperature and composition within the melt, increasing speeds in the dissolution of alloy additions, and improved the absorption of inclusions into the slag.

Induction heating and stirring of molten metals in induction furnaces is one of the most common applications of electromagnetic phenomena in materials processing.[4,5] In coreless induction furnaces, high frequency magnetic fields are applied to a scrap charge. This generates eddy currents, melting the charge by resistive heating, and, at the same time, causing a high degree of stirring within the molten metal. Metallurgical advantages include good compositional control and homogeneity, rapid melting, and good temperature uniformity and control. Induction stirring is also employed in ladle metallurgy, where the uniform and thorough stirring process accelerates reactions and improves homogeneity. It also promotes inclusion coalescence, but is unfavorable for the floating out of inclusions.[6]

Electromagnetic stirring has been used quite extensively for the control of solidification patterns in continuously cast billets, blooms and slabs.[7-10] Stirring the melt below the mold breaks off dendrites and improves temperature uniformity. These dendrite fragments act as nucleant to increase the central equiaxed zone. The stirring also reduces the centerline segregation of solute elements.

1.1.2 Applications of Irrotational EMVF

Irrotational EMVF has been used in electromagnetic separations,[11-26] in simulations of space manufacturing conditions,[27-29] for ore enrichment,[30] for electromagnetic brakes,[31,32] for electromagnetic valves,[33,34] and finally for damping flow motions.[35-40]

Electromagnetic separation can be employed to separate non-metallic inclusions from liquid tin, aluminum, and steel,[15,16,19,20] and to eliminate tramp elements, such as iron, manganese and zinc in aluminum scraps, from molten metals,[21] to recover metals from slags,[22,23] and to intensify the flotation of small bubbles in vacuum degassing processes.[24,25] The underlying principle for these separations is that when a liquid metal is subjected to an irrotational EMVF, the pressure gradient distribution within the metal can exactly balance these EMVF forces. Any particle with an electrical conductivity different from that of the metal experiences a force. This force is in the same direction as the EMVF for particles which are more conductive than the liquid metal, but acts in the opposite direction to the EMVF for particles that are less conductive. However, the practical realization of these separations depends on the suppression of fluid motion. In general, imposing a uniform EMVF in a melt is difficult, and the rotational part of the force induces fluid motions which agitate the melt together with inclusions, thereby making electromagnetic separation impractical. Suppression of the circulating flows can be achieved by adopting a bundle of thin pipes or a filter brick through which the melts flow,[21] or imposing pulse EMVF with various duty factors and duration.[26] In the former case, the motion of the melts in a small channel or a filter pore is strongly constrained by the surrounding walls, and the agitation which could have been caused by the rotational part of the EMVF can be suppressed. In the latter case, circulating flows do not have time to develop due to the large inertia of the fluid medium.

Simulating space manufacturing conditions on the ground provides unique methods for producing composites composed of immiscible metals. For example, the Al-Pb system[27] gives good anti-friction performance if a homogeneous alloy can be produced. However, under normal crystallization conditions, lead separates from aluminum very rapidly, sinking to the bottom of the melt. Irrotational EMVF can be applied to compensate for the gravity force, causing a quasi-weightless condition allowing one to obtain homogeneous Al-Pb materials. This method has also been proposed for producing space used Zn-Pb materials and porous metals.[29]

Electromagnetic brakes have been developed to reduce the flow velocity and suppress turbulence in continuous casting molds.[31,32] This prevents mold powder entrapment and the penetration of inclusions into the solidification front. To accomplish this, a strong DC magnetic field is applied across the width of the mold, inducing a current and generating a braking force in the direction opposing that of the liquid metal flow.

In other metallurgical applications, irrotational EMVF can act as electromagnetic valves to control the flow rate of a stream of liquid metal from a tundish into a casting mold, thereby providing a valve with precise control, no moving parts, and fewer refractory components than in the traditional stopper rod system.[33,34] The use of fewer refractory components reduces the chances of exogenous non-metallic inclusions entering into the product.

Irrotational EMVF can also be used to dampen fluid flow in Czochralski and Bridgeman crystal growth systems in the production of high quality single crystals.[35-39] The flow fields in these systems are due to natural convection arising from thermal gradients, to forced convection from rotation of the crystal and/or crucible, and to surface tension driven flows. Damping the flow can reduce the transport of impurities from crucible walls and free surface to the solidifying crystal. Irrotational EMVF is also useful in controlling the edge shape in direct strip casting process[40] by damping the fluid motion.

1.1.3 Applications of Both Rotational and Irrotational EMVF

In some materials processing operations, both rotational and irrotational components of EMVF are utilized to stir and confine the molten metals simultaneously.[41-51] Levitation melting[41-43] of small droplets has been a useful scientific tool to study gas-melt reactions as well as undercooled melts.[41,42] In this process, the droplets can be held in free space by the magnetic pressure force, avoiding contact with any solid surfaces. This avoids the contamination of the melt and reduces the initiation sites for nucleation during solidification. Thus, large amounts of super-cooling can be attained in solidification experiments. In addition, efficient electromagnetic stirring results in a homogeneous product.[43]

The electromagnetic levitation continuous casting process[44] can be used to produce high quality cast rods. EMVF holds the shape of the charge and stirs the liquid during solidification. The advantages are high casting speed, excellent dimensional control, and a homogeneous, equiaxed, fine-grained structure.

Magnetic suspension melting processes combine melting, melt treatment and casting into one single operation.[45,46] In this case, EMVF supports the metal at all stages of melting, and provides vigorous stirring in the melt as well. The castings are free from inclusions and gas porosity, and have fine-grained equiaxed structures, irrespective of the cooling rate in the mold.

In the DC electromagnetic casting process, the lateral supporting effect of a conventional DC mold is obtained by a horizontal magnetic pressure force field located within the upper liquid part of the ingot.[47-51] This potential force also contributes to the shape of the meniscus, while the rotational force causes the stirring. An electromagnetic screen is usually necessary to dampen the flow motion on the free surface induced by the stirring. By this process, ingots can be obtained with improved surface quality, no contamination from the mold, reduced dendrite arm spacing, and homogeneous chemical composition.

1.1.4 Unintentionally Applied EMVF Involved in High-Current Processes

Electromagnetic forces are not always present in metallurgical systems to achieve a specific objective. In cases where an electric current is applied, usually for the purpose of heating, melting, inclusion detecting (LiMCA systems), or causing an electrolytic reaction, magnetic fields arise as a natural consequence. This gives rise to an electromagnetic force which must be accounted for in analyzing the systems.

In both electroslag refining (ESR) furnaces and slag resistance furnaces (SRF), one or more electrodes are immersed in a slag and an electric current is applied between the electrodes. In ESR, a single or multiple consumable electrodes are immersed from the top into a slag. The current passes through the slag into the cylindrical resolidified ingot being withdrawn from the bottom, which constitutes the bottom electrode. The axial current generates a tangential magnetic field, and the interaction between the magnetic field and the current generates an EMVF directed both axially downward and radially inward. The axial current and tangential magnetic field generate an irrotational inward radial force which does not contribute to the fluid flow, while the radial current and tangential magnetic field generate a rotational axial force downward which causes the circulation inside the furnaces. A significant effect of the radial inward EMVF is to move the droplets of liquid metal towards the axis of the bath as they pass through the slag, which is extremely unfavorable for the process.[52,53] In SRF,[54] the electric current and its self-induced magnetic field also create a radial inward and axial downward EMVF. The electric current also heats the slag due to its electrical resistance, creating an upward buoyancy force. Whether the flow in the slag is dominated by convection or EMVF depends on the geometry of the system and the physical properties of the materials involved.

In vacuum arc remelting (VAR) furnaces, electric arc furnaces (EAF) and ladle refining furnaces, the situation is similar to ESR system, with the major exceptions being that the electrodes are generally not submerged and the electric current also travels through the arc.

In welding operations, the electromagnetic effects are very similar to the cases described above, depending on the type of the welding process. Electroslag welding (ESW) is very similar in principle to the electroslag refining (ESR) process. Different geometries, however, can result in markedly different flow behavior.[55] Arc welding operations, such as tungsten inert gas (TIG) or gas tungsten arc welding (GTAW), are similar to the electric arc furnace. Electromagnetics plays a role in both the plasma flow in the arc and in the molten weld pool stirring.[56] Hall-Heroult cells are employed in the electrolytic production of aluminum.[57,58] The EMVF causes stirring in the molten salt which enhances the desired dissolution of aluminum oxide, but also contributes to undesired effects such as disturbance of the interface between aluminum and the carbon floor which leads to carbide formation, to interfacial oscillatory wave motions between the electrolyte and metal that limits the thinness of the electrolyte between the upper carbon anodes and the cathode pool of molten aluminum. This in return leads to lower cell efficiencies, owing to the I^2R heating of a thicker electrolyte layer sandwiched between the carbon anode and the molten aluminum accumulating on the floor of the cell.

Another technique that employs high currents is the LiMCA system. LiMCA (Liquid Metal Cleanliness Analyzer) was first developed at McGill University in the early 1980s,[59,60] and is an on-line rapid quantitative method for evaluating the cleanliness of molten metals. It has the advantage of providing not only information on the volume concentration of inclusions, but also on their size distribution both quickly and accurately. This technique has been successfully used in the aluminum industries,[61] and is being extended to other metals, such as alloys of copper,[62] magnesium[63,64] and liquid steel.[65,66]

LiMCA is based on the electric sensing zone (ESZ) principle or Coulter Counter principle,[67] in which a constant current is maintained across two electrodes that are separated by an insulating sampling tube. A small orifice is built into the tube wall, through which liquid metal flows. When suspended particles pass through this orifice, the electrical resistance across the orifice increases or decreases in direct proportion to a particle's volume depending on the relative conductivity of the particle to that of the melt. Voltage pulses generated by an inclusion's passage through the orifice in the presence of an electric current can be measured, allowing the number and size of particles to be counted.

As confirmed in aqueous systems, the amplitude of the resistance change produced when a particle passes through the orifice depends not only on its size,[68,69] but also its shape,[70-75] aspect ratio,[75-77] orientation,[73,74] physical properties,[78-81] and path through the orifice.[82-89] Moreover, the motion of particles within the orifice is reflected in the shapes of the voltage pulses.[73,74,76,77]

In molten metals, the electric current density flowing through the orifice can be as high as 840 amperes/mm^2. This high current interacts with its self-induced magnetic field, resulting in a strong EMVF within the orifice. The EMVF may be irrotational or rotational depending on the geometry of the orifice. Thus, the motion of the particles will depend on both the hydrodynamic and electromagnetic conditions within the orifice, as well as the physical properties of the particles.

Particles of different density should follow different trajectories as they pass through the orifice. Correspondingly, the shape of voltage pulse should have its own characteristics, based on which particle discrimination should be possible. Distinguishing heavy, hard solid particles from light, soft gas bubbles or droplets in molten metals is very important in view of the role played by different kinds of inclusions in affecting the properties of materials. For this purpose, the DSP (Digital Signal Processing) technology[90] was introduced to replace analogue-based LiMCA systems. The DSP-based LiMCA system is shown in Appendix A. In such a LiMCA system, the resistive pulse generated by the passage of particle is amplified, the signal digitized and the data stored on a host computer. With DSP, more information can be extracted by characterizing each voltage pulse with not only the peak height as per the analogue detector but also peak width, peak time, starting time, transit time, starting slope and ending slope. The ability of the new DSP monitoring system to discriminate gas bubbles from denser particles has been proved experimentally in a water-based LiMCA system.[91]

Successful operation of LiMCA systems depends on a procedure called conditioning,[92] prior to each sampling. It involves passing a 200−300 amperes electric current surge through an orifice of around 300 μm. The application of this high current, compared to 20−60 amperes working current, apparently removes particles attached to the inner wall of the orifice, thereby preventing the orifice from being blocked. However, when the size of a particle is equal to, or even bigger than, the orifice, blockage still happens. In aqueous electrolyte medium, two or more tubes with different apertures,[93,94] a removable orifice,[95] an expandable orifice,[96] or an orifice fixed with a micromesh screen[97] were suggested to surmount the blockage problem. However, none of these proposals for aqueous seems practical for liquid metals considering the hostile thermal and chemical environments in molten metals.

As can be seen from above, all these materials processing operations are related to the motion of particles in molten metals or slags under the action of electromagnetic forces. Therefore, the understanding of the fluid flow in electromagnetic fields and the motion of particles within the fluid is very important in terms of improving productivity and materials quality control. To date, many efforts have been devoted to the theoretical study and mathematical and physical modeling of these processes, as will be reviewed in the next section.

1.2 Review of Mathematical and Physical Modeling in Electromagnetic Materials Processing

This section begins with a brief description of the underlying theory on which the mathematical modeling of fluid flows and particle motions in electromagnetic materials processing is based. Next, previous work is summarized, first on mathematical modeling, and then on physical modeling and experimental measurements.

1.2.1 Theory

1.2.1.1 Fluid flow and electromagnetic fields

The mathematical modeling of fluid flows in electromagnetic materials processing is accomplished by solving the Navier-Stokes equations for the fluid flow, Maxwell's equations for the electromagnetic fields, and including the Lorentz force field as a source term in the Navier-Stokes equations. In the case of turbulent flow, a turbulence model, such as the well known $k-\varepsilon$ model,[98] needs to be supplemented. In addition, theoretical relationships for mass and heat transfer, two-phase flow, and solidification may be needed for a specific problem. In this section, only the basic laminar steady state equations, which are related to the studies reported in this thesis, are described.

The equation of continuity is:

$$\vec{\nabla} \bullet \vec{u} = 0 \tag{1.2}$$

The equation of motion is:

$$\vec{u} \bullet \vec{\nabla} \vec{u} = -\frac{1}{\rho_f} \vec{\nabla} p + \nu_f \nabla^2 \vec{u} + \vec{F}_b \tag{1.3}$$

where $\vec{u}$ is the fluid velocity, ρ_f is the fluid density, p is the pressure, and ν_f is the kinematic viscosity.

The body force term, $\vec{F}_b$, includes the effect of gravity as well as the electromagnetic force (Lorentz force) due to the interaction of electric current density ($\vec{J}$) and magnetic flux density ($\vec{B}$):

$$\vec{F} = \vec{J} \times \vec{B} \tag{1.4}$$

The boundary conditions are defined based on the particular situation being modeled. In order to solve for the electromagnetic force term, Maxwell's equations need to be solved. These may be written as follows, using the MHD approximation:[99,100]

$$\bar{\nabla} \times \bar{E} = -\frac{\partial \bar{B}}{\partial t} \quad \text{(Faraday's law)} \tag{1.5}$$

$$\bar{\nabla} \times \bar{B} = \mu_m \bar{J} \quad \text{(Ampere's law)} \tag{1.6}$$

$$\bar{\nabla} \bullet \bar{J} = 0 \tag{1.7}$$

$$\bar{\nabla} \bullet \bar{B} = 0 \tag{1.8}$$

where $\bar{E}$ is the electric field (volts/m).

The calculation of the electric current density and magnetic flux density from Maxwell's equations depends on how the fields are generated. If a DC current is applied, then the most appropriate way to solve for $\bar{J}$ is through the Laplace equation. For the case of spatially-variable conductivity, it can be described as:

$$\bar{\nabla} \bullet (\sigma_e \bar{\nabla} \varphi) = 0 \tag{1.9}$$

where φ is the electrical potential and σ_e is the electrical conductivity. The current density can then be calculated from Ohm's law, shown here including the interaction term between the fluid velocity and the magnetic field:

$$\bar{J} = \sigma_e(-\bar{\nabla}\varphi + \bar{u} \times \bar{B}) = \sigma_e(\bar{E} + \bar{u} \times \bar{B}) \tag{1.10}$$

Once the current density is known throughout the system, $\bar{B}$ can be calculated from the Biot-Savart law:

$$\bar{B}(\bar{r}) = \frac{\mu_m}{4\pi} \int_{V'} \frac{\bar{J}(r') \times \bar{i}_{rr'}}{|r - r'|^2} dV' \tag{1.11}$$

where $\vec{J}(r')$ is the electric current density at the source, and $\vec{i}_{rr'}$ is the unit vector from $\vec{r}$ to $\vec{r}'$. The Biot-Savart law is extremely useful in the case of three dimensional configurations, since the magnetic field only needs to be calculated at positions of interest instead of throughout the entire geometry being modeled. It is, however, important to include all of the current sources which could have an influence on the magnetic field, including the electrodes, cables and busses carrying current into, and out of, the system.

In the case of alternating current (AC), the equations for DC are still applicable if the scale of the system is much smaller than the electromagnetic skin depth, δ, which is the measure of the depth to which a magnetic field can penetrate a conducting material:

$$\delta = \sqrt{\frac{2}{\mu_m \sigma_e \omega}} \tag{1.12}$$

where ω is the angular frequency.

In systems with constant magnetic fields such as permanent magnets or DC electromagnets, the magnetic field may be calculated using the magnetic scalar potential, ψ, given that the boundary conditions can be determined properly:

$$\vec{\nabla} \bullet (\mu_m \vec{\nabla} \psi) = 0 \tag{1.13}$$

The form of the equation accounts for spatial variation in magnetic permeability. The magnetic flux density, $\vec{B}$, can then be calculated from the potential as follows:

$$\vec{B} = -\mu_m \vec{\nabla} \psi \tag{1.14}$$

Combining Ampere's law (1.6) with Ohm's law (1.10), Faraday's law (1.5) and magnetic flux conservation equation (1.8), and rearranging in terms of the magnetic flux density, leads to the magnetic transport equation, which contains both diffusive and convective terms:[99]

$$\frac{\partial \bar{B}}{\partial t} = \eta_m \nabla^2 \bar{B} + \bar{\nabla} \times (\bar{u} \times \bar{B}) \qquad (1.15)$$

where $\eta_m = 1/\sigma_e \mu_m$ is the magnetic diffusivity. The first term on the right hand side of equation (1.15) is the diffusive term, and the second term is the convective term. The magnetic transport equation is frequently used in problems with time-varying magnetic fields. In these cases, the magnetic flux density is calculated first, then $\bar{J}$ is calculated from $\bar{B}$ using Ampere's law (1.6). When the magnetic Reynolds number is much smaller than unity, i.e. $\mathrm{Re}_m = uL/\eta_m << 1$ with L standing for the characteristic length, diffusive transport dominates, and the convective term can be ignored. This is the case in many materials processing systems, which means that the electromagnetic equations and the fluid flow equations are decoupled, allowing for separate calculations first of the electromagnetic forces and then of the fluid flow.

The electromagnetic force field was also calculated using mutual inductance technique, first in induction furnace,[101] and later in levitation melting of metal droplets.[41] In this technique, the system is divided into a set of electrical circuits with the current in each dependent on the current in the others.

If the heat generated by the passage or induction of electric currents within the system needs to be considered, it can be accounted for in the source term, S_h, and calculated from the electric current density distribution:

$$S_h = \frac{|\vec{J}|^2}{\sigma_e} \tag{1.16}$$

1.2.1.2 Particle motions

In conventional hydrodynamics (without electromagnetic force), several equations accounting for the unsteadiness of the particle motion have been developed wherein a superposition of the steady drag and the unsteady (history) drag is used to obtain the forces on the particle.

Originally, the motion of a sphere settling out under gravity in an incompressible, viscous fluid that was otherwise at rest was examined.[102-104] The flow disturbance produced by the motion of the sphere was assumed to be at a sufficiently low Reynolds number that the fluid force on the sphere could be calculated based on the results of unsteady Stokes flow. The Stokes drag on the sphere, which is in an accelerated motion, still carries the same formula as the steady drag, $6\pi\mu_f a u_p(t)$, where μ_f represents the dynamic viscosity of the fluid, a the radius of the particle, and $u_p(t)$ the instantaneous particle velocity. Two new force terms, the added mass and Basset force, result from the unsteady motion. Later, the work was extended to non-uniform creeping flow,[105,106] and the motion of particles was described by the following equation:

$$\begin{aligned} m_p \frac{d\vec{u}_p}{dt} &= (m_p - m_f)\vec{g} + m_f \frac{D\vec{u}}{Dt} - \frac{1}{2} m_f \frac{d}{dt}(\vec{u}_p - \vec{u} - \frac{1}{10} a^2 \nabla^2 \vec{u}) - \\ & 6\pi a \mu_f (\vec{u}_p - \vec{u} - \frac{1}{6} a^2 \nabla^2 \vec{u}) - \frac{6\pi a^2 \mu_f}{(\pi \nu_f)^{1/2}} \int_0^t \frac{d(\vec{u}_p - \vec{u} - \frac{1}{6} a^2 \nabla^2 \vec{u})}{d\tau} \frac{d\tau}{(t-\tau)^{1/2}} \end{aligned} \tag{1.17}$$

where ν_f is the kinematic viscosity of the fluid, $\bar{u}$ the velocity of the fluid, m_p and m_f are the particle mass and fluid mass displaced by the particle, respectively. The inclusion of velocity gradients leads to modifications of the added mass, the Stokes drag and the Basset history term due to the curvature in the velocity profile.

A widely used equation[107] for non-creeping flow was obtained by empirically modifying the Stokes drag to drag force for finite Reynolds number:

$$m_p \frac{d\bar{u}_p}{dt} = \frac{1}{2} C_{D_\infty} \pi a^2 \rho_f \left|\bar{u} - \bar{u}_p\right| (\bar{u} - \bar{u}_p) + \frac{1}{2} m_f \frac{d(\bar{u} - \bar{u}_p)}{dt} + m_f \frac{D\bar{u}}{Dt} + \\ 6a^2 (\pi \mu_f \rho_f)^{\frac{1}{2}} \int_0^t \frac{d(\bar{u} - \bar{u}_p)/d\tau}{(t-\tau)^{1/2}} d\tau + (m_p - m_f)\bar{g} \tag{1.18}$$

where C_{D_∞} is the standard drag coefficient from the steady standard drag curve. The added mass term $\frac{1}{2} m_f \frac{d(\bar{u} - \bar{u}_p)}{dt}$ was corrected to $\frac{1}{2} m_f (\frac{D\bar{u}}{Dt} - \frac{d\bar{u}_p}{dt})$ in studying the potential flow about a spherical bubble where the ambient flow is irrotational and non-uniform.[108] More recent numerical studies[109-112] confirmed that the added mass term for finite Reynolds number fluid flows is the same as that predicted both by creeping flows and potential flow theory.

The force on a guided sphere rectilinearly oscillating in an otherwise stagnant fluid for $0 \leq \mathrm{Re} \leq 62$ was studied experimentally, and an equation for the motion of a sphere proposed[113,114]:

$$m_p \frac{d\bar{u}_p}{dt} = -\frac{1}{2} C_{D_\infty} \pi a^2 \rho_f \left|\bar{u}_p\right| \bar{u}_p - C_a \frac{1}{2} m_f \frac{d\bar{u}_p}{dt} - C_h 6a^2 (\pi \mu_f \rho_f)^{\frac{1}{2}} \int_0^t \frac{d\bar{u}_p/d\tau}{(t-\tau)^{1/2}} d\tau \tag{1.19}$$

with C_a and C_h were obtained experimentally and were given by:

$$C_a = 2.1 - 0.132 M_{A1}^2 / (1 + 0.12 M_{A1}^2)$$

$$C_h = 0.48 + 0.52 M_{A1}^3 / (1 + M_{A1})^3$$

where M_{A1} is the dimensionless relative acceleration defined by:

$$M_{A1} = \frac{2a}{\left|\bar{u} - \bar{u}_p\right|^2} \left| \frac{d\left|\bar{u} - \bar{u}_p\right|}{dt} \right| \tag{1.20}$$

Study of an unsteady flow over a stationary sphere with small fluctuations in the free-stream velocity at finite Reynolds number ($0.1 \le \mathrm{Re} \le 40$) showed that the Basset-force term in the equation of particle motion should have a kernel which must decay much faster than $(t-\tau)^{-1/2}$ at large time.[110] A modified expression for the Basset force was proposed[115,116] based on the analytical result at small Reynolds number for low frequency free-stream fluctuations, the numerical result at finite Reynolds number for low frequency fluctuations, and the unsteady Stokes result for high frequency fluctuations:

$$\begin{aligned} m_p \frac{d\bar{u}_p}{dt} &= \frac{1}{2} C_{D_{ss}} \pi a^2 \rho_f \left|\bar{u} - \bar{u}_p\right| (\bar{u} - \bar{u}_p) + \frac{1}{2} m_f \left(\frac{D\bar{u}}{Dt} - \frac{d\bar{u}_p}{dt}\right) + m_f \frac{D\bar{u}}{Dt} + \\ & 6 a \pi \mu_f \int_{-\infty}^{t} K(t-\tau, \tau) \frac{d(\bar{u} - \bar{u}_p)}{d\tau} d\tau + (m_p - m_f)\bar{g} \end{aligned} \tag{1.21}$$

with the broad-frequency-range approximation for the integral kernel given by:

$$K(t-\tau, \tau) = \left\{ \left[\frac{\pi (t-\tau) \nu_f}{a^2} \right]^{\frac{1}{4}} + \left[\frac{\pi}{2} \frac{\left|\bar{u}(\tau) - \bar{u}_p(\tau)\right|^3}{a \nu_f f_H^3(\mathrm{Re}_t)} (t-\tau)^2 \right]^{\frac{1}{2}} \right\}^{-2} \tag{1.22}$$

where $f_H(\mathrm{Re}_t) = 0.75 + 0.105\mathrm{Re}_t(\tau)$ and $\mathrm{Re}_t = \dfrac{2a|\bar{u}(\tau) - \bar{u}_p(\tau)|}{\nu_f}$. Equation (1.22) shows that the history kernel decays initially as $t^{-\frac{1}{2}}$ but as t^{-2} at large time. When the initial velocity difference between the sphere and the carrier fluid is not zero, an additional term, $6a^2(\pi\mu_f\rho_f)^{\frac{1}{2}}(\bar{u}(0) - \bar{u}_p(0))\big/t^{\frac{1}{2}}$, needs to be added to the above particle motion equation.[117] The motion of spheroidal particles is also affected by the shapes and orientations. In creeping flow, the equation of motion for a sphere was generalized for a spheroid moving parallel to its axis of symmetry as follows:[118]

$$m_p \frac{d\bar{u}_p}{dt} = R^D 6\pi a\mu_f \bar{u}_p + M^A \frac{m_f}{2}\frac{d\bar{u}_p}{dt} + B6a^2(\pi\rho_f\mu_f)^{\frac{1}{2}} \int_{-\infty}^{t} \frac{d\bar{u}_p/d\tau}{(t-\tau)^{1/2}} d\tau \quad (1.23)$$

where a is the equatorial radius of the spheroid and R^D, M^A, and B are the correction factors for drag, added mass and Basset forces, respectively. These correction factors are functions of aspect ratio (E), which is b/a with b representing the half axis of symmetry.[119-122] For a spheroidal particle moving perpendicular to its axis of symmetry, the equation of motion takes a similar form to Equation (1.23), but with different correction factors, which are also functions of aspect ratio.[120,123-125] For finite Reynolds numbers, the correction factor for the drag force has a very complex dependence on E and was obtained numerically.[126,127] More complications are introduced when the direction of motion of a spheroid is not along the principal axes of the particle. In this situation, besides a net drag which is parallel to the direction of motion, a lift force also exists, which is perpendicular to the direction of motion.[128] The total of the drag and lift forces depend strongly on particle shape, aspect ratio and the angle between the direction of motion and the axis of symmetry.[127]

All these studies are based on particle motions in fluids of infinite extent. In reality, the presence of solid surfaces in the vicinity of the moving particles may markedly affect the drag force.[120] In essence, the movement of a particle in the vicinity of solid surfaces may be affected in two ways. One is due to the fact that the velocity gradients may cause an imbalance in the forces acting on the particle, which results in rotation of the particle. The other is due to the fact that when a particle approaches a solid surface, fluid has to be displaced. The viscous resistance to the fluid flow will cause an apparent increase in the drag force. The interaction of a particle with walls depends on the particle shape, orientation, position, and geometry of the containing walls, as well as Reynolds number. At low Reynolds number, a wall correction factor, which equals the ratio of the drag in the bounded fluid to the drag in a fluid of infinite extent, has been determined for a sphere moving a) along,[128-131] or eccentrically parallel to, the axis of a circular cylindrical tube,[132] b) parallel to one[132] or two[133] stationary parallel walls, and c) perpendicular to a plane wall.[132,134] Wall correction factors have also been determined for a spheroid moving between two parallel walls, parallel to a plane wall with its symmetry axis at an arbitrary angle to the wall, and along the axis of a circular tube.[132] At high Reynolds number, the configuration that has been studied to determine the wall correction factor is for a sphere moving along the axis of a cylindrical tube.[131, 135-137]

In the field of electromagnetic processing of materials, the motion of particles is affected by both the hydrodynamic and the electromagnetic conditions within the fluids. In applied magnetohydrodynamics, considerable efforts have been given to derive the electromagnetic volume force on inclusions in an electrically conductive liquid. A theoretical formulation for the EMVF on a spherical particle with an electrical conductivity different from that of the surrounding liquid was given as:[138]

$$\bar{F}_p = -\frac{3}{2}\left(\frac{\sigma_f - \sigma_p}{2\sigma_f + \sigma_p}\right)\frac{4\pi a^3}{3}\bar{F} \tag{1.24}$$

where σ_f and σ_p are the electrical conductivity of the fluid and the particle, respectively.

Electromagnetic forces on non-conductive particles of different shapes and orientations suspended inside a current-carrying circular cylinder were derived without considering the disturbance of the current by the presence of the particles, and the formulae are:[139]

$$F_p = 2\mu_m J^2 la^2(a+h) \tag{1.25}$$

for a cylindrical particle with its axis parallel to the tube axis,

$$F_p = \frac{1}{4}\pi\mu_m J^2 a(2hl + l^2) \tag{1.26}$$

for a cylindrical particle with its axis perpendicular to the tube axis, and

$$F_p = \pi\mu_m J^2 ha^3 \tag{1.27}$$

for a sphere. J is the electric current density, l is the length of the cylindrical particle, and h is the distance from the axis of the tube to the generatrix of the cylindrical particle or the center of the sphere.

Taking into account of the disturbance of the electric current by the particles, the electromagnetic force on a sphere suspended in a current-carrying circular cylinder[18] or in a solenoid fed by an alternating current[17] were derived. The force has three components which are 1) the electromagnetic Archimedes force generated by the unperturbed electric current, 2) the electromagnetic propulsion force generated by the perturbed electric current, and 3) the Lorentz force generated by the current inside the conducting particle. The total force can be represented as:

$$\bar{F}_p = \frac{3(1-\chi)}{4}\bar{F} \tag{1.28}$$

$$\chi = \frac{3\sigma_p}{\sigma_p + 2\sigma_f} \tag{1.29}$$

In fact, the force has the same value as from Equation (1.24), which was derived for an infinite fluid with crossed electric and magnetic fields.

The electromagnetic force on cylindrical particles of different orientation were also derived by accounting for the disturbance of the electric current streamlines.[12]

1.2.2 Mathematical and Physical Modeling of MHD and Experimentation

Electric energy has been used in metallurgy for processes such as melting, refining and solidification, where magnetohydrodynamic (MHD) phenomena are involved. The theoretical basis for MHD phenomena comes from plasma physics, astrophysics, fusion and nuclear energy.

In the western world, the first attempt to intentionally apply MHD to metallurgy was the establishment of the research center MADYLAM in France in 1978. The second was a Symposium of IUTAM (the International Union of Theoretical and Applied Mechanics) entitled "Metallurgical Applications of Magnetohydrodynamics" at Cambridge, UK in 1982. Thereafter, significant progress has been made in both fundamental research and in the development of new technologies.

1.2.2.1 Mathematical modeling

1.2.2.1.1 Fluid flow

In the computation of MHD flows in metallurgical systems, some important advances have been made: The use of primitive variables instead of vorticity and stream function, numerical rather than analytical solutions of the magnetic diffusion equations, the introduction of solidification models, the use of the mutual inductance technique, computations for non-Newtonian fluids, solutions in spherical and three-dimensional (3D) coordinate systems, and the calculation of free surface equilibrium shapes and free surface behavior of EM-levitated and stirred systems.

Early studies of fluid flow and electromagnetics in continuous casting[140] and induction furnaces[141] employed vorticity and stream function solutions of the full Navier-Stokes equations, the k-w turbulence model, analytical expressions for the solution of the two-dimensional (2D) axisymmetric magnetic diffusion equation, and the differential form of Ampere's law for the induced current density. For the calculation of the induced current in an induction furnace, the mutual inductance technique[101] was also used by solving the integral form of Ampere's law. In an ESR system, 2D axisymmetric magnetic transport equation was used in the calculation of the induced magnetic field and Ampere's law for the applied current.[142] 2D axisymmetric simulation of welding was carried out with hemispherical pool shapes, a distributed current source, and a finite-size electrode.[143,144]

Compared with the work on induction furnaces, a very different approach was used in the first 2D Cartesian mathematical modeling of the Hall-Heroult cell. The Laplace equation was used to solve the electrical potential distribution, the current density was calculated from Ohm's law, and the magnetic field was calculated from the Biot-Savart law. Fluid flow was calculated by turbulent form of Navier-Stokes equation, employing the k-ε turbulence model.[145] Later, the different electrical conductivities of materials were also taken into account in calculating the current path[57].

The free surface computation for the EM-driven flow in an induction furnace was initially based on a 2D axisymmetric system, where the free surface was calculated by balancing the gravitational and electromagnetic forces.[146]

Later on, the computation of fluid flow in an electromagnetically levitated sphere was conducted for the limiting cases of high surface tension and high frequency in a 2D spherical coordinate system,[147] and welding pool modeling was developed to include the complete solution of the laminar Navier-Stokes equations, electromagnetics, surface tension, buoyancy and heat transfer.[56] The fluid flow in the Czochralski system under an applied magnetic field was also studied numerically.[148]

Subsequently, the mutual inductance technique was used in the levitated sphere problem, which was completely solved in 2D spherical coordinates for electromagnetics, heat transfer, mass transfer, and turbulent fluid flow.[41] During this time, solidification was added in the calculation of melt pool profiles in ESR and weld pool models.[149,150]

Recently, the 3D Cartesian transient computation of the interface distortion in a Hall-Heroult cell was conducted.[151] The electric current was solved using the Laplace equation and the magnetic fields were solved using the Biot-Savart law. Inductive stirring in billet and slab caster configurations was also modeled in 3D using a combination of magnetic diffusion equation and the magnetic scalar potential.[152] Stirring in an induction furnace was calculated in 2D in the presence of a magnetic shield.[153] In this study, the mutual inductance technique was used to account for the combined effects of currents in the coils, melt and shield. Another noteworthy study was the 2D computation of EM stirring in non-Newtonian fluids.[154]

Electromagnetic braking was also modeled in 3D in a continuous caster mold[32] and shallow tundishes.[155,156] The former employed a non-orthogonal grid with an assumed magnetic field distribution, the latter used a Cartesian grid also with an assumed field distribution.

More recently, a mathematical model for electromagnetic casting in 3D was proposed,[157,158] where the mutual inductance technique was extended to 3D in order to solve Maxwell's equations for the electromagnetic field in and around the caster. The computations were self-consistent in that the free surface of the molten metal is adjusted in response to the supporting electromagnetic forces which are themselves dependent on the shape of that surface.

The behaviour of free surfaces in melts subjected to electromagnetic forces was studied with a sophisticated 3D model.[159] The calculations started with Maxwell's equations and Ohm's law, which were solved by a novel "modified hybrid technique", where the instantaneous instead of time-averaged continuity and Navier-Stokes equations were employed.

The computation of fluid flow and electromagnetic fields provide the hydrodynamic and electromagnetic conditions for studying the motion of particles within the liquid metals in these systems.

1.2.2.1.2 Particle motion

In many practical situations, the particle acceleration effects may be safely neglected because the major portion of the path traveled by the particle will be at the steady, terminal velocity. An example is the settling of solid particles in quiescent liquids, where the path to be traveled is many hundred or thousand times larger than the particle diameter.

There exists, however, an important group of problems where the trajectory of a solid particle in a fluid is dominated by the acceleration effects. In a study of the injection of alloy additions into stagnant steel baths, simulations were performed by dropping wooden spheres into water, and good theoretical predictions were made on sphere trajectories and immersion times by taking into account standard drag and added mass effects.[160] The subsurface trajectories of spherical particles in recirculating flows were also computed for simulating the motion of alloy additions during the furnace to ladle tapping operations.[161] The model employed for particle motion included particle inertia, gravity, buoyancy, added mass, and drag force terms. The same model was also used to predict subsurface trajectories of spherical addition in the CAS (composition adjustment by sealed argon bubbling systems) procedure,[162] and to calculate the trajectories of particles in a continuous billet caster.[163] The probability of entrapment of inclusions within the mushy zone was predicted based on the particle trajectories.

The behavior of both buoyant and non-buoyant particles in an inductively stirred melts were analyzed with a model including only particle inertia, gravity and drag force terms.[6] It was argued that the simplified model for particle motion was used because more complex relationships had not been experimentally verified for flows with strongly fluctuating components.

The motion of particles in levitated molten droplets was studied by balancing the Stokes drag and electromagnetic force on the particles.[164] A more sophisticated model which included particle inertia, fluid acceleration, drag, added mass, gravity and buoyancy, as well as the electromagnetic force, was used to study the effect of electromagnetic brake on inclusion behavior in a slab continuous caster.[165]

The dynamic motion of particles in a cylindrical MHD separator was studied by considering only the electromagnetic force and drag force in the radial direction.[166] The trajectories of particles in a current-carrying liquid metal in an infinitely long vertical pipe were investigated under the assumptions of small particle Reynolds number and negligible particle inertia with a prescribed fully developed Poiseuille flow. The radial velocity of the particle was derived by balancing the electromagnetic force and Stokes drag force, while the vertical velocity was obtained by superimposition of the terminal Stokes velocity on the metal velocity.[15]

A more comprehensive model for particle motion under the action of electromagnetic force, which included particle inertia, electromagnetic force, Stokes drag, and added mass, as well as Basset history force, was used to study the motion of particles released in a stagnant liquid contained in a solenoid.[18] The most significant finding is that Basset history force is very important in determining a particle's trajectory. A particle which is more conductive than the carrier liquid moved towards the axis of the solenoid, and performed at least one oscillation about the axis, the equilibrium position of the particle, in consistent with experimental observations.

There are many other studies where the convective-diffusion equation was used to determine particle concentrations and fluxes, the implicit assumption involved is that the particle inertia is negligible and particle trajectories can be computed from the fluid flow field plus a superimposed Stokes velocity component. One example is the study of particle separation within tundishes,[167-169] and another is the study of the effect of ultrahigh magnetic fields on dopant distribution in Czochralski crystal growth system.[39]

1.2.2.2 Physical modeling and experimentation

Physical modeling and experimentation are often employed to verify the validity of the predictions of the mathematical modeling.

In one of the earlier studies, radioactive tracers were used to measure the rate of mixing in an industrial ASEA-SKF ladle furnace.[141] The model predicted the tracer dispersion quite well, and the mean values of the eddy diffusivity to within a factor of two to three. In another study, surface velocities measured in a laboratory scale mercury-filled induction furnace were generally within 10% of the calculated value.[145] The same model was used to compare calculated versus measured surface velocities in a 12-ton induction furnace.[170] The results were somewhat poorer, with velocities calculated to within a factor of two of that measured, and a calculated maximum radial surface velocity at 77% of the radius versus at 89% radius measured.

Force probe technique which could measure two components of the velocity as well as the turbulence intensity was applied on a laboratory scale induction furnace.[171] Independent computational work showed good agreement with those measured values.[172,173]

The invention of Vive's probe[174] was a major breakthrough in velocity measurement devices. This probe allowed the measurement of velocities at much higher temperatures (as high as 670 °C) than could be accomplished by other means, such as hot film anemometry. With this probe, measurements were made in a rectangular aluminum ingot mold stirred with a linear motor.[175] The calculated stirring patterns were very similar to those measured although the measured velocity magnitudes are within 10% to a factor of 5 of those calculated. With the Vive's probe, velocities were also measured in a laboratory induction furnace with and without magnetic shields.[153] The measurements were compared with the computational results, and good agreement was obtained on the stirring patterns. Individual velocity values were generally within 25% to 50% between measured and computed. Surface velocities were also measured in a laboratory scale ESR system, and the maximum predicted velocities were calculated to be within 25% of the measured value.[176]

The rod dissolution technique has been used to measure velocities in both aluminum and steel systems. In the case of aluminum, velocities in a prototype Hall-Heroult cell were calculated to within about 10% to 50% of the measured values, with a generally good agreement of the flow patterns.[177] In the steel induction furnace, mass transfer coefficients were calculated to be within a factor of two of the measured values.[178]

Hot film anemometry has also been an important tool in the study of low temperature (<100°C) flow in EM-stirred liquid metals. Flow fields and turbulence in an ESR system were calculated to within 5–10% of the measured values.[179]

More recently, a physical model of an electromagnetic caster, which used Wood's metal, was constructed and measurements of electric and magnetic fields, deformation of the liquid surface and flow velocities were performed.[159] Electric fields were measured using an inverted "T" fashioned from a pair of insulated wires with their tips exposed. Vive's probe was used to measure the flow velocities and the shape of the molten metal surface was determined by lowering a titanium needle to make contact with the surface, thereby closing a circuit, which was recognized by a sharp drop in resistance. The predictions of all these values with a 3D mathematical model are in good agreement with the measurements.

In most studies on electromagnetic separations[11-26] or simulating space manufacturing conditions,[27-29] experiments were carried out to verify the reliability of the methods that seemed possible from a theoretical point of view. A quantitative experiment was designed, which measured the lateral deflection of the water drops flowing through a vertical channel filled with mercury in an electromagnetic fields. The theoretical prediction was in a reasonable agreement with the measurements.[12]

In LiMCA technology, a water based LiMCA system — APS II (Aqueous Particle Sensor) system, has been used to study the hydrodynamic conditions within the electric sensing zone and particle discrimination with DSP technology.[90] The study confirmed the importance of maintaining laminar flow conditions within ESZ and the possibility of discriminating heavy solid particles from light gas microbubbles. However, no equivalent computations were performed for model validation. Moreover, the applicability of the results to molten metals needs further investigation because the electromagnetic phenomena are much stronger in liquid metals than in aqueous solutions.

As can be seen from the above, although the fluid flows and the influences of electromagnetic fields on the flows have been investigated extensively, the study of the motion of particles within these fluids is quite limited. However, in many practical applications, such as electromagnetic separation, ESR, and LiMCA systems, the understanding of the particle motion is very important. This subject constitutes the main theme of this thesis, and will be detailed in the next section.

1.3 Objectives and Outline of This Thesis

As reviewed in the above two sections, all the previous studies concerning the effect of electromagnetic fields on the fluid flow and particle motions in electromagnetic materials processing can be generalized into three categories. The first category considered the particle population distribution within the fluids, which involved an implicit assumption that particle inertia is negligible, and particles follow the detailed motion of the fluid. In the second category, the mathematical models for fluid flow and electromagnetic fields are very comprehensive, while the particle motion model was simplified to different extents with either the Basset history term, or history and fluid acceleration terms, or history, fluid acceleration and electromagnetic force terms being neglected. In the third category, the Basset history term was included in the particle motion model. However, the fluid flow field was assumed either stagnant or to be a prescribed distribution, and the electromagnetic fields was given analytically due to the simple geometry considered.

In some applications, such as LiMCA systems and electromagnetic separation in small thin pipes, not only the fluid flow and electromagnetic fields need to be considered, the effect of each force term on the motion of particles needs to be determined as well. These force terms include particle inertia, drag, added mass, history, buoyancy and gravity, as well as electromagnetic. In addition, wall effects should be included considering the relatively small scale of the electric sensing zone in LiMCA systems or the thin pipes in electromagnetic separation compared to particle diameter. Moreover, the flow conditions in the entrance region have to be taken into account.

The aim of this thesis is to develop a general mathematical model regarding the motion of particles in current-carrying liquid metals, and apply it to the operations of LiMCA systems. In LiMCA systems, a study of particle trajectories within the electric sensing zone will help to improve the accuracy of particle size measurement, to realize particle discrimination, and to evaluate and design ESZ probes suitable for specific environments and materials of construction.

In this thesis, the electromagnetic force is generated by an applied DC current and its induced magnetic fields. This is consistent with the practical operations of LiMCA systems. However, it should be noted that the model can be extended to cases where the electromagnetic force is generated by an applied magnetic field or by both electric and magnetic fields.

The thesis is organized in the following sequence:

In Chapter 2, a generalized mathematical model is developed to describe the motion of particles in current-carrying liquid metals flowing through a cylindrical pipe. A numerical method is proposed to solve the Navier-Stokes equations for fluid velocity while particle motions equations incorporate particle inertia, drag, added mass, history, electromagnetic and fluid acceleration forces. A group of dimensionless numbers ($\mathrm{Re}, R_H, k, \gamma$) is employed to represent the fluid velocity, electric current, particle size, and particle density. The relative importance of the various force terms for different operating conditions is discussed. The model was used to predict the movement of spherical inclusions within the ESZ in LiMCA system.

The work in this chapter will be published in Metallurgical and Materials Transactions, vol. 31B, April 2000.[180]

In Chapter 3, the mathematical model developed in Chapter 2 is extended to describe the motion of variously shaped and oriented spheroids entrained in liquid metals passing through an ESZ system. This is achieved by introducing correction factors for drag, added mass, history, and electromagnetic force into the particle motion equations. The effects of each dimensionless number ($\mathrm{Re}, R_H, k, \gamma$) on the trajectories of particles of different shape (E) and orientation are discussed. The motion of spheroidal inclusions through the ESZ of LiMCA system has been predicted based on this model. The work in this chapter has been submitted to Metallurgical and Materials Transactions B.[181]

In Chapter 4, the mathematical model developed in Chapter 2 is modified to study the motion of particles in a water based LiMCA system — the APS II system. A boundary-fitted grid is adopted to accommodate the parabolic shaped orifice. The effects of particle size and density on the trajectories of particles are discussed. The predicted transient times and signal shapes are compared with the experimental measurements of Chris Carozza[91], and the possibility of the particle discrimination is discussed. The work in this chapter has been submitted to the Canadian Metallurgical Quarterly.[182]

In Chapter 5, the mathematical model developed in Chapter 2 is modified to study the motion of particles in aluminum, magnesium and steel LiMCA systems. Boundary-fitted grids are adopted for the parabolic shaped orifice used in the aluminum LiMCA system, and the cylindrical shaped orifice with countersunk cones at the ESZ inlet in the magnesium LiMCA system. The "conditioning current" operation is investigated in terms of the effect of current surge on the fluid velocity. The effects of particle conductivity, density, and size on the particle's trajectories and the possibility of particle discrimination are discussed for the aluminum

LiMCA system. The currently used probe for magnesium and steel LiMCA are analyzed and design improvements are suggested. The work on aluminum LiMCA has been accepted for publication in ISIJ International.[183]

In Chapter 6, the mathematical model developed in Chapter 2 is modified to design a new ESZ probe for the LiMCA system in order to resolve the orifice blocking problem. A boundary-fitted grid is adopted for the new probe, which comprises a contoured orifice and a co-axially built cylindrical extension. The effects of the electric current, orifice size, orifice length, orifice shape, extension length and radius, as well as fluid velocity, are investigated. New probes for magnesium and steel LiMCA systems for detecting particles below the detection limit of conventional probes are proposed. The work in this chapter has been accepted for publication in Metallurgical and Materials Transactions B in December 1999.[184]

In Chapter 7, the general conclusions that can be drawn from the present work are presented.

Appendix A shows schematically the configuration of DSP-based LiMCA system. In Appendix B, the mathematical model construction and validation are outlined.

References

[1] S. Asai and K. Iwai: Journal of the Mining and Materials Processing Institute of Japan, 1993, vol. 109, pp. 587-592.

[2] J. Szekely and K. Nakanishi: Metallurgical Transactions, 1975, vol. 6B, pp. 245-256.

[3] R. Kageyama and J.W. Evans: Metallurgical Transactions, 1998, vol. 29B, pp. 919-928.

[4] Y. Fautrelle: Journal of Fluid Mechanics, 1981, vol. 102, pp. 405-430.

[5] Y. Sundberg: Metallurgical Applications of Magnetohydrodynamics. H.K. Moffatt and M.R.E. Proctor Eds, Cambridge, UK, September 6-10, 1982, pp. 217-223.

[6] O.J. Ilegbusi and J. Szekely: Metallurgical Transactions, 1988, vol. 19B, pp. 557-562.

[7] J.P. Birat and J. Chone: Ironmaking and Steelmaking, 1983, pp. 209-281.

[8] G. Lesoult, P. Neu, and J.P. Birat: Metallurgical Applications of Magnetohydrodynamics. H.K. Moffatt and M.R.E. Proctor Eds, Cambridge, UK, September 6-10, 1982, pp. 164-179.

[9] M.R. Bridge and G.D. Rogers: Metallurgical Transactions, 1984, Vol. 15B, pp. 581-589.

[10] Int. Continuous Casting of Steel 1985 --- A Second Study, Brussels, 1986. Iron and Steel Institute, Committee on Technology.

[11] A. Alemany, J.P. Argous, J. Barbet, M. Ivanes, R. Moreau, and S. Poinsot: French Patent No. 804004430, 1980.

[12] P. Marty and A. Alemany: Metallurgical Applications of Magnetohydrodynamics. H.K. Moffatt and M.R.E. Proctor Eds, Cambridge, UK, September 6-10, 1982, pp. 245-259.

[13] V.A. Miroshnikov: Magnetohydrodynamics, 1979, vol. 15, pp. 365-370.

[14] U.Ts. Andres and B.B. Gul: Magnetohydrodynamics, 1965, vol. 1, pp. 108-112.

[15] S. Taniguchi and J.K. Brimacombe: ISIJ International, 1994, vol. 34, pp. 722-731.

[16]. J.P. Park, K. Sassa and S. Asai: CAMP-ISIJ, 1993, vol. 6, pp. 2.

[17] V.M. Korovin: Magnetohydrodynamics, 1985, vol. 21, pp. 321-326.

[18] V.M. Korovin: Magnetohydrodynamics, 1988, vol. 24, pp. 160-165.

[19] J.P. Park, A. Morihira, K. Sassa, and S. Asai: Journal of the Iron and Steel Institute of Japan, 1994, vol. 80, pp. 31-36. (In Japanese)

[20] Y. Tanaka, K. Sassa, K. Iwai, and S. Asai: Journal of the Iron and

Steel Institute of Japan, 1995, vol. 81, pp. 12-17. (In Japanese)

[21] J.P. Park, Y. Tanaka, K. Sassa, and S. Asai: Magnetohydrodynamics, 1996, vol. 32, pp. 227-234.

[22] V.M. Bazilevskii, V.M. Okunev, I.L. Povkh, V.A. Popov, V.A. Smirnov, and B.V. Chekin: Magnetohydrodynamics, 1970, vol. 6, pp. 299-301.

[23] A. Warczok, A. Godycki-Cwirko, and T.A. Utigard: Magnetohydrodynamics in Process Metallurgy, J. Szekely, J.W. Evans, K. Blazek and N. El-Kaddah Eds, San Diego, California, March 1-5, 1992, pp. 291-298.

[24] Yu.M. Gel'fgat, M.Z. Sorkin, V.P. Polishchuk, and L.P. Puzhailo: Magnetohydrodynamics, 1982, vol. 18, pp. 422-429.

[25] Yu.M. Gel'fgat and M.Z. Sorkin: Magnetohydrodynamics, 1976, vol. 13, pp. 347-352.

[26] Yu.M. Gel'fgat and M.Z. Sorkin: Magnetohydrodynamics, 1980, vol. 16, pp. 396-400.

[27] Yu.M. Gel'fgat, M.Z. Sorkin, and A.E. Mikel'son: Magnetohydrodynamics, 1977, vol. 13, pp. 99-101.

[28] Yu.M. Gel'fgat: Magnetohydrodynamics, 1987, vol. 23, pp. 334-347.

[29] I.T. Belyakov and Yu.D. Borisov: Space Technology, Mashinostroenie, Moscow, 1974. (In Russian)

[30] R.D. Smolkin, A.B. Solodenko, V.N. Gubarevich, O.P. Saiko, and E.V. Gulyaikhin: Magnetohydrodynamics, 1979, vol. 15, pp. 320-327.

[31] H. Hackl, S. Kollberg, and G. Tallback: Magnetohydrodynamics in Process Metallurgy, J. Szekely, J.W. Evans, K. Blazek and N. El-Kaddah Eds, San Diego, California, March 1-5, 1992, pp. 273-276.

[32] K. Takatani, K. Nakai, N. Kasai, T. Watanabe, and H. Nakajima: ISIJ International, 1989, vol. 29, pp. 1063-1068.

[33] M. Garnier: Liquid Metal Flows and Magnetohydrodynamics, H. Branover, P.S. Lykoudis and A. Yakhot Eds, American Institute of Aeronautics and Astronautics, New York, 1983, vol. 84, pp. 433-441.

[34] A.F. Kolesnichenko: ISIJ International, 1990, vol. 30, pp. 8-26.

[35] G.M. Oreper and J. Szekely: Journal of Crystal Growth, 1983, vol. 64, pp. 505-515.

[36] G.M. Oreper and J. Szekely: Journal of Crystal Growth, 1984, vol. 67, pp. 405-419.

[37] O.J. Ilegbusi, J. Szekely, and R.A. Cartwright: PCH PhysicoChemical Hydrodynamics, 1988, vol. 10, pp. 33-51.

[38] R. Cartwright, O.J. Ilegbusi, and J. Szekely: Journal of Crystal Growth, 1989, vol. 94, pp. 321-333.

[39] O.J. Ilegbusi and J. Szekely: Metallurgical Transactions, 1989, vol. 20A, pp. 1637-1646.

[40] T. Kozuka, T. Yuhara, I. Muchi, and S. Asai: ISIJ International, 1989, vol. 29, pp. 1022-1030.

[41] N. El-Kaddah and J. Szekely: Metallurgical Transactions, 1983, vol. 14B, pp. 401-410.

[42] N. El-Kaddah and J. Szekely: Metallurgical Transactions, 1984, vol. 15B, pp. 183-186.

[43] A.J. Mestel: Metallurgical Applications of Magnetohydrodynamics. H.K. Moffatt and M.R.E. Proctor Eds, Cambridge, UK, September 6-10, 1982, pp. 197-204.

[44] H.R. Lowry: Iron and Steelmaker, 1988, vol. 15, pp. 16-17.

[45] N. El-Kaddah, T.S. Piwonka, and J.T. Berry: US Patent 5033948, 1991.

[46] N. El-Kaddah: Magnetohydrodynamics in Process Metallurgy, J. Szekely, J.W. Evans, K. Blazek and N. El-Kaddah Eds, San Diego, California, March 1-5, 1992, pp. 283-289.

[47] Z.N. Getselev: Journal of Metals, 1971, vol. 23, pp. 38-39.

[48] D.E. Tyler, B.G. Lewis, and P.D. Renschen: Journal of Metals, 1985, vol. 37, pp. 51-53.

[49] Ch. Vives and R. Ricon: Metallurgical Transactions, 1985, vol. 16B, pp. 377-384.

[50] C. Vives and B. Forest: Light Metals, 1987, pp. 769-778.

[51] J.P. Riquet and J.L. Meyer: Light Metals, 1987, pp. 779-784.

[52] Ed.V. Shcherbinin: Liquid Metal Magnetohydrodynamics, J. Lielpeteris and R. Moreau Eds, Kluwer Academic, Dordrecht, Netherlands,1989, pp. 169-178.

[53] V.V. Boyarevich, R.P. Millere, and A.Yu. Chudnovskii: Magnetohydrodynamics, 1985, vol. 20, pp. 67-72.

[54] Q. Jiao and N.J. Themelis: Metallurgical Transactions, 1991, vol. 22B, pp. 183-192.

[55] A.H. Dilawari, J. Szekely, and T.W. Eager: Metallurgical Transactions, 1978, vol. 9B, pp. 371-381.

[56] G.M. Oreper and J. Szekely: Journal of Fluid Mechanics, 1984, vol. 147, pp. 53-79.

[57] J. Evans, Y. Zundelevich, and D. Sharma: Metallurgical Transactions, 1981, vol. 12B, pp. 353-360.

[58] T. Sele: Metallurgical Transactions, 1977, vol. 8B, pp. 613.

[59] D. Doutre and R.I.L. Guthrie: US Patent 4555662, 1985.

[60] D. Doutre and R.I.L. Guthrie: US Patent 4600880, 1986.

[61] R.I.L. Guthrie and D. Doutre: Proceedings of International Seminar on Refining and Alloying of Liquid Aluminum and Ferro-Alloys, Trondheim, Norway, 1986, pp. 146-163.

[62] S. Kuyucak and R.I.L. Guthrie: Canadian Metallurgical Quarterly, 1989, vol. 28, pp. 41-48.

[63] C. Carozza, P. Lenard, R. Sankaranarayanan, and R.I.L. Guthrie: Light Metals, 1997, pp. 185-196.

[64] R.I.L. Guthrie, M. Li, and J.Y. Buyan: Proceedings of the First Israeli International Conference on Magnesium Science and Technology, Dead Sea, Israel, November 10-12, 1997, pp. 81-87.

[65] H. Nakajima and R.I.L. Guthrie: Proceedings of JSPS 19th Committee Meeting, Japan, February 1992, pp. 1-15.

[66] R.I.L. Guthrie and H.C. Lee: Steelmaking Conference Proceedings,

1992, pp. 799-805.

[67] W.H. Coulter: US Patent 112819, 1953.

[68] R.W. Deblois and C.P. Bean: Review of Scientific Instruments, 1970, vol. 41, pp. 909-915.

[69] R.W. Deblois, C.P. Bean, and R.K.A. Wesley: Journal of Colloid and Interface Science, 1977, vol. 61, pp. 323-335.

[70] W.R. Smythe: Physics of Fluids, 1964, vol. 7, pp. 633-638.

[71] B.A. Batch: Journal of the Institute of Fuel, 1965, vol. 37, pp. 455.

[72] R.K. Eckhoff: Journal of Scientific Instrument, 1967, vol. 44, pp. 648.

[73] D.C. Golibersuch: Biophysical Journal, 1973, vol. 13, pp. 265-280.

[74] D.C. Golibersuch: Journal of Applied Physics, 1973, vol. 44, pp. 2580-2584.

[75] E.C. Gregg and K.D. Steidley: Biophysical Journal, 1965, vol. 5, pp. 393.

[76] N.B. Grover, J. Naaman, S. Ben-Sasson, and F. Doljanski: Biophysical Journal, 1969, vol. 9, pp. 1398-1414.

[77] N.B. Grover, J. Naaman, S. Ben-Sasson, and F. Doljanski: Biophysical Journal, 1969, vol. 9, pp. 1415-1425.

[78] G. van der Plaats and H. Herps: Powder Technology, 1983, vol. 36, pp. 131-136.

[79] G. van der Plaats and H. Herps: Powder Technology, 1984, vol. 38, pp. 73-76

[80] D. Horak, J. Peska, F. Svec, and J. Stamberg: Powder Technology, 1982, vol. 31, pp. 263-267.

[81] R.K. Eckhoff: Journal of Physics E, 1969, vol. 2, pp. 973-977.

[82] R. Karuhn, R. Davies, B.H. Kaye, and M.J. Clinch: Powder Technology, 1975, vol. 11, pp. 157-171.

[83] R. Davis, R. Karuhn, and J. Graf: Powder Technology, 1975, vol. 12, pp. 157-166.

[84] R. Davies, R. Karuhn, J. Graf, and J. Stockham: Powder Technology,

1976, vol. 13, pp. 193-201.

[85] W.R. Smythe: Review of Scientific Instruments, 1972, vol. 43, pp. 817-818.

[86] L. Spielman and S.L. Goren: Journal of Colloid and Interface Science, 1968, vol. 26, pp. 175-182.

[87] L.I. Berge, T. Jφssang, and J. Feder: Measurement Science and Technology, 1990, vol. 1, pp. 471-474.

[88] C.M.L. Atkinson and R. Wilson: Powder Technology, 1983, vol. 34, pp. 275-284.

[89] L.I. Berge: Journal of Colloid and Interface Science, 1990, vol. 135, pp. 283-293.

[90] Xiaodong Shi: Master Thesis, McGill University, 1994.

[91] C. Carozza: Master Thesis, McGill University, 1999.

[92] D. Doutre: Ph.D Thesis, McGill University, 1984.

[93] W.H. Coulter and W.R. Hogg: US Patent 3444464, 1969.

[94] W.R. Hogg: US Patent 3746977, 1973.

[95] S. Baccarini: US Patent 3638677, 1972.

[96] H. Bader: US Patent 3395344, 1968.

[97] R. Karuhn, R. Davies, and B.H. Kaye: US Patent 3739268, 1973.

[98] B.E. Launder and D.B. Spalding: Computer Methods in Applied Mechanics and Engineering, 1974, vol. 3, pp. 269-289.

[99] W.F. Haughes and F.J. Young: The Electromagnetodynamics of Fluids, Wiley, New York, 1966.

[100] J.D. Jackson: Classical Electrodynamics, Wiley, New York, 1962.

[101] E.D. Tarapore and J.W. Evans: Metallurgical Transactions, 1976, vol. 7B, pp. 345-351.

[102] A.B. Basset: Phil. Trans. R. Soc. Lond., 1888, Vol. 179A, pp. 43-63.

[103] J. Boussinesq: Theorie Analytique de la Chaleur, L'Ecole Polytechnique, Paris, 1903, vol. 2, pp. 224.

[104] C.W. Oseen: Hydrodynamik, Leipzig, 1927, pp. 132.

[105] M.R. Maxey and J.J. Riley: Physics of Fluids, 1983, vol. 26, pp. 883-889.

[106] M.R. Maxey: Physics of Fluids, 1987, vol. 30, pp. 1579-1582.

[107] A. Berlemont, P. Desjonqueres, and G. Gouesbet: International Journal of Multiphase Flow, 1990, vol. 16, pp. 19-34.

[108] T.R. Auton, J.C.R. Hunt, and M. Prud'homme: Journal of Fluid Mechanics, 1988, vol. 83, pp. 199-218.

[109] M. Rivero, J. Magnaudet, and J. Fabre: C. R. Acad. Sci. Paris, 1991, vol. 312, pp. 1499-1506.

[110] R. Mei, C.J. Lawrence, and R.J. Adrian: Journal of Fluid Mechanics, 1991, vol. 233, pp. 613-631.

[111] E.J. Chang and M.R. Maxey: Journal of Fluid Mechanics, 1994, vol. 277, pp. 347-379.

[112] E.J. Chang and M.R. Maxey: Journal of Fluid Mechanics, 1995, vol. 303, pp. 133-153.

[113] F. Odar and W.S. Hamilton: Journal of Fluid Mechanics, 1964, vol. 18, pp. 302-314.

[114] F. Odar: Journal of Fluid Mechanics, 1966, vol. 25, pp. 591-592.

[115] R. Mei and R.J. Adrian: Journal of Fluid Mechanics, 1992, vol. 237, pp. 323-341.

[116] R. Mei: Journal of Fluid Mechanics, 1994, vol. 270, pp. 133-174.

[117] M.R. Maxey: Gas-Solid Flows, ASME/FED, 1993, vol. 166, pp. 57-62.

[118] R.Y.S. Lai and L.F. Mockros: Journal of Fluid Mechanics, 1972, vol.52, pp. 1-15.

[119] T. Aoi: Journal of the Physical Society of Japan, 1955, vol. 10, pp.119-129.

[120] J. Happel and H. Brenner: Low Reynolds Number Hydrodynamics, 2nd ed. Noordhoff, Leyden, Netherlands, 1973.

[121] L.E. Payne and W.H. Pell: Journal of Fluid Mechanics, 1960, vol. 7, pp. 78-92.

[122] C.J. Lawrence and S. Weinbaum: Journal of Fluid Mechanics, 1988, vol. 189, pp. 463-489.

[123] J.A. Stratton: Electromagnetic Theory, McGraw-Hill, New York, 1941, pp. 211, 217.

[124] S.S. Dukhin and V.N. Shilov: Advances in Colloid and Interface Science, 1980, vol. 13, pp. 153.

[125] M. Loewenberg: Physics of Fluids, 1993, vol. A5, pp. 765-767.

[126] J.H. Masliyah and N. Epstein: Journal of Fluid Mechanics, 1970, vol. 44, pp. 493-512.

[127] H.A. Dwyer and D.S. Dandy: Physics of Fluids, 1990, vol. A2, pp. 2110-2118.

[128] R. Clift, J.R. Grace, and M.E. Weber: Bubbles, Drops and Particles, Academic Press, Inc., New York, NY, 1978.

[129] R. Ladenburg: Annalen der Physik (Leipzig), 1907, vol. 23, pp. 447 -458.

[130] A.W. Francis: Physics, 1933, vol. 4, pp. 403-406.

[131] V. Fidleris and R.L. Whitmore: British Journal of Applied Physics, 1961, vol. 12, pp. 490-494.

[132] H. Brenner and J. Happel: Journal of Fluid Mechanics, 1958, vol. 4, pp. 195.

[133] S. Wakiya: Journal of the Physical Society of Japan, 1957, vol. 12, pp. 1130.

[134] H. Brenner: Chemical Engineering Science, 1961, vol. 16, pp. 242.

[135] J.L. Sutterby: Transactions of the Society of Rheology, 1973, vol. 17, pp. 559-585.

[136] E. Achenbach: Journal of Fluid Mechanics, 1974, vol. 65, pp. 113-125.

[137] A.M. Fayon and J. Happel: AICHE Journal, 1960, vol. 6, pp. 55-58.

[138] D. Leenov and A. Kolin: Journal of Chemical Physics, 1954, vol. 22, pp. 683-687.

[139] E.I. Shilova: Magnetohydrodynamics, 1975, vol. 11, pp. 250-251.

[140] J. Szekely and S. Asai: ISIJ Transactions, 1975, vol. 15, pp. 276-285.

[141] J. Szekely and K. Nakanishi: Metallurgical Transactions, 1975, vol. 6B, pp. 245-256.

[142] A.H. Dilawari and J. Szekely: Metallurgical Transactions, 1977, vol. 8B, pp. 227-236.

[143] J.G. Andrew and R.E. Craine: Journal of Fluid Mechanics, 1978, vol. 84, pp. 281-290.

[144] C. Souzou and W.M. Pickering: Proceedings of the Royal Society of London, 1978, vol. 362A, pp. 509-523.

[145] E.D. Tarapore: Light Metals, 1979, vol. 1, pp. 541-550.

[146] J.N. Barbier: Journal de Mecanique Theorique et Appliquee, 1982, vol. 1, pp. 533-556.

[147] A.J. Mestel: Journal of Fluid Mechanics, 1982, vol. 117, pp. 27-43.

[148] K. Hoshikawa: Japanese Journal of Applied Physics, 1982, vol. 21, L545.

[149] M. Choudhary and J. Szekely: ISS Transactions, 1983, vol. 3, pp. 65-75.

[150] G.M. Oreper, T.W. Eagar and J. Szekely: Welding Journal, 1983, vol. 62, pp. 307S-312S.

[151] W.E. Wahnsiedler: Light Metals, 1987, pp. 269-287.

[152] J.L. Meyer, J. Szekely, and N. El-Kaddah: Transactions ISIJ, 1987, vol. 27, pp. 25-33.

[153] J.L. Meyer, N. El-Kaddah, J. Szekely, C. Vives and R. Ricou: Metallurgical Transactions, 1987, vol. 18B, pp. 529-538.

[154] O.J. Ilegbusi and J. Szekely: Transactions ISIJ, 1988, vol. 28, pp. 97-103.

[155] O.J. Ilegbusi and J. Szekely: Ironmaking and Steelmaking, 1989, vol. 16, pp. 110-115.

[156] O.J. Ilegbusi and J. Szekely: ISIJ International, 1989, vol. 29, pp. 1031-1039.

[157] D.P. Cook, and J.W. Evans: Metallurgical and Materials

Transactions, 1995, vol. 26B, pp. 1263-1270.

[158] D.P. Cook, S. Nishioka, and J.W. Evans: Metallurgical and Materials Transactions, 1995, vol. 26B, pp. 1271-1279.

[159] R. Kageyama and J.W. Evans: Metallurgical and Materials Transactions, 1998, vol. 29B, pp. 919-928.

[160] R.I.L. Guthrie, R. Clift, and H. Henein: Metallurgical Transactions, 1975, vol. 6B, pp. 321-329.

[161] M. Tanaka, D. Mazumdar, and R.I.L. Guthrie: Metallurgical Transactions, 1993, vol. 24B, pp. 639-648.

[162] D. Mazumudar and R.I.L. Guthrie: Metallurgical Transactions, 1993, vol. 24B, pp. 649-655.

[163] M.R. Aboutalebi, M. Hasan, and R.I.L. Guthrie: Metallurgical and Materials Transactions, 1995, vol. 26B, pp. 731-744.

[164] T. Sawai and N. El-Kaddah: Magnetohydrodynamics, 1996, vol. 32, pp. 214-220.

[165] K. Takatani: Magnetohydrodynamics, 1996, vol. 32, pp. 128-133.

[166] Yu.A. Krasnitskii and V.I. Popov: Magnetohydrodynamics, 1975, vol. 11, pp. 209-212.

[167] S. Joo and R.I.L. Guthrie: Metallurgical Transactions, 1993, vol. 24B, pp. 755-765.

[168] S. Joo, J.W. Han, and R.I.L. Guthrie: Metallurgical Transactions, 1993, vol. 24B, pp. 766-778.

[169] S. Joo, J.W. Han, and R.I.L. Guthrie: Metallurgical Transactions, 1993, vol. 24B, pp. 779-788.

[170] E.D. Tarapore, J.W. Evans, and J. Langfeldt: Metallurgical Transactions, 1977, vol. 8B, pp. 179-184.

[171] D.J. Moore and J.C.R. Hunt: Liquid-Metal Flows and Magnetohydrodynamics, H. Branover, P.S. Lykoudis, and A. Yakhot Eds. American Institute of Aeronautics and Astronautics, New York, 1983, vol. 84, pp. 359-373.

[172] N. El-Kaddah and J. Szekely: Journal of Fluid Mechanics, 1983, vol. 133, pp. 37-46.

[173] J.W. Evans and S.D. Lympany: Metallurgical Transactions, 1983, vol. 14B, pp. 306-308.

[174] R. Ricou and C. Vives: International Journal of Heat and Mass Transfer, 1982, vol. 25, pp. 1579-1588.

[175] J.L. Meyer, F. Durand, R. Ricou, and C. Vives: Metallurgical Transactions, 1984, vol. 15B, pp. 471-478.

[176] M. Choudhary, J. Szekely, B.I. Medovar, and Yu.G. Emelyanenko: Metallurgical Transactions, 1982, vol. 13B, pp. 35-43.

[177] E.D. Tarapore: Light Metals, 1981, pp. 341-355.

[178] N. El-Kaddah, J. Szekely, and G. Carlsson: Metallurgical Transactions, 1984, vol. 15B, pp. 633-640.

[179] A. Murthy, J. Szekely, and N. El-Kaddah: Metallurgical Transactions, 1988, vol. 19B, pp. 765-775.

[180] Mei Li, R.I.L. Guthrie: "Numerical Studies of the Motion of Particles in Current-carrying Liquid Metals Flowing in a Circular Pipe," Metallurgical and Materials Transactions, vol. 31B, April 2000.

[181] Mei Li, R.I.L. Guthrie: "Numerical Studies of the Motion of Spheroidal Particles Flowing with Liquid Metals through an Electric Sensing Zone (ESZ)," accepted by Metallurgical and Materials Transactions B, February 2000.

[182] Mei Li, C. Carozza, and R.I.L. Guthrie: "Particle Discrimination in Water Based LiMCA System," accepted by Canadian Metallurgical Quarterly, February 2000.

[183] Mei Li and R.I.L. Guthrie: "LiMCA in Molten Aluminum," accepted by ISIJ International, November 1999.

[184] Mei Li and R.I.L. Guthrie: "On the Detection, and Selective Separation of Inclusions in Liquid Metal Cleanliness Analyzer (LiMCA) System," accepted by Metallurgical and Materials Transactions B, December 1999.

CHAPTER 2

Numerical Studies of the Motion of Particles in Current-Carrying Liquid Metals Flowing in a Circular Pipe

2.1 Introduction

The motion of particles in current-carrying liquid metals constitutes the basis for a number of electro-metallurgical processing operations. Examples include the deposition of non-conductive oxide particles on the inner walls of induction furnaces,[1] the acceleration, deceleration and transverse motions of liquid metal droplets passing through liquid slag in electro-slag smelting and welding operations,[2] the electromagnetic separation[3,4] and its application to the design of split tundish in continuous casting to move the inclusions to the wall of the heating system[5] and to conventional casting mold to move inclusions to the boundary of the solidifying shell,[6] the filtration of non-metallic inclusions by pumping the melt through a bundle of current-applied thin pipes in aluminum scrap recycling,[7] as well as the on-line Liquid Metal Cleanliness Analyzer (LiMCA)[8,9] by measuring the voltage pulse produced when a particle with different electrical conductivity from that of liquid metal passes through an Electric Sensing Zone (ESZ),[10] a small orifice built in an electrically insulating probe, in the presence of an electric current applied between an electrode outside and another inside the sampling tube. Essentially, all these processes involve the motion of particles in current-carrying liquid metals in a circular pipe. Therefore, a numerical study of the particle trajectory in current-carrying liquid metals in a circular pipe is necessary both to the understanding of these processes and to the corresponding engineering design. Especially, a numerical study of the particle trajectory in a current-carrying liquid metal in a finite length circular tube will help LiMCA to realize particle discrimination due to the fact that the height and shape of the small voltage pulse depend on the size[11,12] and also the trajectory of the particles,[13,14] and possibly enable LiMCA to register only the signals from harmful solid particles.

Much effort has been devoted to study the motion of particles in current-carrying liquids. Leenov and Kolin[15] derived the electromagnetic force on a spherical particle whose electrical conductivity is different from that of the surrounding liquid. Shilova[1] studied the motion of non-conducting particles suspended in a stagnant conducting liquid contained within a cylindrical tube through which a uniform electric current flows along the axis. He found that the pinch force generated by the electric current and its induced magnetic field was directed along the radius towards the center of the tube and was balanced by a radial pressure gradient, resulting in an outwards radial motion of the particle towards the tube wall. The study was later extended to the motion of conducting particles within the same configurations.[2] The dynamic motion of particles in a cylindrical MHD (magnetohydrodynamic) separator was studied[16] by considering only the electromagnetic force and drag force in the radial direction. The trajectories of particles in a current-carrying liquid metal in an infinite long vertical pipe were investigated[5] under the assumptions of small particle Reynolds number and negligible particle inertia with a fully developed Poiseuille flow. In this study the vertical velocity of the particle was calculated by superimposition of the terminal Stokes velocity on the metal velocity, while the radial velocity was derived by balancing the electromagnetic force and the Stokes drag force. These studies only considered the electromagnetic force and the Stokes drag force. In reality, a more complete consideration of the hydrodynamic force terms are needed for the calculation of particle motion in conventional hydrodynamics. These forces include the particle inertia, drag, buoyancy, gravity and added mass, as well as fluid acceleration and history forces.[17] The importance of the added mass and Basset history terms in determining the particle trajectory in a stagnant current-carrying liquid was also confirmed by Korovin.[18]

In this chapter, a generalized mathematical model was developed for the motion of particles in current-carrying liquid metals entering a circular pipe under laminar flow conditions. The Navier-Stokes equations were solved for predicting the flow field, while particle trajectories were obtained by solving the equations for motion of the particle that include the force terms associated with conventional hydrodynamics, together with the electromagnetic force generated by the applied current. The entrance region was included to extend the model to pipe of finite length. Wall effects of the pipe inner surface on the particle trajectory were also considered. The model developed in this work has been applied to the LiMCA system to evaluate the latter's performance.

2.2 Mathematical Model and Numerical Methods

The present study considered the trajectories of particles entrained within a homogeneously conducting current-carrying liquid flowing into a circular pipe. Two-dimensional simulation in a cylindrical coordinate system was employed since the applied electric currents are sufficiently strong as to confine any particle motion to the plane containing the mass center of the particle and the axis of the pipe in applications such as particle separation and the operation of LiMCA. The problem can be schematically represented in Figure 2.1, where D is the diameter of the pipe, u_0 is the inlet flow velocity which is assumed to be uniform, J_0 is the electric current density at the inlet, and d is the radius of the particle which is centered at (x_p, y_p), where x and y are the respective axial and radial coordinates.

2.2.1 The Flow Field in the Pipe

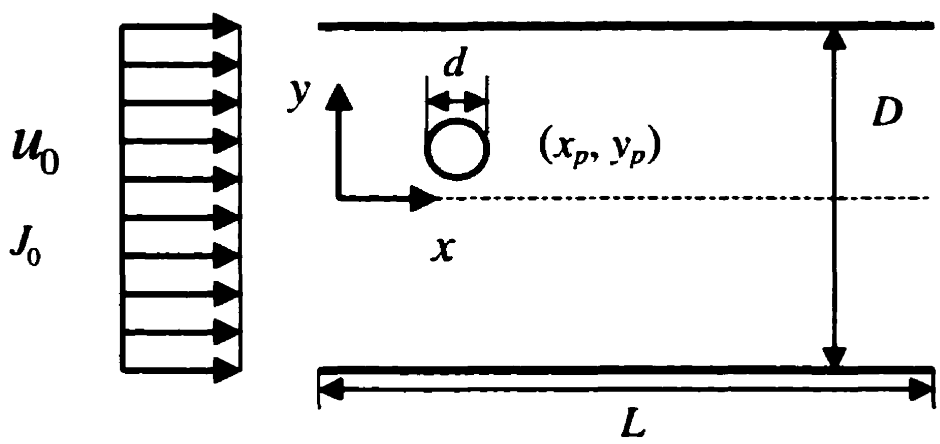

Figure 2.1 — The schematic representation of a particle flowing in a current-carrying liquid in a circular pipe.

The liquid metal is assumed incompressible and has constant properties, and the flow is considered laminar and steady. Under these assumptions, the problem may be stated by writing the Navier-Stokes equations with the Lorentz or electromagnetic force $\vec{F}(F_x, F_y)$ constituting the body force as follows:

$$\vec{\nabla} \bullet \vec{u} = 0 \qquad (2.1)$$

$$\vec{u} \bullet \vec{\nabla}\vec{u} = -\frac{\vec{\nabla}p}{\rho_f} + \nu_f \nabla^2 \vec{u} + \frac{1}{\rho_f}\vec{F} \qquad (2.2)$$

where $\vec{u}(u, v)$ is the fluid velocity vector, p is the pressure, ρ_f and ν_f are the density and kinematic viscosity of the fluid. $\vec{F}$, the Lorentz force, is defined by the following equation:

$$\vec{F} = \vec{J} \times \vec{B} \qquad (2.3)$$

where $\vec{J}$ is the electric current density, $\vec{B}$ is the self-induced magnetic field in the pipe. Maxwell's equations need to be solved for the electromagnetic field. In the present work, $\vec{J}$ is obtained through the Laplace equation:

$$\frac{\partial^2 \varphi}{\partial x^2} + \frac{1}{y}\frac{\partial}{\partial y}\left(y\frac{\partial \varphi}{\partial y}\right) = 0 \tag{2.4}$$

where φ is the electrical potential. The current density can be calculated from Ohm's law which is described in equations (2.5) and (2.6) since the secondary current induced by the convective motion of the liquid metal is negligible.[19]

$$J_x = -\sigma_e \frac{\partial \varphi}{\partial x} \tag{2.5}$$

$$J_y = -\sigma_e \frac{\partial \varphi}{\partial y} \tag{2.6}$$

where σ_e is the electrical conductivity and is $4.132\times10^6\ \Omega^{-1}m^{-1}$ for aluminum.

The self-induced magnetic field is derived from Ampere's law with μ_0 as the magnetic permeability of free space ($\mu_0 = 4\pi\times10^{-7}\ Wb/A-m$):

$$B_\theta = \frac{\mu_0}{y}\int_0^y J_x \xi d\xi \tag{2.7}$$

where θ is the azimuthal co-ordinate in cylindrical coordinate system.

Since it is more convenient to work with dimensionless variables, the following non-dimensional quantities are introduced:

$$x^* = \frac{x}{R}, \quad y^* = \frac{y}{R}, \quad u^* = \frac{u}{u_0}, \quad v^* = \frac{v}{u_0}, \quad p^* = \frac{p}{\rho_f u_0^2},$$

$$F_x^* = \frac{J_y B_\theta}{\mu_0 J_0^2 R}, \quad F_y^* = \frac{J_x B_\theta}{\mu_0 J_0^2 R}$$

where $R = \frac{D}{2}$ is the radius of the pipe. With these dimensionless quantities, the vector forms of the conservation equations (2.1) and (2.2) can be rewritten as equations (2.8) - (2.10), in dimensionless form, using cylindrical coordinates (the asterisk has been omitted):

$$\frac{\partial u}{\partial x} + \frac{\partial v}{\partial y} + \frac{v}{y} = 0 \tag{2.8}$$

$$u\frac{\partial u}{\partial x} + v\frac{\partial u}{\partial y} = -\frac{\partial p}{\partial x} + \frac{1}{\mathrm{Re}}\left(\frac{\partial^2 u}{\partial x^2} + \frac{\partial^2 u}{\partial y^2} + \frac{1}{y}\frac{\partial u}{\partial y}\right) + R_H F_x \tag{2.9}$$

$$u\frac{\partial v}{\partial x} + v\frac{\partial v}{\partial y} = -\frac{\partial p}{\partial y} + \frac{1}{\mathrm{Re}}\left(\frac{\partial^2 v}{\partial x^2} + \frac{\partial^2 v}{\partial y^2} + \frac{1}{y}\frac{\partial v}{\partial y} - \frac{v}{y^2}\right) + R_H F_y \tag{2.10}$$

where $\mathrm{Re} = \frac{u_0 R}{\nu_f}$ is the fluid Reynolds number and $R_H = \frac{\mu_0 J_0^2 R^2}{\rho_f u_0^2}$ is the magnetic pressure number.

The boundary conditions applying to the above equations are zero-slip along and across and zero electric current flux across the insulating wall. At the inflow boundary, the fluid velocity and electric current density are assumed to be uniform. At the outflow boundary, the electrical potential is assumed to be constant across the pipe, while the exit fluid velocity gradient is taken to be zero and corrections are made in the numerical calculations to match the mass inflow rate and thereby respect continuity.

2.2.2 The Equation of Motion of the Particles

In conventional hydrodynamics, the motion of particles has been investigated extensively. Basset[20] studied the unsteady creeping motion of a sphere in a stagnant incompressible viscous fluid, and found that besides the Stokesian drag on a particle for steady translational motion $6\pi\mu_f a\vec{u}_p(t)$ (where $\vec{u}_p(t)$ representing the instantaneous particle velocity, and $a=\frac{d}{2}$, the radius of the particle), there are two other force terms that result from unsteady motions. One is the added mass term which derives from acceleration of liquid surrounding an accelerating particle. The volume of the added mass of the surrounding fluid is equal to one-half of the particle volume. The other is the Basset history force term due to the transient formation of a boundary layer near the particle surface. This force term is expressed as the time integral of the particle acceleration weighted by $(t-\tau)^{1/2}$, where $(t-\tau)$ is the time elapsed since the past acceleration. For high Reynolds number motions of particle in a fluid which is also in motion itself, a widely used equation is proposed as[21]:

$$
\begin{aligned}
m_p\frac{d\vec{u}_p}{dt} &= \frac{1}{2}C_{Dstd}\pi a^2\rho_f\left|\vec{u}-\vec{u}_p\right|(\vec{u}-\vec{u}_p)+\frac{1}{2}m_f\frac{d(\vec{u}-\vec{u}_p)}{dt}+m_f\frac{D\vec{u}}{Dt} \\
&+6a^2(\pi\mu_f\rho_f)^{1/2}\int_0^t\frac{d(\vec{u}-\vec{u}_p)/d\tau}{(t-\tau)^{1/2}}d\tau+(m_p-m_f)\vec{g}
\end{aligned}
\qquad (2.11)
$$

where $\vec{u}_p(u_p,v_p)$ and $\vec{u}(u,v)$ represent the instantaneous velocity of the particle and the undisturbed fluid velocity at the center of the particle that would apply in the absence of that particle. C_{Dstd} represents the drag coefficient from the steady standard drag curve[22] based on the particle Reynolds number $\mathrm{Re}_p=\frac{\rho_f\left|\vec{u}-\vec{u}_p\right|d}{\mu_f}$, m_p is the particle mass and m_f is the fluid mass displaced by the particle and μ_f is the dynamic viscosity of the fluid. Auton[23] pointed out that the added mass term should be $\frac{1}{2}m_f(\frac{D\vec{u}}{Dt}-\frac{d\vec{u}_p}{dt})$, where $\frac{d}{dt}$ is used to denote a time derivative following a moving particle, and $\frac{D}{Dt}$ a time derivative following a fluid element.

As to the motion of particle in a current-carrying liquid metal, the electromagnetic force on the particle[18] has to be included. Therefore, in this study, the prediction of the trajectory of a non-conducting, rigid, spherical particle was based on the following equation, written in vector form:

$$\begin{aligned}\rho_p V_p \frac{d\vec{u}_p}{dt} &= \frac{1}{2}C_{Dstd}\pi a^2\rho_f\left|\vec{u}-\vec{u}_p\right|(\vec{u}-\vec{u}_p)+\frac{1}{2}\rho_f V_p(\frac{D\vec{u}}{Dt}-\frac{d\vec{u}_p}{dt})+\rho_f V_p\frac{D\vec{u}}{Dt}+\\ &6a^2(\pi\mu_f\rho_f)^{1/2}\int_0^t\frac{d(\vec{u}-\vec{u}_p)/d\tau}{(t-\tau)^{1/2}}d\tau+(m_p-m_f)\vec{g}-\frac{3}{4}V_p\vec{F}\end{aligned} \tag{2.12}$$

where ρ_p and V_p are the density and volume of the particle, and $\vec{F}$ represents the electromagnetic force per unit volume of the fluid at the position of the particle.

It should be noted that C_{Dstd} for a particle in a current-carrying liquid metal depends not only on the particle Reynolds number, but also on the magnetic pressure number R_H.[24] For a non-conducting particle, C_{Dstd} can increase significantly with R_H owing to a slight shift forward of the separation point of the boundary layer making for a larger wake length and is larger than that of no-current situation. In this paper, all the studies were carried out with $R_H < 1$, the effect of R_H on C_{Dstd} could be neglected.

Equation (2.12) can be rewritten in dimensionless form as equations (2.13) and (2.14) for particle motion in a horizontal pipe (omitting the asterisks for convenience) by introducing four more non-dimensional variables:

$$u_p^* = \frac{u_p}{u_0},\ v_p^* = \frac{v_p}{u_0},\ t^* = \frac{u_0 t}{R}, \text{ and } \tau^* = \frac{u_0 \tau}{R}.$$

For axial (x) motion:

$$\frac{du_p}{dt} = \frac{1}{\gamma + \frac{1}{2}}[\frac{3}{8k} C_{Dstd} |\vec{u} - \vec{u}_p| (u - u_p) + \frac{3}{2}(u\frac{\partial u}{\partial x} + v\frac{\partial u}{\partial y}) + \frac{9}{2k}(\frac{1}{\pi \mathrm{Re}})^{1/2} \int_0^t \frac{d(u - u_p)/d\tau}{(t - \tau)^{1/2}} d\tau - \frac{3}{4} R_H F_x] \tag{2.13}$$

For radial (y) motion:

$$\frac{dv_p}{dt} = \frac{1}{\gamma + \frac{1}{2}}[\frac{3}{8k} C_{Dstd} |\vec{u} - \vec{u}_p| (v - v_p) + \frac{3}{2}(u\frac{\partial v}{\partial x} + v\frac{\partial v}{\partial y}) + \frac{9}{2k}(\frac{1}{\pi \mathrm{Re}})^{1/2} \int_0^t \frac{d(v - v_p)/d\tau}{(t - \tau)^{1/2}} d\tau - \frac{3}{4} R_H F_y + (1 - \gamma) Fr] \tag{2.14}$$

where Re and R_H are the respective fluid Reynolds number and magnetic pressure number as in the dimensionless Navier-Stokes equations. $Fr = \frac{gR}{u_0^2}$ is the Froude number, $\gamma = \frac{\rho_p}{\rho_f}$ is the particle - fluid density ratio, and $k = \frac{a}{R}$ is the blockage ratio.

2.2.3 Wall Effects

The presence of a solid surface in the vicinity of a moving particle will affect the drag force. In this study, the axial drag force was approximated using the equation developed by Fayon and Happel:[25]

$$C_D = C_{D\infty} + (24/\mathrm{Re}_p)(W-1) \tag{2.15}$$

where $C_{D\infty}$ is the drag coefficient in the absence of the wall, and W is given by Haberman and Sayre:[22]

$$W = \frac{1-0.75857k^5}{1-2.1050k+2.0865k^3-1.7068k^5+0.72603k^6} \tag{2.16}$$

The wall effects in the radial direction can be estimated by using the tabulated correction factor for the drag force on a solid particle moving perpendicular to a plane wall.[26] The correction factor is a function of the ratio of the distance of the particle center from the wall to the particle radius, and linear interpolation is employed to obtain the factor for the ratio in question.

2.2.4 *Numerical Methods*

The conservation equations for mass and momentum with the boundary conditions were solved using the finite volume approach and a collocated arrangement of variables.[27] The SIMPLE (Semi-Implicit-Method for Pressure-Linked Equations) algorithm was employed for the calculation of the velocity field.[28] Grids of variable spacing were used to enhance the accuracy of the calculation, *i.e.*, a finer spacing was adopted near the wall and inflow boundary and a coarser grid further away. Central differences were used to approximate both convection and diffusion fluxes. The iterative procedure was continued until the sum of the absolute values of the residuals in all control volumes normalized by the inlet flow momentum flux in calculating the fluid velocity or by inlet flow mass in calculating the fluid pressure field fell to the order of 10^{-5}. For the calculation of the electromagnetic field, the continuity of the electric current was checked, along with an analysis of the residuals, so as to ensure that the amount of electric current entering into the system matched the amount of current leaving.

The solution of the fluid flow equations provides the hydrodynamic conditions for the calculation of the motion of particle. The fluid velocity at the instantaneous center of the particle was obtained by bi-linear interpolation of the grid values. At t=0, the particle flows into the pipe at the same velocity as the fluid at a certain radial position. The equation of particle motion was solved by employing a fourth-order Runge-Kutta method. The history integral needed special attention because of the singular point at the upper integration limit. It is evaluated through the following expression:[29]

$$\int_0^t \frac{\dot{U}}{f(t-\tau)}d\tau = \int_0^{n\Delta t} \frac{\dot{U}}{f(t-\tau)}d\tau = \frac{\Delta t}{6}\sum_{i=1}^{n-1}\left[\frac{\dot{U}_{i-1}}{f(n\Delta t-(i-1)\Delta t)} + \frac{2(\dot{U}_{i-1}+\dot{U}_i)}{f(n\Delta t-(i-0.5)\Delta t)} + \frac{\dot{U}_i}{f(n\Delta t-i\Delta t)}\right] + \frac{0.9\Delta t}{6}\left[\frac{\dot{U}_{n-1}}{f(\Delta t)} + \frac{2(\dot{U}_{n-1}+\dot{U}_n)}{f(0.55\Delta t)} + \frac{\dot{U}_n}{f(0.1\Delta t)}\right] + \frac{0.1\Delta t}{2}\left[\frac{8\sqrt{2}}{3}\frac{\dot{U}_n}{f(0.05\Delta t)} - \frac{4}{3}\frac{\dot{U}_n}{f(0.1\Delta t)}\right] \quad (2.17)$$

with $\dot{U} = \frac{d(\bar{u}-\bar{u}_p)}{d\tau}$, $f(t-\tau)=(t-\tau)^{1/2}$. Δt is the dimensionless time step whose value is set as 0.001 to maintain the accuracy of the calculation.

2.3 Results and Discussion

Equations (2.13) and (2.14) show that the motion of particle is determined by five non-dimensional parameters: Re, R_H, γ, k, and Fr. Among them, Re and R_H are related to the flow field. In practical operations involving intensive electric current density such as in the LiMCA system, Fr is four orders smaller than R_H. Fr is related to the buoyancy force term $(1-\gamma)Fr$, while R_H to the electromagnetic force term $-\frac{3}{4}R_H F_r$ as shown in equation (2.14). Compared to the electromagnetic force, which increases linearly with radial distance from the axis in the pipe, the buoyancy force is negligibly small and can be ignored provided the particle density is not very high compared to liquid density and its initial position is not very close to the axis of the pipe. Under such circumstances, the particle trajectory can be taken as symmetric with respect to the axis of the pipe, and calculations performed on the positive initial particle positions.

An effective method to study the effects of Re, R_H, γ and k on the motion of particles is to examine a parameter while holding the others constant. In this study, the effects of γ and k were investigated in the same flow field by keeping Re and R_H constant. In practical operations, the flow field is controlled by the fluid velocity u_0 and the applied electric current I. In the computation, the velocity u_0 is represented by Reynolds number Re, while the electric current I is contained in the magnetic pressure number R_H. The effect of R_H on the motion of particles is considered by keeping Re, γ and k constant, while the effect of Re can be revealed by holding γ and k constant, and maintaining $\mathrm{Re}^2 R_H = \dfrac{\rho_f \mu_0 I^2}{\pi^2 \mu_f^2}$ constant so as to neutralize the effect of the inertial force, leaving electric current I fixed for a specific molten metal. In this study, $\mathrm{Re}^2 R_H$ was taken as 8.55×10^4, which represents an electric current of 30 amperes flowing through a circular pipe containing molten aluminum. The particle is considered to have reached the wall when its center is one radius from the wall. The initial position of the particle flowing into the pipe was set at $(x_0, y_0) = (0, 0.3)$ for most of the simulations, except in the study of the effect of the initial position where y_0 varies from 0.1 to 0.6.

2.3.1 The Effect of R_H

The effect of magnetic pressure number R_H on the particle trajectory is shown in Figure 2.2. It can be seen that at the same axial position x_p, a

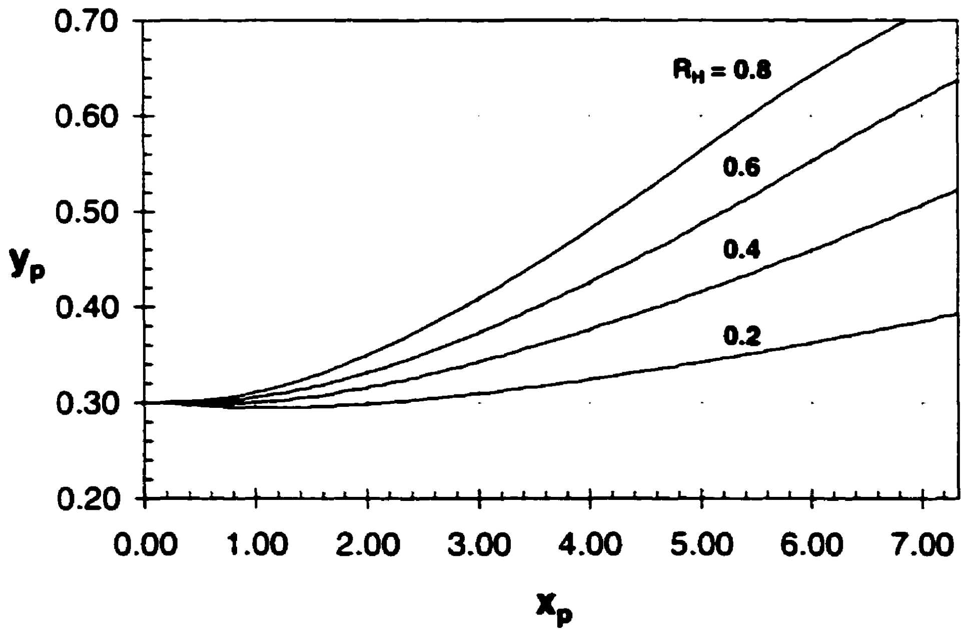

Figure 2.2 — The effect of R_H on the particle trajectory. Re = 500, γ = 1.0, k = 0.3.

particle moves further away from the axis of the pipe as the magnetic pressure number increases. This effect can be understood by examining the relative importance of the force terms on the right hand sides of the equations of motion (2.13) and (2.14). As an example, the variations of forces in the axial, x and radial, y directions during the motion of a particle with a blockage ratio k of 0.3 whose relative density with the fluid is $\gamma = 1.0$, are shown in Figures 2.3 and 2.4, respectively, for the case $\mathrm{Re} = 500$ and $R_H = 0.4$ shown in Fig. 2.2. It can be seen from both figures

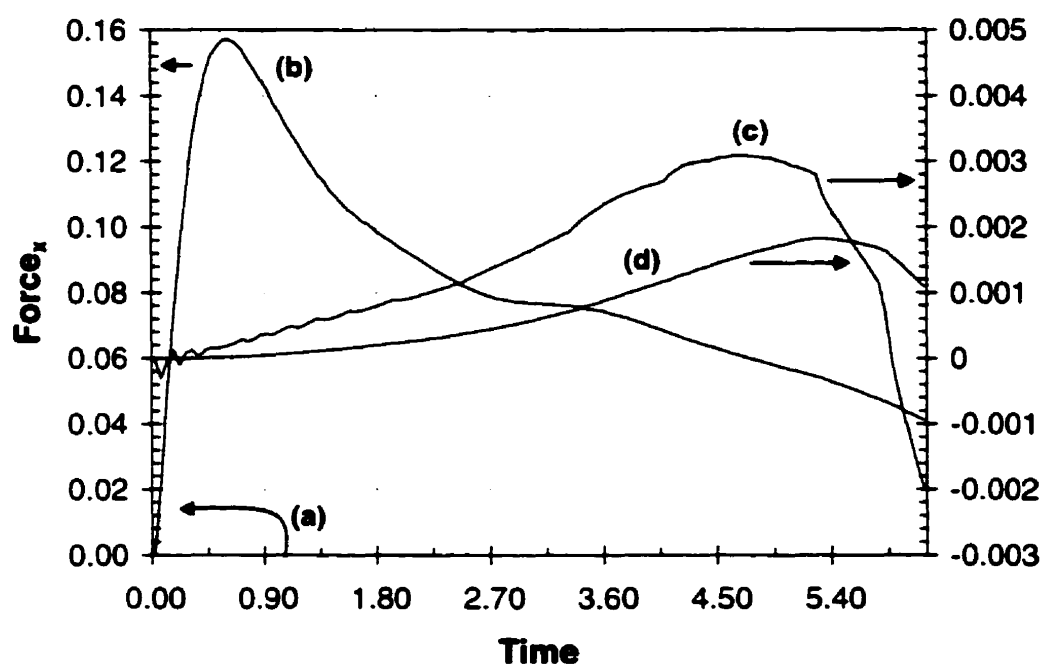

Figure 2.3 — Force terms in the axial direction. Re = 500, $R_H = 0.4$, $\gamma = 1.0$, $k = 0.3$.

(a) Electromagnetic force (virtually zero); (b) Fluid acceleration force; (c) History force; (d) Drag force.

that the fluid acceleration forces (Fig. 2.3(b) and Fig. 2.4(b)) are significant in the entrance region of the pipe, and diminish as the flow develops downstream. The electromagnetic force in the radial direction (Fig. 2.4(a)) is the dominant force term and this drives the particle towards the pipe wall. In the axial direction (Fig. 2.3(a)), by contrast, this force is zero. The drag force (Fig. 2.3(d)) and the history force (Fig. 2.3(c)) are seen to be relatively small in the axial direction, due to the fact that the particle follows the fluid velocity closely. However, both forces (Fig. 2.4(d) and (c)) become important in the radial direction. It is interesting to see that the history force is even higher than the drag force at the entrance because the relative velocity between the particle and the fluid flow is small while the relative acceleration is large.

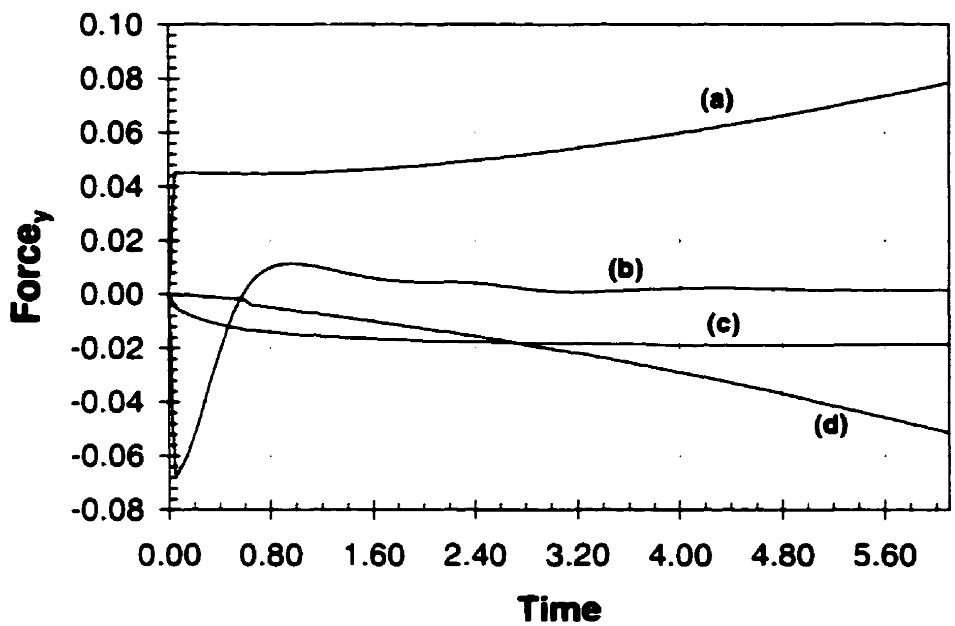

Figure 2.4 — Force terms in the radial direction. Re = 500. $R_H = 0.4$. $\gamma = 1.0$. $k = 0.3$.

(a) Electromagnetic force; (b) Fluid acceleration force; (c) History force; (b) Drag force.

The effect of increasing R_H is to increase the electromagnetic force in the radial direction. As a consequence, particles move faster towards the wall at higher R_H. It is also noted in Fig. 2.2 that at small R_H, immediately after entering the pipe, the particle actually acquires a negative radial velocity and moves a little towards the center before moving to the wall. This is related to the fluid acceleration term (Fig. 2.4(b)) which is stronger than the electromagnetic force (Fig. 2.4(a)) in the entrance region in radial direction. As R_H increases, the phenomenon becomes less obvious, and eventually the particle moves directly towards the wall at a magnetic pressure number R_H of 0.8.

2.3.2 *The Effect of* Re

The effect of the fluid flow velocity is characterized by Re. The effect of Re on the particle trajectory is shown in Figure 2.5. It can be seen that

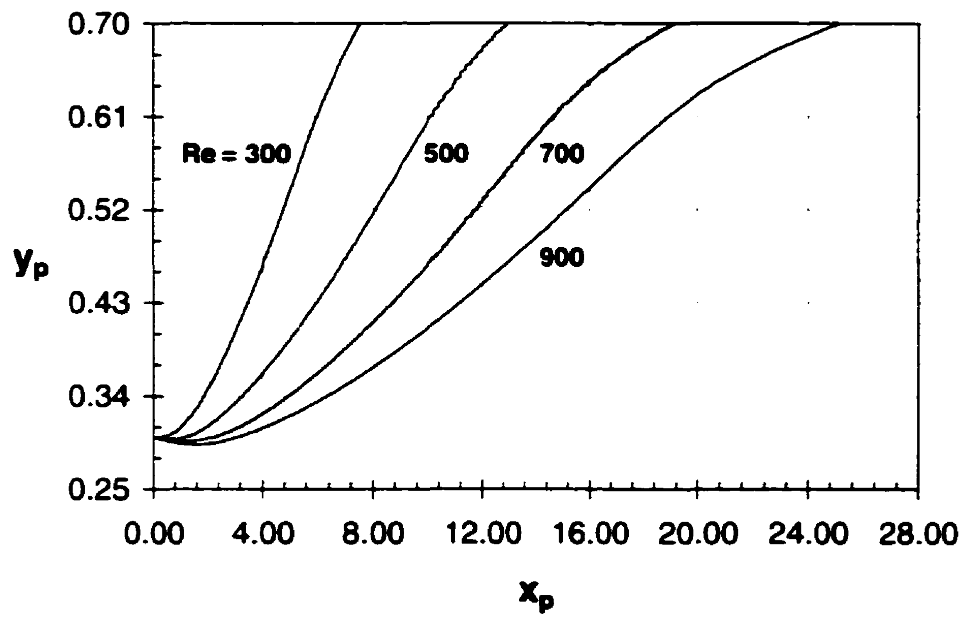

Figure 2.5 — The effect of Re on the particle trajectory. $\gamma = 1.0$, $k = 0.3$.

the axial distance traversed before the particle touches the wall increases with an increase in fluid Reynolds number. The axial distance traversed for Re = 900 is more than two times longer than that for Re = 300. The explanation for this is that as Re becomes larger, the fluid acceleration term becomes stronger and its action is felt by the particle further downstream. The increase in the fluid acceleration force in the radial direction is responsible for the increase in the initial negative velocity, driving particles closer towards the central axis of the pipe before moving to the wall. As explained in Fig. 2.3, the particle follows the fluid flow closely in the axial direction. Therefore, increasing Re will dramatically increase the axial distance traveled by the particle before it reaches the wall.

2.3.3 The Effect of γ

The inertia of the particle is reflected in its dimensionless density ratio, γ. It is found that the density only slightly affects the particle motion in the axial direction due to the fact that the particle constantly adjusts to the fluid velocity through the drag force on the particle. However, in the radial direction, it makes big difference. The effect of γ on the particle trajectory is illustrated in Figure 2.6. A particle with a relative density ratio of zero ($\gamma = 0$) represents the gas bubble in the liquid metal, and assumes a finite acceleration due to the added mass effect. A higher density particle, for example, $\gamma = 2.0$, accelerates slower than one of lower density in the radial direction, and thus moves longer distance in axial direction before reaching the wall.

2.3.4 The Effect of Blockage Ratio k

The particle size relative to the tube can be characterized by the dimensionless blockage ratio, k. The effect of k on the particle axial distance when reaching the wall is shown in Figure 2.7 for two different densities: $\gamma = 0$ and $\gamma = 1.5$. These ratios approximate the density of a micro bubble and an Al_2O_3 particle in a molten aluminum melt. It can be seen that the larger k, the shorter the axial distance traveled before reaching the wall. This can be explained by the fact that the electromagnetic force in the radial direction, which is proportional to the third order of k, increases the acceleration of the particle with increases in k. It is also noted from Fig. 2.7 that the density effect becomes larger when particles are bigger.

2.3.5 The Effect of the Entry Point to the Pipe

The trajectory of the particle flowing into a current-carrying cylindrical pipe from different radial co-ordinate positions is shown in Figure 2.8 for Re=700 and $R_H = 0.8$. An important feature in immediate vicinity of the entrance region, where the axial velocity is uniform, is that the radial velocity increases with increasing radial distance with respect to the pipe axis from 0.1 to 0.5. This is due to the electromagnetic force, which increases linearly with the radial coordinate. However, near the wall, the radial velocity becomes lower ($y_0 = 0.6$), which results from a dominating increase of the fluid acceleration force over the electromagnetic force. It is also shown in Fig. 2.8 that the radial velocity decreases as the particle moves close to the wall. This can be attributed to an increase in the drag force in the radial direction, resulting from wall effects.

2.3.6 The Application of the Model to LiMCA System

A basic requirement of the LiMCA system to measure the melt cleanliness accurately is that all particles flowing into the ESZ should pass through, rather than depositing on the sidewalls. The practical operating condition of the LiMCA system operating in the aluminum industry employs electric currents of 60 amperes passing through a $300\mu m$ diameter orifice. The average fluid velocity is 4 m/s, and the effective ESZ length is

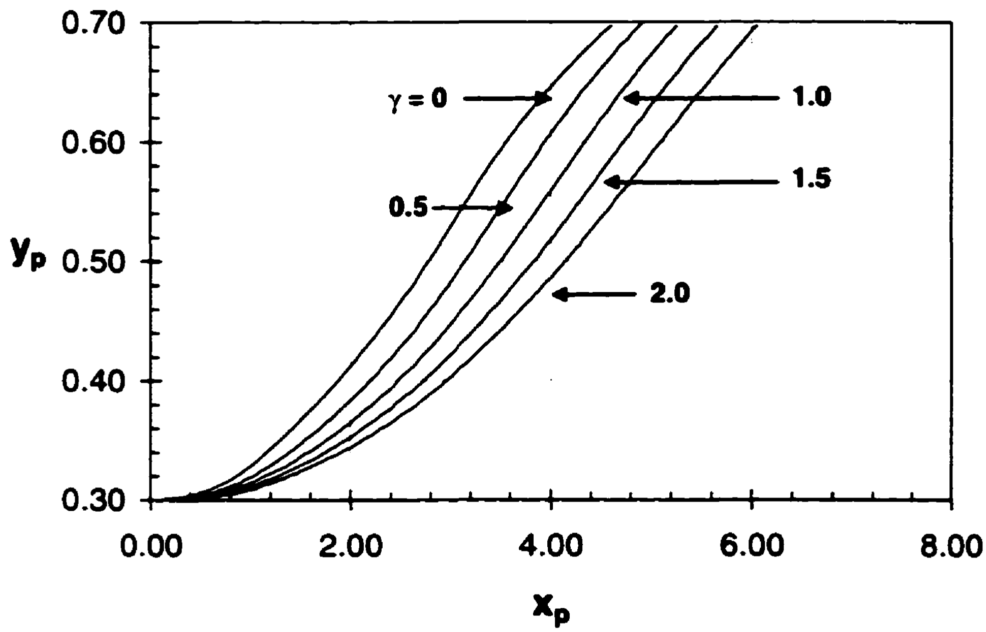

Figure 2.6 — The effect of γ on the particle trajectory. Re = 700, R_H = 0.8, k = 0.3.

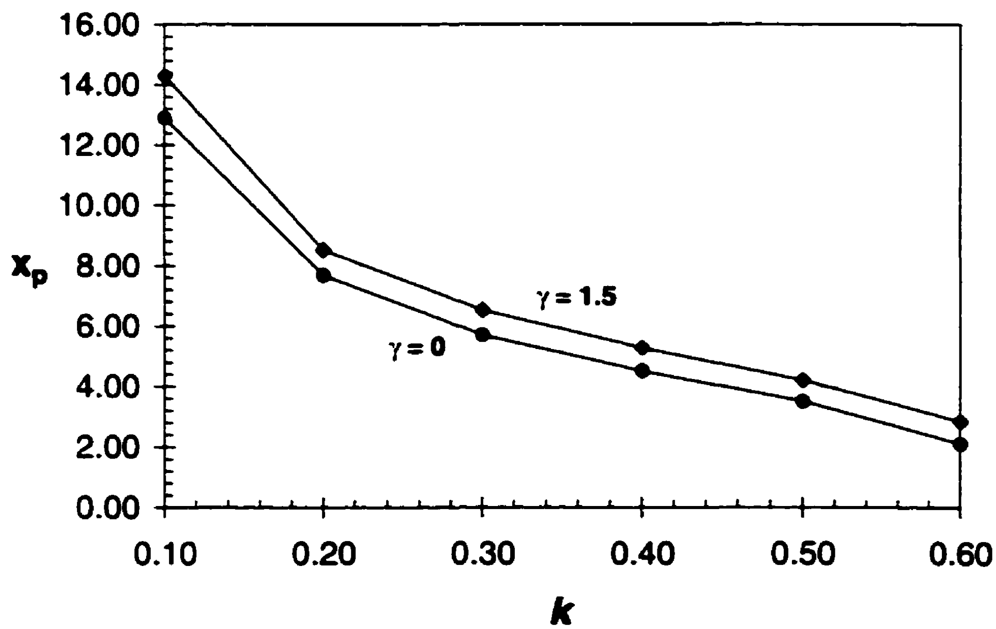

Figure 2.7 — The effect of k on the particle axial distance upon reaching the wall for different density particles. Re = 700, R_H = 0.8.

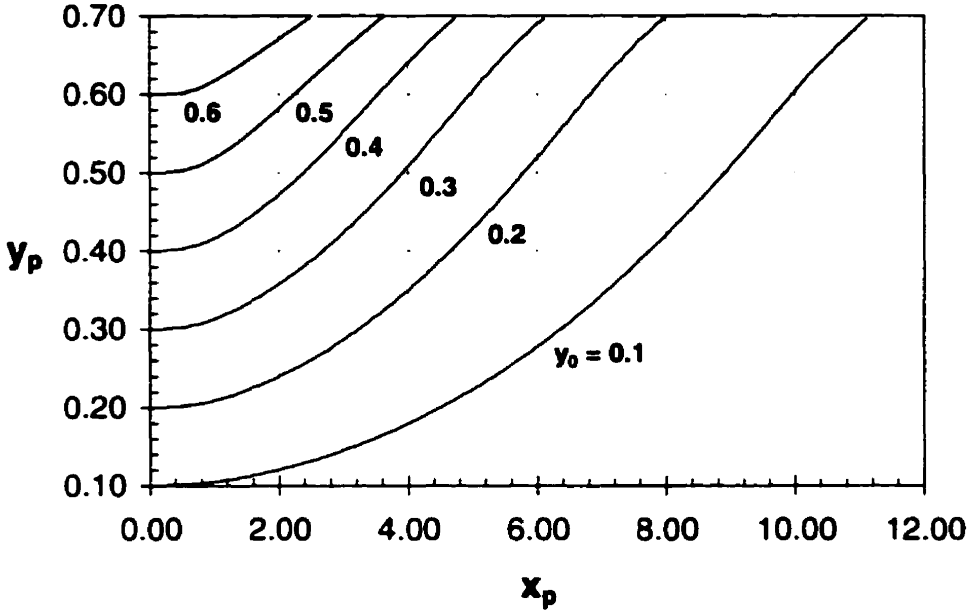

Figure 2.8 — The effect of entry point y_0 on the particle trajectory. $\gamma = 1.0$, $R_H = 0.8$, Re = 700, $k = 0.3$.

0.3 mm.[30] If we take the particle distribution at the inlet to be uniform for all particle sizes, the simulations can be carried out for $\gamma = 0$ and $\gamma = 1.6$ representing micro bubbles and Al_2O_3 inclusions within the aluminum melt. The predicted pass-through fraction for particle sizes ranging from 20 μm to 240 μm is shown in Figure 2.9. It is seen that the percentage of particles passing through the orifice decreases with increasing particle sizes. This tendency is more dramatic for the gas bubbles versus the solid particles. More than 90 percent of solid inclusions with sizes up to 75 μm and around 79 percent of solid inclusions even with sizes up to 240 μm successfully pass through the ESZ without grazing the sidewalls. This proves that LiMCA system can be used in liquid aluminum despite contradictory conclusions of previous analyses.[31] Meanwhile, it is also noted that the relative percentage of micro bubbles that pass through the orifice is high, especially for small size bubbles. For practical applications, micro bubbles need to be distinguished from the solid particles because the cleanliness of the melt is evaluated based on the number and size distribution of solid particles which are evidently more harmful compared with the gas bubbles.

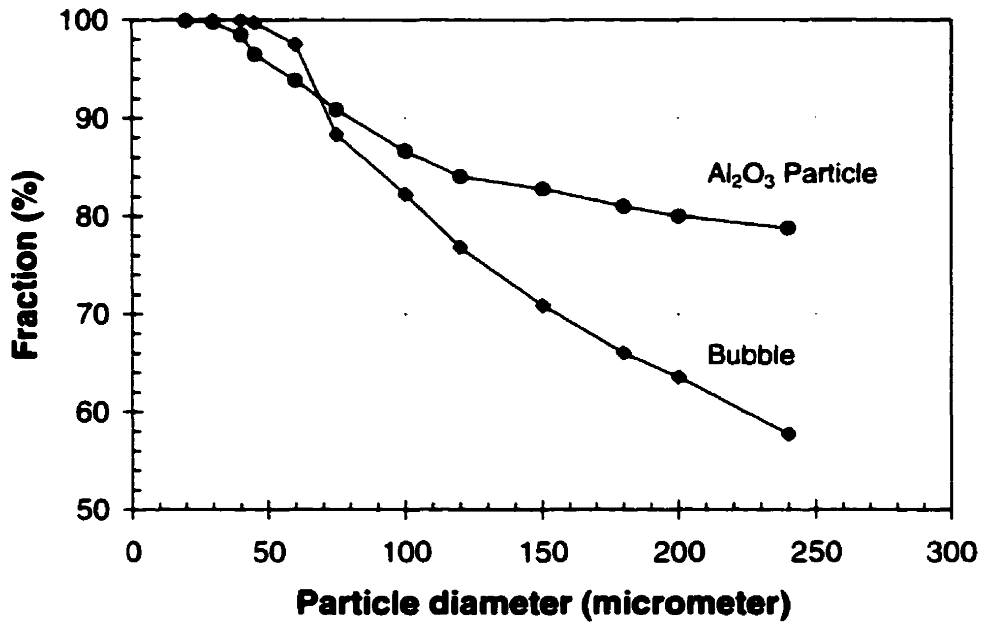

Figure 2.9 — Predicted pass-through fraction for different size particles flowing into the ESZ of LiMCA in molten aluminum.

2.4 Conclusions

A mathematical model has been developed for the motion of particles in current-carrying liquid metals flowing in a circular pipe. The fluid field was obtained by solving the Navier-Stokes equations, and the trajectories of particles by equations for the motion of particles. These involve transient motion and incorporate the drag force, the added mass force, the fluid acceleration force, the history force and the electromagnetic force on the particle. The results show that the particle trajectories are affected by the magnetic pressure number R_H, the Reynolds number Re, the blockage ratio k and the particle-fluid density ratio γ through the relative importance of those force terms. In the axial direction, the particles follow the fluid velocity closely, and move further down the axis of the tube before reaching the wall with increasing in fluid velocity (Re). In the radial direction, the electromagnetic force increases with the distance from the axis, the electric current (R_H), and the size (k) of the particle. The competition between the electromagnetic force and the radial fluid acceleration force in the entrance region first causes particle movement towards the center prior to a subsequent outward motion to the wall, at low electric currents (low R_H) and directly towards the wall for large currents (high R_H). The low inertia (γ) of bubbles allows them to move more rapidly towards the wall than heavier particles. The radial velocity of inclusion movement close to the sidewalls will decrease due to the wall effects. Finally, the model was applied to the LiMCA system under the operational conditions in aluminum industries, and the results show that more than 90 % of solid inclusions of size 75 μm and about 79 % of the solid inclusions of size 240 μm go through a 300 μm diameter ESZ. These results confirm from a theoretical standpoint that the LiMCA system can be used in aluminum industries.

References

[1] E.I. Shilova: Magnetohydrodynamics, 1976, vol. 12, pp. 250-251.

[2] V.V. Boyarevich, R.P. Millere, and A.Yu. Chudnovskii: Magnetohydrodynamics, 1985, vol. 21, pp. 53-58.

[3] A. Alemany, J.P. Argous, J. Barbet, M. Ivanes, R. Moreau, and S. Poinsot: French Patent 804004430, 1980.

[4] P. Marty and A. Alemany: Metallurgical Applications of

Magnetohydrodynamics, The Metals Society, Cambridge, UK, 1982, pp. 245-259.

[5] S. Taniguchi and J.K. Brimacombe: ISIJ International, 1994, vol. 34, pp. 772-731.

[6] J.C.R. Hunt and R. Moreau: J. Fluid Mech., 1976, vol. 78, pp. 261-288.

[7] J.P. Park, Y. Tanaka, K. Sassa, and S. Asai: Magnetohydrodynamics, 1996, vol. 32, pp. 227-234.

[8] D. Doutre and R.I.L. Guthrie: US Patent 4555662, 1985.

[9] R.I.L. Guthrie and D. Doutre: Proc. Intl. Seminar on Refining and Alloying of Liquid Aluminum and Ferro-Alloys, Trondheim, Norway, 1986, pp. 146-163.

[10] W.H. Coulter: US Patent 112819, 1953.

[11] R.W. Deblois and C.P. Bean: Rev. Sci. Instr., 1970, vol. 41, pp. 909-915.

[12] R.W. Deblois, C.P. Bean, and R.K.A. Wesley: J. of Colloid and Interface Science, 1977, vol. 61, pp. 323-335.

[13] W.R. Smythe: Rev. Sci. Instr., 1972, vol. 43, pp. 817-818.

[14] L.I. Berge, T. Jφssang, and J. Feder: Meas. Sci. Technol., 1990, vol. 1, pp. 471-474.

[15] D. Leenov and A. Kolin: J. Chem. Phys., 1954, vol. 22, pp. 683-687.

[16] Yu.A. Krasnitskii and V.I. Popov: Magnetohydrodynamics, 1975, vol. 11, pp. 209-212.

[17] I. Kim, S. Elghobashi, and W.A. Sirignano: J. Fluid Mech., 1998, vol. 367, pp. 221-253.

[18] V.M. Korovin: Magnetohydrodynamics, 1987, vol. 23, pp. 160-165.

[19] J. Szekely: Fluid Flow Phenomena in Metals Processing, Academic Press, Inc., New York, NY, 1979, pp. 179.

[20] A.B. Basset: Phil. Trans. R. Soc. Lond. , 1888, vol. 179A, pp. 43-63.

[21] A. Berlemont, P. Desjonqueres, and G. Gouesbet: Intl. J. Multiphase

Flow, 1990, vol. 16, pp. 19-34.

[22] R. Clift, J.R. Grace, and M.E. Weber: Bubbles, Drops, and Particles, Academic Press, Inc., New York, NY, 1978, pp. 112 and 225.

[23] T.R. Auton, J.C.R. Hunt, and M. Prud'homme: J. Fluid Mech., 1988, vol. 83, pp. 199-218.

[24] C.Y. Chow: Phys. Fluids, 1969, vol. 12, pp. 2317-2322.

[25] A.M. Fayon and J. Happel: AICHE Journal, 1960, vol. 6, pp. 55-58.

[26] J. Happel and H. Brenner: Low Reynolds Number Hydrodynamics, Printice-Hall, Inc., Englewood Cliffs, N.J., 1965, pp. 331.

[27] M. Peric, R. Kessler, and G. Scheuerer: Comput. Fluids, 1988, vol. 16, pp. 389-403.

[28] S.V. Patankar and D. B. Spalding: Int. J. Heat and Mass Trans., 1972, vol. 15, pp. 1787.

[29] J.N. Chung: Journal of Heat Transfer, 1982, vol. 104, pp. 438-445.

[30] F. Dallaire: Electric Sensing Zone Signal Behavior in Liquid Aluminum, Master Thesis, McGill University, 1990, pp. 11.

[31] S.T. Johansen: International Symposium on Electromagnetic Processing of Materials, ISIJ, Nagoya, Japan, 1994, pp. 104-109.

CHAPTER 3

Numerical Studies of the Motion of Spheroidal Particles Flowing with Liquid Metals through an Electric Sensing Zone (ESZ)

In Chapter 2, a model for particle motion in current-carrying liquid metals has been developed based on spherical particles. However, irregular shaped particles, reasonably approximated as spheroids with different aspect ratios, exist commonly in many materials processing processes. In this chapter, the model developed in Chapter 2 is generalized to describe the motion of spheroidal particles.

3.1 Introduction

The electric sensing zone technique[1] is a method of determining the number and size of particles suspended in a conducting medium by passing them through a small orifice on either side of which is immersed an electrode. A constant current is applied between the two electrodes. When a non-conducting particle passes through the orifice, the resistance is changed, giving rise to a voltage pulse signal. The principle is shown schematically in Figure 3.1 for a spherical particle passing through the ESZ along the central axis of the orifice, where I is the constant current applied, ρ_e is the electrical resistivity of the fluid, and A and L are the cross sectional area and the length of the orifice, respectively. R_1 is the resistance of the orifice without a particle, and ΔR is the resistance increase when a particle goes through the orifice. For a particle of diameter d which is far less than the orifice diameter D, ΔR is given by:[2]

$$\Delta R = \frac{4\rho_e d^3}{\pi D^4} \qquad (3.1)$$

This expression shows that the resistive pulse is proportional to the particle volume. If d is not small compared to D, ΔR should be modified as equation (3.2) by a factor $f(d/D)$:[3]

$$\Delta R = \frac{4\rho_e d^3}{\pi D^4} f(d/D) \qquad (3.2)$$

where $f(d/D)$ was obtained according to the numerical results of Symthe[4] in analyzing an ideal fluid flow around a sphere in a circular tube.

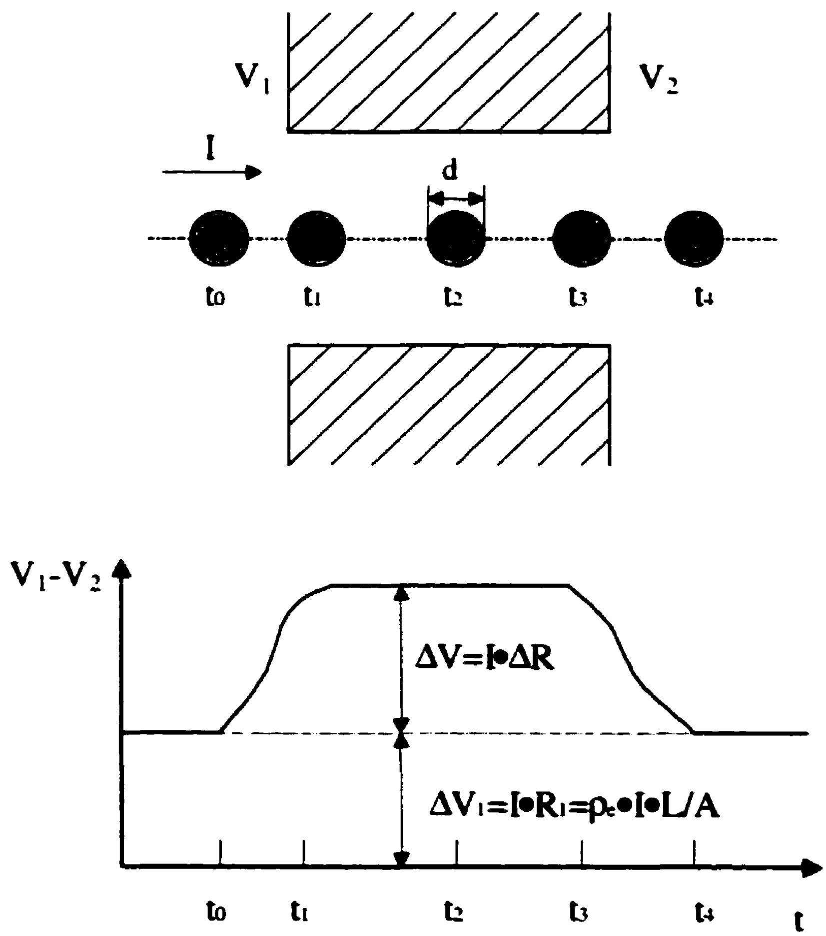

Figure 3.1 — Schematic representation of ESZ principle of particle size measurement.

In addition to the volume dependence, the amplitude of the resistance change also depends on the shape,[5] orientation[6,7] and radial position[8] of the particle inside the orifice. Taking the effects of shape and orientation into account, the resistance change can be expressed as:[6]

$$\Delta R = S_p \frac{V_p}{V} R_1 \qquad (3.3)$$

where V_p is the particle volume, V is the orifice volume, and S_p is the shape factor of the particle, which is $\frac{3}{2}$ for a sphere. For a general ellipsoid of revolution, S_p is given by:

$$S_p = S_{p_\perp} + (S_{p_{//}} - S_{p_\perp})\cos^2\alpha \qquad (3.4)$$

where $S_{p_{//}}$ is the shape factor for the case of the electric field directed parallel to the symmetric axis of the ellipsoid, $S_{p_\perp}$ is the corresponding factor for the perpendicular orientation, and α is the angle between the axis of symmetry and the electric field. For a prolate ellipsoid with a ratio of the dimension of the symmetric axis to equatorial diameter $E = 2.0$, the shape factors are $S_{p_\perp} = 1.7$ and $S_{p_{//}} = 1.2$.[7] This means that, a prolate ellipsoid with its axis of symmetry parallel to the axis of the orifice will be measured as a sphere whose volume is only 80 percent of the true value when ignoring the shape and orientation effects. In the perpendicular orientation, its volume will be overestimated by 13 percent. The radial position of the particle inside the orifice also affects the measurement.[8] According to the theoretical predictions of Smythe,[8] a spherical particle of $d/D = 0.2$, moving very close to the orifice wall, will be evaluated as a sphere 30 percent more in volume than the same sphere moving along the orifice axis. This position-dependent response has been confirmed by experiments[9,10] although it seems that the results are less drastic than that suggested by the numerical calculations. As such, numerical simulations revealing the relationship between the particle trajectory and its shape and orientation will facilitate the accurate measurement of particles by the ESZ technique. Furthermore, it was noticed that the amplitude-time history of a pulse reflects the characteristics of the particle motion through an electric sensing zone.[9] Since these signals are unique to individual particles of different sizes, shapes, orientations, and densities, a numerical study of the particle trajectories in an ESZ will also help realize particle discrimination.

Many theoretical and experimental studies have been carried out on the electrical and hydrodynamic factors involved during the passage of a suspended particle in an aqueous eletrolyte medium through an ESZ[6,7,10-14]. A common feature of all these studies is the assumption that the path followed by the particle does not depend on the electric, but rather the hydrodynamic field. This is because the electric currents applied in these aqueous systems are very weak, usually in the order of microamperes to milliamperes as a result of the high electrical resistivity of the electrolyte. However, the passage of a particle through an ESZ in a liquid metal system, such as in the case of LiMCA systems,[15,16] is quite different. The heavy current involved ($\sim 20-60\,A$) gives rise to strong radial electromagnetic force. This force accelerates particles towards the inner sidewall of the ESZ. In Chapter 2, the study on the motion of spherical particles in current-carrying liquid metals flowing in a circular pipe has confirmed the strong dependence of particle trajectories on both the hydrodynamic and the electric fields. A study of particle trajectory will help to determine if all particles to be measured can pass through the ESZ without being collected on the inner wall of the orifice, a basic requirement for the operation of LiMCA system to molten metals, besides the enhancement of the accuracy of particle size measurement and particle discrimination.

In this chapter, the general mathematical model that has been developed in Chapter 2 was extended to describe the motion of spheroidal particles of different shapes and orientations entrained within liquid metals flowing through an ESZ. The Navier-Stokes equations were solved for predicting the flow field, while particle trajectories were obtained by solving the equations for the motion of spheroidal particles that included the particle inertia, drag, buoyancy, gravity and added mass, fluid acceleration and history forces, as well as the electromagnetic forces generated by the applied current. Particle shape and orientation were taken into account through the correction factors to these force terms. The effects of ESZ sidewall proximity in modifying the trajectories of spheroidal particles were also considered. Finally, the model developed in this work was applied to the ESZ of the LiMCA system, now in worldwide use within the aluminum industry, in order to evaluate its performance under actual operational conditions.

3.2 Mathematical Model and Numerical Methods

The present study considered the trajectories of spherodial particles of different shapes and orientations entrained within a homogeneously conducting liquid metal flowing through an ESZ. Previous work indicated that the convergent entrance flow of the ESZ orients the oblate and prolate spheroidal particles. As a result, an oblate ellipsoid enters the orifice with its axis of symmetry perpendicular to the orifice axis,[6] while a prolate ellipsoid assumes its symmetric axis parallel to the orifice axis when entering the orifice near the center line, but orients its axis of symmetry perpendicular to the orifice axis[7] when traversing near the orifice wall. The rotation of the particle in the ESZ was neglected due to the fact that, in the core region of the orifice, the velocity is so uniform that the rotation resulting from the shear of the flow is negligible. Furthermore, near the inner wall of the orifice, the high pressure gradient generated from the applied electric current would prevent the rotation of a prolate spheroid whose axis of symmetry is perpendicular to the orifice axis. A two-dimensional simulation in a cylindrical coordinate system was employed since the electromagnetic force is sufficiently strong as to confine any particle motion to the plane containing the mass center of the particle and the axis of the orifice. The shape and orientation of the spheroidal particles and the coordinate system used in this study are shown schematically in Figure 3.2, where D and L are the respective diameter and length of the

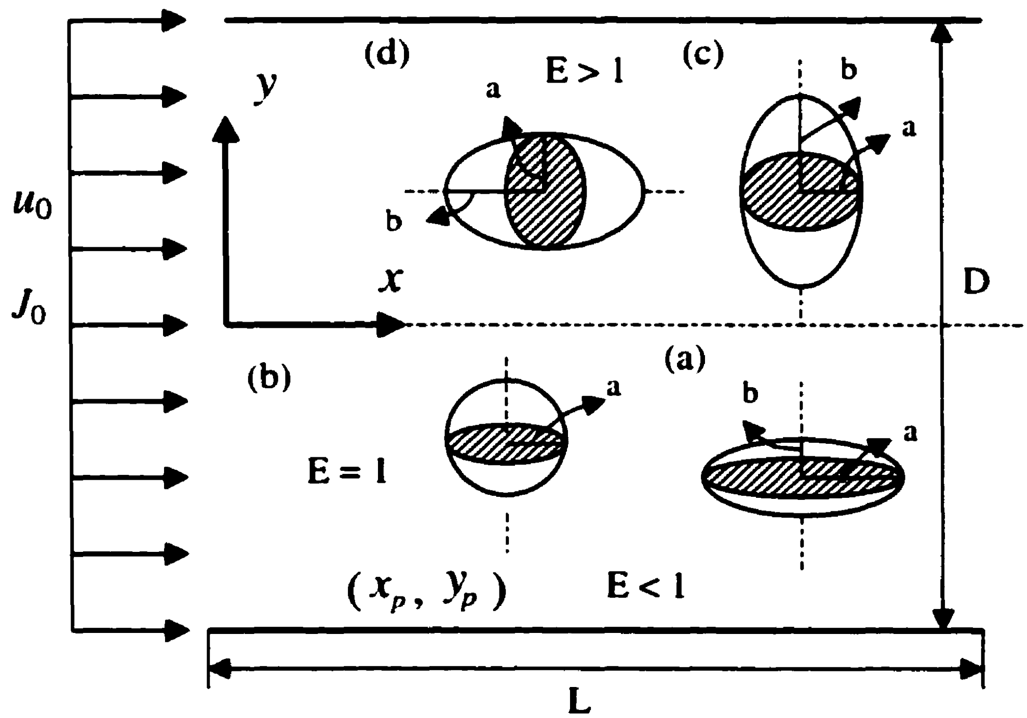

Figure 3.2 — Schematic representation of the system used in the computation. (a) An oblate with its symmetric axis perpendicular to the axis of the ESZ; (b) A sphere; (c) A prolate with its symmetric axis perpendicular to the axis of the ESZ; (d) A prolate with its symmetric axis parallel to the axis of the ESZ.

orifice, u_0 is the inlet flow velocity, and J_0 is the electric current density. The center of particle is located at (x_p, y_p), where x and y are the respective axial and radial coordinates. The symmetric axis dimension of the spheroidal particle is $2b$, and the dimension normal to the axis of symmetry, the equatorial diameter, is $2a$. The aspect ratio b/a of the particle is denoted by E which is less than 1 for an oblate and larger than 1 for a prolate ellipsoid. A sphere is a special case, where E equals to 1.

3.2.1 The Flow Field in the ESZ

The mathematical model for the fluid flow and electromagnetic fields are the same as those used in Chapter 2, which was described in 2.2.1, and will not be detailed here.

3.2.2 The Equation of Motion for Spheroidal Particles

As described in Chapter 2, in conventional hydrodynamics, high Reynolds number motions of a spherical particle in a fluid which is also in motion itself can be represented by an equation which was given by Berlemont, Desjonqueres and Gouesbet.[17] Non-spherical particles are more difficult to consider than spherical ones because of the influence of particle orientation and the lack of a single unambiguous dimension upon which to base dimensionless parameters. Based on the studies by Loewenberg[18] and Lawrence and Weibaum,[19] the following equation is proposed for the motion of a spheroidal particle along its principal axes which is generalized from the equation for spheres:

$$m_p \frac{d\bar{u}_p}{dt} = \frac{1}{2} R^D C_D A_P \rho_f \left|\bar{u} - \bar{u}_p\right| (\bar{u} - \bar{u}_p) + M^A m_f \left(\frac{D\bar{u}}{Dt} - \frac{d\bar{u}_p}{dt}\right) + m_f \frac{D\bar{u}}{Dt}$$
$$+ 6Ba^2 (\pi\mu_f \rho_f)^{1/2} \int_0^t \frac{d(\bar{u} - \bar{u}_p)/d\tau}{(t-\tau)^{1/2}} d\tau + (m_p - m_f)\bar{g} \qquad (3.5)$$

where $\bar{u}_p(u_p, v_p)$ and $\bar{u}(u, v)$ represent the instantaneous velocity of the particle and the undisturbed fluid velocity at the center of the particle that would apply in the absence of that particle. C_D represents the drag coefficient from the steady standard drag curve[20] for a sphere with the particle Reynolds number based on the equatorial diameter of a spheroidal ellipsoid. $\mathrm{Re}_p = \dfrac{2\rho_f \left|\bar{u} - \bar{u}_p\right| a}{\mu_f}$. A_p is the cross-sectional area of the spheroidal particle projected on a plane perpendicular to the direction of motion, whose value is πa^2 or πab depending on whether the particle motion is parallel or perpendicular to the axis of symmetry of the particle. m_p is the particle mass, m_f is the fluid mass displaced by the particle, and μ_f is the dynamic viscosity of the fluid. R^D, M^A and B are the respective correction factors for drag force, added mass and history force terms, and are functions of particle shape and orientation. For the motion of particle relative to the fluid flow parallel or perpendicular to the axis of symmetry of the spheroid, these factors can be expressed as follows for oblate ($E < 1$), spherical ($E = 1$) and prolate ($E > 1$) particles: [18]

$$M_{//}^A = -\frac{\sqrt{1-E^2} - E\cos^{-1} E}{E^2\sqrt{1-E^2} - E\cos^{-1} E}; \qquad E < 1$$
$$= \frac{1}{2}; \qquad E = 1 \qquad (3.6)$$

$$= -\frac{\sqrt{E^2-1} - E\cosh^{-1}E}{E^2\sqrt{E^2-1} - E\cosh^{-1}E}; \qquad E > 1$$

$$M_\perp^A = (1 + 2M_{//}^A)^{-1} \tag{3.7}$$

$$B_{//} = \frac{1}{6\pi E}(1 + M_{//}^A)^2 I_{//} \tag{3.8}$$

$$B_\perp = \frac{1}{6\pi E}(1 + M_\perp^A)^2 I_\perp \tag{3.9}$$

where

$$I_{//} = 2\pi E^2 [\frac{2-E^2}{(1-E^2)^{3/2}}\cosh^{-1}\frac{1}{E} - \frac{1}{1-E^2}]; \qquad E < 1$$

$$= \frac{8\pi}{3}; \qquad E = 1$$

$$= 2\pi E^2 [\frac{E^2-2}{(E^2-1)^{3/2}}\cos^{-1}\frac{1}{E} + \frac{1}{E^2-1}]; \qquad E > 1$$

$$I_\perp = -\frac{\pi}{E^2}[\frac{E^4}{(1-E^2)^{3/2}}\cosh^{-1}\frac{1}{E} - \frac{2-E^2}{1-E^2}]; \qquad E < 1$$

$$= \frac{8\pi}{3}; \qquad E = 1$$

$$= \pi[\frac{E^4}{(E^2-1)^{3/2}}\cos^{-1}\frac{1}{E} + \frac{E^2-2}{E^2-1}]; \qquad E > 1$$

For particle motion at low Reynolds number Re_p, the drag force correction factor R^D may be expressed in terms of $M_{//}^A$:

$$R_{//}^D = \frac{2}{3}E[(M_{//}^A + 1)/(E^2 M_{//}^A + \frac{1}{2})] \tag{3.10}$$

$$R_\perp^D = \frac{4}{3}[(M_{//}^A + 1)/(E^2 M_{//}^A + \frac{3}{2})] \tag{3.11}$$

while at high Reynolds number Re_p, R^D has a very complex dependence on E and was obtained numerically.[21, 22]

As to the motion of spheroidal particles in an ESZ, the electromagnetic force on the particle has to be included. Therefore, in this study, the prediction of the trajectory of a non-conducting, rigid, spheroidal particle was based on the following equation, written in vector form:

$$\begin{aligned}
\rho_p V_p \frac{d\bar{u}_p}{dt} &= \frac{1}{2} R^D C_D A_p \rho_f \left|\bar{u}-\bar{u}_p\right|(\bar{u}-\bar{u}_p) + M^A \rho_f V_p \left(\frac{D\bar{u}}{Dt} - \frac{d\bar{u}_p}{dt}\right) \\
&+ \rho_f V_p \frac{D\bar{u}}{Dt} + 6Ba^2 (\pi\mu_f \rho_f)^{1/2} \int_0^t \frac{d(\bar{u}-\bar{u}_p)/d\tau}{(t-\tau)^{1/2}} d\tau \\
&+ (\rho_p - \rho_f) V_p \bar{g} - E^M V_p \bar{F}
\end{aligned} \tag{3.12}$$

where ρ_p and V_p are the density and volume of the particle, and $\bar{F}$ represents the electromagnetic force per unit volume of fluid at the position of the particle. E^M is the correction factor for the electromagnetic force which accounts for the disturbance of the uniform electric current distribution by the presence of the particle. This disturbance is reflected in the electrical shape factor S_p of a spheroidal particle. The values of S_p for the case of an electric field directed parallel to the axis of symmetry of spheroidal particle, $S_{p//}$, and for the perpendicular orientation, $S_{p\perp}$, are given as a function of the aspect ratio E.[6] A higher electric shape factor, which means stronger disturbance to the electromagnetic field by the particle, corresponds to lower electromagnetic force correction factor E^M. In the case of a sphere, $S_{p//}$ and $S_{p\perp}$ are equal and both have the value of $\frac{3}{2}$. $E^M_{//}$ and $E^M_{\perp}$ are $\frac{3}{4}$ for a sphere.[23] For a general spheroidal particle, $E^M_{//}$ and $E^M_{\perp}$ can be obtained approximately by keeping the product of $S_{p//}$

and $E_{//}^{M}$ or $S_{p_\perp}$ and $E_{\perp}^{M}$ equal to the corresponding value of a sphere which is $\frac{9}{8}$. This approximation results in an error of 12.5% in the extreme situation of $E \to \infty$, where $E_{//}^{M}$ and $S_{p_{//}}$ should be 1.

From Chapter 2, the numerical results of the motion of spherical particles in a current-carrying liquid metal flowing through a cylindrical pipe show that the particles follow the fluid flow closely in the axial direction. In this study, it is consequently assumed that, at any instant, the axial velocity of a spheroidal particle flowing within an ESZ is equal to the undisturbed fluid flow velocity in the axial direction at the instantaneous center of that particle. The radial velocity, however, needs to be obtained according to equation (3.12). When a spheroidal particle flows into the ESZ with its axis of symmetry parallel to the orifice axis, the radial motion may be expressed as:

$$\begin{aligned}\rho_p V_p \frac{dv_p}{dt} &= \frac{1}{2} R_{\perp}^{D} C_D (\pi ab) \rho_f \left| v - v_p \right| (v - v_p) + M_{\perp}^{A} \rho_f V_p \left(\frac{Dv}{Dt} - \frac{dv_p}{dt}\right) \\ &+ \rho_f V_p \frac{Dv}{Dt} + 6 B_{\perp} a^2 (\pi \mu_f \rho_f)^{1/2} \int_0^t \frac{d(v - v_p)/d\tau}{(t-\tau)^{1/2}} d\tau \\ &+ (\rho_f - \rho_p) V_p g - E_{//}^{M} V_p F_v\end{aligned} \tag{3.13}$$

While in the case of a spheroidal particle flowing into the ESZ with its axis of symmetry perpendicular to the orifice axis, the radial motion may be expressed as:

$$\begin{aligned}\rho_p V_p \frac{dv_p}{dt} &= \frac{1}{2} R_{//}^{D} C_D (\pi a^2) \rho_f \left| v - v_p \right| (v - v_p) + M_{//}^{A} \rho_f V_p \left(\frac{Dv}{Dt} - \frac{dv_p}{dt}\right) \\ &+ \rho_f V_p \frac{Dv}{Dt} + 6 B_{//} a^2 (\pi \mu_f \rho_f)^{1/2} \int_0^t \frac{d(v - v_p)/d\tau}{(t-\tau)^{1/2}} d\tau \\ &+ (\rho_f - \rho_p) V_p g - E_{\perp}^{M} V_p F_v\end{aligned} \tag{3.14}$$

Equations (3.13) and (3.14) can be written in dimensionless form as equations (3.15) and (3.16) (omitting the asterisks for convenience) by introducing three more non-dimensional variables:

$$v_p^* = \frac{v_p}{u_0},\ t^* = \frac{u_0 t}{R},\ \text{and}\ \tau^* = \frac{u_0 \tau}{R}$$

For spheroidal particle with its symmetric axis parallel to the ESZ axis:

$$\begin{aligned}\frac{dv_p}{dt} = \frac{1}{\gamma + M_\perp^A}[&\frac{3}{8k} R_\perp^D C_D |v - v_p|(v - v_p) + (M_\perp^A + 1)(u\frac{\partial v}{\partial x} + v\frac{\partial v}{\partial y}) + \\ &\frac{9B_\perp}{2k}(\frac{1}{\pi \mathrm{Re}})^{1/2}\int_0^t \frac{d(v - v_p)/d\tau}{(t-\tau)^{1/2}} d\tau - E_{//}^M R_H F_v + (1-\gamma)Fr]\end{aligned} \tag{3.15}$$

For spheroidal particle with its symmetric axis perpendicular to the ESZ axis:

$$\begin{aligned}\frac{dv_p}{dt} = \frac{1}{\gamma + M_{//}^A}[&\frac{3}{8kE} R_{//}^D C_D |v - v_p|(v - v_p) + (M_{//}^A + 1)(u\frac{\partial v}{\partial x} + v\frac{\partial v}{\partial y}) + \\ &\frac{9B_{//}}{2k}(\frac{1}{\pi \mathrm{Re}})^{1/2}\int_0^t \frac{d(v - v_p)/d\tau}{(t-\tau)^{1/2}} d\tau - E_\perp^M R_H F_v + (1-\gamma)Fr]\end{aligned} \tag{3.16}$$

where Re and R_H are the respective fluid Reynolds number and magnetic pressure number as in the dimensionless Navier-Stokes equations. $Fr = \frac{gR}{u_0^2}$ is the Froude number, $\gamma = \frac{\rho_p}{\rho_f}$ is the particle - fluid density ratio, and $k = \frac{a}{R}$ is the blockage ratio, and $E = \frac{b}{a}$ is the aspect ratio of the spheroid.

3.2.3 *Wall Effects*

The presence of a solid surface in the vicinity of a moving particle will affect the drag force. In this study, the wall effects in the radial direction for a spheroidal particle was estimated by using the correction factor for a sphere[24] with the same cross-sectional area projected along the radial direction. The correction factor is a function of the ratio of the distance of the particle center from the wall to the particle radius, and linear interpolation is employed to obtain the factor for the ratio in question.

3.2.4 Numerical Methods

The conservation equations for mass and momentum with the boundary conditions, and Equations (3.15) and (3.16) for the motion of spheroidal particles were solved using the same methods as described in 2.2.4.

3.3 Results and Discussion

Equations (3.15) and (3.16) describe the radial motion of a spheroidal particle when its symmetric axis is parallel or perpendicular to the axis of the ESZ, respectively. These equations show that the motion of a spheroidal particle is also affected by the particle shape and orientation besides the five non-dimensional parameters, Re, R_H, γ, k, and Fr, which have been considered for the trajectories of a sphere in Chapter 2. Non-dimensional parameters Re and R_H are related to the flow field, Fr is related to the buoyancy force term $(1-\gamma)Fr$, while R_H to the electromagnetic force term $-E^M R_H F_v$ as shown in Equations (3.15) and (3.16). In practical operations employing intensive electric current density such as in the ESZ of LiMCA system, Fr is four orders smaller than R_H.

Compared to the electromagnetic force on a particle, which increases linearly with the radial distance from the central transverse axis of the ESZ, the buoyancy force is negligibly small and can be ignored, provided the particle density is not very high and its initial position is not very close to the axis of the ESZ. Under such circumstances, the particle trajectory can be taken as symmetric with respect to the axis of the ESZ, and calculations are performed only on the positive initial particle positions.

In this chapter, the effects of Re, R_H, γ and k on the motion of spheroidal particles were investigated on volume-equivalent oblate ($E<1$), sphere ($E=1$), and prolate ($E>1$) of different orientations, since the ESZ method measures the volume of particles. The effects of γ and k were investigated in the same flow field by keeping Re and R_H constant. In practical operations, the flow field is controlled by the fluid velocity u_0, and the applied electric current I. In the computation, the velocity u_0 is represented by the Reynolds number Re, while the electric current I is contained in the magnetic pressure number R_H. The effect of R_H on the motion of particles is considered by keeping Re, γ and k constant, while the effect of Re can be revealed by holding γ and k constant, and maintaining $\mathrm{Re}^2 R_H = \dfrac{\rho_f \mu_0 I^2}{\pi^2 \mu_f^2}$ constant so as to neutralize the effect of the inertial force, leaving electric current I fixed for a specific molten metal. In this study, $\mathrm{Re}^2 R_H$ was taken as 8.55×10^4, which represents an electric current of 30 amperes flowing through a 300 μm diameter ESZ containing molten aluminum. The particle is considered to have reached the wall when its center is an equatorial radius or half axis of symmetry away from the inner wall of the ESZ for particle with symmetric axis parallel or perpendicular to the axis of the ESZ, respectively. The initial position of the particle flowing into the ESZ was set at dimensionless coordinates

$(x_0, y_0) = (0, 0.3)$ for most of the simulations, except in the study of the effect of k where $y_0 = 0.1$ and in the study of the initial position where y_0 varies from 0.1 to 0.6.

3.3.1 The Effect of R_H

The effect of magnetic pressure number R_H on the trajectory of a spheroidal particle is shown in Figure 3.3. It can be seen from Figure 3.3 that as the magnetic pressure number R_H increases, the particles move further away from the axis of the ESZ at the same axial position x_p for a sphere (Figure 3.3(b)), an oblate (Figure 3.3(a)), a prolate with its symmetric axis perpendicular to the axis of the ESZ (Figure 3.3(c)) and a prolate with its symmetric axis parallel to the axis of the ESZ (Figure 3.3(d)).

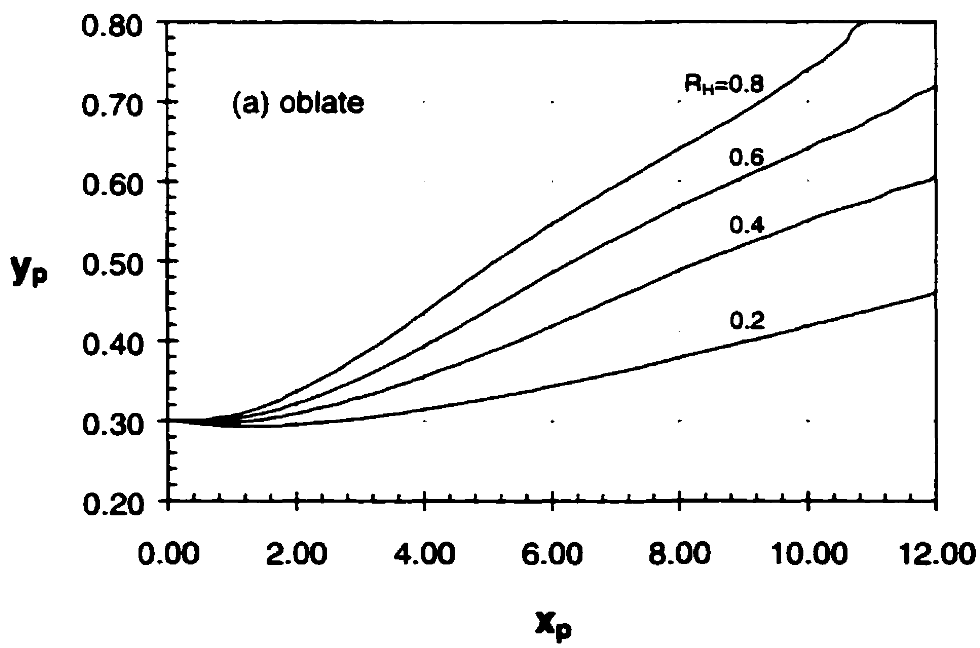

(a) Oblate ($E = 0.5$)

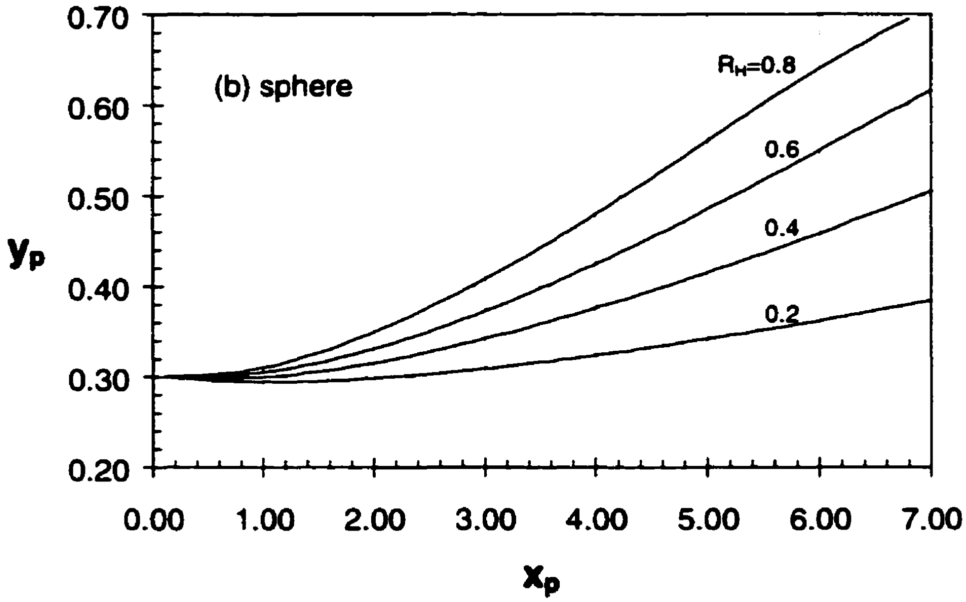

(b) Sphere ($E = 1.0$)

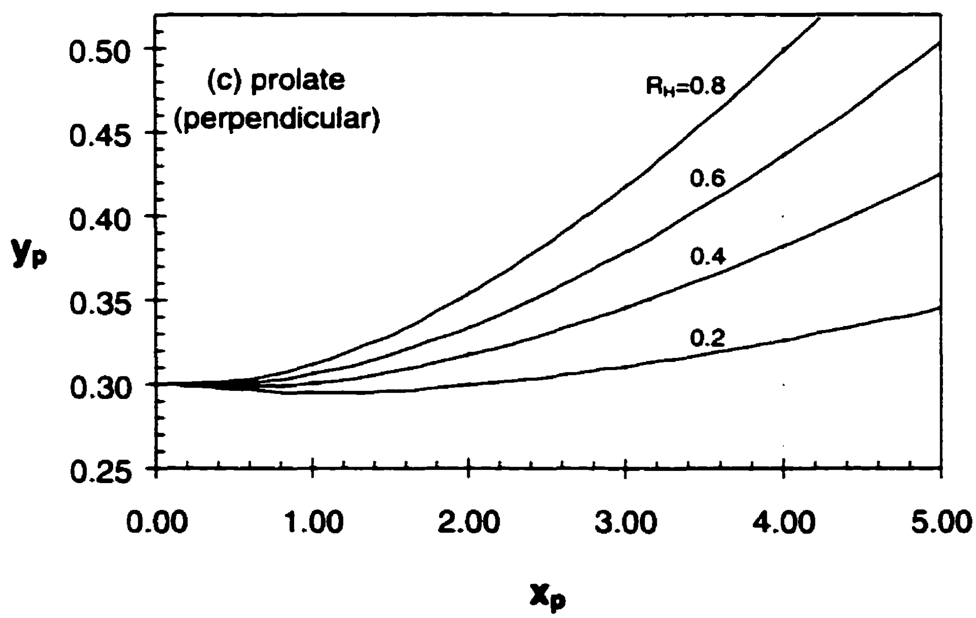

(c) Prolate ($E = 2.0$) with its symmetric axis perpendicular to the axis of the ESZ

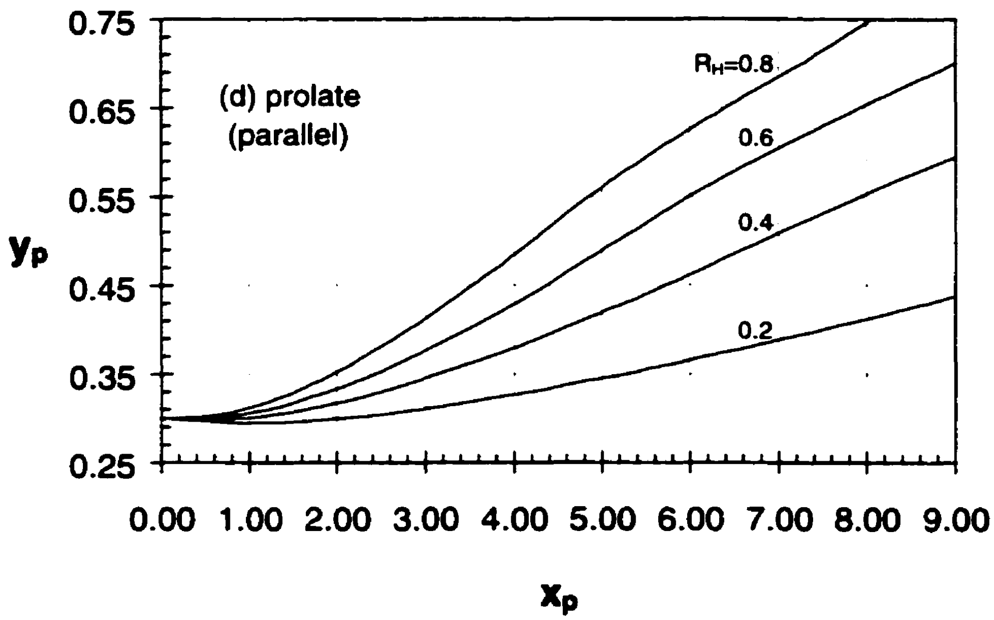

(d) Prolate ($E = 2.0$) with its symmetric axis parallel to the axis of the ESZ

Figure 3.3 — The effect of R_H on the trajectories of spheroidal particles of different shape and orientation. $\mathrm{Re} = 500$, $\gamma = 1.0$, particle volume is equivalent to that of a sphere of $k = 0.3$.

The effect of R_H on particle trajectories can be understood by examining the relative importance of the force terms on the right side of the equations of motion (3.15) and (3.16), noting that the fluid acceleration forces in these equations contain the contribution from the added mass M^A. As an example, the variations of forces in the radial direction during the motion of spheroidal particles of volume equivalent to a sphere of $k = 0.3$, whose particle-fluid density ratios are $\gamma = 1.0$, are shown in Figure 3.4 for the case $\mathrm{Re} = 500$ and $R_H = 0.8$. It can be seen that the force terms have some common features irrespective of the particle shape and orientation. The fluid acceleration forces (Figure 3.4(a)) are significant in the entrance region of the ESZ, and diminish as the flow develops downstream. The electromagnetic forces are the dominant force term and drive the particles towards the sidewalls of the ESZ. Furthermore, it can be seen from Figure 3.4(b) that the history force is even higher than the drag force at the entrance because the relative velocity between the particle and the fluid flow is small while the relative acceleration is large.

The effect of increasing R_H is to increase the electromagnetic force in the radial direction. As a consequence, particles move faster towards the wall at higher R_H. It is also noted that at small R_H, for example $R_H = 0.2$, immediately after entering the ESZ, the particles in all cases actually

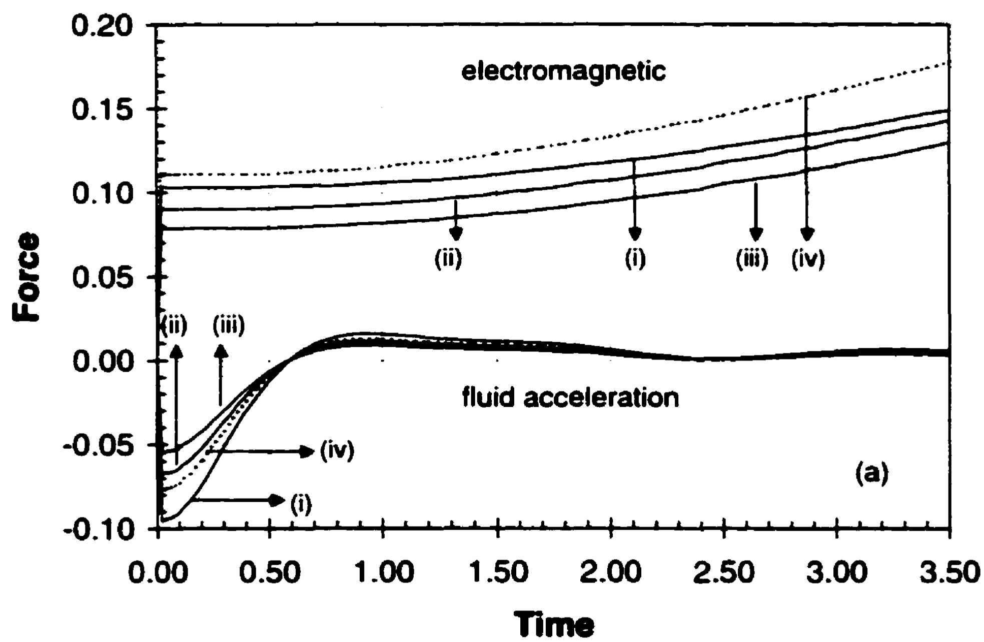

(a) Electromagnetic and fluid acceleration forces (i) oblate ($E = 0.5$), (ii) sphere ($E = 1.0$), (iii) prolate ($E = 2.0$) with its symmetric axis perpendicular to the axis of the ESZ, (iv) prolate ($E = 2.0$) with its symmetric axis parallel to the axis of the ESZ

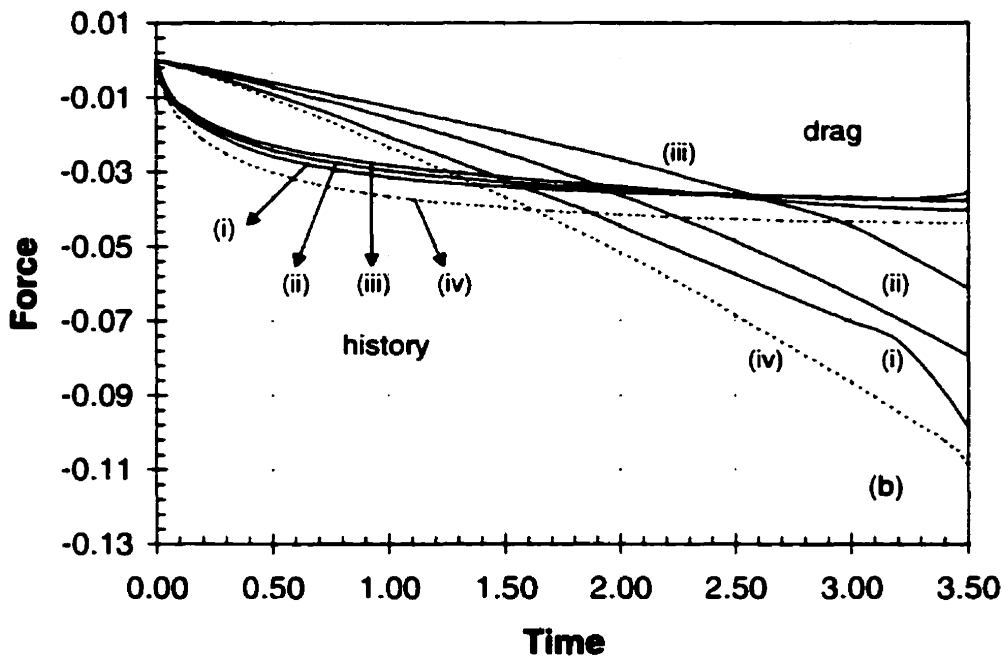

(b) Drag and history forces (i) oblate ($E = 0.5$), (ii) sphere ($E = 1.0$), (iii) prolate ($E = 2.0$) with its symmetric axis perpendicular to the axis of the ESZ, (iv) prolate ($E = 2.0$) with its symmetric axis parallel to the axis of the ESZ

Figure 3.4 — Force terms in the radial direction on spheroidal particles of different shape and orientation in a flow field of Re = 500 and $R_H = 0.8$ with a particle-fluid density ratio of $\gamma = 1.0$, particle volume is equivalent to that of a sphere of $k = 0.3$.

acquire a negative radial velocity and move a little towards the center before moving to the wall. This is related to the fluid acceleration terms which are stronger than the electromagnetic forces in the entrance region in radial direction. As R_H increases, the phenomenon becomes less obvious, and eventually the particles move directly towards the wall at a magnetic pressure number R_H of 0.8.

Although the effect of R_H on the particle trajectories and the force characteristics are similar for particles of different shapes and orientations, the absolute trajectory in each situation is different. This is clearly demonstrated in Figure 3.5, which shows the trajectories of particles of different aspect ratio E and orientation in a flow field of $\mathrm{Re} = 500$ and $R_H = 0.8$. When the particle traverses within the ESZ with its symmetric axis perpendicular to the axis of the ESZ, the lower E, the closer it travels

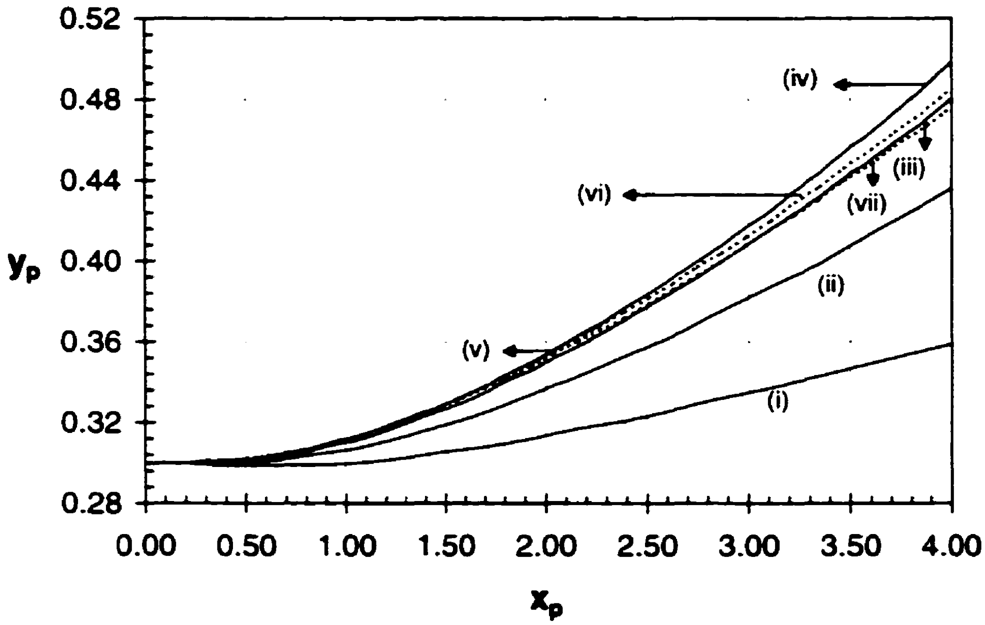

Figure 3.5 — Comparison of the trajectories of spheroidal particles of different shape and orientation in a flow field of $\mathrm{Re} = 500$ and $R_H = 0.8$ with a particle-fluid density ratio of $\gamma = 1.0$, particle volume is equivalent to that of a sphere of $k = 0.3$. (i) Oblate ($E = 0.2$), (ii) obalte ($E = 0.5$), (iii) sphere ($E = 1.0$), (iv) prolate ($E = 2.0$) with its symmetric axis perpendicular to the axis of the ESZ, (v) prolate ($E = 3.0$) with its symmetric axis perpendicular to the axis of the ESZ, (vi) prolate ($E = 2.0$) with its symmetric axis parallel to the axis of the ESZ, (vii) prolate ($E = 3.0$) with its symmetric axis parallel to the axis of the ESZ.

near the central axis of the ESZ. For example, an oblate of $E=0.5$ (Figure 3.5(ii)) moves more than twice the distance in the radial direction of that of an oblate of $E=0.2$ (Figure 3.5(i)) at $x_p=4.00$, while a sphere of $E=1.0$ (Figure 3.5(iii)) traverses about three times the distance of that of $E=0.2$ oblate at the same axial distance. As E increases to greater than 1, that is, the particles are prolate, the shape effect becomes less dramatic. For example, the prolate of $E=2.0$ moves only 10% more distance in the radial direction than that of a sphere at $x_p=4.00$. While for particles of $E=2.0$ and $E=3.0$, the trajectories overlap each other. Figure 3.5(iv) shows that particle orientation also has effects on particle trajectory, although not very strong. The prolate of $E=2.0$ travelling with its symmetric axis perpendicular to the axis of the ESZ moves 8% further to the wall at $x_p=4.00$ than those particles travelling with its axis of symmetry parallel to the ESZ axis.

The effects of shape and orientation on the particle trajectories result from the dependence of the correction factors E^M, M^A, R^D and B on the particle shape and orientation. This dependence is reflected in Figure 3.6 for particles with relative density of $\gamma=1.0$. When the spheroidal particle traverses with its symmetric axis perpendicular to the axis of ESZ, increasing E will decrease both $E_\perp^M$ and $M_{//}^A$ (Figure 3.6(a)), corresponding to the decreases in electromagnetic forces and fluid acceleration forces shown in Figure 3.4(a). However, the ratio $E_\perp^M/(M_{//}^A+1.0)$, where 1.0 denotes the case of particle relative density $\gamma=1.0$, increases with E. This increase is dramatic for oblate, and tends to be stabilized as E increases beyond 2.0. From Equation (3.15), it can be seen that increasing the ratio of $E_\perp^M/(M_{//}^A+1.0)$ will give higher acceleration to the spheroidal particle in the radial direction. The strong dependence of the ratio $E_\perp^M/(M_{//}^A+1.0)$ on

E for oblate particles contributes to the increased radial distance traveled by the oblate of 0.2, 0.5 and sphere, while the relatively stable value of the ratio on E for spherical and prolate particles results in the slight difference in the particle trajectories from $E=1.0$ to $E=3.0$. As to the orientation effect, the insert in Figure 3.6(a) shows that the ratios $E_{\perp}^{M}/(M_{//}^{A}+1.0)$ and $E_{//}^{M}/(M_{\perp}^{A}+1.0)$ are very close, resulting in nearly the same particle trajectories. The drag coefficients for a particle travelling with its axis parallel or perpendicular to the axis of the ESZ which are $\frac{1}{k}R_{\perp}^{D}C_{D}$ and $\frac{1}{kE}R_{//}^{D}C_{D}$, respectively, are shown in Figure 3.6(b), and the history force correction factors B are shown in Figure 3.6(c). These two figures show

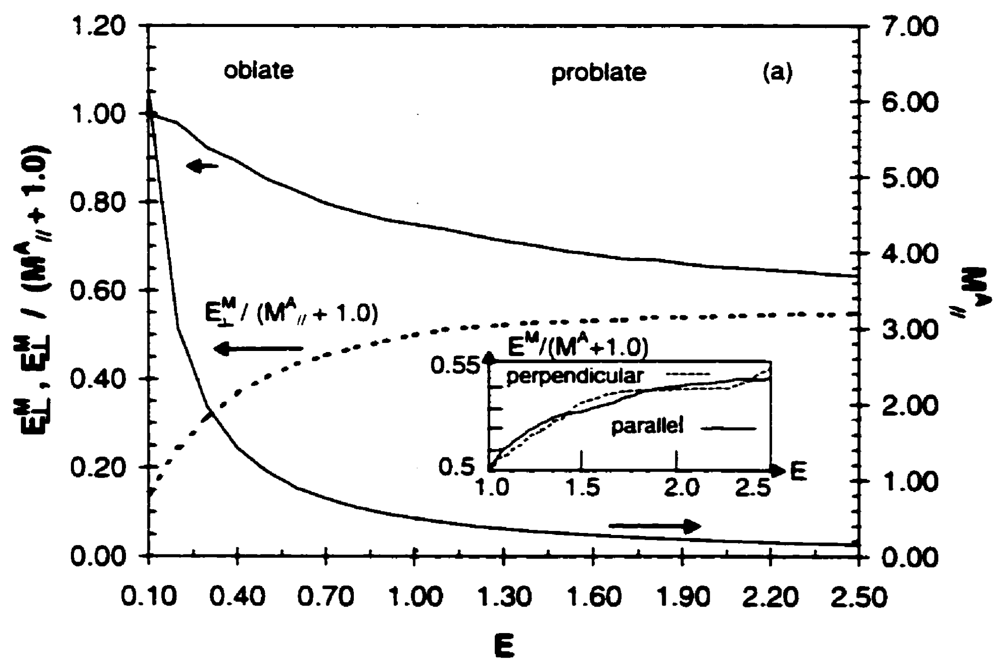

(a) Correction factors for electromagnetic ($E_{\perp}^{M}$), added mass forces ($M_{//}^{A}$) and the ratio $E_{\perp}^{M}/(M_{//}^{A}+1.0)$. The insert is a comparison of the ratio $E_{\perp}^{M}/(M_{//}^{A}+1.0)$ for a prolate with symmetric axis perpendicular or parallel to the axis of the ESZ

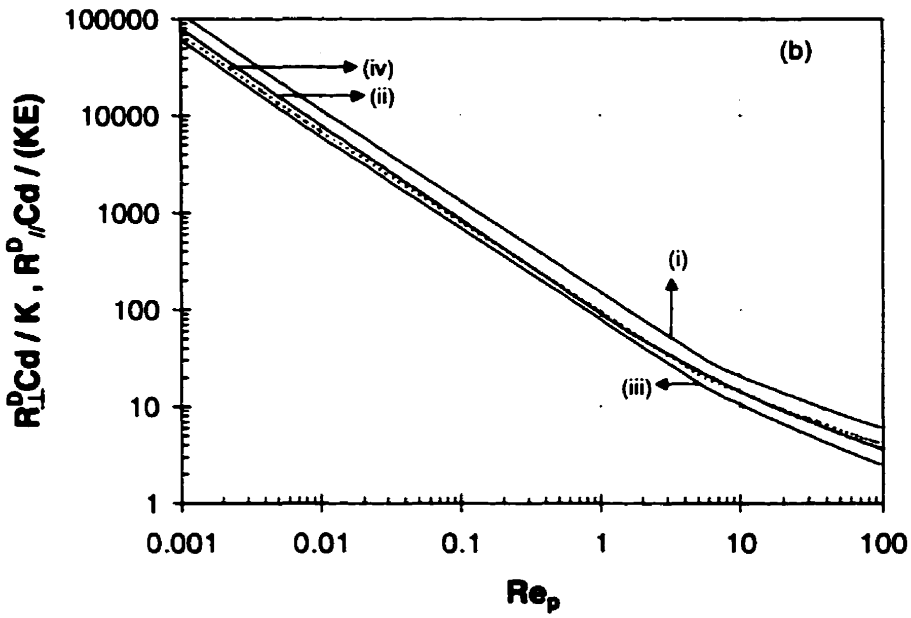

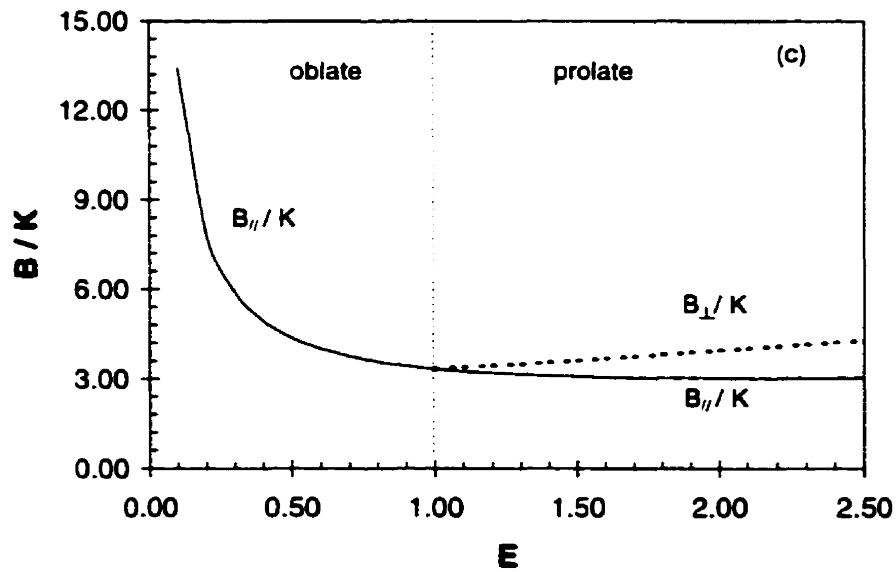

Figure 3.6 — Effect of particle shape and orientation on correction factors for added mass, electromagnetic, drag and history forces. (b) Correction factors of drag force (i) oblate ($E = 0.5$), (ii) sphere ($E = 1.0$), (iii) prolate ($E = 2.0$) with symmetric axis perpendicular to the axis of the ESZ, (iv) prolate ($E = 2.0$) with symmetric axis parallel to the axis of the ESZ; (c) Ratio of correction factor of history force to particle blockage ratio (B/k).

that both the drag coefficient and history correction factor for a prolate with its symmetric axis parallel to the axis of the ESZ (dashed lines) are higher than the corresponding values of a prolate particle with its symmetric axis perpendicular to the axis of the ESZ. It is these two factors that give more resistance to the movement towards the wall for particles with symmetric axes parallel to the axis of the ESZ, resulting in trajectories relatively close to the ESZ axis.

3.3.2 The Effect of Re

The effect of the fluid flow velocity is characterized by Re. The effect of Re on the trajectories of particles of different shape and orientation is shown in Figure 3.7. It can be seen that the axial distance traversed before a spheroidal particle touches the wall increases with increasing fluid Reynolds number Re, irrespective of its shape and orientation. For example, the axial distance traversed by an oblate of $E = 0.5$ for $\mathrm{Re} = 900$ is

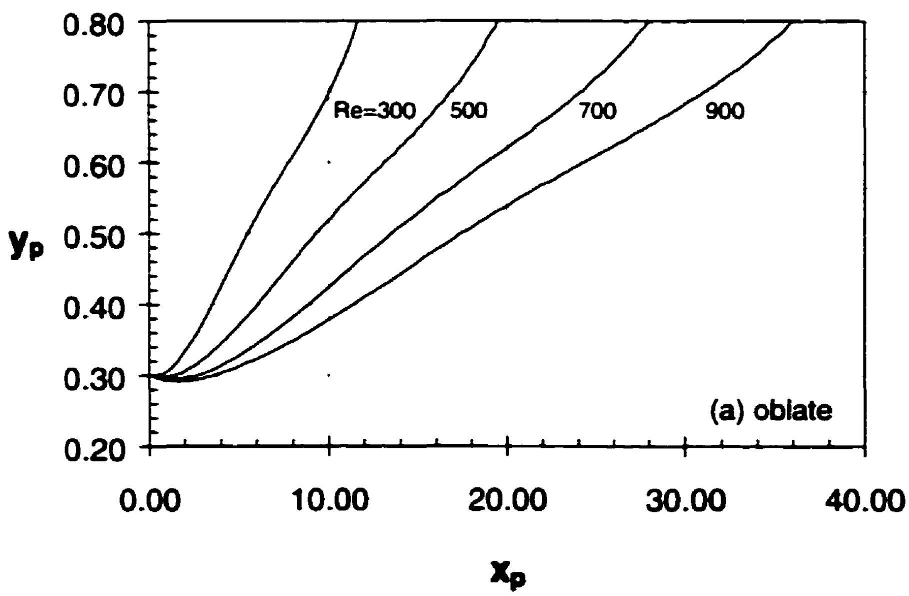

(a) Oblate ($E = 0.5$)

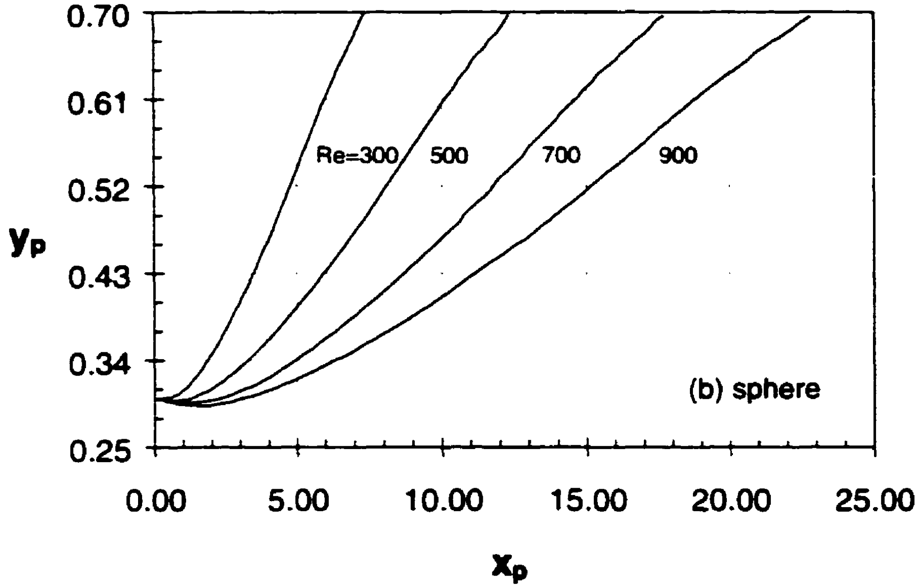

(b) Sphere (E = 1.0)

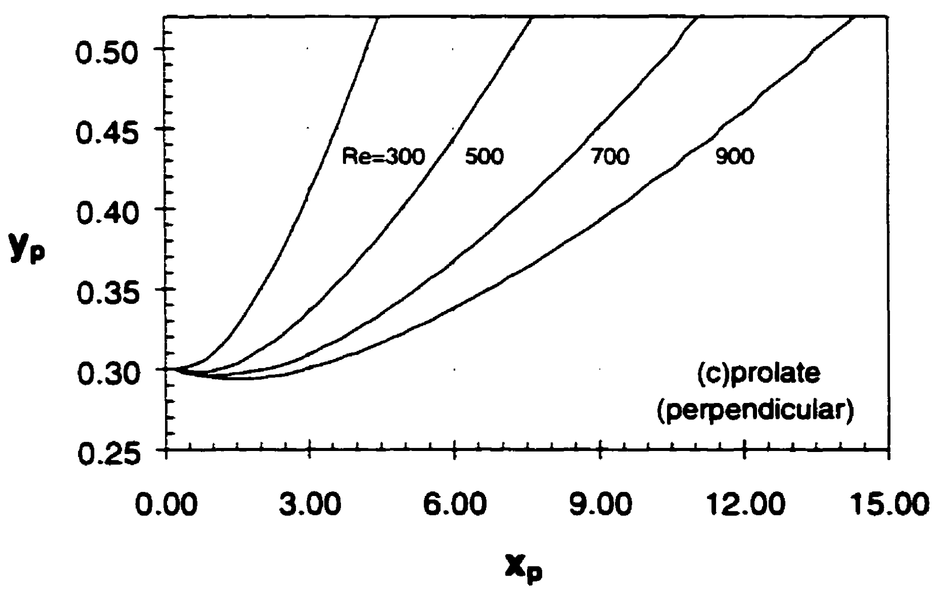

(c) Prolate (E = 2.0) with its symmetric axis perpendicular to the axis of the ESZ

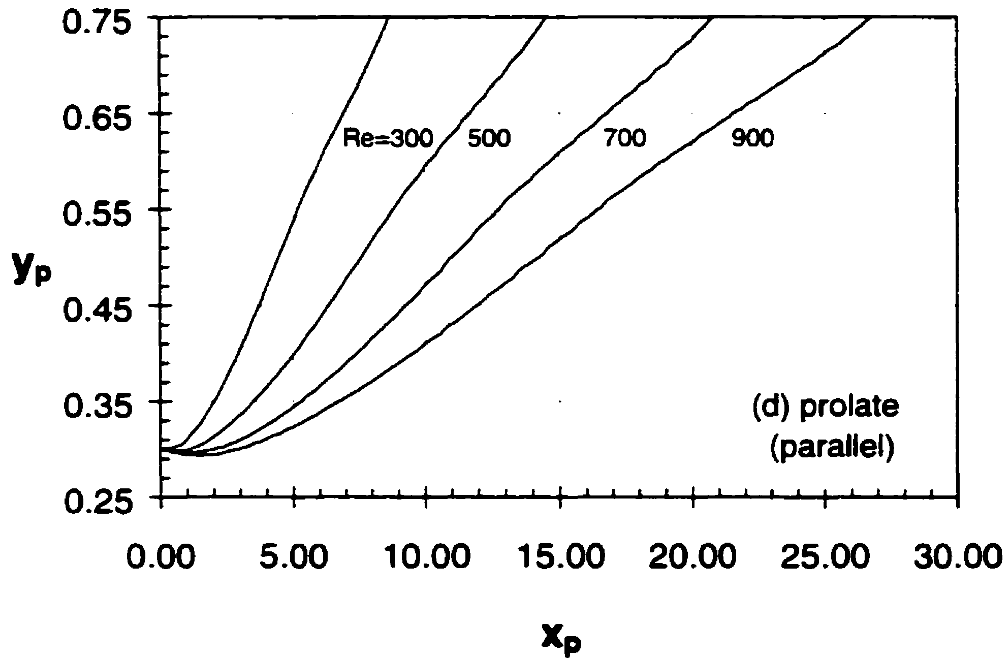

(d) Prolate ($E = 2.0$) with its symmetric axis parallel to the axis of the ESZ

Figure 3.7 — The effect of Re on the trajectories of spheroidal particles of different shape and orientation, $\gamma = 1.0$, particle volume is equivalent to that of a sphere of $k = 0.3$.

more than three times the distance of that for $Re = 300$. In the same way, the distance traveled by a sphere and a prolate with its symmetric axis perpendicular or parallel to the axis of the ESZ increases three times as Re increases from 300 to 900. This can be explained considering that the fluid velocity in the axial direction at any position inside the ESZ becomes higher as Re becomes larger, giving rise to a higher axial velocity of the particle. Since the particle follows the fluid flow velocity at any instant, this will result in a further distance in the axial direction. Moreover, increasing Re increases the fluid acceleration force in radial direction, which is responsible for the increase in the initial negative velocity, driving particles closer towards the central axis of the ESZ before moving to the wall. This also helps to increase the traversed axial distance.

Although the dependence of particle trajectories of different shape and orientation on the fluid Reynolds number Re is similar, an oblate moves longer distance in the axial direction than a sphere or a prolate at the same Re. Furthermore, a prolate traverses further in the axial direction with its symmetric axis parallel than perpendicular to the axis of the ESZ. The reason is that the ratio $E_{\perp}^{M}/(M_{//}^{A}+1.0)$ becomes larger when the shape of the particle changes from oblate through sphere to prolate, making the enhancements in electromagnetic effects larger than the increase in added mass effect, giving rise to a higher radial acceleration towards the wall. As to the effect of orientation of prolate particles, the bigger drag force on the prolate particle with its symmetric axis parallel to the axis of the ESZ gives stronger resistance to the particle moving to the wall, and thus a longer axial distance. The contribution of the electromagnetic effect and the added mass effect to the trajectories of prolate particles with its symmetric axis parallel or perpendicular to the axis of the ESZ is nearly equal, because the ratios $E_{//}^{M}/(M_{\perp}^{A}+1.0)$ and $E_{\perp}^{M}/(M_{//}^{A}+1.0)$ are comparable.

3.3.3 The Effect of γ

The inertia of the particle is reflected in its dimensionless density ratio γ. The effect of γ on the trajectories of spheroidal particles of different shape and orientation is illustrated in Figure 3.8. It can be seen that a higher density particle, for example, $\gamma = 2.0$, moves longer distance in axial direction before reaching the wall, irrespective of the particle shape and orientation. On the other hand, it can also be seen from Fig. 3.8 that the increase in the traversed axial distance with the particle relative density γ becomes stronger as the aspect ratio of the particle E increases when the particle travels with its symmetric axis perpendicular to the axis of ESZ. For instance, when γ increases from 0 to 2.0, the axial distance traversed by the oblate of $E = 0.5$ increases 15%, by sphere nearly 40%, while by prolate of $E = 2.0$ more than 80%. Compared to the prolate travelling with its symmetric axis perpendicular to the axis of the ESZ, the increase in the axial distance with γ is less pronounced when the prolate orientation changes into being parallel with the axis of the ESZ. An increase in axial distance of a bit more than 20% with γ increasing from 0 to 2.0 is observed in Figure 3.8(d). The above phenomenon is related to the added mass effect M^A. Both the particle density γ and the added mass M^A increase the inertia of the particle and the sum of these two constitutes the denominator of the equations of motion (3.15) and (3.16). $M_{//}^A$ decreases with E (Figure 3.6(a)), leaving the effect of γ stronger. For prolate, $M_{\perp}^A$ is

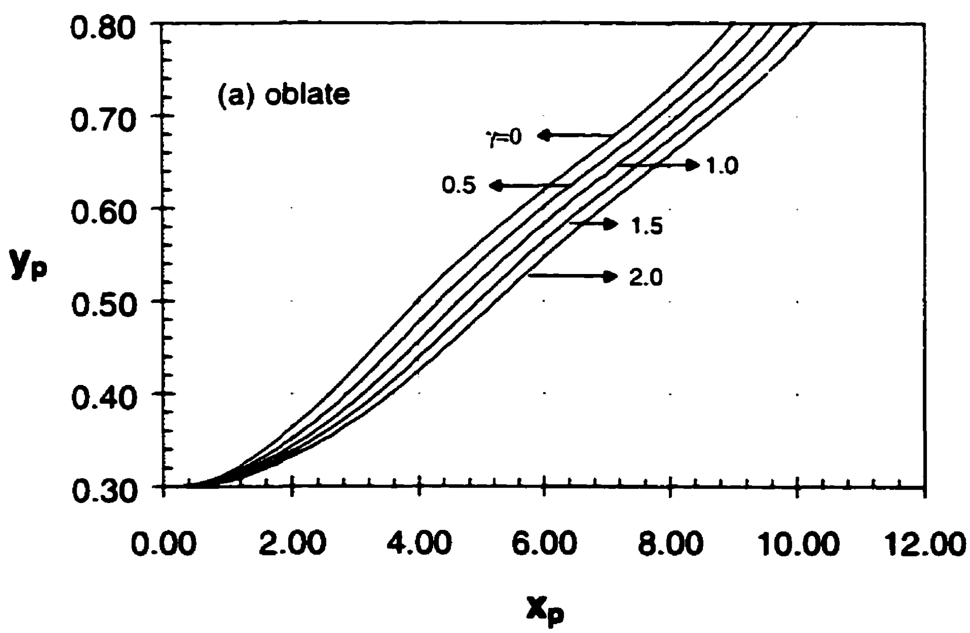

(a) Oblate ($E = 0.5$)

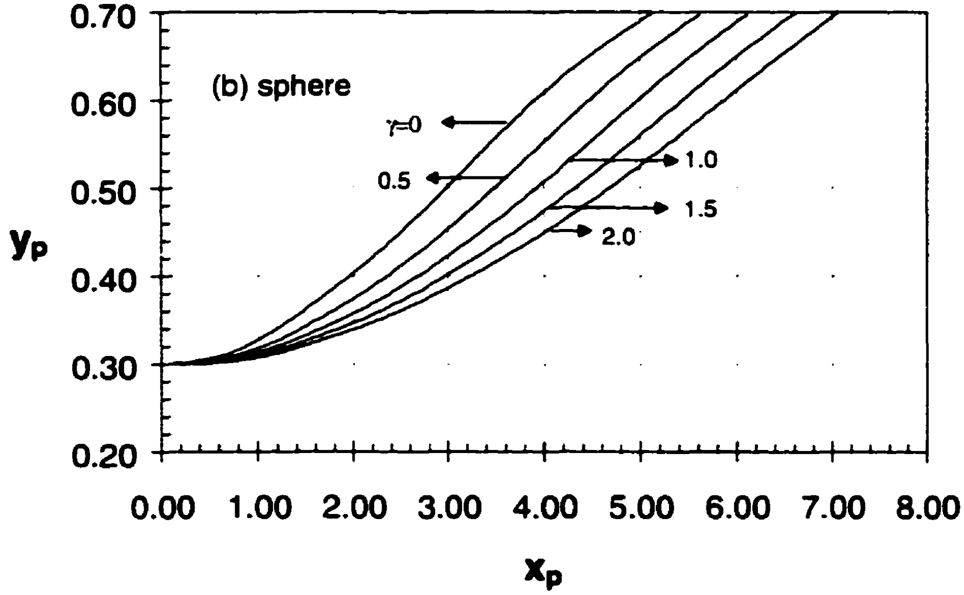

(b) Sphere ($E = 1.0$)

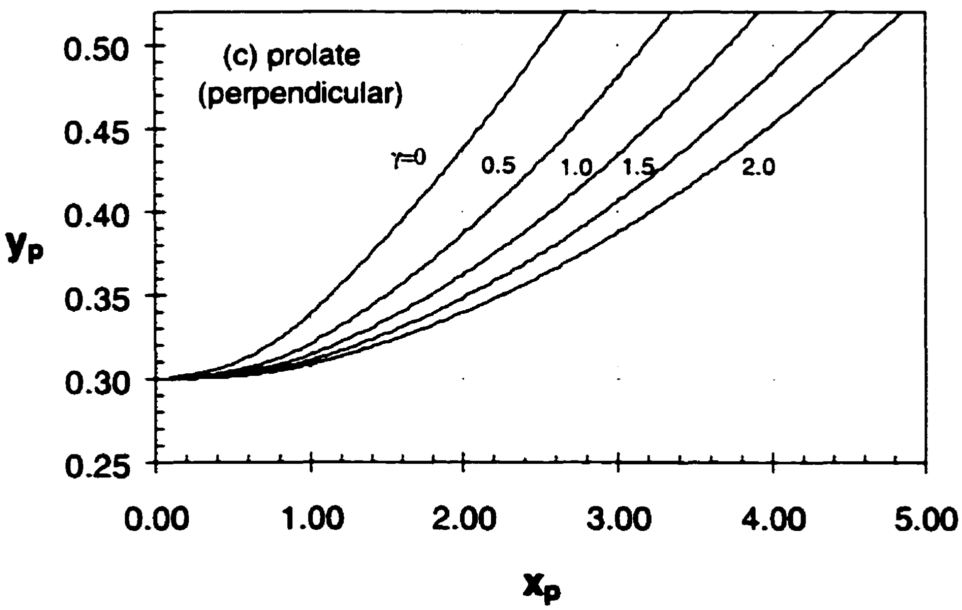

(c) Prolate ($E = 2.0$) with its symmetric axis perpendicular to the axis of the ESZ

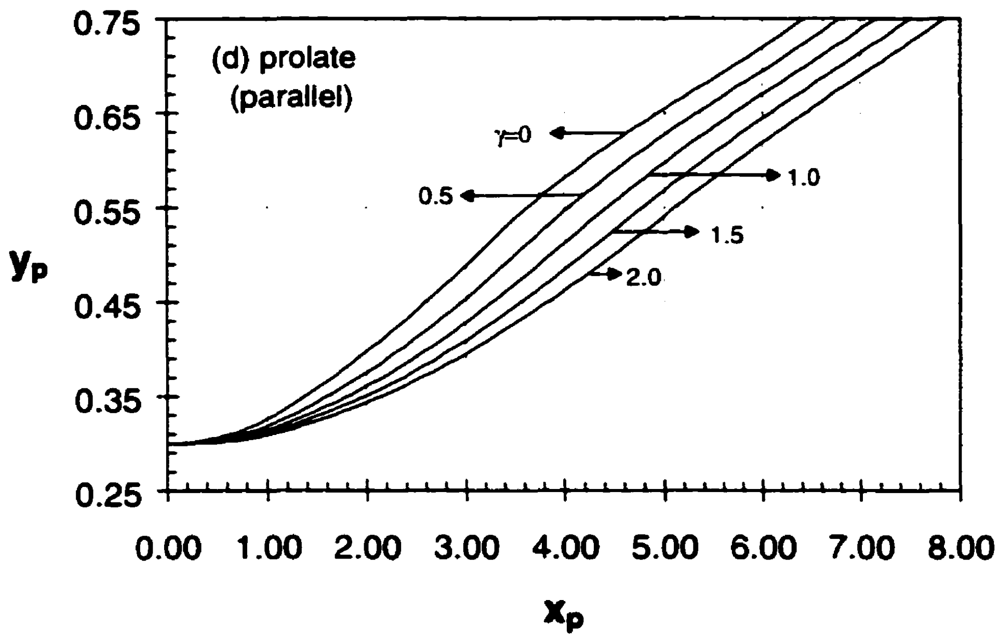

(d) Prolate ($E = 2.0$) with its symmetric axis parallel to the axis of the ESZ

Figure 3.8 — The effect of γ on the trajectories of spheroidal particles of different shape and orientation in a flow field of Re = 500 and $R_H = 0.8$, particle volume is equivalent to that of a sphere of $k = 0.3$.

larger than $M_{//}^{A}$, which explains the stronger effect of γ for prolate particles traversing with their symmetric axes perpendicular rather than parallel to the axis of the ESZ.

3.3.4 The Effect of Blockage Ratio k

In this study, the consideration of the trajectories of spheroidal particles of different shape and orientation was based on particles with the same volume as a sphere of blockage ratio k. The effect of k on the axial distance traversed by particle before reaching the wall is shown in Figure

3.9 in a flow field of Re = 700 and R_H = 0.8. It can be seen from Figure 3.9 that the larger k, the shorter the axial distance traveled by the particle before reaching the wall, and this holds true for oblates, spheres and prolates of different orientations. This can be explained by the fact that the electromagnetic force in the radial direction, which is proportional to the third order of k, increases the acceleration of the particle with increase in k. It is also noted from Figure 3.9 that for particles of the same volume, an oblate traverses further in the axial direction before reaching the wall than a sphere or a prolate, and this difference increases with particle size k. On the other hand, a prolate traverses longer distance in the axial direction with its symmetric axis parallel than perpendicular to the axis of the ESZ.

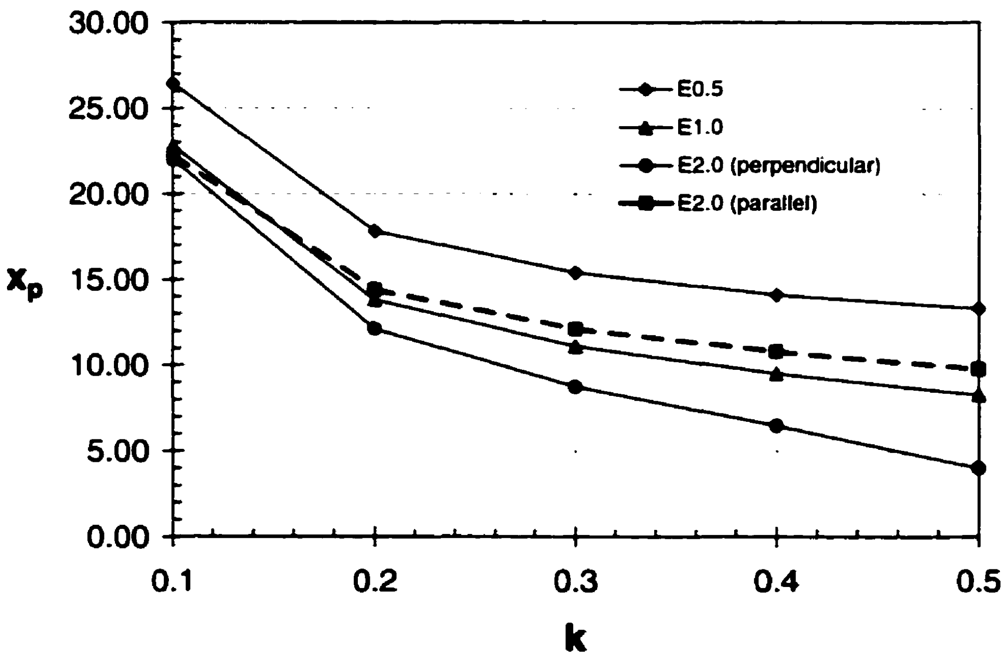

Figure 3.9 — The effect of k on the axial distance traversed by spheroidal particles of different shape and orientation upon reaching the wall in a flow field of Re = 500 and R_H = 0.8 with a particle-fluid density ratio of $\gamma = 1.0$.

This is due to the fact that the decrease in the added mass effect surpasses the decrease of the electromagnetic effect as E increases from 0 to more than 1, resulting in a higher radial acceleration towards the wall as the particle shape changes from oblate through sphere to prolate. On the other hand, the bigger drag force on the prolate particle with its symmetric axis parallel to the axis of the ESZ gives stronger resistance to the particle moving to the wall, giving rise to a longer axial distance.

3.3.5 The Effect of the Entry Point to the ESZ

The trajectories of the particles of different shape and orientation flowing into the ESZ from different radial coordinate positions in a fluid field of $\mathrm{Re}=700$ and $R_H=0.8$ are shown in Figure 3.10. An important common feature in the immediate vicinity of the entrance region, where

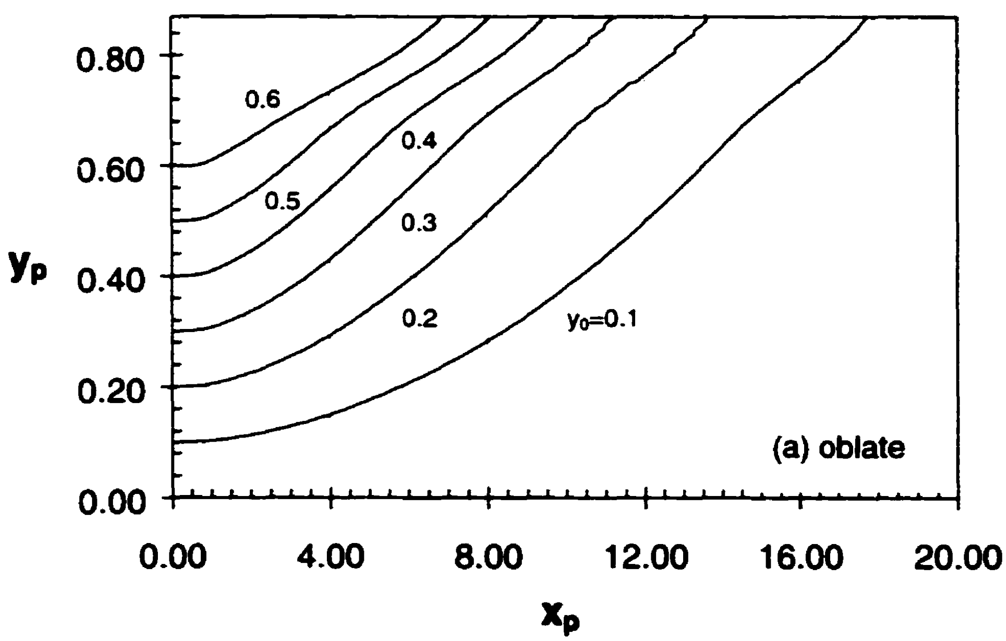

(a) Oblate ($E=0.5$)

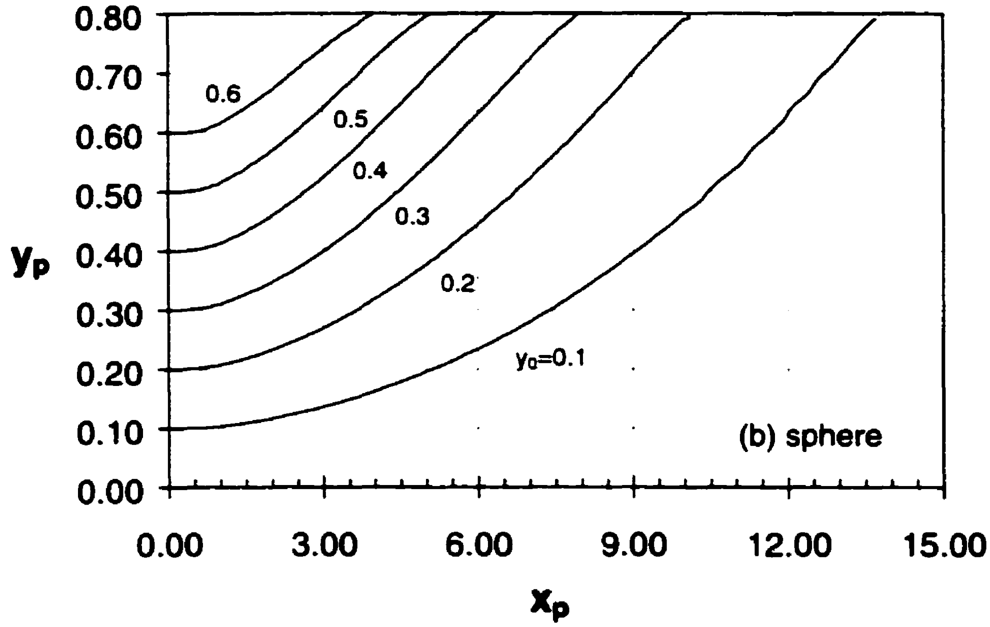

(b) Sphere ($E = 1.0$)

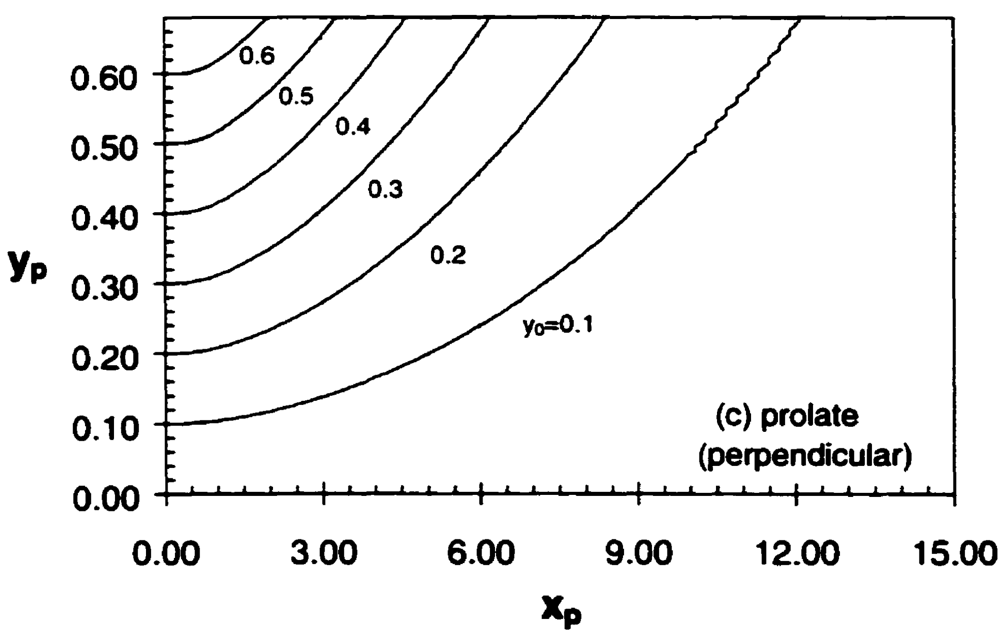

(c) Prolate ($E = 2.0$) with its symmetric axis perpendicular to the axis of ESZ

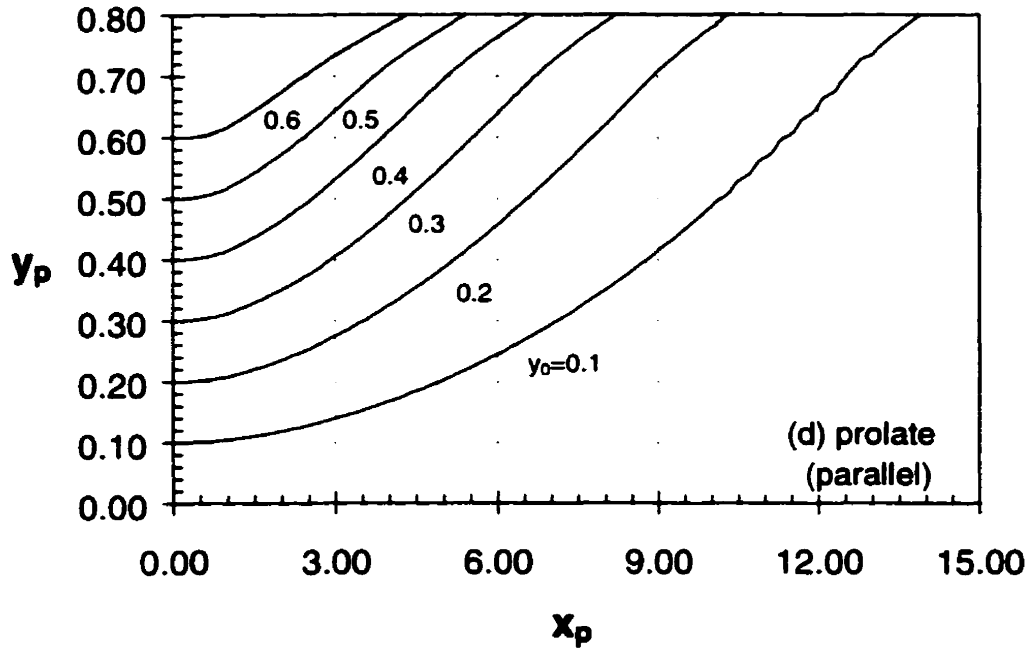

(d) Prolate ($E = 2.0$) with its symmetric axis parallel to the axis of the ESZ

Figure 3.10 — The effect of entry point y_0 on the trajectories of spheroidal particles of different shape and orientation in flow field of Re = 500 and $R_H = 0.8$ with a particle-fluid density ratio of $\gamma = 1.0$, particle volume is equivalent to that of a sphere of $k = 0.2$.

the axial velocity is uniform, is that the radial velocity increases with increasing radial distance with respect to the ESZ axis. This is due to the electromagnetic force, which increases linearly with the radial coordinate. However, near the wall, the radial velocities become lower, which results from a dominating increase of the fluid acceleration force over the electromagnetic force. From Figure 3.10 it is also noted that when flowing into the ESZ from the same initial position, an oblate moves a longer distance in the axial direction than does a sphere, which also moves further than a prolate. A prolate traverses further in the axial direction when its symmetric axis is parallel rather than perpendicular to the axis of the ESZ. As discussed before, this can be attributed to the dominating increase in the added mass effect over the electromagnetic effect as E decreases. Consequently, the inertia of the particle increases, and thus lowers the radial acceleration. As to the prolate of different orientation, the relatively higher drag force in the radial direction for the prolate traversing with its symmetric axis parallel than perpendicular to the axis of the ESZ is the main reason to keep it going further in the axial direction. Figure 3.10(a) to Figure 3.10(c) also show that the radial velocity decreases as the particle moves closer to the wall, and that this decrease becomes less noticeable when E increases from 0.5 to 2.0. This decrease in radial velocity is due to an increase in drag force resulted from the wall effect, which becomes weaker when the equatorial radius k of the particle of the same volume decreases with E. For prolate with its symmetric axis parallel to the axis of the ESZ (Figure 3.10(d)), wall effects are stronger than that for a particle with its symmetric axis perpendicular to the axis of the ESZ. This can be attributed to the fact that the projected area in the radial direction is bigger for a prolate traversing with its symmetric axis parallel than perpendicular to the axis of the ESZ.

3.3.6 The Application of the Model to LiMCA System in Aluminum Industries

A basic requirement of the LiMCA system to measure the melt cleanliness accurately is that all inclusions flowing into the ESZ should pass through it, rather than depositing on the sidewalls. The practical operating condition of the LiMCA system operating in the aluminum industry employs electric currents of 60 amperes passing through a 300 μm diameter orifice. The average fluid velocity is 4 m/s, and the effective ESZ length is 0.3 mm.[25] If we take the distribution of particles at the inlet to be uniform, the simulation can be carried out for $\gamma = 1.6$ representing solid inclusions of Al_2O_3 within the aluminum melt ($\rho_f = 2.368\times10^3$ kg/m^3, $\mu_f = 1.63\times10^{-3}$ Pa s). The predicted pass-through fraction for spheroidal particles of different shape and orientation with volume equivalent to that of a sphere of sizes ranging from 20 to 240 μm is shown in Figure 3.11. It can be seen that the percentage of particles passing through the orifice decreases with increasing particle sizes. This tendency is dramatic especially for prolate spheroids. An oblate has a lower pass-through percentage than does a sphere when the particle size is smaller than 150 μm, but a higher pass-through percentage when the particle size is

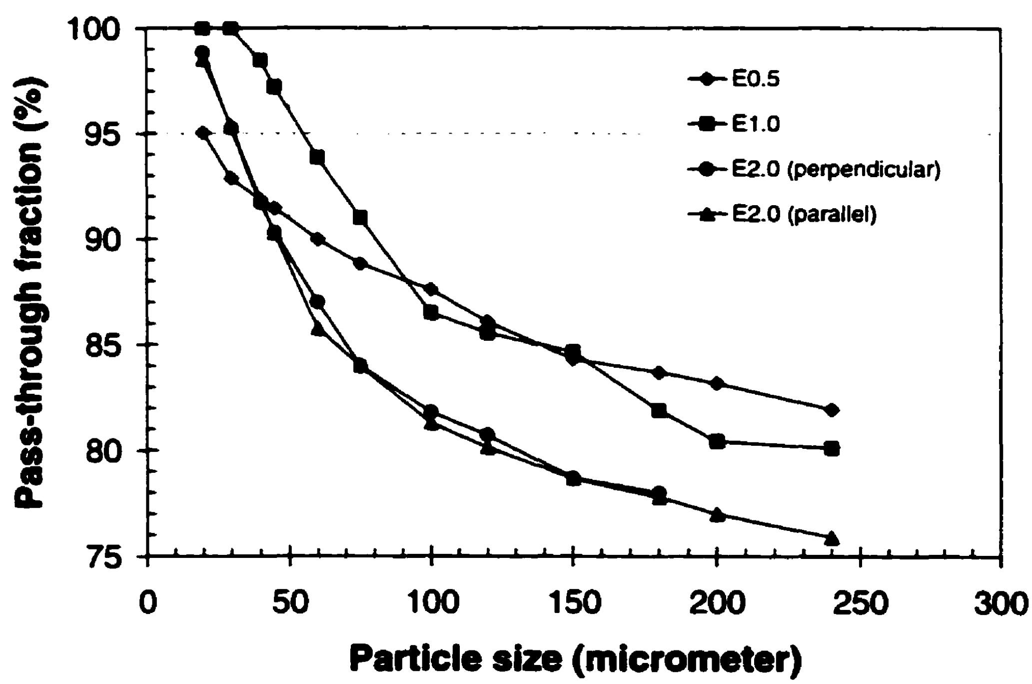

Figure 3.11 — The predicted pass-through fraction for spheroidal particles of different shape and orientation with a volume equivalent to that of a sphere of size marked on the abscissa.

beyond 150 μm. The pass-through percentage for spheres is higher than that of a volume-equivalent prolate over the whole particle size range studied. For prolate particles with sizes ranging from 20 μm to 180 μm, the pass-through fraction is very close when its symmetric axis is perpendicular or parallel to the axis of the ESZ. Beyond 180 μm, it is physically impossible for a prolate to move with its symmetric axis perpendicular to the axis of the ESZ.

From the study on the trajectories of spheroidal particles of different shape and orientation, it is known that a prolate with its symmetric axis perpendicular to the axis of the ESZ moves faster towards the wall than a sphere, and much faster than an oblate. Correspondingly, it seems that oblate particles should have higher pass-through percentage than those of spheres and much higher than those of prolates. In fact, in the LiMCA system, an oblate does not have a higher predicted pass-through percentage than that of a sphere. This is because the half symmetric axis of an oblate is smaller than the radius of a sphere with equivalent volume, allowing a number of oblates to flow into the ESZ with an entry position very close to the wall, increasing the percentage of oblates being collected by the wall. On the other hand, from our previous studies, it is known that under the same condition, a prolate reaches the wall faster with its symmetric axis perpendicular than parallel to the axis of the ESZ. However, this does not result in large difference in the pass-through percentage of prolate particles with both orientations. The reason is that a prolate with its symmetric axis parallel to the axis of the ESZ has the opportunity of flowing into the ESZ from entry points that are so close to the wall. Those particles are easy to be collected on the inner wall, resulting in nearly the same pass-through percentage for both orientations.

Figure 3.11 shows that more than 80 percent of spheroidal particles with sizes up to 100 μm and around 75 percent even with sizes up to 240 μm can successfully pass through the ESZ without grazing the sidewalls.

These fundamental analyses confirm that LiMCA type systems can be used to detect inclusions in liquid aluminum, despite contradictory conclusions of previous analyses.[26]

3.4 Conclusions

A mathematical model has been developed to describe the motion of spheroidal particles of different shapes and orientations flowing with liquid metals through an ESZ. The fluid velocity field was obtained by solving the Navier-Stokes equations, and the trajectories of particles were calculated using equations of motion for particles. These incorporate the drag, added mass, history, electromagnetic and fluid acceleration forces. The effects of particle shape and orientation were taken into account by including the correction factors for drag R^D, added mass M^A, history B, and electromagnetic force E^M. The results based on the motion of volume-equivalent spheroidal inclusions of different shapes and orientations show that the trajectories are affected by the magnetic pressure number R_H, the Reynolds number Re, the blockage ratio k, the particle-fluid density ratio γ. In the axial direction, the spheroidal particles follow the fluid velocity, and move further axially before reaching the wall as the fluid velocity (Re) increases. In the radial direction, the outwardly directed electromagnetic force on the non-conducting spheoridal inclusions increases with radial distance from the axis, with increasing electric current (R_H), and with increasing size (k) of particle. The competition between the electromagnetic force and the radial fluid acceleration force in the entrance region results in particle movement towards the central axis before moving towards the wall for small electric current (low R_H), but directly towards the wall for large current (high R_H). Spheroidal particles with symmetric axes perpendicular to the transverse axis of the ESZ travel faster towards the sidewall as the particle aspect ratio (E) increases. The dominating increase in the added mass (M^A) force over the increase in the electromagnetic force (E^M) with decreasing E makes this effect much stronger for oblate ($E<1$) than for prolate ($E>1$) spheroids. The stronger drag force (R^D) on a prolate inclusion with its symmetric axis parallel to the axis of the ESZ makes it move slower towards the wall than for a prolate spheroidal inclusion with its axis of symmetry perpendicular to the axis of the ESZ. Low inertia (low γ) spheroidal particles move faster towards a sidewall than do heavier particles. This effect becomes much stronger for a prolate traversing with its axis perpendicular rather than parallel to the axis of the ESZ, owing to its smaller added mass (M^A), while the effect of γ is stronger for a prolate than an oblate spheroid traversing with its symmetric axis perpendicular to the axis of the ESZ, owing to the decrease in the added mass effect (M^A) as E increases. The radial velocity of the particle movement as it approaches the wall is predicted to decrease due to the wall effects. Finally, the model was applied to the LiMCA system under the operational conditions in aluminum industries, and the results show that more than 80% of spheroidal inclusions of size 100 μm and about 75% of the spheroidal inclusions of size 240 μm go through a 300 μm diameter ESZ. These results confirm from a theoretical standpoint that the LiMCA system can be used in aluminum industries.

References

[1] W.H. Coulter: US Patent 112819, 1953.

[2] R.W. Deblois and C.P. Bean: Rev. Sci. Instr., 1970, vol. 41, pp. 909-915.

[3] R.W. Deblois, C.P. Bean, and R.K.A. Wesley: J. Colloid and Interface Sci., 1977, vol. 61, pp. 323-335.

[4] W.R. Smythe: Physics of Fluids, 1961, vol. 4, pp. 756-759.

[5] W.R. Smythe: Physics of Fluids, 1964, vol. 7, pp. 633-638.

[6] D.C. Golibersuch: Biophysical Journal, 1973, vol. 13, pp. 265-280.

[7] D.C. Golibersuch: J. Appl. Phys., 1973, vol. 44, pp. 2580-2584.

[8] W.R. Smythe: Rev. Sci. Instr., 1972, vol. 43, pp. 817-818.

[9] L. Spielman and S.L. Goren: J. Colloid and Interface Sci., 1968, vol. 26, pp. 175-182.

[10] L.I. Berge, T. Jφssang, and J. Feder: Meas. Sci. Technol., 1990, vol. 1, pp. 471-474.

[11] N.B. Grover, J. Naaman, S. Ben-Sasson, and F. Doljanski: Biophysical Journal, 1969, vol. 9, pp. 1398-1414.

[12] N.B. Grover, J. Naaman, S. Ben-Sasson, F. Doljanski, and E. Nadav: Biophysical Journal, 1969, vol. 9, pp. 1415-1425.

[13] R. Karuhn, R. Davies, B.H. Kaye, and M.J. Clinch: Powder Technology, 1975, vol. 11, pp. 157-171.

[14] R. Davis, R. Karuhn, and J. Graf: Powder Technology, 1975, vol. 12, pp. 157-166.

[15] D. Doutre and R.I.L. Guthrie: US Patent 4555662, 1985.

[16] R.I.L. Guthrie and D. Doutre: Proc. Intl. Seminar on Refining and Alloying of Liquid Aluminum and Ferro-Alloys, Trondheim, Norway, 1986, pp. 146-163.

[17] A. Berlemont, P. Desjonqueres, and G. Gouesbet: Intl. J. Multiphase Flow, 1990, vol. 16, pp. 19-34.

[18] M. Loewenberg: Phys. Fluids, 1993, vol. A5, pp. 765-767.

[19] C.J. Lawrence and S. Weinbaum: J. Fluid Mech., 1988, vol. 189, pp. 463-489.

[20] R. Clift, J.R. Grace, and M.E. Weber: Bubbles, Drops, and Particles, Academic Press, Inc., New York, NY, 1978, pp. 112 and 225.

[21] J. H. Masliyah and N. Epstein: J. Fluid Mech., 1970, vol. 44, pp. 493-512.

[22] H. A. Dwyer and D. S. Dandy: Phys. Fluids, 1990, vol. A2, pp. 2110-2118.

[23] V.M. Korovin: Magnetohydrodynamics, 1987, vol. 23, pp. 160-165.

[24] J. Happel and H. Brenner: Low Reynolds Number Hydrodynamics, Printice-Hall, Inc., Englewood Cliffts, NJ, 1965, pp. 331.

[25] F. Dallaire: Electric Sensing Zone Behavior in Liquid Aluminum, Master Thesis, McGill University, 1990, pp. 11.

[26] S.T. Johansen: International Symposium on Electromagnetic Processing of Materials, ISIJ, Nagoya, Japan, 1994, pp. 104-109.

CHAPTER 4

Particle Discrimination in Water Based LiMCA System

The LiMCA system using a parabolic shaped ESZ probe has been successfully used in aluminum industries for on-line inclusion monitoring. However, microbubbles and salt droplets generated in degassing procedures give rise to signals, which need to be distinguished from solid, potentially harmful inclusions. A water based LiMCA system (APS II) was used to physically model and study the possibility of particle (inclusion) discrimination. Experiments[1] showed that particles of different physical properties induced different shaped signals. These observations warrant theoretical analysis. In this chapter, the model developed in Chapter 2 is modified to describe the motion of particles of different physical properties flowing within a parabolic shaped ESZ in the APS II system. The mathematical model's predictions are compared with experimental results.

4.1 Introduction

The presence of non-metallic inclusions in metals often leads to impaired mechanical properties such as a reduction in fatigue strength, and processing problems such as tear-offs in deep drawing and increased breakage rates in wire drawing operations. Similarly, inclusions cause a variety of surface defects in rolled or extruded products.

Prior to the development of the LiMCA system[2] at McGill University in the early 1980's, it was not possible to measure inclusions, *in situ*, in liquid metals. Compared with other techniques, such as sedimentation, filtration and metallography, which require considerable amounts of labor and time, LiMCA has the advantage of providing not only the information of volume concentration but also of size distribution of inclusions rapidly and accurately.

LiMCA is based on the Electric Sensing Zone (ESZ) principle,[3] in which a constant current is maintained across two electrodes that are separated by an insulating sampling tube. A small orifice built in the tube wall allows liquid to flow into, and out of the sampling tube. When a non-conducting particle passes through the sensing zone orifice, the resistance is changed, giving rise to a voltage pulse signal. The principle is shown schematically in Figure 4.1 for a spherical particle passing through a parabolic shaped ESZ along the central axis of the orifice.

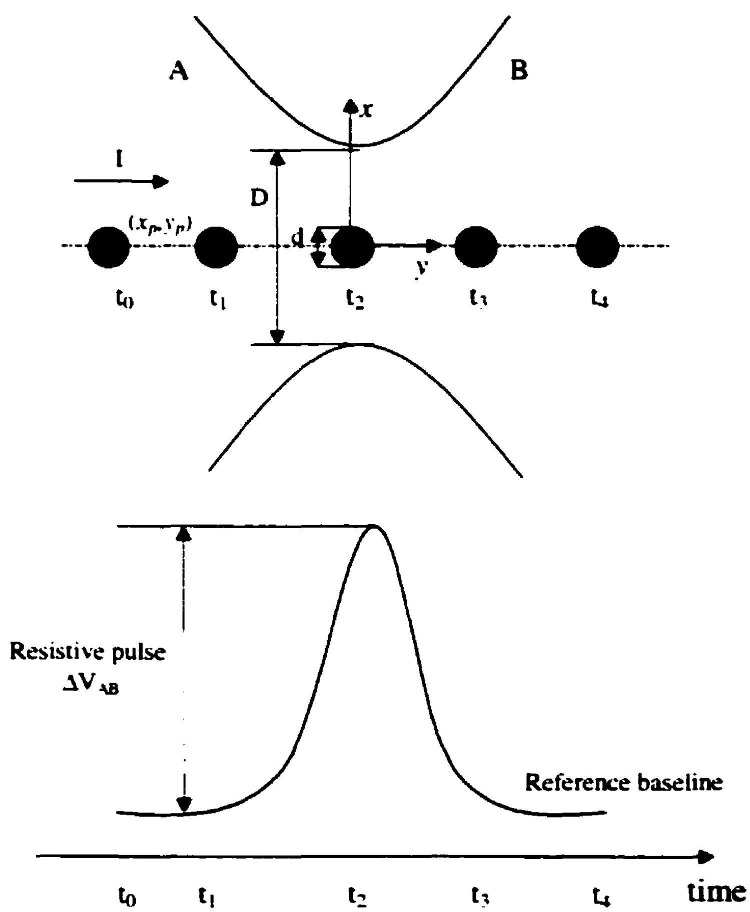

Figure 4.1 — Schematic representation of ESZ principle for particle size measurement.

As described in Chapter 3, the transient change in resistance, ΔR_{AB}, caused by the introduction of a small non-conducting particle into an orifice is given by:[4]

$$\Delta R_{AB} = \frac{4\rho_e d^3}{\pi D^4} \qquad (4.1)$$

where ρ_e is the electrical resistivity of the liquid, d and D are the respective diameter of the particle and the orifice. By applying an electric current I, the transient pulse voltage can be expressed as:

$$\Delta V_{AB} = \frac{4\rho_e I d^3}{\pi D^4} \qquad (4.2)$$

If d is not small compared to D, ΔR_{AB} is increased through distortion of the electric field flowing around the spherical inclusion and needs to be modified by a factor $f(d/D)$ in equation (4.1),[5] resulting in a ΔV_{AB}:

$$\Delta V_{AB} = \frac{4\rho_e d^3 I}{\pi D^4} f(d/D) \qquad (4.3)$$

$f(d/D)$ was obtained according to the numerical results of Smythe[6] in analyzing an ideal fluid flow around a sphere in a circular tube.

According to Equation (4.3), every particle registers a pulse when passing through ESZ orifice, and particles of the same size but of different type give rise to voltage pulses of the same height, disallowing the LiMCA technology from discriminating between hard deleterious solid particles, liquid droplets and harmless microbubbles. However, in the metallurgical industry, it would be very useful for the LiMCA system to be able to discriminate between hard solid particles, liquid droplets and gaseous bubbles given the opaque nature of the system, the difficulty of analyzing inclusion types in real time and the different roles played by these different kinds of inclusions in affecting final materials properties. For example, microbubbles and microdroplets of salt generated in proprietary degassing units in molten aluminum (e.g. SNIF, ALPUR) are often counted by the LiMCA system as inclusions, leading to an over-estimate in the number of harmful inclusions within a melt. In order to achieve particle discrimination, in McGill the LiMCA system was upgraded with Digital Signal Processing (DSP) technology[7] so as to extract more information from the particle signals measured besides pulse height. With DSP, each pulse is characterized not only by peak height, but six other parameters (start slope, end slope, time to reach the maximum voltage, total signal duration, start time and end time of each pulse).

In this chapter, the feasibility of particle discrimination was studied in water based LiMCA system. The mathematical model developed in Chapter 2 was modified to study the dynamic processes that would be experienced by different kinds of particles passing through the ESZ. The dynamic trajectories of particles, together with an Ohmic model of the ESZ,[8] which correlates ESZ resistance change with particle position inside the ESZ, were used to predict the transit times and signal shapes for different kinds of particles (i.e. dense inclusions vs gas bubbles) through the ESZ. Experimental data obtained in water based LiMCA system[1] with DSP technology were used to test against the numerical predictions.

4.2 Theory

The present study considered the dynamic motions of particles entrained within water flowing through the ESZ, and corresponding change in resistance of the ESZ, during their transient. A two dimensional simulation using a cylindrical coordinate system was employed, as shown in Figure 4.1. There, the position of the inclusion (spherical particle) is designated as (x_p, y_p), where x and y are the respective axial and radial coordinates.

4.2.1 Flow Field in the ESZ

The liquid was assumed incompressible, to have constant properties, and the entry flow into the ESZ to be laminar and steady. This is in keeping with practical operating conditions for the APS II system, for which the Reynolds number based on the diameter of the orifice is below 1800. Under these assumptions, the problem may be stated by writing the continuity and Navier-Stokes equations as follows:

$$\bar{\nabla} \bullet \vec{u} = 0 \qquad (4.4)$$

$$\vec{u} \bullet \bar{\nabla}\vec{u} = -\frac{\bar{\nabla}p}{\rho_f} + \nu_f \nabla^2 \vec{u} \qquad (4.5)$$

where $\vec{u}(u,v)$ is the fluid velocity vector, p is pressure, ρ_f and ν_f are density and kinematic viscosity of the fluid, respectively. Unlike liquid metal system, the Lorentz force, $\bar{F}_e$, is much smaller than the pressure force, due to the high electrical resistivity of water, and can be neglected. The properties of water used in this study are listed in Table 4.1.

The computational domain for the flow field is shown in Figure 4.2. The inlet boundary was taken to be a spherical cap centered at point C, point of the cross intersection between the central axis and the conical tangent to the ESZ wall at the edge E. The outlet boundary was taken to be the minimum cross section (throat) of the orifice. The boundary condition applied was zero-slip along the insulating ESZ wall. At the inflow boundary, the fluid velocity was assumed to be normal to the entry boundary and uniform. At the outflow boundary, the exit fluid velocity

Table 4.1 Physical properties of water and particles used in the particle discrimination study

Water properties:			
Temperature (^{0} C)		15	
Density (kg/m^3)		1000	
Electrical resistivity (Ωm)		30	
Viscosity (kg/ms)		1.14×10^{-3}	
Particle properties:			
	Microbubble of Ar	Latex	Silica
Density (kg/m^3)	0	1050	2650
Physical description	Argon gas (T=298k, P=1.013×10^5Pa)	Solid	Solid

gradient was taken to be zero. Corrections were made in the numerical calculations to match the mass inflow and outflow rates, so as to respect continuity. Beyond the throat of the ESZ, jet flow was assumed. That is, the fluid flow ignores the walls and simply passes on through the exit side

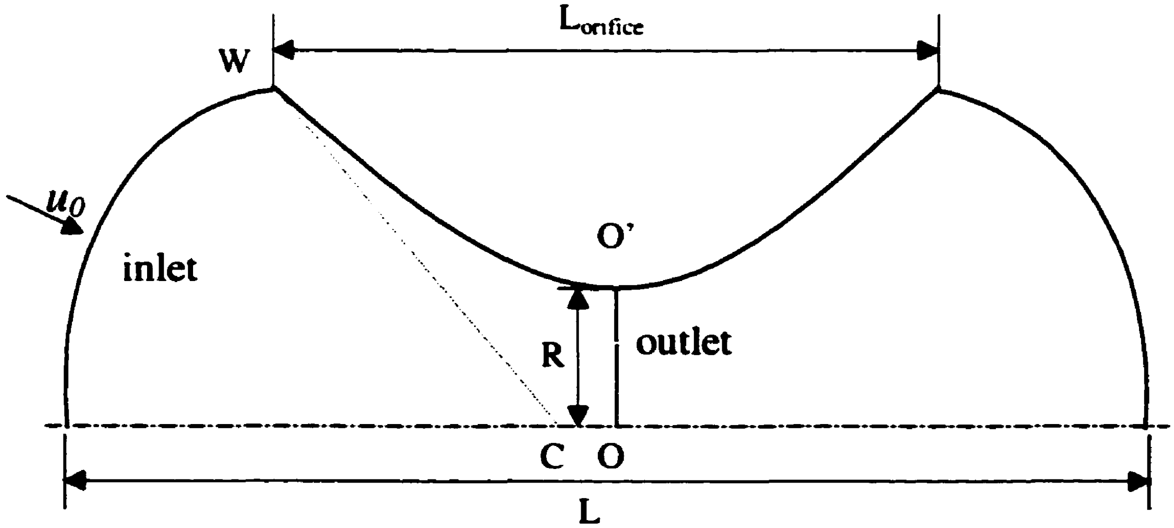

Figure 4.2 — The computational domain used in this study.

of the ESZ as an axial jet, at an axial velocity profile equal to that at the throat.

4.2.2 The Equation of Motion of Particles

Particle motion in the flow within the ESZ is complicated in that it is not only related to the undisturbed ambient flow, but also to the disturbance the particle causes to the flow. As described in Chapter 2, for high Reynolds number motions of a spherical particle in a fluid which is also in motion itself, a widely used equation was proposed by Auton et al.[9,10]:

$$m_p \frac{d\vec{u}_p}{dt} = \frac{1}{2} C_{Dstd} \pi a^2 \rho_f \left|\vec{u} - \vec{u}_p\right| (\vec{u} - \vec{u}_p) + \frac{1}{2} m_f \left(\frac{D\vec{u}}{Dt} - \frac{d\vec{u}_p}{dt}\right) + m_f \frac{D\vec{u}}{Dt} \\ + 6a^2 (\pi \mu_f \rho_f)^{1/2} \int_0^t \frac{d(\vec{u} - \vec{u}_p)/d\tau}{(t-\tau)^{1/2}} d\tau \tag{4.6}$$

where $\vec{u}_p(u_p, v_p)$ and $\vec{u}(u, v)$ respectively represent the instantaneous velocity of the particle and the undisturbed fluid velocity at the center of the particle that would apply in the absence of that particle. The gravitational and buoyancy forces, as well as the electromagnetic force can be omitted as they are negligible in comparison with other body forces acting on the particle flowing inside the ESZ, such as the fluid acceleration force $m_f \frac{D\vec{u}}{Dt}$. In this study, a microbubble is considered to behave as a rigid spherical particle, and its motion is also represented by Equation (4.6).

The presence of a solid surface in the vicinity of a moving particle will affect its drag force. In this study, the axial drag force was approximated using the equation developed by Fayon and Happel:[11]

$$C_D = C_{D\infty} + (24/\mathrm{Re}_p)(W-1) \tag{4.7}$$

where, Re_p is the particle Reynolds number, $C_{D\infty}$ is the drag coefficient in the absence of the wall, and W is given by:[12]

$$W = \frac{1-0.75857k^5}{1-2.1050k+2.0865k^3-1.7068k^5+0.72603k^6} \tag{4.8}$$

where k is the ratio of the diameter of the particle to that of the cross section of ESZ at the center of the particle. The wall effects in the radial direction can be estimated by using a tabulated correction factor for the drag force on a solid particle moving perpendicular to a plane wall.[13] The correction factor is a function of the ratio of the distance of the particle center from the wall to the particle radius, and linear interpolation is employed to obtain the factor for the ratio in question.

4.2.3 Ohmic Model of ESZ

The electrical resistance of the ESZ without a particle inside is given by Ohm's law:

$$R_{ESZ} = \rho_e \int \frac{dx}{A(x)} \tag{4.9}$$

where ρ_e is the electrical resistivity of the fluid inside ESZ, $A(x)$ is an equipotential surface, and x is the axial distance with respect to the central vertical plane of the ESZ as shown in Figure 4.1.

The equipotential surfaces can be obtained by solving Laplace equation for electrical potential φ:

$$\frac{\partial^2 \varphi}{\partial x^2} + \frac{1}{y}\frac{\partial}{\partial y}\left(y\frac{\partial \varphi}{\partial y}\right) = 0 \qquad (4.10)$$

The computational domain employed is the same as that for flow field and shown in Figure 4.2. The current density can be calculated from Ohm's law as described in Equations (4.11) and (4.12):

$$J_x = -\sigma_e \frac{\partial \varphi}{\partial x} \qquad (4.11)$$

$$J_y = -\sigma_e \frac{\partial \varphi}{\partial y} \qquad (4.12)$$

where σ_e is the electrical conductivity of the liquid, which, for water, is $3.33\times10^{-2}\ \Omega^{-1}m^{-1}$.

The boundary conditions for calculating the electrical potential field are constant potential across the central vertical plane of the ESZ, uniform electric current density at the inflow boundary and zero electric current flux across the insulating wall. The calculated electrical potential field (Figure 4.14) shows that the equipotential surfaces inside the ESZ are quite flat, especially near the middle of the orifice where the minimum diameter is reached. Therefore, the surface $A(x)$ was chosen to be planar, perpendicular to the axis of the orifice so as to simplify the computation. When a non-conducting spherical particle is introduced into the orifice, the generated resistive pulse is given by:

$$\Delta R_{ESZ} = \frac{\rho_e}{\pi}\int \frac{r^2(x)dx}{R^2(x)(R^2(x) - r^2(x))} \qquad (4.13)$$

where $R(x)$ and $r(x)$ are the radii of the cross-section of the orifice and the particle, respectively. The numerical integration of Equation (4.13) was performed, with respect to x coordinate, every 1 μm according to:

$$\Delta R_{ESZ}(x_p) = \sum_{x_p-a}^{x_p+a} \frac{\rho_e \Delta x}{\pi} [\frac{r^2(x)}{R^2(x)(R^2(x) - r^2(x))}] \qquad (4.14)$$

where x_p is the axial position of the particle of radius a. Based on Equation (4.14), ESZ resistance variation with the position of a spherical particle of different diameter inside the orifice can be obtained.

4.2.4 Numerical Methods

In this study, a non-orthogonal, boundary-fitted grid of variable spacing was adopted to enhance the accuracy of the calculation (Figure 4.3). The conservation equations for mass and momentum with the boundary conditions, and Equation (4.6) for the motion of particles were

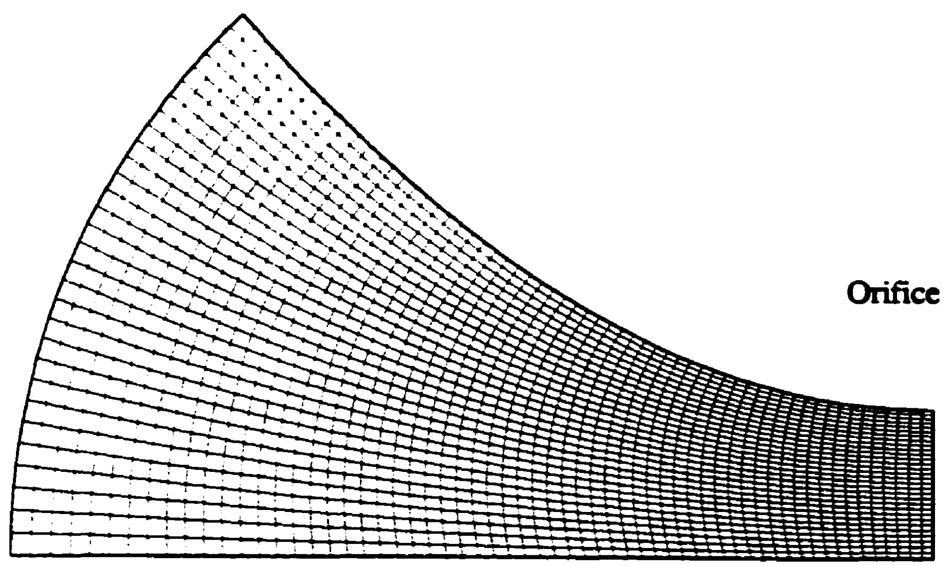

Figure 4.3 — Non-orthogonal, boundary-fitted grid used in this study.

solved using the same methods as described in Chapter 2. The time step used in solving particle motion equation, Δt, is set as 10^{-5} ms to maintain the accuracy of the calculation.

4.3 Experiment

4.3.1 Water Based LiMCA System — APS II System

The APS II system[14] was designed as a robust industrial quality amplifier which can measure the cleanliness of aqueous solutions as does the LiMCA system used in molten metals. The probe used to model the metal based LiMCA probe was designed on a one-to-one scale to ensure geometrical similarity. A schematic of the APS II system's experimental setup is shown in Figure 4.4. The probe head essentially consists of an

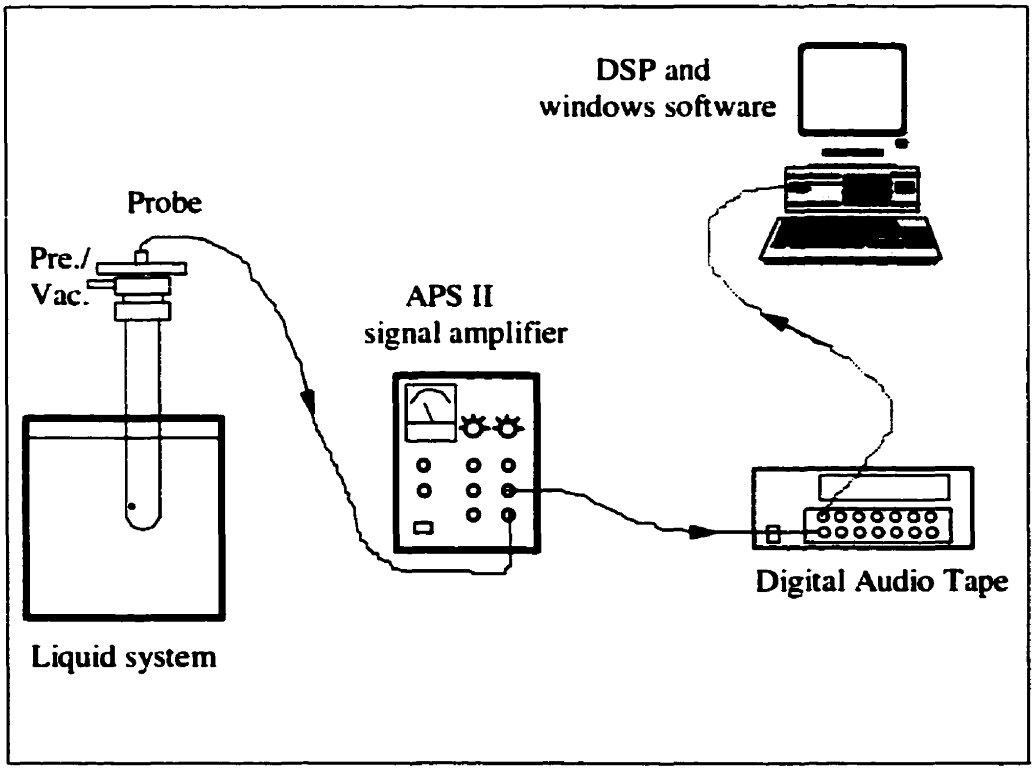

Figure 4.4 — Schematic experimental set up of APS II system.

electrically insulating sampling tube and two electrodes. The inner electrode is fixed to the interior, while the outer electrode is connected directly to the tube surrounding the orifice. By alternate use of moderate vacuum and pressure, aqueous samples are aspirated into, and then exhausted from, the sampling tube through the orifice, i.e., the electric sensing zone. To minimize noise generation, two Venturi tubes were connected in parallel to generate the vacuum. Probe vacuum could be controlled by increasing or decreasing the flow rate of air through the Venturi tubes, which in turn determined the sampling flow rate. Compressed gas was used to cycle pressure inside the probe tube. The APS II system amplifier maintains a constant potential across the orifice. When a particle passes through the ESZ, the voltage signal is amplified by the APS II system, and then simultaneously sent to the oscilloscope and DAT (Digital Audio Tape). The oscilloscope was used to display the signals and the DAT recorder was used to record the incoming signals. The recorded data on the DAT tape were subsequently sent to the computer which digitized and analyzed the signals using a custom designed DSP program which passed the processed information onto a windows based software program "MetalWindows™". In the DSP analysis step, seven characteristic parameters were generated for every signal. These comprised pulse height, pulse width, start slope, end slope, time to pulse peak, start time and end time (Figure 4.5). It is noted that all these parameters are dependent on the two noise thresholds set, i.e., NOISEHI and NOISELO, which mark the margins of the noise band of the signal. The noise band reflects the operational conditions and determines the minimum size of the particles that the system can detect under such conditions.

4.3.2 Particle Discrimination Test

In the particle discrimination tests, orifices with a size of $270\mu m$ and $320\mu m$ were used. The shape of the orifices were parabolic and could be represented as:

$$y = 1.0 \bullet x^2 + R \tag{4.15}$$

where R is the radius of the circular orifice's throat, and x and y are the axial and radial coordinates, respectively, in millimeter. The wall

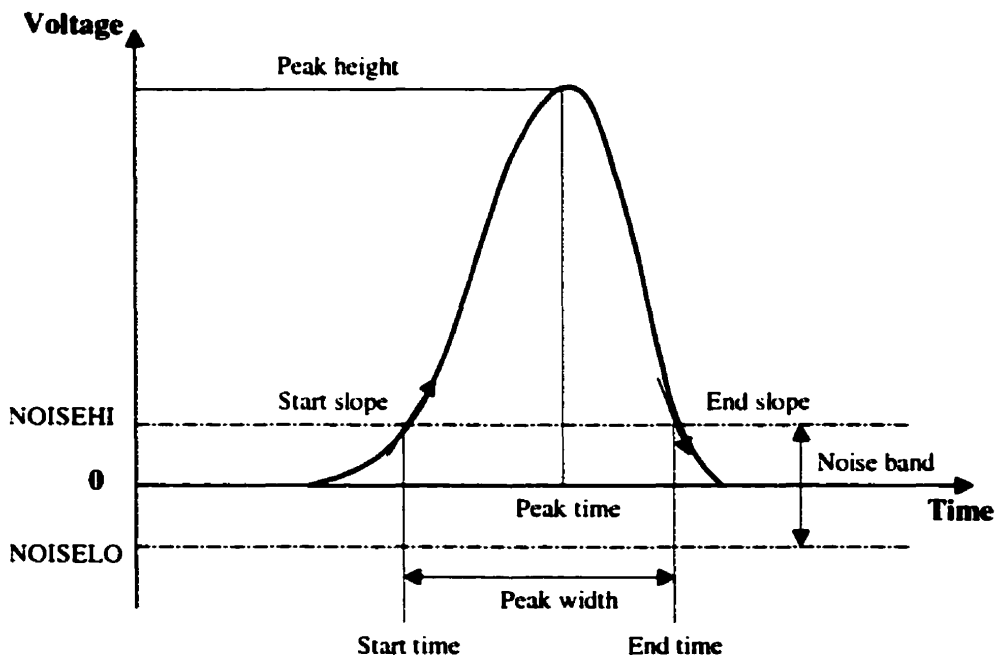

Figure 4.5 — The peak parameters generated by DSP in LiMCA system.

thickness of the sampling tube $L_{orifice}$, was 1.2 mm (Figure 4.2). The orifice currents used were $30\mu Amps$ and $36\mu Amps$, while the noise thresholds were $\pm 2mV$ and $\pm 15mV$ for $270\mu m$ and $320\mu m$ diameter orifices, respectively. The effect of liquid acceleration on the relative velocity of the particles was studied by changing the flow rate of liquid through the orifice, which was regulated by applying different levels of vacuum: 100mmHg, 150mmHg and 250mmHg. While the flow rate of fluid through the orifice was changed, particles of the same size, but of varying density were measured to determine the effect of particle density on the time needed to pass through the orifice and the shapes of the signals. Particles tested included latex, silica and microbubbles of argon. Their physical properties are also listed in Table 4.1. High purity argon gas was used to generate the microbubbles, which were injected into water using a fine glass needle. The diameter of the argon bubble was controlled by adjusting the pressure drop across the needle.[1]

4.4 Results and Discussion

4.4.1 Fluid Flow

Hydrodynamic experiments were used to determine the discharge coefficient for the APS II orifice as this gives an indication of flow energy losses across the orifice. When fluid flows through a converging-diverging nozzle, the mean velocity attained at the throat of the nozzle without energy losses can be determined from the following expression derived from the Bernoulli equation:

$$u_{m_{theory}} = \sqrt{\frac{2(\Delta p + \rho_f g \Delta h)}{\rho_f}} \tag{4.16}$$

where Δp is the differential pressure applied by the vacuum (Pa), ρ_f is the fluid density (kg/m^3), g is the gravitational acceleration (m/s^2), and Δh is the difference in the fluid levels outside and inside the tube (m). To calculate the discharge coefficient, the flow rate of water passing through the orifice was measured and compared with theoretical calculations based on Equation (4.16). The differences were reflected in the correction factors, or discharge coefficients, for each probe and are listed in Table 4.2. The measured velocity was used to set the inlet boundary conditions in numerical computation of fluid flow fields within the orifice. The predicted flow fields for $270\mu m$ orifice with $u_m = 5.63 m/s$ and $320\mu m$ orifice with $u_m = 7.5 m/s$ are shown in Figures 4.6(a) and 4.7(a). The axial and radial velocity component profiles at three different positions inside the ESZ for these two probes are illustrated in Figures 4.6(b) and 4.6(c), 4.7(b) and 4.7(c), respectively. It can be seen that the axial velocity is very uniform at each cross section along the ESZ, while the radial velocity, which is negative, has a maximum near the wall and damps out towards the central axis at each cross section. Moreover, the axial velocity at the throat of the ESZ is much higher than the radial velocity, proving that it is reasonable to assume that beyond the throat of the orifice, the jet flow has only axial velocity and the same velocity profile as that at the throat. The above arguments also hold for the other two $270\mu m$ probes with $u_m = 4.5 m/s$ and $u_m = 7.4 m/s$, respectively.

Table 4.2 Discharge coefficient for the probes used in particle discrimination study

Orifice size (μm)	Differential vacuum (mmHg)	Measured flow rate (ml/s)	Measured orifice velocity u_m (m/s)	Theoretical orifice velocity $u_{m_{theory}}$ (m/s)	Discharge coefficient
270	100	0.258	4.50	5.26	0.86
270	150	0.322	5.63	6.40	0.88
270	250	0.424	7.40	8.22	0.90
320	250	0.603	7.50	8.22	0.91

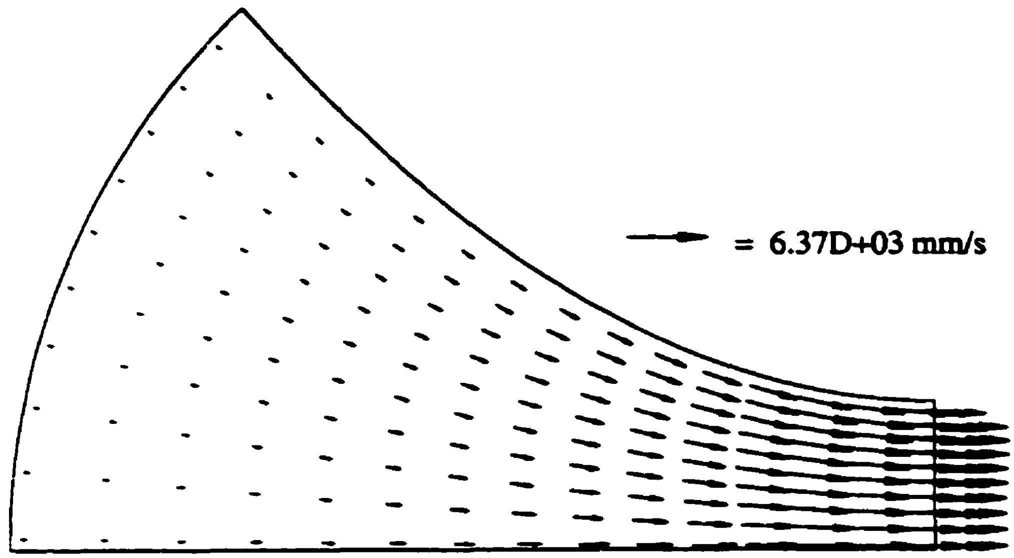

(a) Velocity vectors

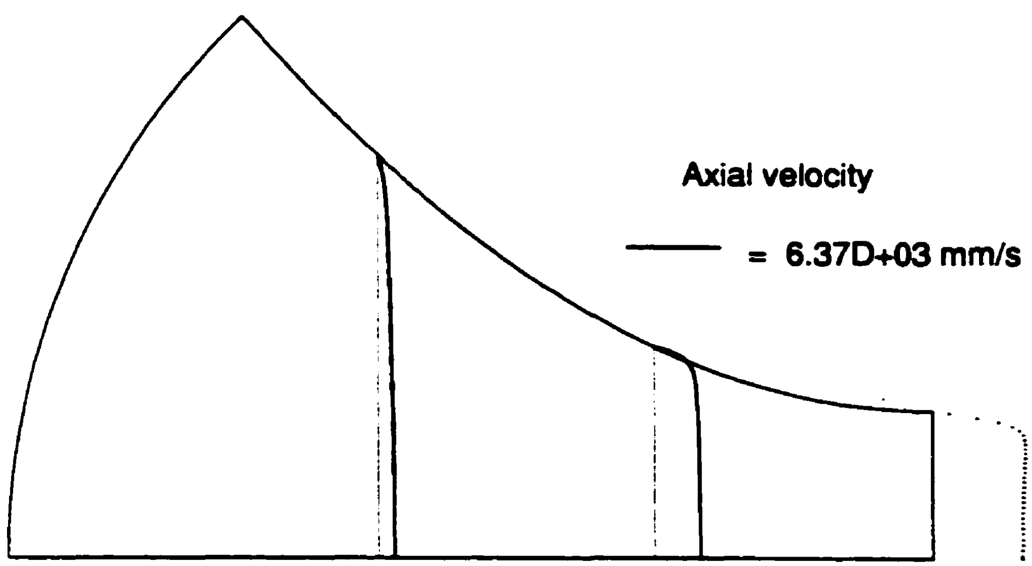

(b) Axial velocity profiles

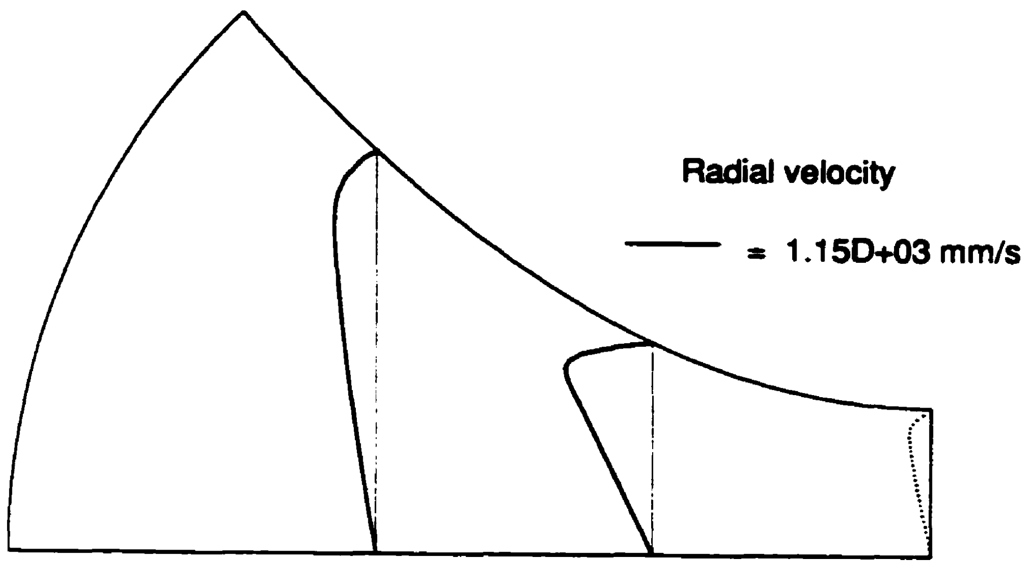

(c) Radial velocity profiles

Figure 4.6 — Velocity vectors and the axial and radial velocity profiles at the cross sections of $x/L = 0$, -0.15, and -0.3 in an ESZ of $270\mu m$ with $u_m = 5.63\,m/s$.

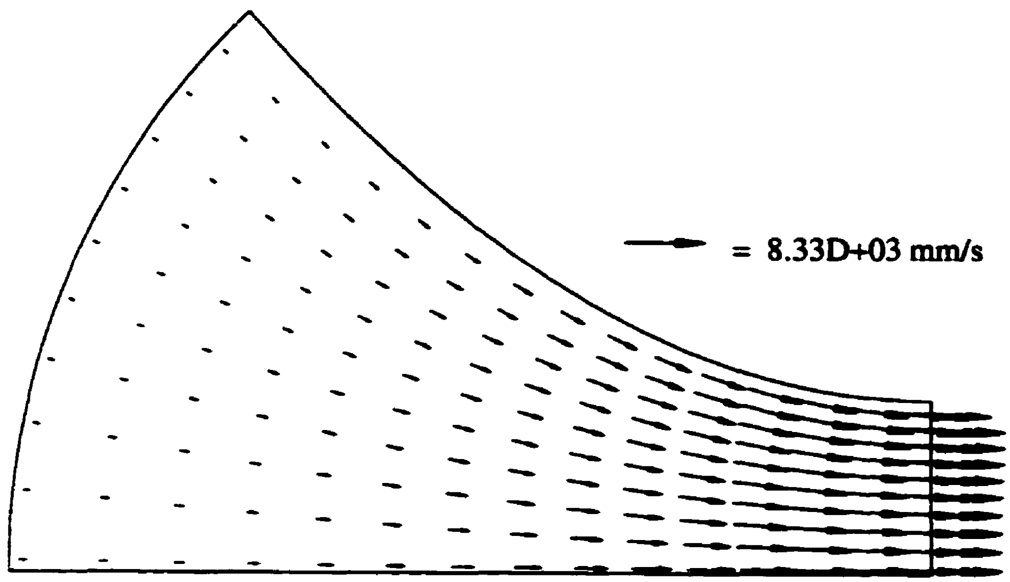

(a) Velocity vectors

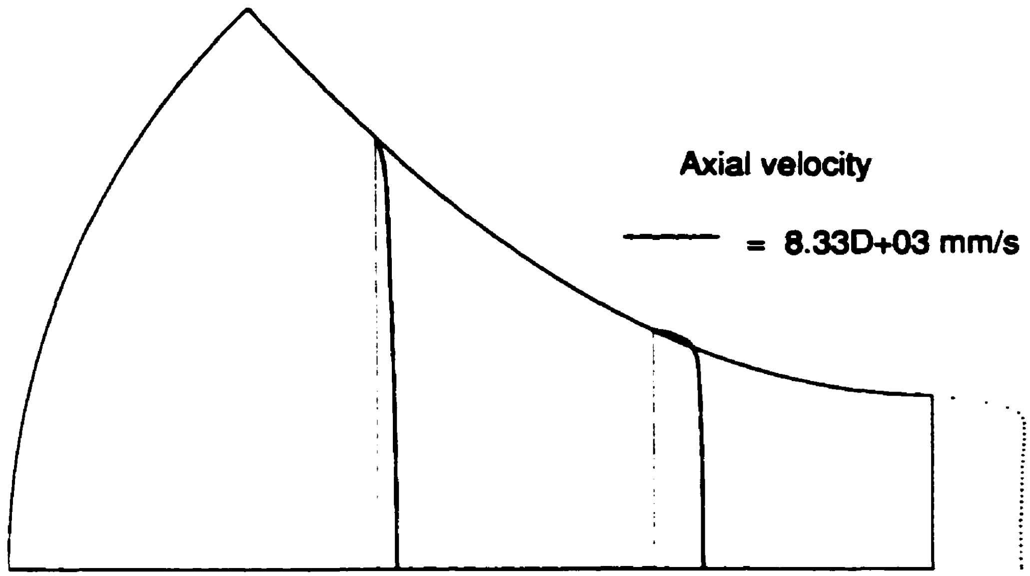

(b) Axial velocity profiles

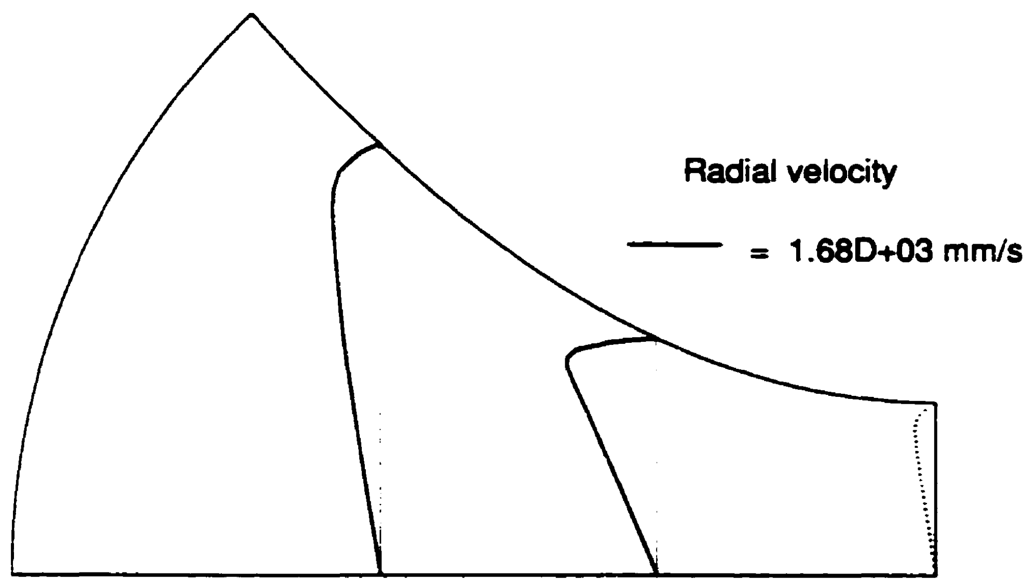

(c) Radial velocity profiles

Figure 4.7 — Velocity vectors and the axial and radial velocity profiles at the cross sections of $x/L = 0$, -0.15, and -0.3 in an ESZ of $320\mu m$ with $u_m = 7.5\,m/s$.

4.4.2 Particle Motion

Once the fluid flow field within the ESZ is known, Equation (4.6) can be solved to predict the motions of particles of different densities and sizes.

4.4.2.1 Effect of particle density

The effect of particle density on the motion of particles was studied for $60\mu m$ diameter particles with three different densities of 0, 1.05×10^3 and $2.65\times10^3 kg/m^3$, respectively. The results are shown in Figure 4.8 for particles flowing through along the central axis of a $270\mu m$ diameter orifice at a velocity of $u_m = 4.5m/s$. It can be seen from Figure 4.8 that particles with higher density are predicted to take longer to pass through

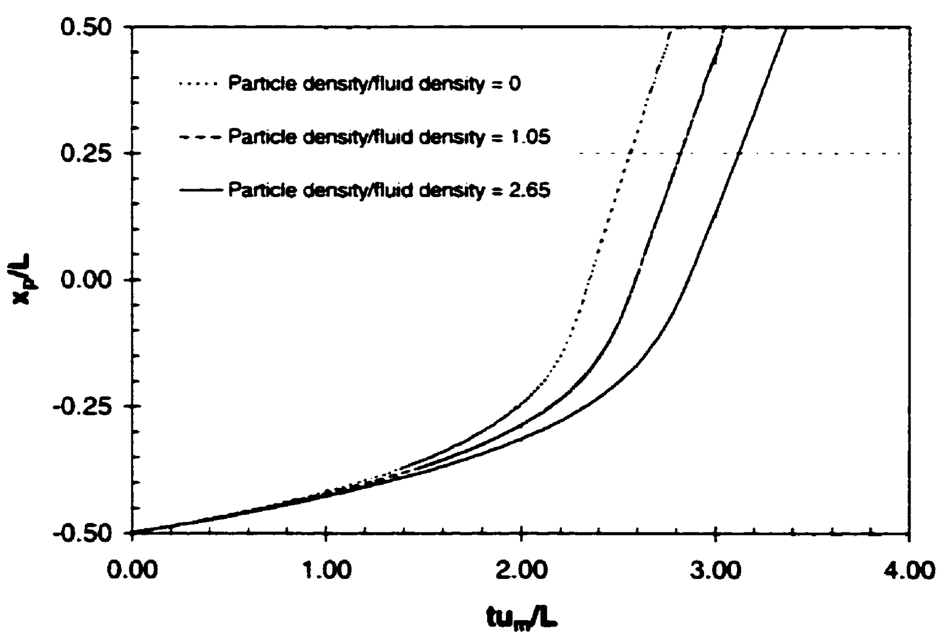

Figure 4.8 — Effect of particle density on the motion of particles in an ESZ of $270\mu m$ with $u_m = 4.5m/s$.

the ESZ. This phenomenon is the result of the strongly accelerative flow within the converging region of the ESZ. This induces different relative velocities for particles of different densities. Figure 4.9 shows the axial velocity and the relative axial velocity corresponding to the particle motions shown in Figure 4.8. During the whole process of particle motion through the ESZ, bubbles travel faster (Figure 4.9(i)) than particles which are slightly denser than fluid (Figure 4.9(ii)) and much faster than particles which are much denser than the fluid (Figure 4.9(iii)). In the converging region of the ESZ ($x_p/L \le 0$), particles of all densities accelerate, while beyond the throat, velocities converge to match the fluid's velocity.

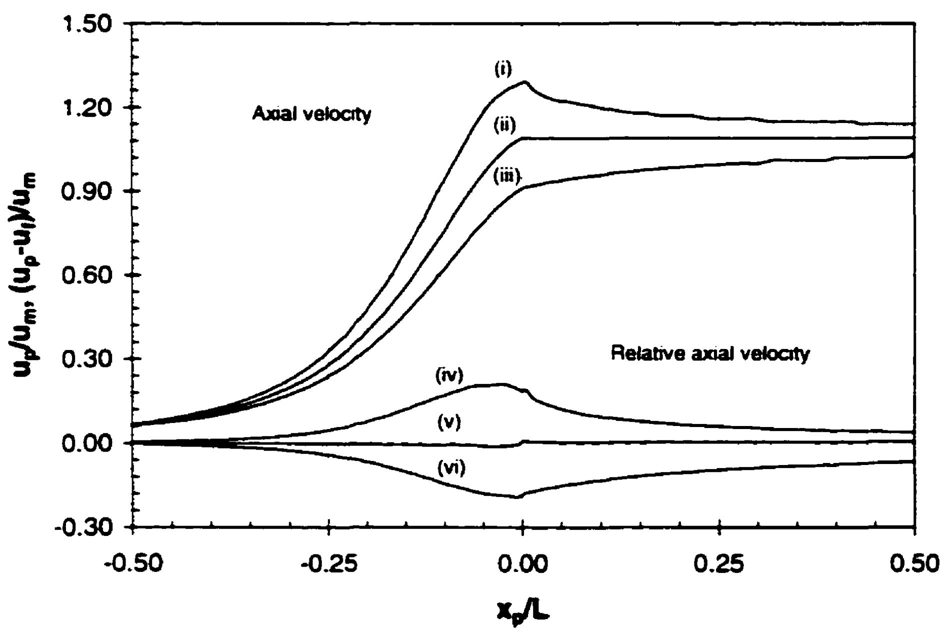

Figure 4.9 — Effect of particle density on the axial velocity and relative axial velocity of particles inside an ESZ of $270\mu m$ with $u_m = 4.5 m/s$. (i) Axial velocity, $\rho_p/\rho_f = 0$; (ii) Axial velocity, $\rho_p/\rho_f = 1.05$; (iii) Axial velocity, $\rho_p/\rho_f = 2.65$; (iv) Relative axial velocity, $\rho_p/\rho_f = 0$; (v) Relative axial velocity, $\rho_p/\rho_f = 1.05$; (vi) Relative axial velocity, $\rho_p/\rho_f = 2.65$.

$u_p/u_m \to 1.00$. The positive value of the relative velocity for bubbles (Figure 4.9(iv)) implies that the bubbles move faster than the fluid. For heavy particles (Figure 4.9(vi)), on the other hand, the relative velocity is negative, which means the particles move slower than the fluid. Particles which are slightly denser than fluid (Figure 4.9(v)) follow the fluid flow closely, resulting in a very small relative velocity.

4.4.2.2 Effect of particle size

The effect of particle size on the motion of particles was studied for particles of $60\mu m$ and $100\mu m$ diameter. The particles flow along the central axis of a $270\mu m$ orifice with $u_m = 4.5 m/s$. This particle size effect was studied for bubbles of $\rho_p = 0 kg/m^3$ and for denser particles of $\rho_p = 2.65\times10^3 kg/m^3$. The simulation results are shown in Figure 4.10. Again, heavy particles (Figure 4.10(ii)) take longer to pass through the orifice than do the bubbles (Figure 4.10(i)). However, the size effects are different for bubbles and dense particles. When the density of the particle is higher than that of the fluid, the larger the particle, the longer it takes to flow out of the ESZ. By contrast, when the density of the particle is smaller than that of the fluid, the larger the particle, the shorter it takes to flow out of the ESZ. This phenomenon is related to the different particle size dependence of the relative velocity developed inside the ESZ for bubbles and dense particles. Figure 4.11 shows the axial velocity and the relative axial velocity for bubbles ($\rho_p = 0 kg/m^3$) and particles ($\rho_p = 2.65\times10^3 kg/m^3$) with a size of $60\mu m$ and $100\mu m$, respectively. For bubbles, axial velocity of size $100\mu m$ is larger than that of size $60\mu m$ (Figure 4.11(i)), and correspondingly larger bubbles assume larger positive relative velocity, outpacing further the fluid flow than the smaller bubbles (Figure 4.11(iii)). On the contrary, larger dense particles move slower than

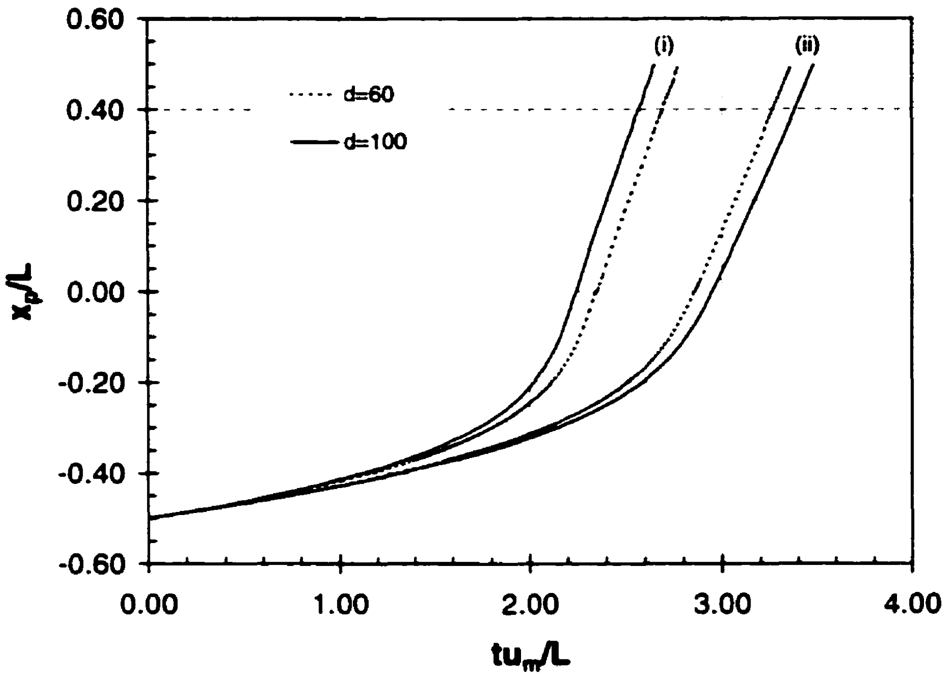

Figure 4.10 — Effect of particle size on the motion of particles in an ESZ of $270\mu m$ with $u_m = 4.5 m/s$. (i) $\rho_p/\rho_f = 0$; (ii) $\rho_p/\rho_f = 2.65$.

smaller ones (Figure 4.11(ii)), and consequently have larger negative relative velocities, lagging further behind the fluid flow (Figure 4.11(iv)).

A simple qualitative analysis of the magnitude of the relative velocity developed in the converging region of the ESZ for particles of different sizes and densities can be carried out using the theory developed by Brennen,[15] who considers a steady fluid flow in a converging nozzle characterized by a velocity u_m and a typical dimension l. A particle in this flow will experience a typical fluid acceleration of u_m^2/l for a typical time given by l/u_m, and hence develops a velocity u_R relative to the fluid. When the particle Reynolds number $\frac{\rho_f u_R a}{\mu_f} << 1$, u_R/u_m is given by:

$$u_R/u_m = (1 - \frac{m_p}{\rho_f V_p})(\frac{\rho_f u_m a}{\mu_f})(\frac{a}{l}) \tag{4.17}$$

and when $\frac{\rho_f u_R a}{\mu_f} >> 1$, $|u_R|/u_m$ is given by:

$$|u_R|/u_m = \left|1 - \frac{m_p}{\rho_f V_p}\right|^{\frac{1}{2}} \frac{1}{C_D^{\frac{1}{2}}} (\frac{a}{l})^{\frac{1}{2}} \tag{4.18}$$

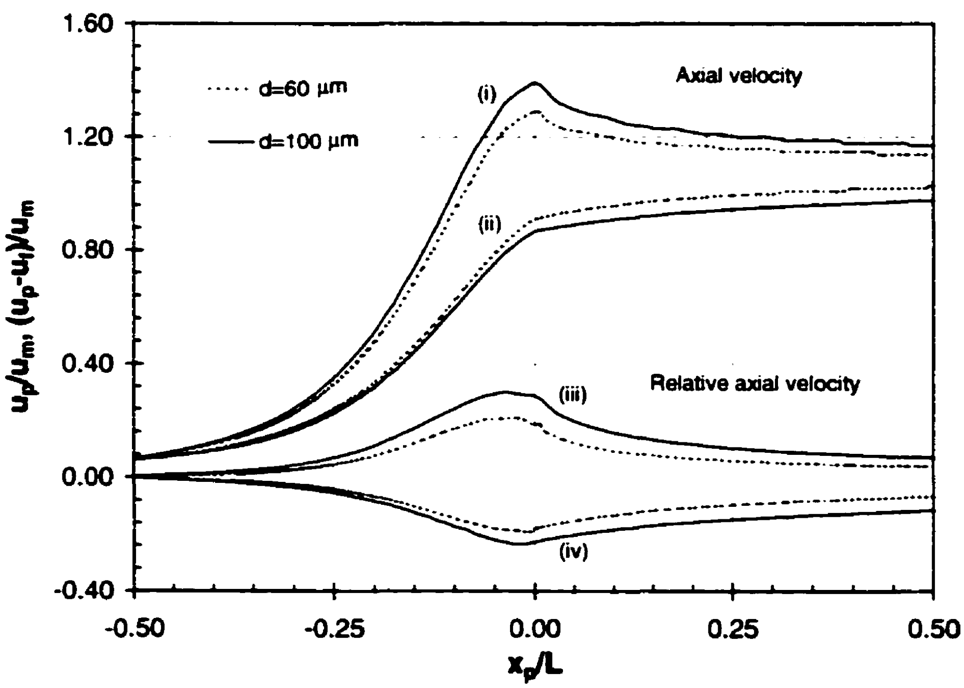

Figure 4.11 — Effect of particle size on the axial velocity and relative axial velocity of particles inside an ESZ of $270\mu m$ with $u_m = 4.5 m/s$. (i) Axial velocity, $\rho_p/\rho_f = 0$; (ii) Axial velocity, $\rho_p/\rho_f = 2.65$; (iii) Relative axial velocity, $\rho_p/\rho_f = 0$; (iv) Relative axial velocity, $\rho_p/\rho_f = 2.65$.

The qualitative estimation of the relative velocity of the particles from Equations (4.17) and (4.18) is compared with the numerical simulations, and the results are shown in Figure 4.12. The agreement between these two methods is considered reasonable.

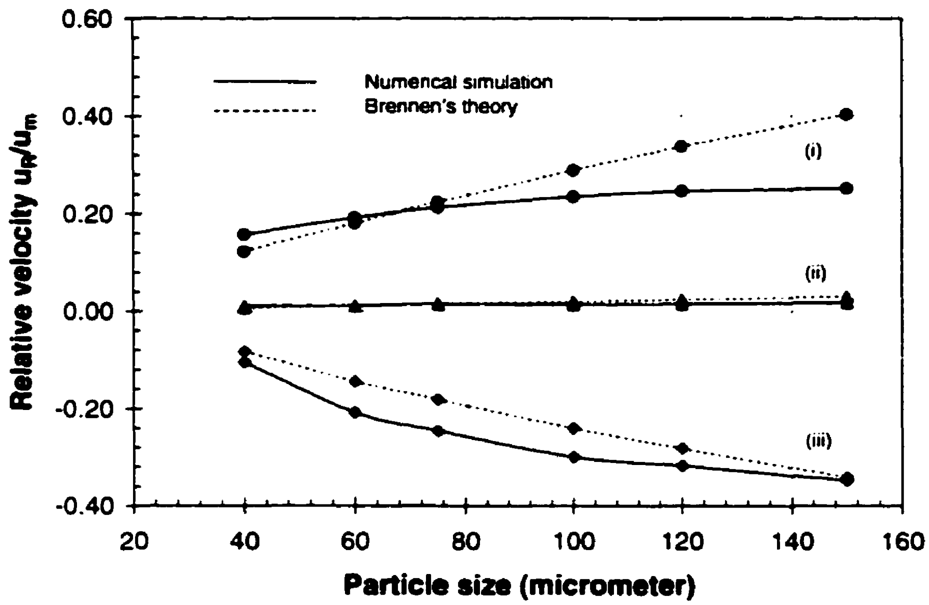

Figure 4.12 — Comparison of the relative velocity for particles of different size and density obtained by Brenen's theory and numerical simulation. (i) $\rho_p/\rho_f = 0$; (ii) $\rho_p/\rho_f = 1.05$; (iii) $\rho_p/\rho_f = 2.65$.

4.4.2.3 Effect of entry point

When particles flow into the ESZ from positions other than the central axis, they develop not only a relative axial velocity but also relative radial velocity to the fluid. Figure 4.13 shows the axial and radial components of the velocity (Figure 4.13(a)) and relative velocity (Figure 4.13(b)) for particles of size $60\mu m$ with density of $0 kg/m^3$ and $2.65\times10^3 kg/m^3$, flowing into the ESZ from a radial position of $y_0/R = 1.0$. Generally speaking, the velocity and relative velocity in the radial direction are much smaller than their axial counterparts. Particles with density lower than that of the fluid lead the fluid flow not only in the axial direction, but also in the radial direction (Figures 4.13b(i) and 4.13b(iii)). On the other hand, particles with density higher than that of the fluid lag behind the fluid flow in both directions (Figures 4.13b(ii) and 4.13b(iv)). Apparently, particles of density $0 kg/m^3$ take shorter time to flow out of the orifice than those of density $2.65\times10^3 kg/m^3$.

4.4.3 Particle Discrimination in APS II System

As discussed before, particle discrimination in LiMCA system seems feasible thanks to DSP technology. For every transient pulse generated when a particle passes through the ESZ, seven parameters are used to

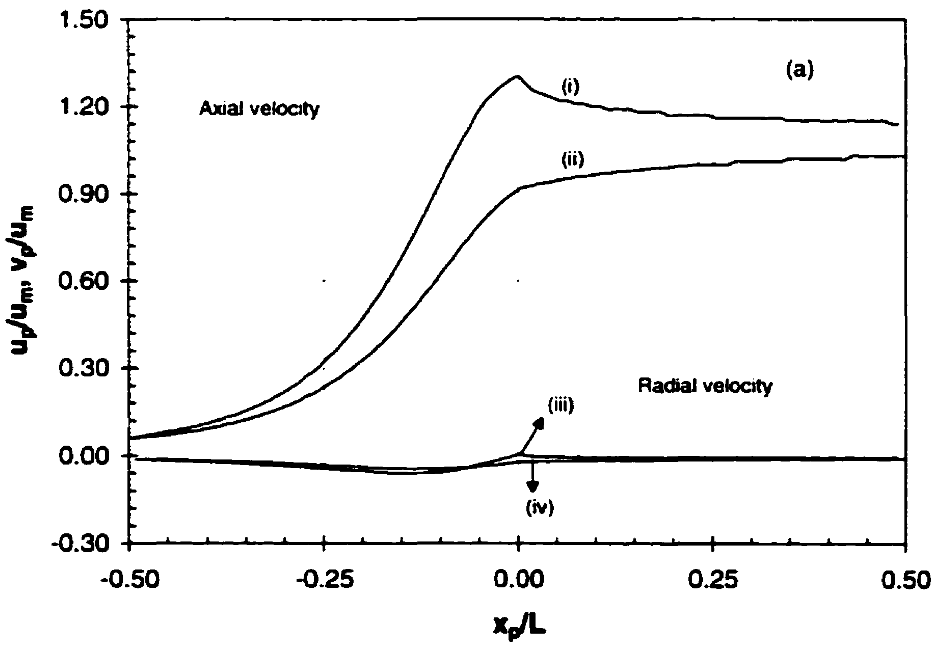

(a) Axial and radial velocity (i) Axial velocity, $\rho_p/\rho_f = 0$; (ii) Axial velocity, $\rho_p/\rho_f = 2.65$; (iii) Radial velocity, $\rho_p/\rho_f = 0$; (vi) Radial velocity, $\rho_p/\rho_f = 2.65$

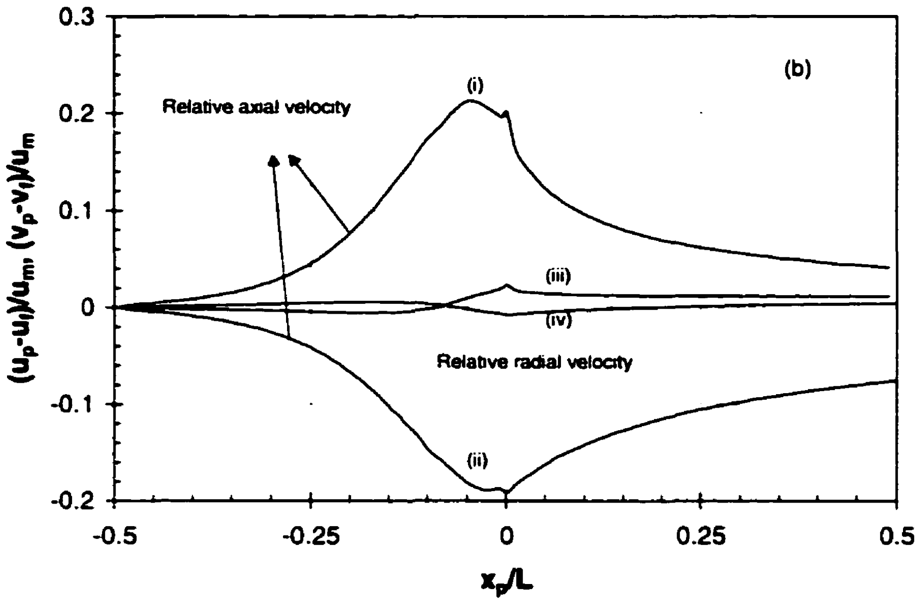

(b) Relative axial and radial velocity (i) Relative axial velocity, $\rho_p/\rho_f = 0$; (ii) Relative axial velocity, $\rho_p/\rho_f = 2.65$; (iii) Relative radial velocity, $\rho_p/\rho_f = 0$; (iv) Relative radial velocity, $\rho_p/\rho_f = 2.65$

Figure 4.13 — Axial and radial components of velocity and relative velocity of particles flowing into an ESZ of $270\mu m$ with $u_m = 4.5 m/s$ from entry point of $y_0/R = 1.0$.

characterize the pulse (Figure 4.5). These parameters are related to the motion of the particle, which depends on the physical properties of the particle and the fluid flow conditions within the ESZ, as discussed in the previous section. Figure 4.5 also shows that the transient time of the particles flowing through the ESZ in LiMCA system is not the time the particle takes to traverse the physical length of the ESZ, but rather the time it takes to pass through the region where the pulse height generated by the particle is higher than the threshold. Therefore, in the following, a numerical study of particle discrimination was carried out by relating the ESZ resistance change using the Ohmic model (Equation (4.14)) to the motion of the particle inside the ESZ. The calculation of the ESZ resistance according to Equation (4.9) needs the equipotential surface $A(x)$, shown in Figure 4.14 for an ESZ of $270\mu m$ with $I = 30\mu A$ in water, to be determined.

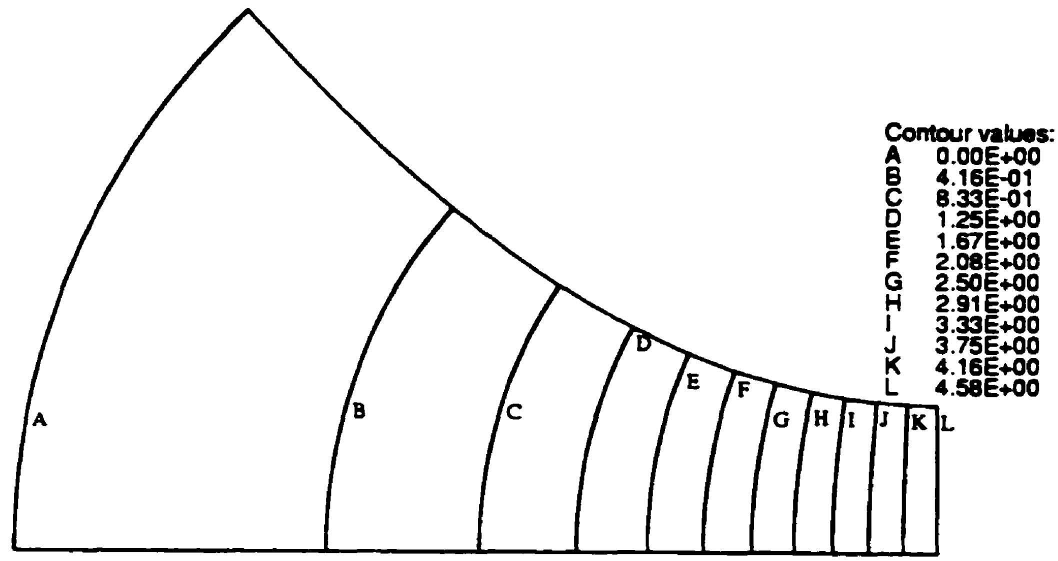

Figure 4.14 — Electrical potential (volt) distribution inside an ESZ of $270\mu m$ with electric current $I = 30\mu A$.

It is seen that the equipotential surfaces are quite flat, especially near the central region of the ESZ. Thus, to simplify the computations, the surface $A(x)$ was chosen to be planar, perpendicular to the axis of the orifice. Figure 4.15 shows the variation in ESZ resistance as particles of different diameter pass through orifices of $270\mu m$ (Figure 4.15(a)) and $320\mu m$ (Figure 4.15(b)). It can be seen from Figure 4.15 that larger particles reach the noise threshold resistance further away from the orifice center than do smaller particles. Therefore, smaller particles travel shorter distance when the transient time is measured by APS II system. For example, in the $320\mu m$ orifice, a particle of size $100\mu m$ reaches the noise

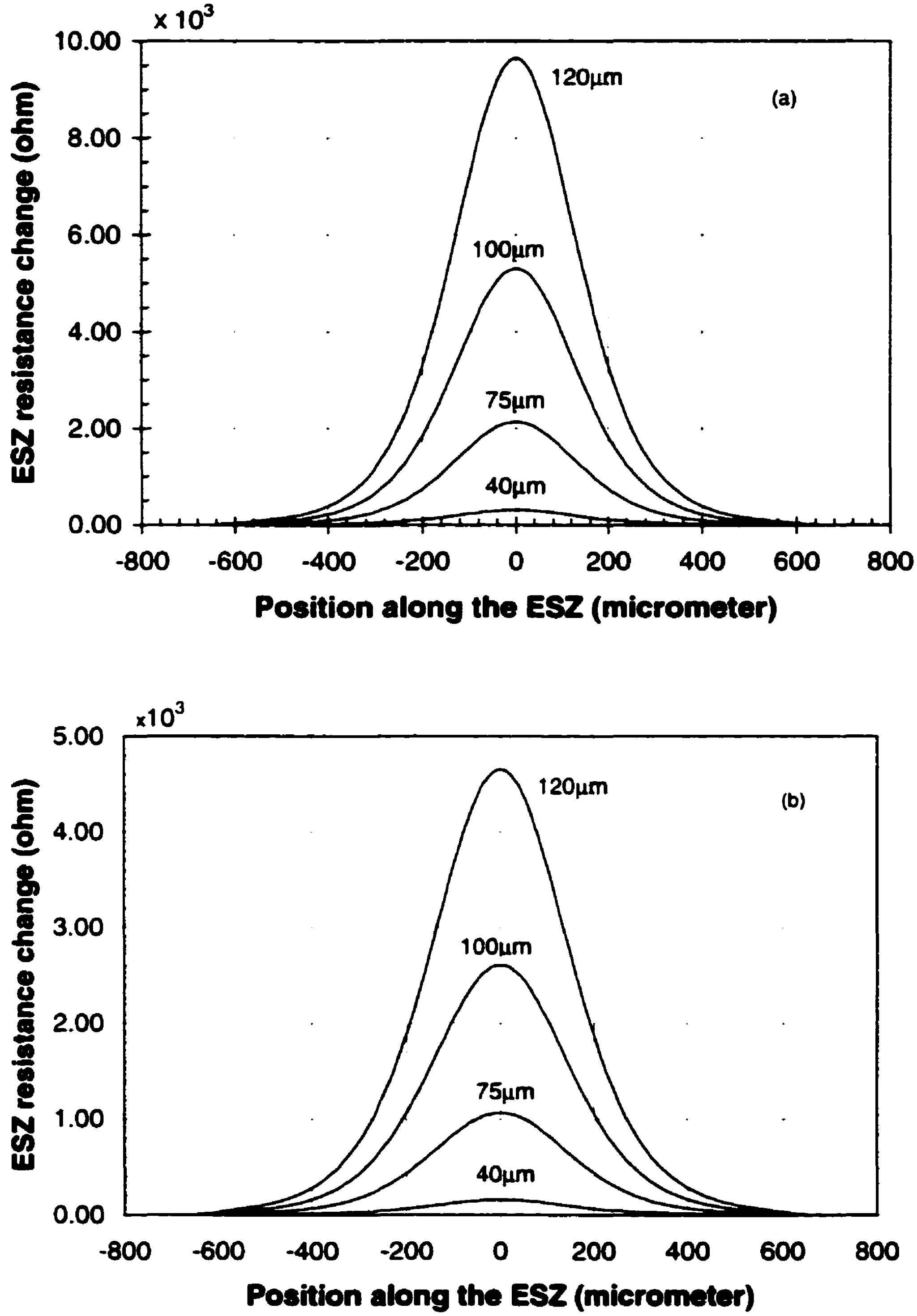

Figure 4.15 — ESZ resistance change with the position of particles of various diameter. (a) 270μm orifice; (b) 320μm orifice.

threshold of $15mV$ at $0.305mm$ from the center of the orifice, while it is $0.102mm$ for a particle of $60\mu m$. Therefore, the transient time measured for a particle of $60\mu m$ is the time it takes to travel $0.204mm$ near the center of the orifice, while for a particle of $100\mu m$, it is the time to travel $0.610mm$.

To study the particle discrimination numerically, Equations (4.4) and (4.5) for the fluid flow and Equation (4.6) for the motion of particles were solved first for particles of varying density and size flowing through the whole orifice. Then, the transient time (Figure 4.5) was obtained by considering the noise threshold of the APS II system. The studied situations include a $270\mu m$ orifice with three different mean fluid velocity of $4.5m/s$, $5.63m/s$, and $7.4m/s$, and a $320\mu m$ orifice with a mean fluid velocity of $7.5m/s$. Predictions are shown in Figure 4.16, together with the experimental results.[11]

It can be seen that the agreement between the experimental data and the predictions calculated by the mathematical model was satisfactory.

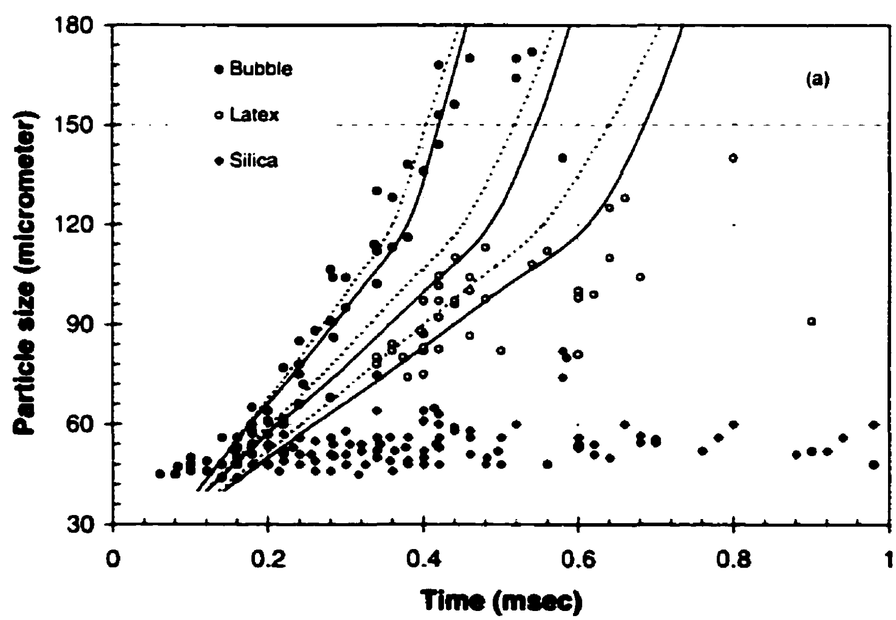

(a) $270\mu m$ orifice, $u_m = 4.5m/s$

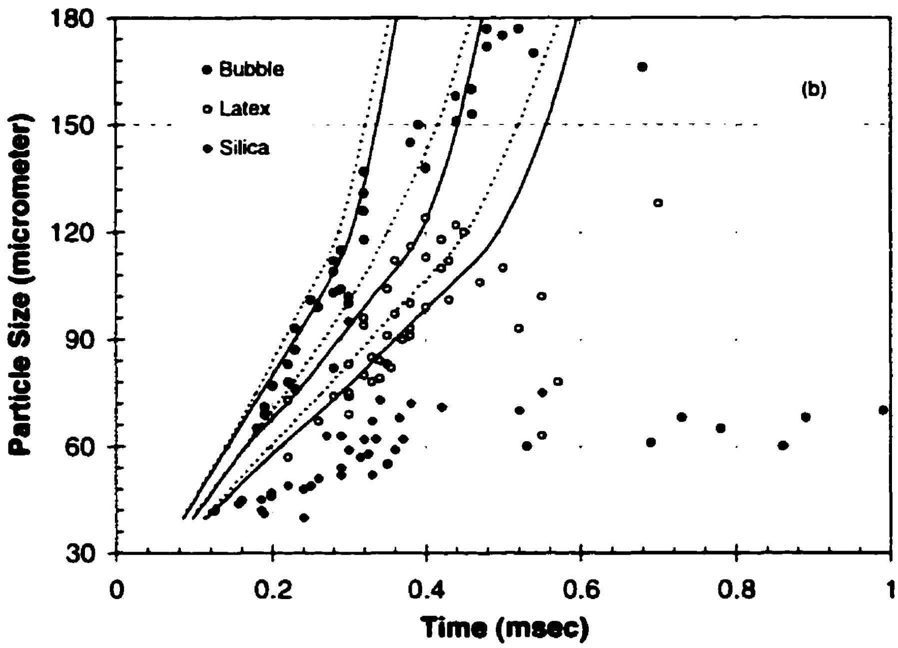

(b) 270μm orifice, $u_m = 5.63 m/s$

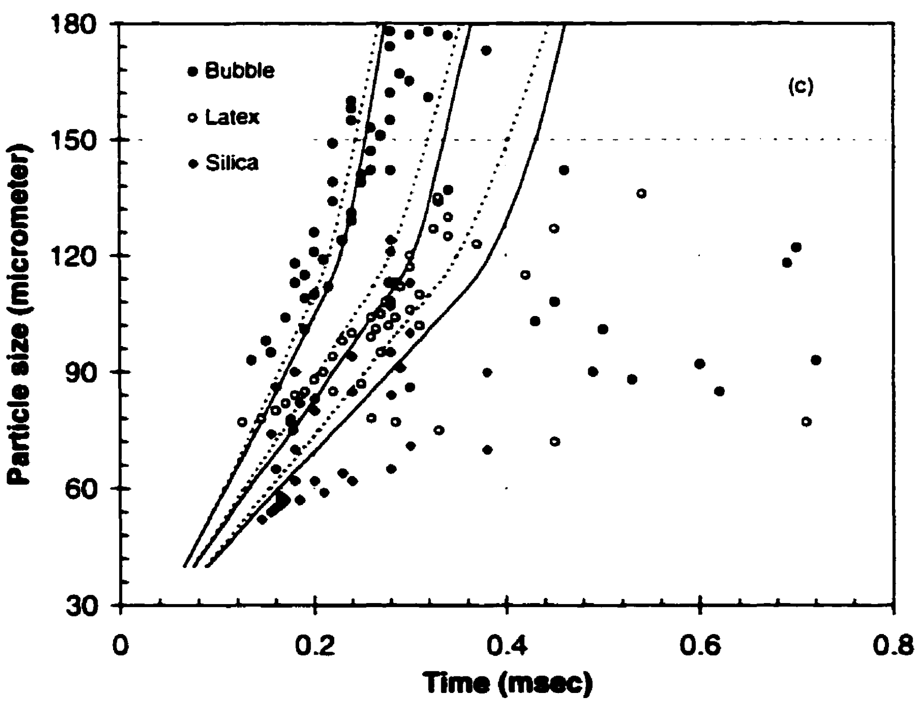

(c) 270μm orifice, $u_m = 7.4 m/s$

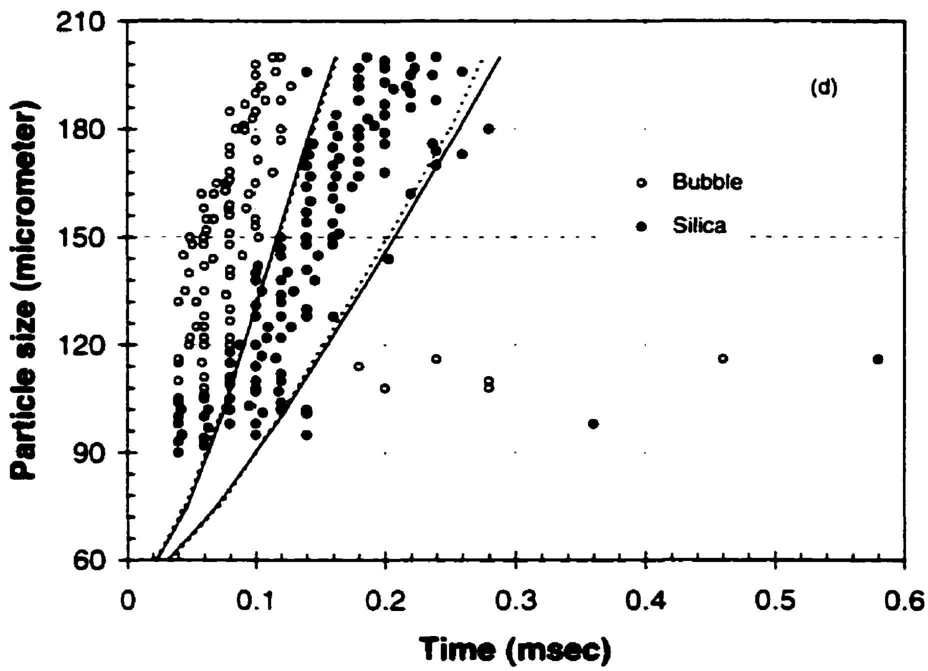

(d) $320\mu m$ orifice. $u_m = 7.5 m/s$

Figure 4.16 — Comparison of experimentally measured and numerically predicted transient time versus particle size. (∘ , •, ◆ measured. ----- particles flowing into the ESZ along central axis. — particles flowing into the ESZ near wall).

Bubbles were found to have shorter transient times than solid particles of the same size. which can be explained by the different relative velocity developed when they move through the ESZ. as shown in Figure 4.9. Bubbles. which lead the fluid flow. travel faster than the latex microspheres which are slightly denser than the fluid and follow the fluid flow closely. Silica particles are much denser than the fluid and thus lag behind the fluid flow when traveling inside the ESZ, resulting in lower velocity and longer transient time than both latex microspheres and bubbles.

It is also noted from Figure 4.16 that larger particles have longer transient times than smaller ones of the same density. This is easy to explain for solid particles. As shown in Figure 4.11, for solid particles, the larger the size, the lower the velocity. On the contrary, for bubbles, the larger the size, the higher the velocity. It seems that larger bubbles should have lower transient times than smaller bubbles. In fact, the transient times of larger bubbles, which were measured in APS II system, are longer than smaller bubbles, because larger bubbles reach the threshold much further away from the orifice center, resulting in a longer distance to travel.

Comparing Figures 4.16(a), (b) and (c), it can be seen that the overall transient time decreases as the fluid flow velocity inside the orifice increases. On the other hand, the difference in transient times for bubbles, latex microspheres and silica particles becomes more significant as particle size increases, improving the discrimination between particles of different densities. This is in accordance with Figure 4.12, which shows that relative particle motion decreases with decreasing particle diameter.

Also shown in Figure 4.16 are the transient time versus particle size for bubbles, latex microspheres and silica particles flowing into the ESZ from near wall positions (solid lines). The dashed lines are the results for particles flowing into the ESZ along the central axis. The difference between these two situations is not significant, especially for bubbles and small solid particles.

Besides the transient time, based on which particle discrimination can be carried out, pulse shape is also of characteristics for different particles. Figure 4.17 shows the signal shapes of a typical bubble and silica particle generated in APS II system. The dotted lines correspond to the predictions of the numerical simulations. Again, satisfactory agreement was achieved. The bubble, which has a lower density, undergoing acceleration as it approaches the center of the converging ESZ, arriving more rapidly than the silica particle of higher density and inertia, which, accelerates more slowly.

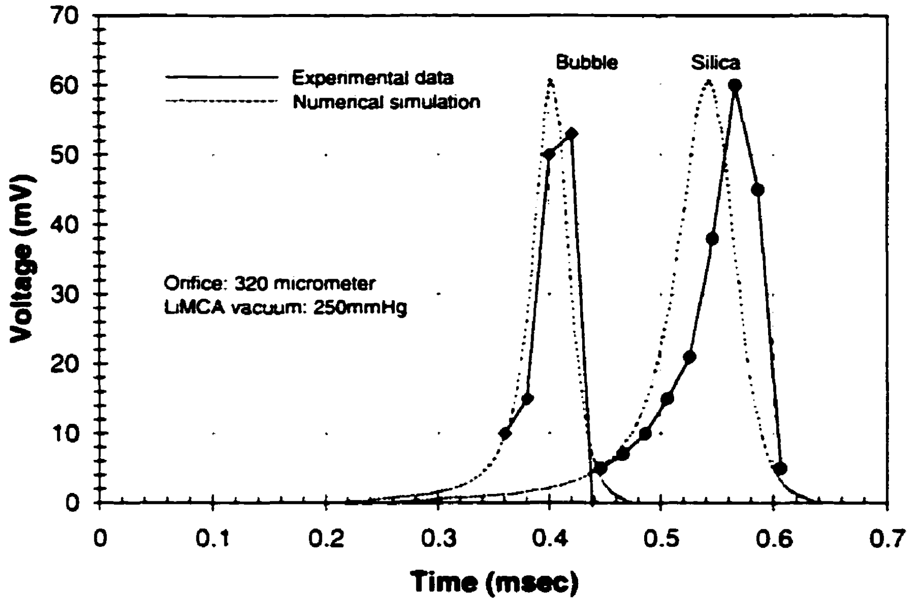

Figure 4.17 — Comparison of experimentally observed and numerically predicted particle signal shapes generated by different particles using the APS II system.

4.5 Conclusions

A mathematical model has been developed to describe the motion of particles in a water based LiMCA system — APS II system. The fluid field was obtained by solving the Navier-Stokes equations, and the trajectories of particles by equations for the motion of particles. These involve transient motion and incorporate the drag force, the added mass force, the fluid acceleration force, and the history force. The results show that the motion of the particles inside the parabolic shaped orifice are affected by particle density and particle size. Bubbles lead the fluid flow and travel faster than do latex microspheres which are slightly denser than the fluid and follow the fluid flow closely. Silica particles which are much denser than the fluid lag behind the flow and travel slower than latex microspheres, and much slower than bubbles. The relative velocity decreases with decreasing diameter of particles of the same density. The transient times of bubbles, latex microspheres and silica particles of different sizes in the APS II system were studied experimentally and theoretically by considering the noise voltage threshold of the ESZ, satisfactory agreement was achieved between the prediction and the experimental data. The results show that larger particles have longer transient times than do smaller ones. The transient times of bubbles are shorter than those of latex spheres, and much shorter than those of silica particles of the same size, and the difference of transient time is more pronounced for larger particles. The results prove that particle discrimination in water based LiMCA system is realizable.

References

[1] C. Carozza: Water Modeling of Particle Discrimination Using LiMCA Technology, Master Thesis, McGill University, 1999.

[2] D. Doutre and R.I.L. Guthrie: US Patent 4555662, 1985.

[3] W.H. Coulter: US Patent 112819, 1953.

[4] R.W. Beblois and C.P. Bean: Review of Scientific Instruments, 1970, vol. 41, pp. 909-915.

[5] R.W. Deblois, C.P. Bean, and R.K.A. Wesley: J. Colloid and Interface Sci., 1977, vol. 61, pp. 323-335.

[6] W.R. Smythe: Physics of Fluids, 1961, vol. 4, pp. 756-759.

[7] Xiaodong Shi: Updating Liquid Metal Cleanliness Analyzer (LiMCA) with Digital Signal Processing (DSP) Technology, Master Thesis, McGill University, 1994.

[8] G. Carayannis, F. Dallaire, X. Shi, and R.I.L. Guthrie: Symposium on Artificial Intelligence in Materials Processing Operations, Edmonton, 1992, pp. 227-244.

[9] A. Berlemont, P. Desjonqueres, and G. Gouesbet: Intl. J. Multiphase

Flow, 1990, vol. 16, pp. 19-34.

[10] T.R. Auton, J.C.R. Hunt, and M. Prud'homme: J. Fluid Mech.,1988, vol. 83, pp. 199-218.

[11] A.M. Fayon and J. Happel: AICHE Journal, 1960, vol. 6, pp. 55-58.

[12] R. Clift, J.R. Grace, and M.E. Weber: Bubbles, Drops, and Particles, Academic Press, Inc., New York, NY, 1978, pp. 112 and 225.

[13] J. Happel and H. Brenner: Low Reynolds Number Hydrodynamics, Printice-Hall, Inc., Englewood Cliffs, N.J., 1965, pp. 331.

[14] Aqueous Particle Sensor System — User's Manual, McGill Metals Processing Center, McGill University, 1996.

[15] C.E. Brennen: Cavitation, and Bubble Dynamics, Oxford University Press, New York, 1995, pp. 151.

CHAPTER 5

LiMCA in Molten Aluminum, Magnesium and Steel

In contrast to the APS II system, much stronger DC currents ($20-60A$) are applied in molten metal LiMCA systems, such as in aluminum, magnesium, and steel LiMCA systems. For molten aluminum, the LiMCA probe and operating procedures, including the conditioning operation, are well established. Efforts are now being devoted to study the possibility of particle discrimination and to extend this possibility to other applications, such as monitoring grain refining TiB_2 additions which are more conductive than molten aluminum. On the other hand, for molten magnesium and steel LiMCA systems, probes are still being developed and operation procedures are not yet established. A theoretical understanding of particle motion in the ESZ will facilitate the further development of LiMCA systems for molten metals. In this chapter, the particle motion and conditioning effect in aluminum LiMCA are studied employing the model used in Chapter 4 for the APS II system while accounting for the effect of the strong DC current. Subsequently, probes and operating conditions presently used in magnesium and steel LiMCA systems are analyzed, and design improvement are suggested.

5.1 LiMCA in Molten Aluminum

5.1.1 Introduction

One of the major concerns within aluminum industry is metal cleanliness. This relates to the number and size distribution of nonmetallic inclusions suspended within a melt. Inclusions whose diameter exceed $15\mu m$ in aluminum alloys are considered potentially detrimental. Their presence within a solidified product can lead to various types of defects which, in turn, can increase breakage or rejection rates. For example, the production of beverage can bodies is very sensitive to the presence of any inclusions within the can walls, whose dimensions are in the order of 80μm thick. Harder, larger inclusions (~ 60μm) can cause the metal to tear during deep drawing or the can to perforate when its content is pressurized.

Prior to the development of the LiMCA system[1,2] at McGill University in the early 1980's, it was not possible to measure inclusions, *in situ*, in liquid metals. Compared with other techniques, such as sedimentation, filtration and metallography, which require considerable amounts of labor and time, the LiMCA method has the advantage of providing not only information on the volume concentration of inclusions, but also on the size distribution of inclusions immediately and quantitatively. LiMCA has now been successfully used in quality and process control operations by leading aluminum companies, such as Alcan, Alusuisse, Alcoa, Reynolds and Pechiney.

The LiMCA technique is based on the Electric Sensing Zone (ESZ) principle,[3] in which a constant current is maintained between two electrodes that are separated physically by an electrically insulating sampling tube. A 300μm orifice within the non-conductive tube wall allows molten aluminum to flow into, and out of, the tube in a cyclic manner. This cycling sequence is controlled pneumatically by a differential pressure control system. When a non-conductive particle passes through the 300μm orifice, the resistance within the ESZ rises, causing a voltage pulse.

Since every particle registers a pulse when passing through the ESZ, and non-conductive particles of the same size but of different type give rise to voltage pulses of the same magnitude, it has previously been impossible to discriminate between different types of inclusions within a melt. In the aluminum industry, proprietary degassing units generate microbubbles and microdroplets of salt in molten aluminum. These microbubbles and microdroplets interfere with the LiMCA probe and its inclusion counts. In practice, microbubbles are relatively harmless compared to hard solid inclusions, and one therefore needs to distinguish one from the other in terms of a metal quality control point of view. In order to attempt particle discrimination, the analogue LiMCA system was updated with Digital Signal Processing (DSP) technology to determine whether more information could be extracted from particle signals besides pulse height. Using the McGill DSP,[4] each pulse was characterized by not only the peak height, but six other pulse parameters (start slope, end slope, time to maximum voltage, total signal duration, start time and end time). The studies in Chapter 4 using an aqueous based ESZ system confirmed that inclusions of different density could be discriminated on the bases of differently shaped voltage transients generated during their passage through the electric sensing zone. The possibility of inclusion discrimination using DSP technology for molten aluminum remains to be addressed.

Besides monitoring the quality of liquid metals in terms of the number and size distribution of non-conductive extraneous inclusions, the LiMCA technology has also been extended to the analysis of grain refining additions of titanium diboride (TiB_2) in aluminum silicon casting alloys.[5] Negative voltage pulses were observed using TiB_2 grain refiners containing less than 2% Ti, since TiB_2 is more conductive electrically than molten aluminum. For monitoring these more conducting particles, a relationship between the electrical conductivity of a particle and its induced signal needs to be defined.

Furthermore, the successful operation of LiMCA system depends on a procedure termed conditioning,[6] which involves passing a 200—300 Amperes electric current through the orifice for about 300 ms before taking a new sample when inflow rates decrease, or when voltage baseline instabilities are observed. In practice, the application of this high current, compared to the 60 Amperes working current, usually stabilizes the baseline of the signal, presumably by removing any obstructions to molten aluminum flowing through the orifice. The mechanism for this conditioning effect was a key to LiMCA's successful implementation in melts of aluminum but still needs to be clarified.

In section 5.1, the ESZ principle was described to predict the magnitude of resistive pulses generated by particles of arbitrary conductivity passing through the orifice. The mathematical model developed in Chapter 4 was modified by taking into account the electromagnetic force in order to study fluid flow within the ESZ and the dynamic motions experienced by particles of different conductivity, size and density in aluminum LiMCA. The mechanism of the conditioning operation was discussed based on the effect of electric current on the fluid flow within the ESZ. The dynamic processes of non-conductive particles, together with an Ohmic model of the ESZ,[7] which correlates ESZ resistance change with particle position inside the ESZ, were used to predict the transient times and signal shapes for microbubbles and solid particles in molten aluminum. Based on these predictions, the feasibility for particle discrimination via DSP technology is discussed.

5.1.2 Mathematical Model and Numerical Methods

The present study considered the dynamic motions of particles entrained within molten aluminum flowing through the electric sensing zone, and corresponding changes in electrical resistance within the ESZ. Two dimensional simulation using a cylindrical coordinate system was employed. As shown in Figure 5.1, the position of the particle is designated as (x_p, y_p), where x and y are the respective axial and radial coordinates. The properties of molten aluminum and particles used in this study as well as typical operating conditions for the LiMCA system in molten aluminum are given in Table 5.1.

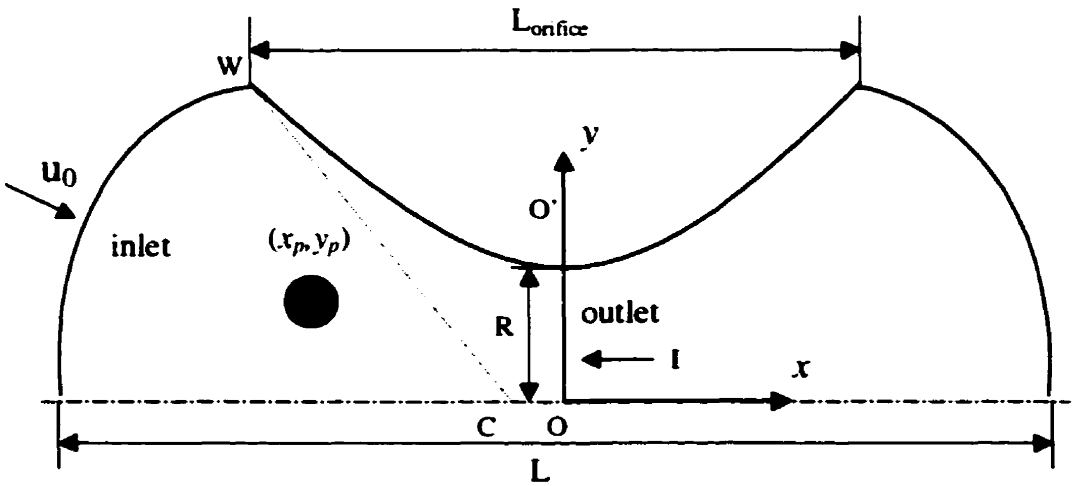

Figure 5.1 — Computational domain employed for aluminum LiMCA.

Table 5.1 Physical properties of liquid aluminum and particles used in this study as well as typical operating conditions of LiMCA in molten aluminum

Liquid aluminum:			
Temperature (^{0} C)		700	
Density (kg/m^3)		2.368×10^3	
Electrical resistivity (Ωm)		0.25×10^{-6}	
Viscosity (kg/ms)		1.63×10^{-3}	
Particles:			
	Microbubble	TiB_2	Alumina
Density (kg/m^3)	0	4.5×10^3	3.8×10^3
Electrical resistivity(Ωm)	Non-conductive	0.09×10^{-6}	Non-conductive
Typical operating conditions:			
Orifice size (mm)			0.3
Coefficient of the polynomial representing parabolic orifice			2.15
Electric current (Ampere)			60
Pre-amplifier gain			1000
Noise threshold set (μV)			± 15

5.1.2.1 Electric Sensing Zone (ESZ) principle

LiMCA is based on the electric sensing zone principle. The central theoretical problem of the principle is determining the resistance change of the ESZ by the insertion of an inclusion inside.

Maxwell[8] showed that the resistance of the ESZ with an inclusion inside is given by:

$$R = \rho_{eff} \int \frac{dx}{A(x)} \qquad (5.1)$$

where $A(x)$ is the area of the cross-section of the ESZ and ρ_{eff} is the effective electrical resistivity of a compound conducting media. The media is composed of one continuous material of resistivity ρ_e and sparsely distributed spherical inclusions of resistivity ρ_{e_p}. When the particles are sufficiently scattered so that the distance between each other is large enough so as to not disturb the course of the surrounding current, then ρ_{eff} can be expressed as:

$$\rho_{eff} = [\frac{2\rho_{e_p} + \rho_e + f(\rho_{e_p} - \rho_e)}{2\rho_{e_p} + \rho_e - 2f(\rho_{e_p} - \rho_e)}]\rho_e \qquad (5.2)$$

where f is the volume fraction of inclusions contained within the ESZ.

In a cylindrical orifice used in the theoretical pulse calculation, the resistance of the ESZ without the introduction of inclusion is given by :

$$R_1 = \frac{4\rho_e L}{\pi D^2} \qquad (5.3)$$

where D and L are the diameter and length of the ESZ, respectively.

If an inclusion of diameter d is introduced, then the volume fraction of this inclusion to the ESZ volume is:

$$f = \frac{2d^3}{3D^2L} \tag{5.4}$$

The resistance of the ESZ with a small inclusion within it is given by:

$$R_2 = \frac{4\rho_{eff}L}{\pi D^2} \tag{5.5}$$

Thus, the change in resistance

$$\Delta R = R_2 - R_1 = \frac{4L}{\pi D^2}(\rho_{eff} - \rho_e) \tag{5.6}$$

is determined by the dimensions of the orifice, the size of the particle, and the electrical resistivity of both the particle and the liquid media.

5.1.2.1.1 Non-conductive particle ($\rho_{e_p} >> \rho_e$)

For a non-conductive inclusion, the expression for ρ_{eff} can be approximated as:[9]

$$\rho_{eff} = \frac{1}{2}\left(\frac{2+f}{1-f}\right)\rho_e \tag{5.7}$$

Expanded into a power series, Equation (5.7) becomes

$$\rho_{eff} = \rho_e(1 + \frac{3}{2}f + \frac{3}{2}f^2 + \cdots) \qquad (5.8)$$

Since f is very small, present calculations only consider the first two terms and ignore the higher order ones. Substituting Equations (5.4) into (5.8) and then into Equation (5.6):

$$\Delta R_{non-conductive} = \frac{4\rho_e d^3}{\pi D^4} \qquad (5.9)$$

This expression is used in the Coulter Couter[3] for aqueous system and the LiMCA[6] for liquid metal system for non-conducting particle measurement.

5.1.2.1.2 Perfectly conducting particle ($\rho_{e_p} << \rho_e$)

For a perfectly conducting particle, the expression for ρ_{eff} can be approximated as:

$$\rho_{eff} = \frac{1}{2}(\frac{1-f}{1+2f})\rho_e \qquad (5.10)$$

Expanded into a power series, Equation (5.10) becomes

$$\rho_{eff} = \rho_e(1 - 3f + 6f^2 + \cdots) \qquad (5.11)$$

Ignoring higher order terms, Equations (5.11) is substituted into Equation (5.6):

$$\Delta R_{conductive} = -\frac{8\rho_e d^3}{\pi D^4} \qquad (5.12)$$

It can be seen that the voltage pulse generated by a perfectly conducting particle is negative, opposite to that of a non-conductive particle, and has a peak resistive height two times that of a non-conductive particle of the same size.

5.1.2.1.3 TiB_2 particle in molten aluminum

In accordance with the procedure used in deriving the resistance change of the ESZ with a non-conductive or perfectly conducting particle inside, the change in the resistance of ESZ in molten aluminum with a TiB_2 particle inside can be obtained, for the properties shown in Table 5.1, as follows:

$$\Delta R_{TiB_2} = -\frac{32}{43}\left(\frac{4\rho_e d^3}{\pi D^4}\right) \qquad (5.13)$$

It is seen that the voltage pulse should be negative because TiB_2 is more conductive than molten aluminum, and that the height of the voltage peak should be about three fourths of that for a non-conductive particle of the same size.

5.1.2.2 The flow field in the ESZ

In order to predict the flow behavior of molten aluminum entering the converging section of a typical sensing zone, the metal was taken to be incompressible, with constant properties, and the flow was considered laminar and steady, in keeping with practical operating conditions. For LiMCA systems, the orifice (ESZ) Reynolds number is about 1700 based on orifice diameter. Given these assumptions, the problem may be stated by the continuity and Navier-Stokes equations (2.1) and (2.2). Owing to the high electrical current densities involved with LiMCA systems, the Lorentz force $\vec{F}_e(F_{e_x}, F_{e_r})$ constituting a body force is important and needs inclusion in the latter equation. The solution of Lorentz force is described as Equations (2.3) — (2.7).

The computational domain is shown in Figure 5.1. The inlet boundary was taken to be a spherical cap centered at point C, this being the intersection of the central axis and the cone tangential to the ESZ wall at the edge E. The outlet boundary for the flow of the fluid and electricity was taken to be the central cross section (throat) of the orifice. The boundary conditions applied were zero-slip along and zero electric current flux across the insulating ESZ wall. At the inflow boundary, the fluid velocity and the electric current density were taken to be both uniform and normal to the spherical cap boundary. At the outflow boundary, the electrical potential was assumed constant, and the exit fluid velocity gradient zero. Iterative corrections were made in the numerical calculations to match the mass outflow rate with the inflow rate, so as to respect continuity. Beyond the throat of the ESZ, jet flow was assumed, that is, the fluid flow ignores the diverging sidewalls on the exit side of the ESZ, and simply passes on through with an axial velocity distribution of the same as that at the throat.

5.1.2.3 The equation of motion of particles

As described in Chapter 2, in conventional hydrodynamics, high Reynolds number motions of a spherical particle in a fluid which is also in motion itself can be represented by the following equation:[10,11]

$$m_p \frac{d\vec{u}_p}{dt} = \frac{1}{2} C_{Dstd} \pi a^2 \rho_f \left|\vec{u} - \vec{u}_p\right| (\vec{u} - \vec{u}_p) + \frac{1}{2} m_f \left(\frac{D\vec{u}}{Dt} - \frac{d\vec{u}_p}{dt}\right) + m_f \frac{D\vec{u}}{Dt}$$
$$+ 6a^2 (\pi \mu_f \rho_f)^{1/2} \int_0^t \frac{d(\vec{u} - \vec{u}_p)/d\tau}{(t-\tau)^{1/2}} d\tau + (m_p - m_f)\vec{g} \qquad (5.14)$$

where $\vec{u}_p(u_p, v_p)$ and $\vec{u}(u, v)$ represent the respective instantaneous velocity of the particle and the undisturbed fluid velocity at the center of the particle that would apply in the absence of that particle.

As to the motion of an inclusion flowing with liquid aluminum through the ESZ, the electromagnetic force on the particle[12] has to be included. Therefore, in this study, predictions on the trajectories of rigid, spherical particles of arbitrary conductivity were made, based on the following equation:

$$\rho_p V_p \frac{d\vec{u}_p}{dt} = \frac{1}{2} C_{Dstd} \pi a^2 \rho_f |\vec{u} - \vec{u}_p| (\vec{u} - \vec{u}_p) + \frac{1}{2} \rho_f V_p \left(\frac{D\vec{u}}{Dt} - \frac{d\vec{u}_p}{dt}\right) + \rho_f V_p \frac{D\vec{u}}{Dt}$$
$$+ 6a^2 (\pi \mu_f \rho_f)^{1/2} \int_0^t \frac{d(\vec{u} - \vec{u}_p)/d\tau}{(t-\tau)^{1/2}} d\tau + V_p(\rho_p - \rho_f)\vec{g} - \frac{3(1-\chi)}{4} V_p \vec{F} \quad (5.15)$$

where ρ_p and V_p are the density and volume of the particle, $\vec{F}$ represents the electromagnetic force per unit volume of the fluid at the position of the particle. $\chi = \dfrac{3\sigma_{e_p}}{\sigma_{e_p} + 2\sigma_e}$, represents the dependence of the electromagnetic force acting on a particle of electrical conductivity (σ_{e_p}) and fluid conductivity (σ_e). As such, χ is zero for non-conductive particles, 3 for perfectly conducting particles and around 1.77 for a TiB_2 inclusion in molten aluminum. In this study, a microbubble was considered to behave as a rigid spherical particle, and its motion was also represented by Equation (5.15).

The presence of a solid surface in the vicinity of a moving particle will affect the drag force on the particle or inclusion. In this study, the axial drag force wall effect was approximated using the equation developed by Fayon and Happet,[13] while the wall effects in the radial direction were estimated using tabulated correction factor for the drag force on a solid particle moving perpendicular to a plane wall.[14]

5.1.2.4 Ohmic model of ESZ

The electrical resistance of the ESZ without a particle inside is given by Ohm's law:

$$R_{ESZ} = \rho_e \int \frac{dx}{A(x)} \tag{5.16}$$

where ρ_e is the electrical resistivity of the fluid inside the ESZ, $A(x)$ is an equipotential surface, and x is the axial distance with respect to the central vertical plane of the ESZ as shown in Figure 5.1.

The calculated electrical potential field (Figure 5.3(a)) shows that the equipotential surfaces inside the ESZ are quite flat, especially near the middle of the orifice where the minimum diameter is reached. Therefore, the surfaces $A(x)$ were chosen to be planar, perpendicular to the axis of the orifice in order to simplify the computation. When a non-conductive spherical particle is introduced into the orifice, the generated resistive pulse is given by:

$$\Delta R = \frac{\rho_e}{\pi} \int \frac{r^2(x)dx}{R^2(x)(R^2(x) - r^2(x))} \tag{5.17}$$

where $R(x)$ and $r(x)$ are the radii of the cross-section of the orifice and the inclusion, respectively. The numerical integration of Equation (5.17) was performed, with respect to x coordinate, every $1\mu m$ according to:

$$\Delta R = \sum_{x_p - a}^{x_p + a} \frac{\rho_e \Delta x}{\pi} \frac{r^2(x)}{R^2(x)(R^2(x) - r^2(x))} \qquad (5.18)$$

where x_p is the axial position of the particle. Based on Equation (5.18), ESZ resistance variation with a spherical particle of different diameter passing through the orifice can be obtained.

5.1.2.5 Numerical methods

As shown in Figure 5.2, a non-orthogonal, boundary-fitted grid of variable spacing was adopted in this study to enhance the accuracy of the calculation. The conservation equations for mass and momentum with the

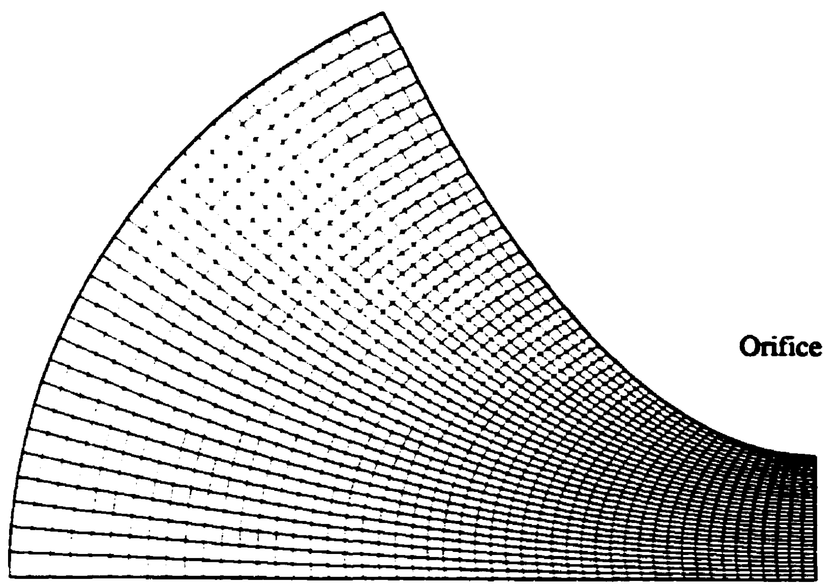

Figure 5.2 — Non-orthogonal, boundary-fitted grid used in this study.

boundary conditions, and Equation (5.15) for the motion of particles were solved using the same methods as described In Chapter 2. The time step used in solving particle motion equation, Δt, is set as 10^{-5} ms to maintain the accuracy of the calculation.

5.1.3 Results and Discussion

5.1.3.1 Fluid flow and electromagnetic fields

The calculation of the fluid flow and electromagnetic fields inside the ESZ for aluminum melts is based on probe dimensions, operating conditions and the physical properties of the melt listed in Table 5.1. The distributions of electrical potential, electric current density, self-induced magnetic flux density, and specific electromagnetic force within the ESZ, are shown in Figures 5.3(a) through 5.3(d), respectively. As can be seen from Figure 5.3(a), the isopotential along the central cross section of the orifice has its highest value, where the current flow from the inner positive electrode enters the throat of the ESZ. The electrical potential gradient is very high near the throat of the orifice and drops gradually towards the entrance or exit of the orifice. The voltage drop over the whole orifice is approximately 0.105 volts. This potential distribution gives rise to the electric current density shown in Figure 5.3(b). Corresponding to the potential distribution, the current density is very high near the central region of the orifice, and decreases with increasing distance from the throat. The self-induced magnetic flux within the orifice (Figure 5.3(c)) increases from the central axis to the wall. The interaction of the electric current and its induced magnetic flux results in an electromagnetic force whose distribution is shown in Figure 5.3(d). It can be seen that the stronger electric current density and magnetic flux density near the throat of the orifice give rise to much stronger electromagnetic forces there than in the entrance or exit regions. The electromagnetic force is high near the wall, but decreases with decreasing distance from the central axis, becoming virtually and theoretically zero along the central axis. In this

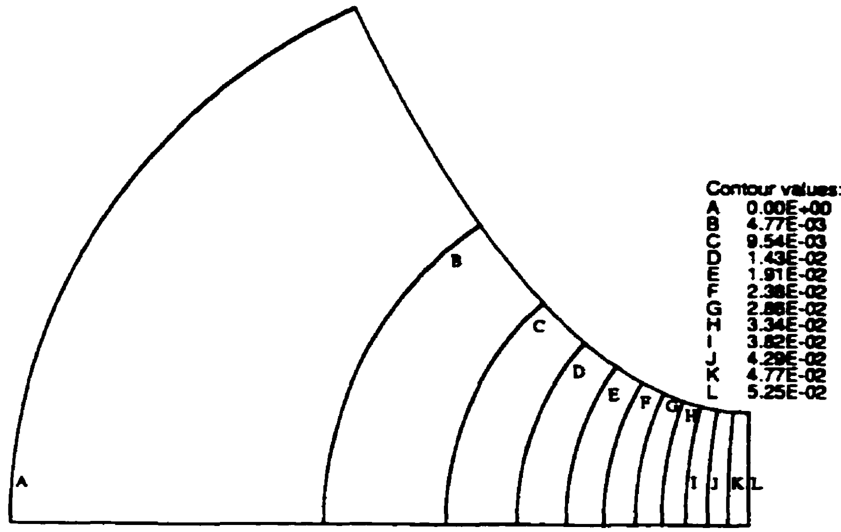

(a) Electrical potential (volt)

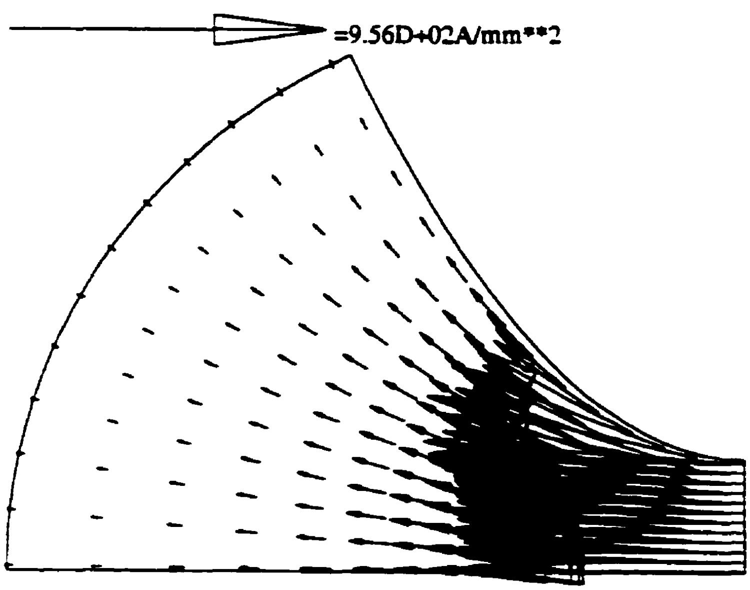

(b) Electric current density

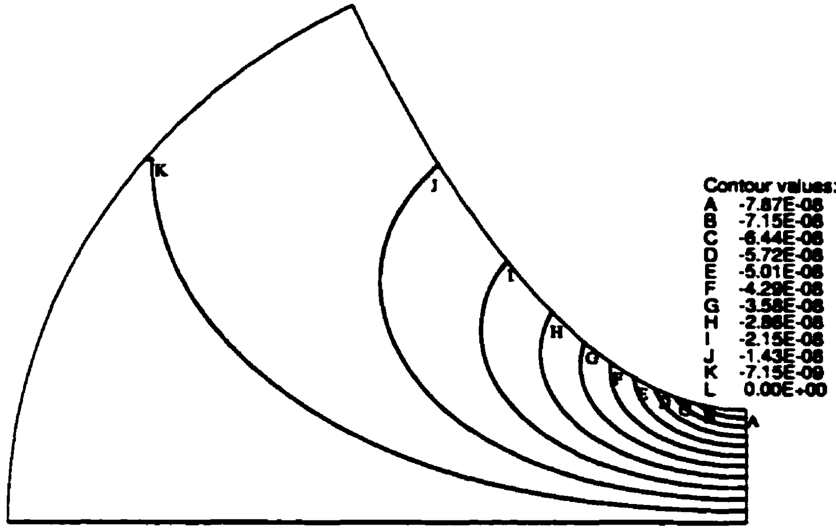

(c) Self-induced magnetic flux density ($Weber/mm^2$)

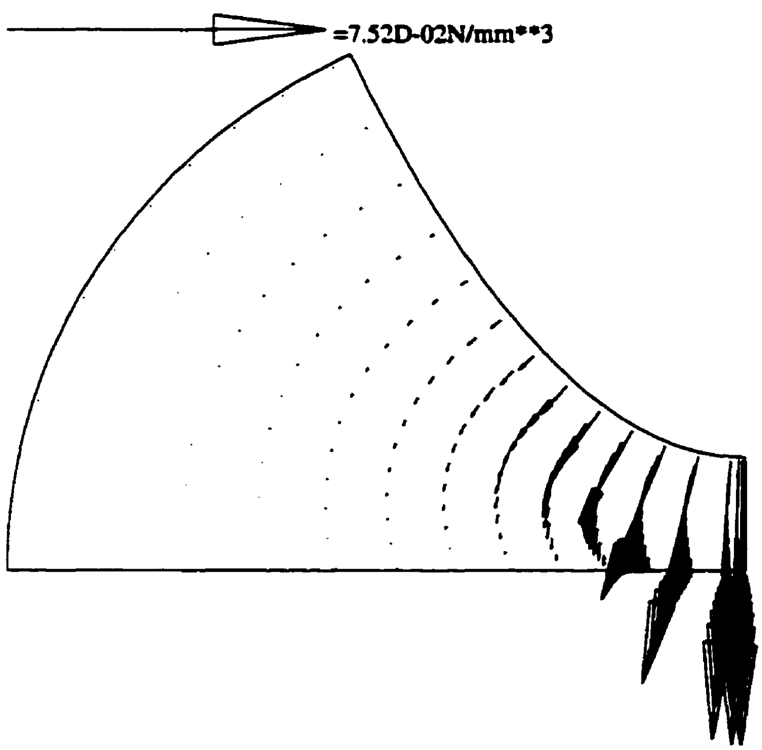

(d) Specific electromagnetic force

Figure 5.3 — Distribution of electrical potential, electric current density, self-induced magnetic flux density, and specific electromagnetic force within a $300\mu m$ orifice of aluminum LiMCA.

force field, particles suspended in molten aluminum that are electrically non-conductive experience a force in the opposite direction, and are squeezed out of the molten metal, while particles that are electrically more conductive than molten aluminum experience a force in the same direction, and are pushed towards the central axis.

The predicted flow field for a $300\mu m$ orifice with a mean fluid velocity at the throat of $u_m = 4.0 m/s$ is shown in Figure 5.4(a). Its axial and radial velocity component profiles at three different positions within the ESZ are illustrated in Figures 5.4(b) and 5.4(c), respectively. It can be seen that the axial velocity is very uniform at each section along the ESZ, while the radial velocity, which is negative, has a maximum near the wall and damps out towards the central axis at each cross section. Moreover, the axial velocity at the throat of the ESZ is much higher than the radial velocity, proving that it is reasonable to assume that beyond the throat of the orifice, the jet flow has only axial velocity and the same velocity profile as that at the throat.

5.1.3.2 Particle motion

Once the fluid flow and the electromagnetic fields within the ESZ are known, Equation (5.15) can be solved to predict the motions of particles of different conductivity, density and size.

5.1.3.2.1 Effect of particle conductivity

The effect of particle conductivity on the motion of particles was studied for $60\mu m$ diameter particles with the same density as molten aluminum. Three electrical resistivities of $\rho_{e_p} >> \rho_e$, $\rho_{e_p} = 0.09 \times 10^{-6} \Omega m$ and $\rho_{e_p} << \rho_e$ were chosen. These represent non-conductive, TiB_2 and perfectly conducting particles, respectively. The results are shown in

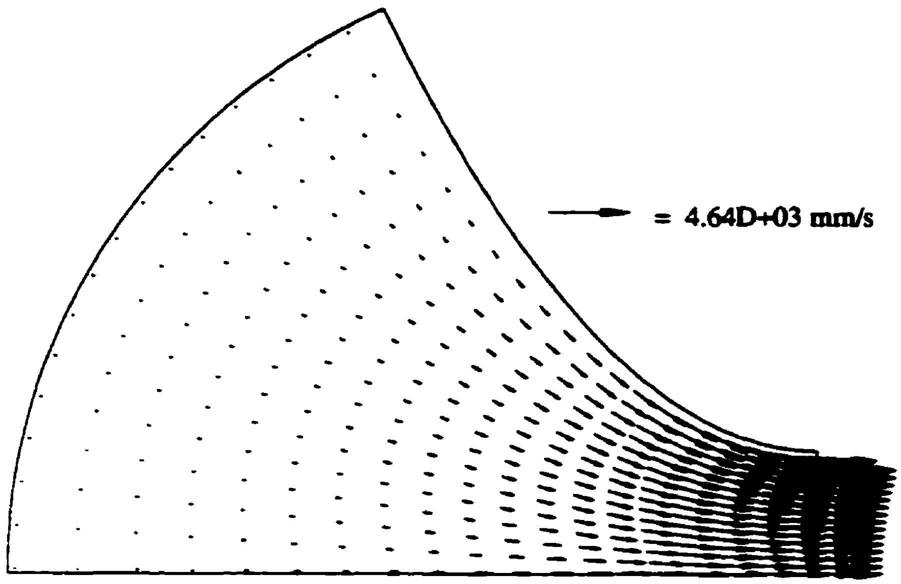

(a) Velocity vectors

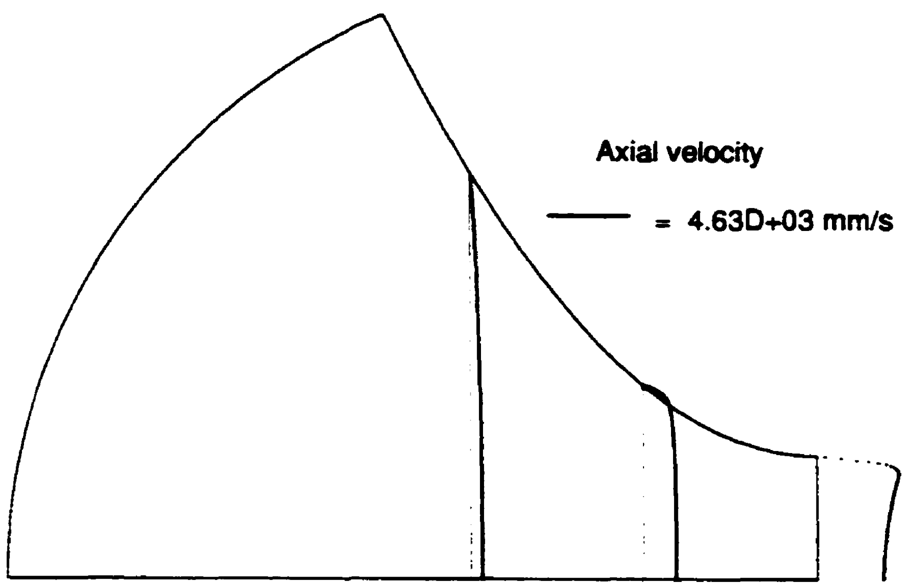

(b) Axial velocity profiles

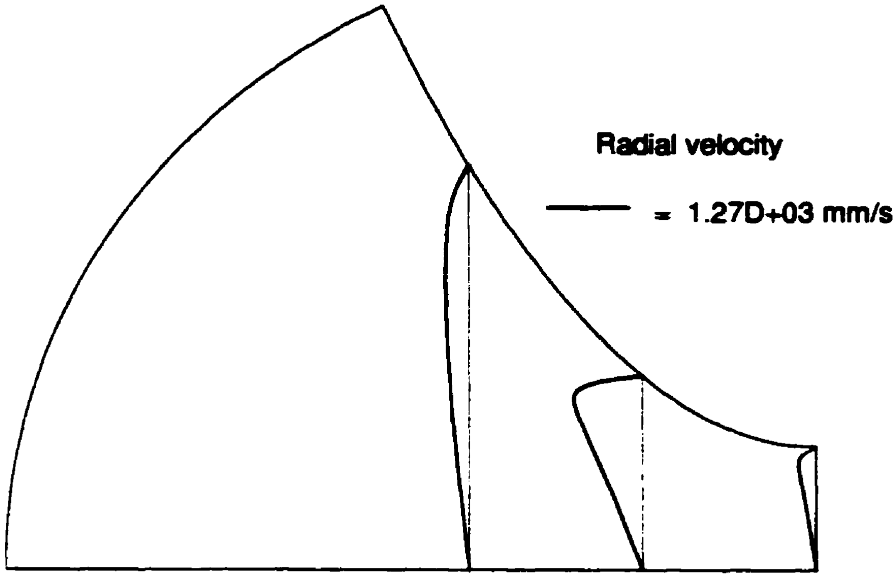

(c) Radial velocity profiles

Figure 5.4 — Velocity vectors and the axial and radial velocity profiles at the cross sections of $x/L_{orifice} = 0$, $-\frac{1}{6}$, and $-\frac{1}{3}$ in an ESZ of $300\mu m$ with $u_m = 4.0 m/s$.

Figure 5.5 for particles flowing into the ESZ from an entry point of $y_0/R = 2.87$. It can be seen that the more conductive the particle, the closer the trajectory to the central axis. This phenomenon can be understood by examining the effect of particle conductivity on the electromagnetic force. Figure 5.6 shows the electromagnetic forces in the x (Figure 5.6(a)) and y directions (Figure 5.6(b)) acting on the particles corresponding to Figure 5.5 as they travel inside the ESZ. Generally speaking, the electromagnetic forces in the y direction are much stronger than those in the x direction. In both directions, the electromagnetic forces on non-conductive particle (Figure 5.6a(i) and Figure 5.6b(i)) are in the opposite direction to those on particles which are more conductive than molten aluminum (Figures 5.6a(ii) and (iii), Figures 5.6b(ii) and (iii)). For conductive particles, the electromagnetic force in the y direction is towards the central axis of the orifice, and the more conductive the particle, the stronger the force. This is the reason why a perfectly conductive particle (Figure 5.5(iii)) moves faster towards the central axis of the orifice than does the less conductive particle (Figure 5.5(ii)). In fact, before passing through the ESZ, the perfectly conductive particle is predicted to have traversed the central axis. Once across the central axis, the electromagnetic force in the y direction is opposite to the particle motion, therefore, the electromagnetic force on a conductive particle tends to keep it moving along the central axis. On the contrary, the electromagnetic force on a non-conductive inclusion is towards the sidewall of the orifice. This explains the slower motion of the non-conductive particle in the y direction (Figure 5.5(i)) flowing in the converging region of the orifice and then turning to the ESZ wall after moving beyond the throat of the orifice.

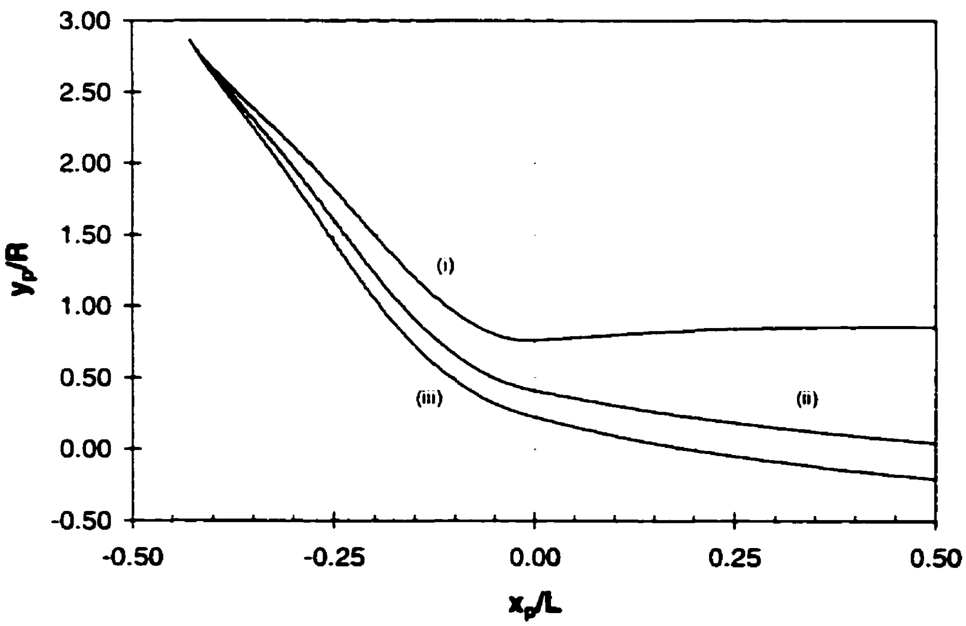

Figure 5.5 — Effect of particle conductivity on the motion of particles.

(i) Non-conductive; (ii) $\rho_{e_p} = 0.09 \times 10^{-6}\,\Omega m$; (iii) Perfect conductive.

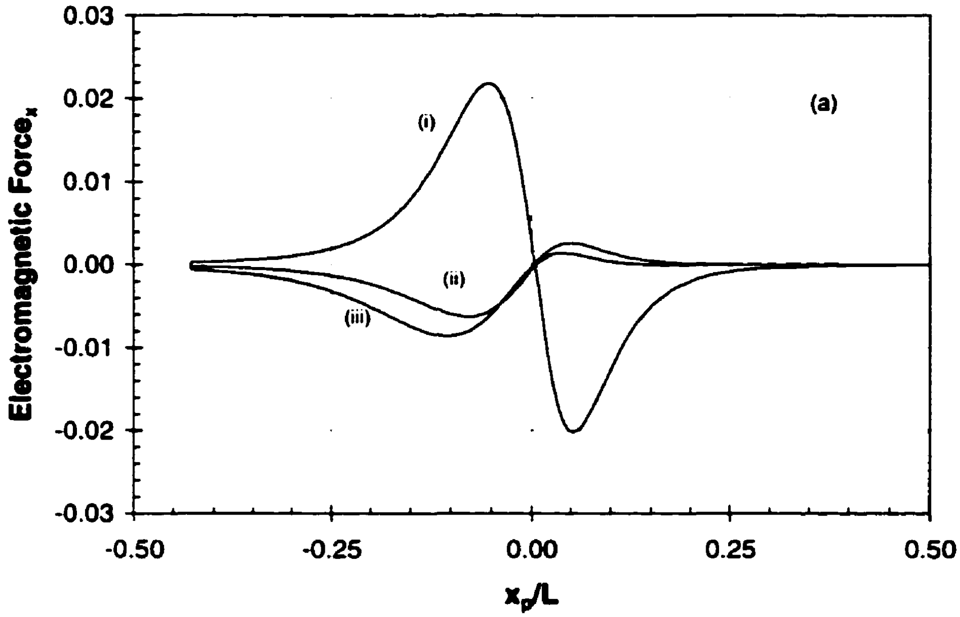

(a) Axial component of electromagnetic force

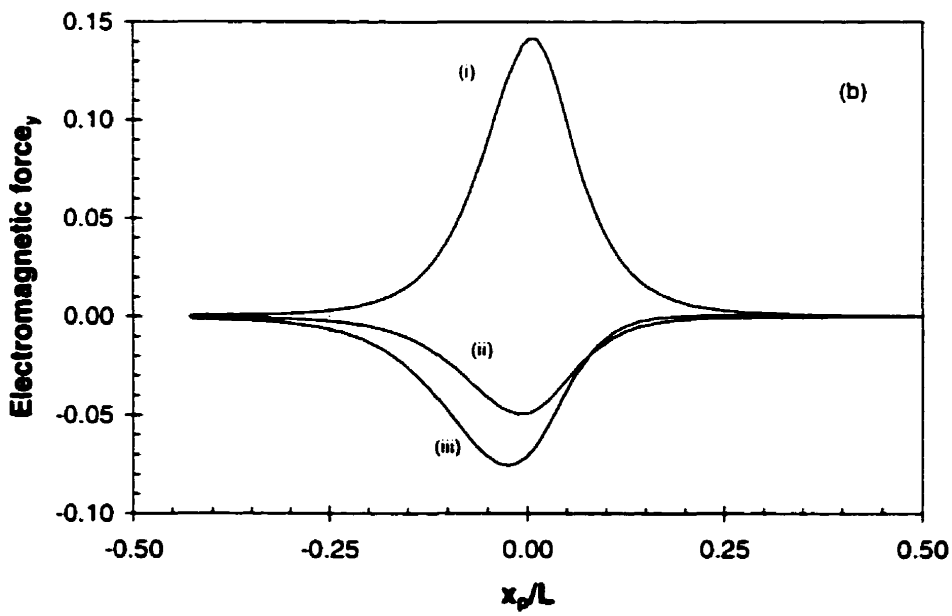

(b) Radial component of electromagnetic force

Figure 5.6 — Electromagnetic force on particles of different conductivity.

(i) Non-conductive; (ii) $\rho_{e_p} = 0.09\times10^{-6}\,\Omega m$; (iii) Perfect conductive.

5.1.3.2.2 Effect of particle density

The effect of particle density on the motion of particles was studied for $60\mu m$ diameter particles with densities of $0 kg/m^3$ and $3.8\times10^3 kg/m^3$, representing microbubbles and inclusions of alumina respectively. The results are shown in Figure 5.7 for particles entering the ESZ from an entry point of $y_0/R = 2.0$. It can be seen that particles with higher density take longer to pass through the ESZ, and this is true for both conductive and non-conductive particles. Moreover, the difference in pass-through times is not significant for particles of different conductivity but of the same density. This phenomenon is the result of the fact that the fluid acceleration force and the electromagnetic force in the converging region of the ESZ induce different relative velocities for particles of different densities. Figure 5.8 (Figure 5.8(a) for non-conductive, and 5.8(b) for perfect conductive particles) shows the velocity and the relative velocity

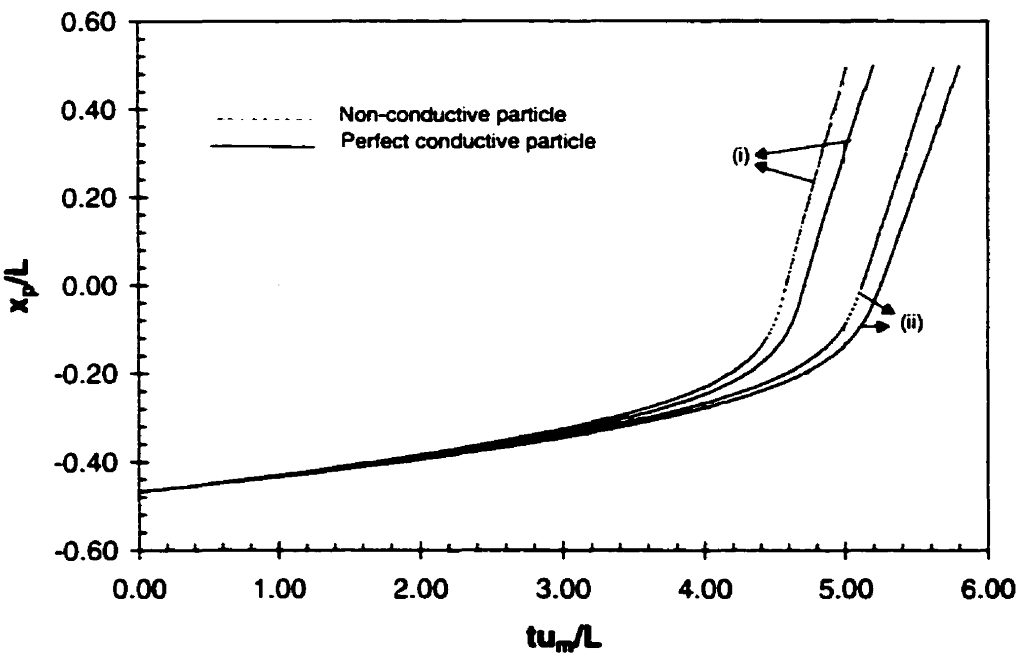

Figure 5.7 — Effect of particle density on the motion of particles.
(i) $\rho_p/\rho_f = 0$; (ii) $\rho_p/\rho_f = 1.6$.

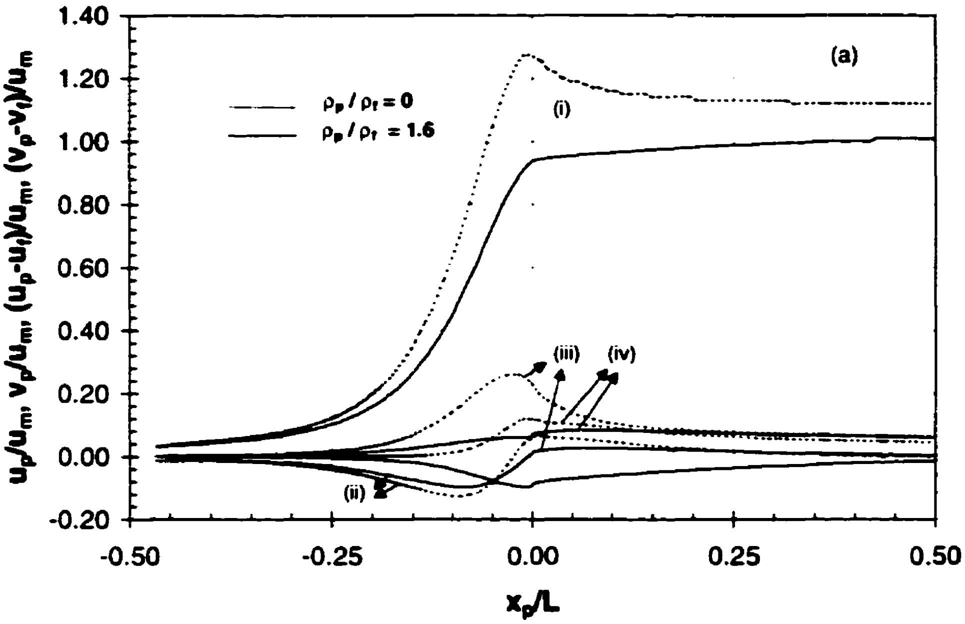

(a) Non-conductive particles

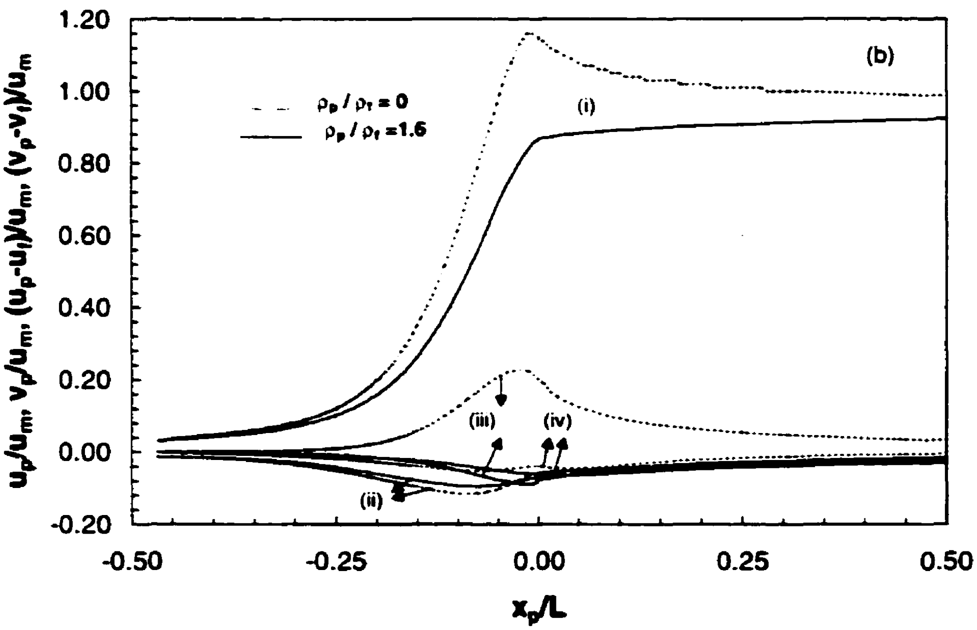

(b) Perfect conductive particles

Figure 5.8 — Effect of particle density on the velocity and relative velocity.
(i) Axial velocity; (ii) Radial velocity; (iii) Relative axial velocity;
(iv) Relative radial velocity.

corresponding to the particle motions shown in Figure 5.7. As expected, during the whole process of particle motion through the ESZ, bubbles travel faster (Figure 5.8a(i) and Figure 5.8b(i)) in the axial direction than alumina particles. In the converging region of the ESZ ($x_p/L \leq 0$), particles of all densities accelerate in the axial direction, while beyond the throat, they try to follow the fluid flow, $u_p/u_m \to 1.00$. The positive value of the relative axial velocity for bubbles implies that the bubbles move faster than the fluid in this direction. For alumina particles, which are denser than the aluminum melt, the relative axial velocity is negative, meaning that these inclusions move slower than the fluid in this direction.

The situation in the axial direction which was discussed above is the same as that in water based LiMCA system (Chapter 4), where the electromagnetic force is negligibly small. The reason is that in the aluminum LiMCA, the electromagnetic force in the axial direction is still very small compared with the strong fluid acceleration force. However, in the radial direction, the effect of the electromagnetic force is significant. As shown in Figure 5.8a(iv), the non-conductive particles lag behind the fluid flow in the radial direction for both bubbles and heavy alumina particles, resulting from the towards-wall electromagnetic force in the radial direction. However, particles which are more conductive than molten aluminum lead the fluid flow in the radial direction, irrespective of the density, because the electromagnetic force on conductive particles is towards the central axis of the orifice. Due to the difference in electromagnetic force on particles of different conductivity, non-conductive particles flow through the ESZ along the trajectories closer to the wall than conductive particles. The axial fluid velocity near the wall is slightly higher than that near the central axis (Figure 5.4(b)), which is responsible for the shorter time taken by non-conductive particles to flow through the ESZ.

5.1.3.2.3 Effect of particle size

The effect of inclusion size on the motion of particles was studied for particles of $40\mu m$ and $100\mu m$ diameter. This particle size effect was studied for both conductive and non-conductive particles of $0 kg/m^3$ and $3.8\times10^3 kg/m^3$. The simulation results are shown in Figure 5.9. Again, particles of higher density (Figure 5.9a(ii) for non-conductive, while 5.9b(ii) for perfect conductive) take longer time to flow through the ESZ than those of lower density (Figure 5.9a(i) and 5.9b(i)). However, the size effects depend on the particle density. When the density of the particle is higher than that of the fluid, the larger the particle, the longer it takes to flow out of the ESZ. In contrast, when the density of the particle is smaller than that of the fluid, the larger the particle, the shorter it takes to flow out of the ESZ. This phenomenon is related to the different particle size dependence of the relative velocity developed inside the ESZ on the particle density. For bubbles, the axial velocity of size $100\mu m$ is larger than that of size $40\mu m$, and correspondingly larger bubbles assume larger

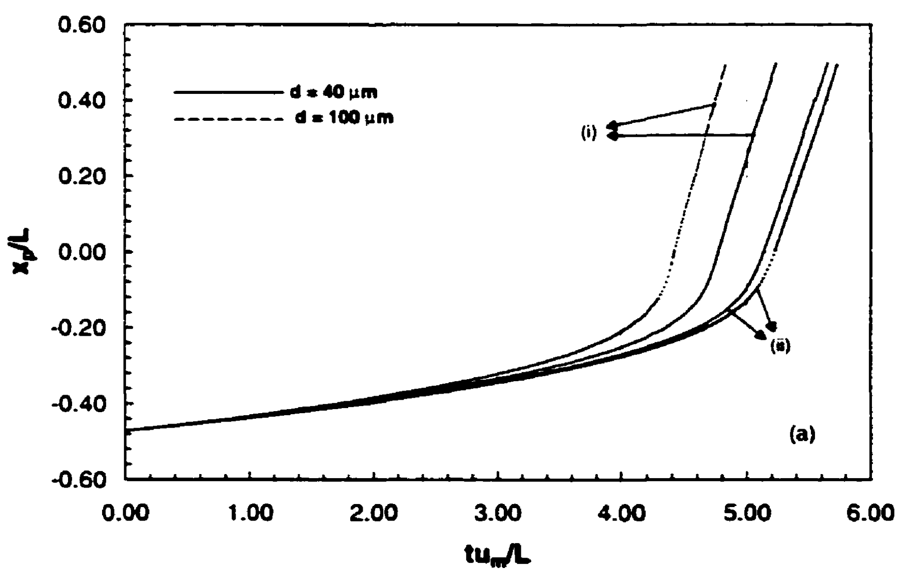

(a) Non-conductive particles

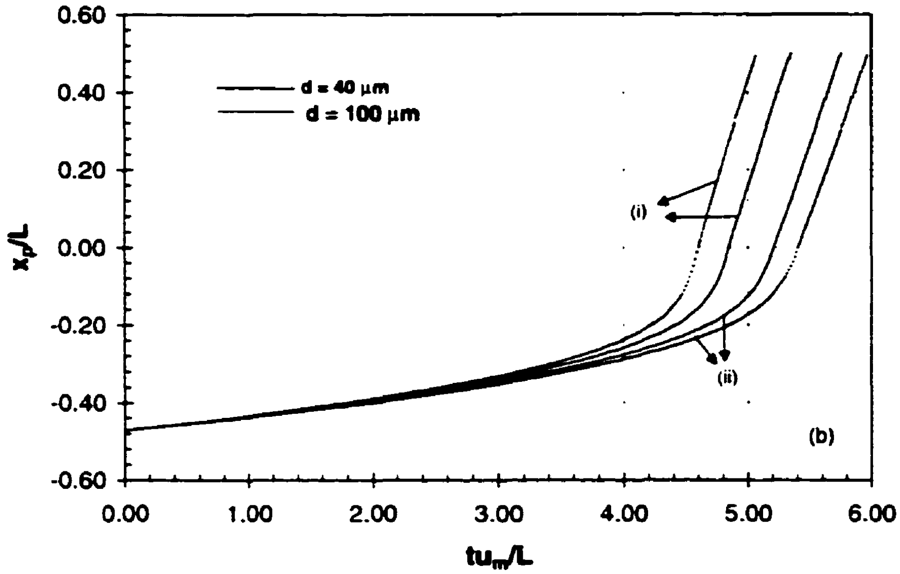

(b) Perfect conductive particles

Figure 5.9 — Effect of particle size on the motion of particles.

(i) $\rho_p/\rho_f = 0$; (ii) $\rho_p/\rho_f = 1.6$.

positive relative velocity, proceeding the fluid flow more than smaller bubbles. On the contrary, larger denser particles accelerate more slowly than their smaller counterparts, and consequently acquire larger negative relative velocities, lagging further behind the fluid flow.

5.1.3.2.4 Effect of electric current

The effect of electric current on the motion of particles was studied for non-conductive and conductive particles of size $60\mu m$ and the same density as molten aluminum. The results for particles flowing from an entry point of $y_0/R = 2.87$ into an ESZ with 40 and 60 amperes electric currents are shown in Figure 5.10. It is seen that the trajectories of the non-conductive particles become even closer to the ESZ wall, while those for perfect conductive particles even closer to the central axis when the electric current increases from 40 to 60 amperes. The reason is that increasing the electric current increases the electromagnetic force on the particles. The radial electromagnetic force directs non-conductive particles towards the ESZ sidewall, but towards the central axis for particles more conductive to molten aluminum.

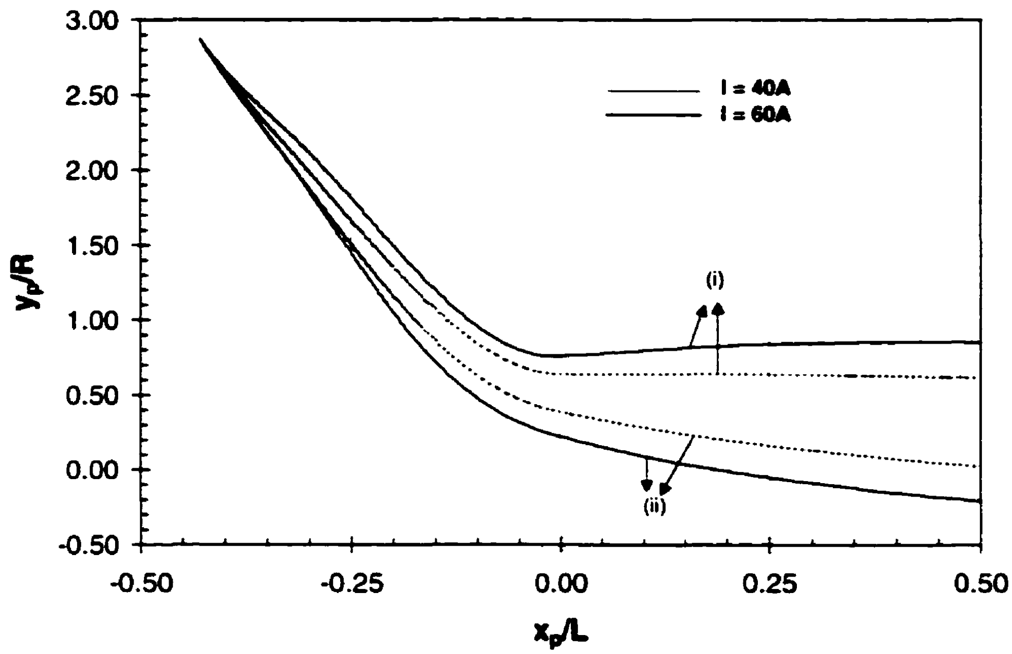

Figure 5.10 — Effect of electric current on the motion of particles.
(i) Non-conductive; (ii) Perfect conductive.

5.1.3.2.5 Effect of fluid velocity within the ESZ

The fluid velocity within the ESZ is characterized by the mean velocity at the throat of the orifice, u_m. The effect of u_m on the motion of particles was studied on non-conductive and perfect conductive particles of size $60\mu m$ and same density as molten aluminum. The results for the particles flowing into the ESZ from an entry point of $y_0/R = 2.0$ are shown in Figure 5.11. It is seen that non-conductive particles flow through the throat of the orifice at positions closer to the ESZ wall, while perfectly conductive particles move closer to the central axis when the fluid velocity u_m decreases from $4m/s$ to $3m/s$. This is due to the fact that particles take longer time to pass through the orifice when the fluid velocity decreases, leaving more time for the electromagnetic force to prove effect. At the entrance region, regardless of the conductivity of the particle, the trajectories in the case of $u_m = 3m/s$ are closer to the ESZ wall due to the decreased fluid acceleration force in the radial direction accompanying the lower fluid velocity.

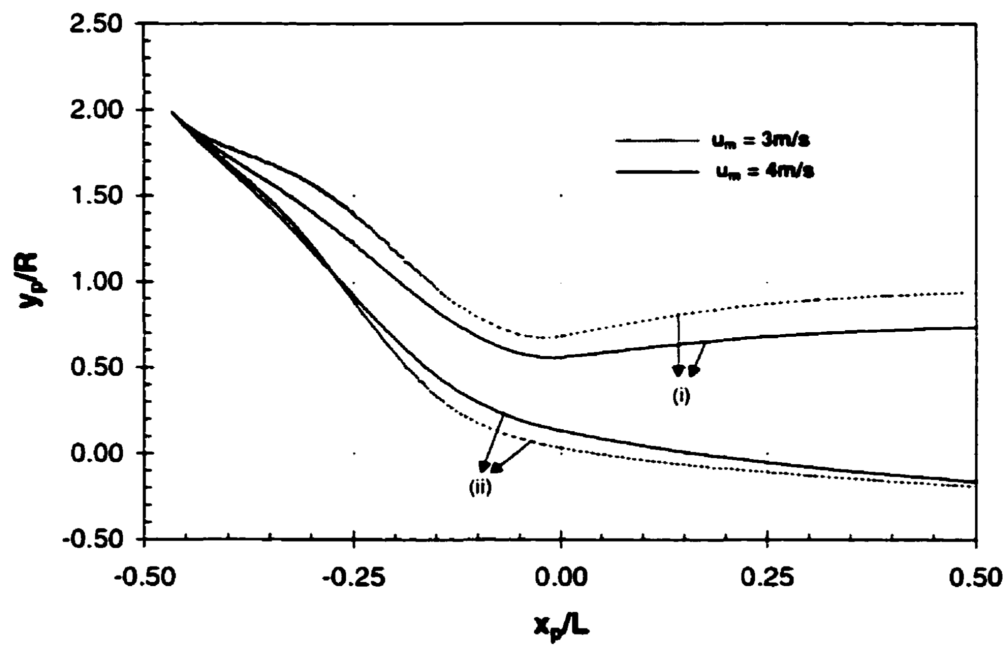

Figure 5.11 — Effect of mean fluid velocity on the motion of particles.
(i) Non- conductive; (ii) Perfect conductive.

5.1.3.2.6 Effect of entry point

The effect of entry point on the motion of particles was studied for non-conductive particles of size $100\mu m$ and the same density as that of molten aluminum. The results for particles entering the ESZ from different entry points and flowing through without even grazing the sidewall are shown in Figure 5.12. It is seen that the difference in the time taken by particles flowing through the physical length of the orifice, $L_{orifice}$, is small. For example, when a non-conductive particle enters the ESZ from an entry point of $y_0/R = 0.6$, it takes $tu_m/L = 1.25$ to flow through the physical length of the orifice, and the time is still $tu_m/L = 1.25$ corresponding to an entry point of $y_0/R = 2.0$, and $tu_m/L = 1.45$ to an entry point of $y_0/R = 3.2$. This is an important feature when discriminating particle is based on the transient times of signals.

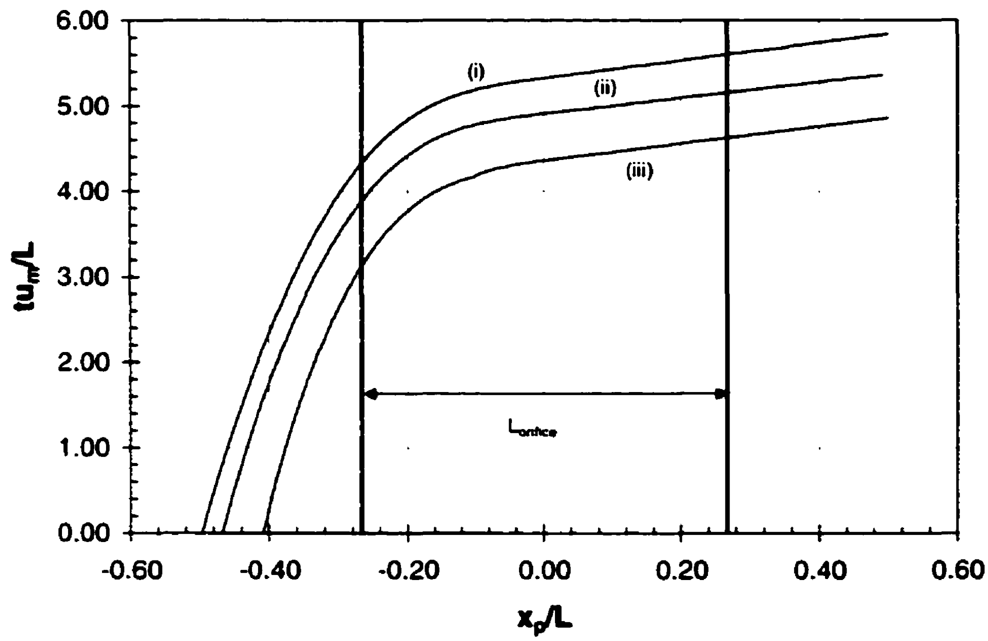

Figure 5.12 — Effect of entry point on the motion of particles.
(i) $y_0/R = 0.6$; (ii) $y_0/R = 2.0$; (iii) $y_0/R = 3.2$.

5.1.3.2.7 Effect of orifice shape

Although all the above discussion is based on the study of a parabolic orifice with a polynomial coefficient of 2.15, it was found that except for the difference in the absolute value of velocity, relative velocity and transient time, all the rules hold for other parabolic orifices with different polynomial coefficients. Another difference is the passing-through fractions of the particles flowing within orifices of different shapes. If a non-conductive particle is considered to be collected by the ESZ wall when it assumes a radial velocity towards the wall instead of towards the central axis, and its center is a radius away from the wall, the calculated collection coefficient for particles of size between 20 to $240 \mu m$ is about 5% in a parabolic orifice with a polynomial coefficient of 2.15 and it is around 8% in a parabolic orifice with a corresponding polynomial coefficient of 1.0.

5.1.3.3 Conditioning operation

The discovery of the conditioning operation, which applies a high current of $200-300$ amperes, compared to a typical operating current of 60 amperes, through the orifice, is the key for the LiMCA system to provide reliable readings when working in molten aluminum. It is seen from the previous section that some inclusions are collected on the inner wall of the ESZ. The build-up of the inclusions inside the ESZ will affect the performance of the LiMCA system. The reason why the conditioning operation can solve the problem can be derived by analyzing the fluid flow field inside the ESZ when applying high currents.

Figure 5.13 shows the fluid flow inside the ESZ when a current of 250 amperes is applied during the conditioning operation. Compared to the fluid flow at the typical operating condition of 60 amperes (Figure 5.4(a)), a large circulation is induced inside the ESZ. This circulation is generated as a result of the high pressure established at the throat of the orifice by the interaction of the strong electric current density and its self-induced magnetic flux density. The negative pressure gradient along the central axis of the orifice in the converging region moves the fluid from the throat to the entrance. A significant phenomenon accompanying the generated circulation inside the orifice is that the fluid velocity near the wall increases dramatically. In the case of 250 amperes electric current, the maximum velocity increases from $4.64 m/s$ to $6.15 m/s$. Based on this fact, it seems reasonable to ascribe the working mechanism of the conditioning operation to the high fluid velocity generated near the wall, which removes the particles collected on the inner wall of the orifice, keeping LiMCA system working reliably and stably.

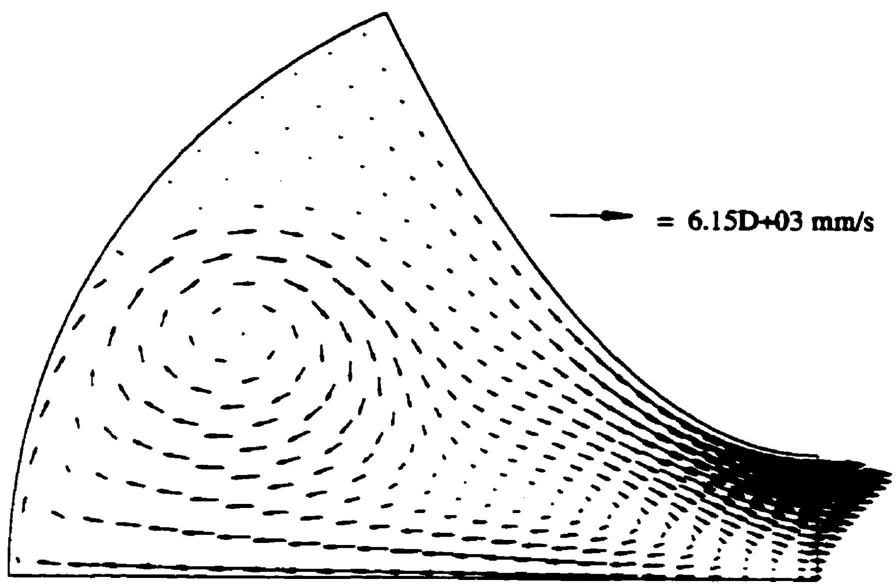

Figure 5.13 — Velocity vectors in the conditioning operation by applying electric currents of 250 amperes.

5.1.3.4 Particle discrimination

5.1.3.4.1 Discrimination of conductive and non-conductive particles

Conductive and non-conductive inclusions can be readily discriminated from one another as they generate negative and positive peak signals, respectively. The magnitudes of the signals, however, are different for particles of the same size but of different conductivity. Figure 5.14 presents a plot of voltage pulse as a function of particle diameter under typical operating conditions of LiMCA in aluminum (Table 5.1), where the particles studied include non-conductive (Equation (5.9)), perfect conductive (Equation (5.12)) and same conductive as TiB_2 (Equation (5.13)). It can be seen that the amplitude of the signals caused by perfectly conductive particles is twice the height as that for non-conductive particles of the same size, while the amplitude for TiB_2 particles is predicted to be only three fourths of that of non-conductive particles of the same size.

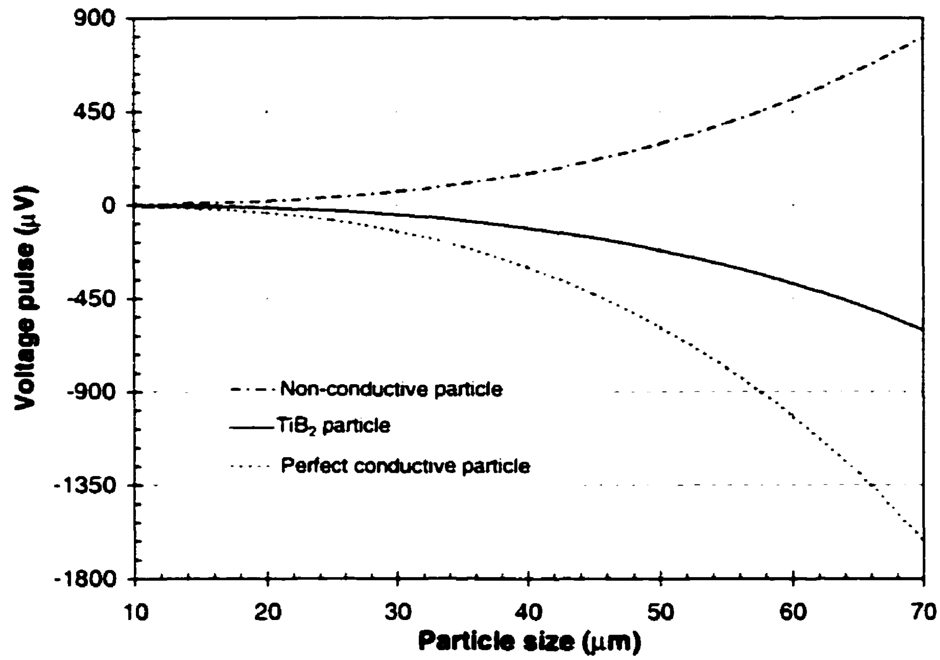

Figure 5.14 — The voltage pulse in molten aluminum as a function of the particle diameter.

5.1.3.4.2 Discrimination of non-conductive particles of different density

As discussed before, particle discrimination in LiMCA system seems feasible thanks to DSP technology. For every transient pulse generated when a particle passes through the ESZ, seven parameters are used to characterize the pulse as shown in Figure 4.5. These parameters are related to the motion of the particle, which depends on the physical properties of the particle and the fluid flow conditions within the ESZ, as discussed in the previous section. Figure 4.5 also shows that the transient time of the particle flowing through the ESZ in LiMCA system is not the time the particle takes to go through the physical length of the ESZ, but rather the time it takes to go through the region where the pulse height generated by the particle is higher than the set thresholds, which marks the margins of the band of signal. Therefore, the numerical study of particle discrimination was carried out by relating the ESZ resistance change using Ohmic model (Equation (5.18)) to the motion of particle inside the ESZ. Figure 5.15 shows the ESZ resistance variation as particles of different diameter pass through an orifice of $300\mu m$ in molten aluminum under typical operating conditions. It can be seen that larger particles reach the noise threshold resistance further away from the orifice center than do smaller particles. Therefore, smaller particles travel shorter distances when transient times are measured by the LiMCA system. For example, a $100\mu m$ particle reaches the noise threshold of $15mV$ at $0.395mm$ from the center of the orifice, while it is $0.206mm$ for a particle of $40\mu m$. Therefore, the transient time measured for a particle of $40\mu m$ is the time it takes to travel $0.412mm$ near the center of the orifice, while for a particle of $100\mu m$, it is the time to travel $0.79mm$.

To study the particle discrimination numerically, Equations (2.1) and (2.2) for the fluid flow and Equation (5.15) for the motion of particles were solved first for microbubbles and alumina particles of varying size flowing through the whole orifice. Since the effect of the entry point on the time the particles take to go through the physical length of the orifice without grazing the wall is very small (as shown in Figure 5.12), an entry point of $y_0/R = 2.0$ was chosen for this study. Then, the transient time (Figure 4.5) was obtained by considering the noise threshold of the LiMCA system, which is usually set as $\pm 15mV$. The results are shown in Figure 5.16.

It can be seen that bubbles have shorter transient times than do alumina particles of the same size, which can be explained by the different

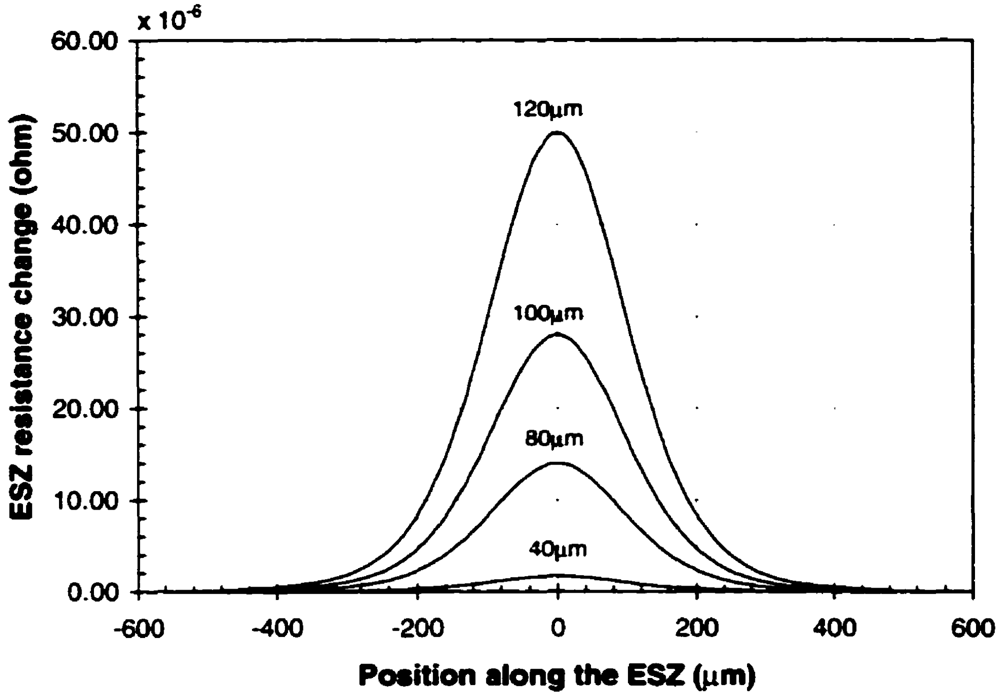

Figure 5.15 — ESZ resistance change with the position of non-conductive particles of various diameter.

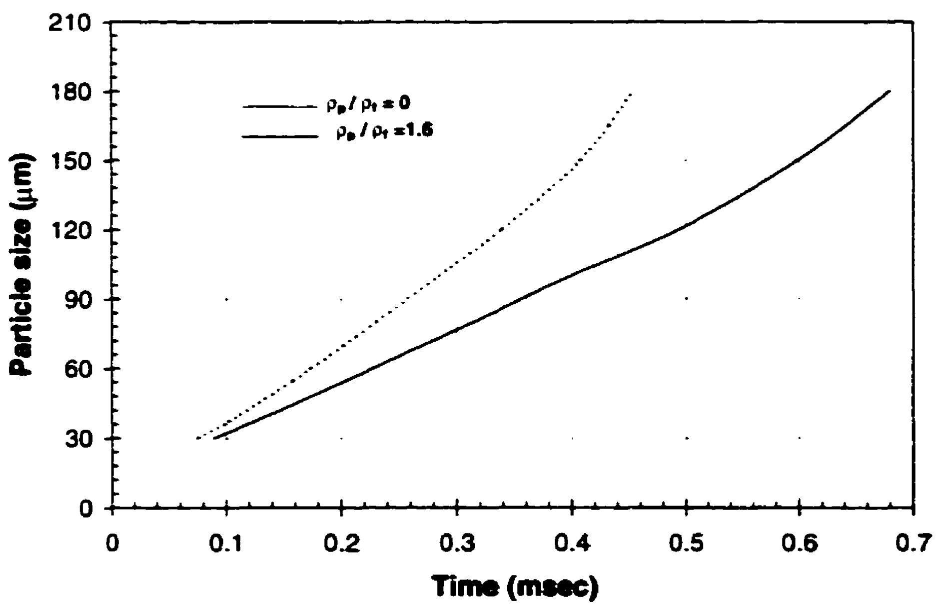

Figure 5.16 — Numerically predicted transient time versus particle size.

relative velocity developed when they move through the ESZ, as shown in Figure 5.8(a). Bubbles, which lead the fluid flow in the axial direction, travel faster than alumina particles, which are denser than the liquid aluminum, and thus lag behind the fluid flow when traveling within the ESZ.

It is also noted from Figure 5.16 that larger particles have longer transit times than smaller ones of the same density. This is easy to explain for alumina particles. For alumina particles, the larger the size, the lower the velocity. On the other hand, for bubbles, the larger the size, the higher the velocity. It seems that larger bubbles should have lower transient times than smaller bubbles. However, because larger bubbles reach the threshold much further away from the orifice center, resulting in longer distance to travel, the transient time of larger bubbles appear larger than that of smaller bubbles. It was also found that the difference in transient times for bubbles, and alumina particles becomes more significant as particle size increases, improving the discrimination between particles of different densities.

Besides the transient time, based on which particle discrimination can be carried out, pulse shape is also of characteristics for different particles. Figure 5.17 shows the predicted signal shapes for a microbubble and an alumina particle of $80\mu m$ flowing into the ESZ from an entry point of $y_0/R = 2.0$. The bubble, which has a lower density, undergoing acceleration as it approaches the center of the converging ESZ, arrives more rapidly than the alumina particle of higher density and inertia, which accelerates more slowly.

5.2 LiMCA in Molten Magnesium

5.2.1 Introduction

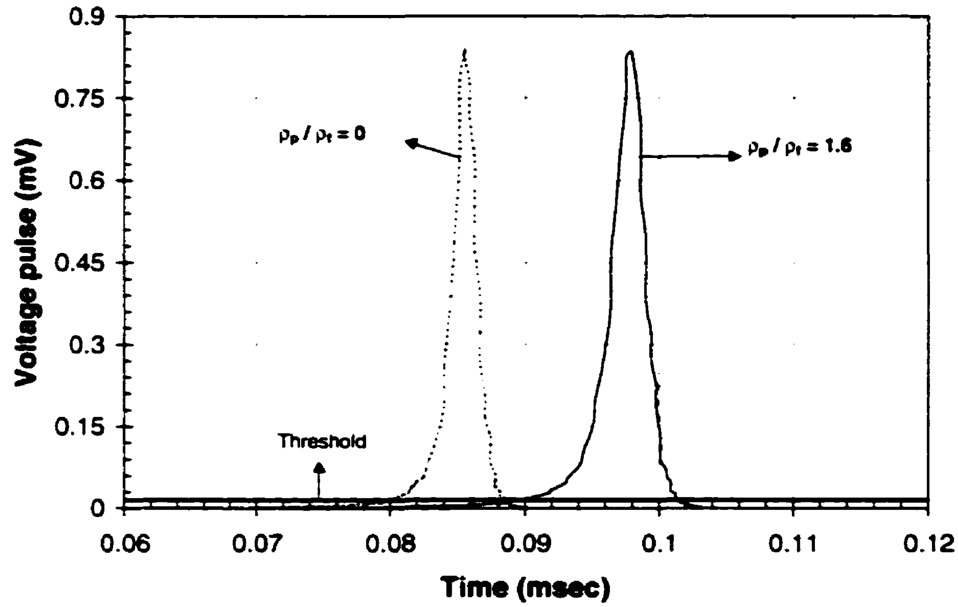

Figure 5.17 — Numerically predicted voltage pulse in aluminum LiMCA system.

Historically, approximately 80% of primary magnesium has been depleted in non-structural applications,[15] such as alloying with aluminum, desulfurization of iron and production of ductile iron. More recently, magnesium has begun to gain acceptance in structural applications, especially in the automotive industry. This is primarily due to the lightness of magnesium, which is one-third lighter than aluminum, three-fourths lighter than zinc, and four-fifths lighter than steel. Magnesium also has the highest strength-to-weight ratio of any of the commonly used metals. The fast growing applications of magnesium have led to the generation of a large amount of magnesium scraps, especially die-casting scraps. Due to both economic and environmental concerns, recycling of these scraps is imperatively demanded. In order to yield high-quality recycled magnesium, the characteristics of inclusions in molten magnesium have to be identified, and techniques to evaluate the cleanliness of molten magnesium must be developed. Compared with other inclusion assessment techniques, such as metallographic examination, filtration, optical technique, which are being used also in aluminum and steel industries, the LiMCA system has distinct features in terms of process control and quality assurance. Measurements can be made available on-line very quickly at time intervals on the order of one minute. This enables LiMCA to monitor metal cleanliness along a cast, either as a function of process parameters, or as a function of time.

In an early study,[16] compacted silica (MASROCK™, a trade mark of Harbison-Walker) tubes has been proved to be resistant to attack by liquid magnesium. This is presumably attributed to an initial reaction of the surface with the melt to form a relatively impervious corrosion product layer. However, these porous MASROCK™ have tended to crack due to thermal shock and residual stresses, and were found to have a failure rate of about 28% depending on supplier. Recently, a reliable and robust LiMCA probe,[17] Concentric Steel Tube Probe (CSTP), was developed and tested in pure magnesium[18] and also in magnesium scrap melts.[19] This probe comprises two concentric steel tubes that are separated, and electrically insulated, one from the other by an annular gas space whose integrity is maintained by a non-conductive boron-nitride ceramic disk containing the ESZ. Extension springs are used to hold the boron-nitride insert against the steel tubes, which are air-cooled. A schematic illustration of the probe is shown in Figure 5.18.

Although the results are quite promising, several problems warrant further investigation. One problem encountered in applying CSTP in molten magnesium is the relatively high background noise, which is usually 30-$50\mu V$ in the laboratory experimental conditions, much higher than that achieved in aluminum melts, which is around $10\mu V$. Another is the practical need for larger size orifice to prevent blockage. For example, in one of our studies,[19] orifice size ranging from $400\mu m$ to $495\mu m$ was found necessary to avoid plugging, compared to the $300\mu m$ orifice typically used in molten aluminum. Larger orifice size and higher background noise all increase the particle detection limit. In the following, the fluid flow and particle motions within a cylindrical ESZ with a countersunk inlet of the CSTP will be studied, and the results are used to explain the existing problems. A new design for the orifice is proposed.

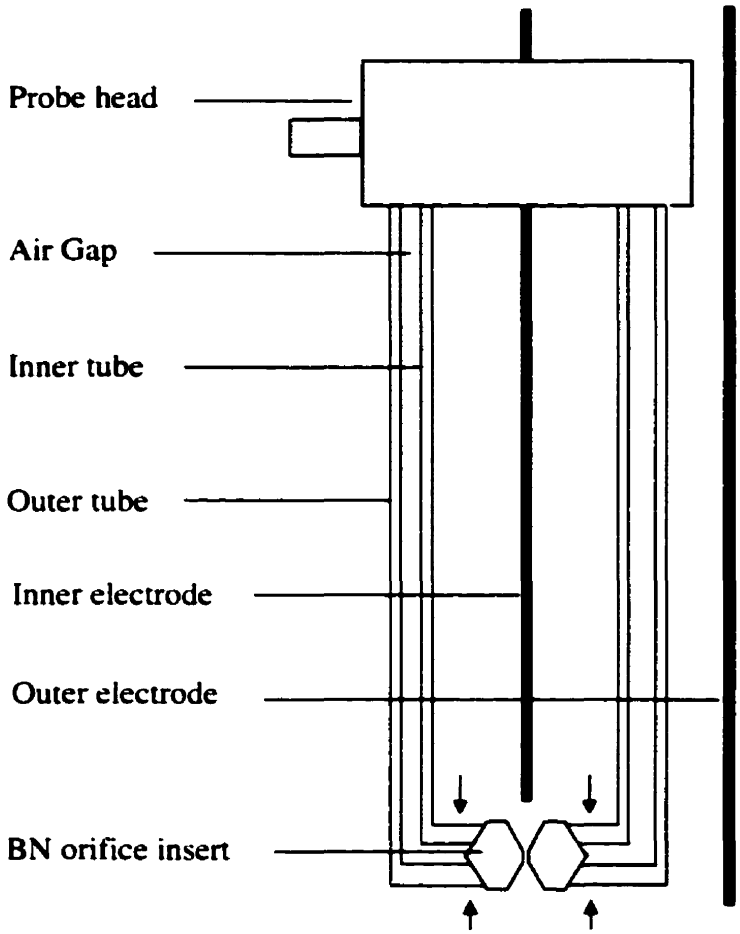

Figure 5.18 — Schematic of the CSTP for magnesium LiMCA.

5.2.2 Fluid Flow and Particle Motions within an ESZ of the CSTP

The ESZ of CSTP is built inside the boron-nitride disk. A cross-sectional view of the ESZ orifice is shown schematically in Figure 5.19, where D and $L_{orifice}$ are the diameter and length of the orifice, respectively.

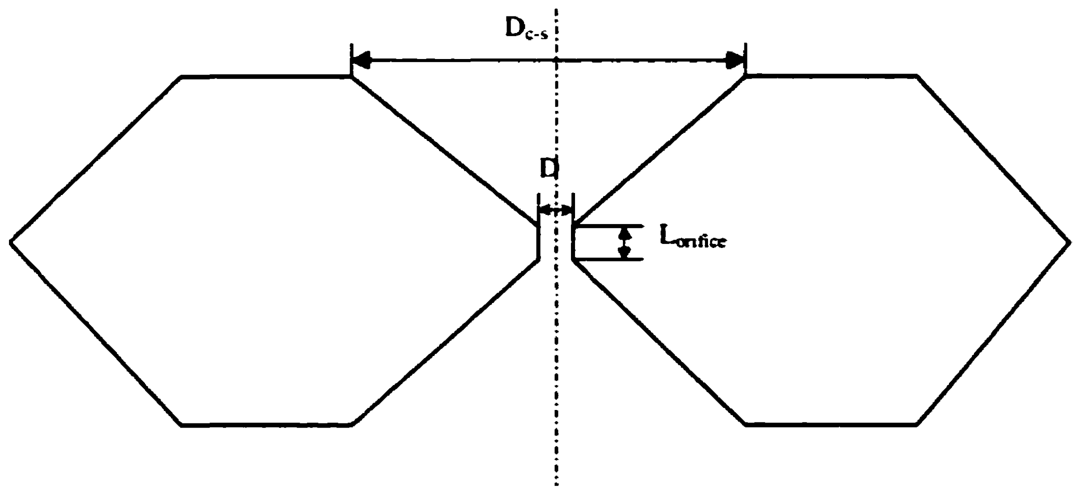

Figure 5.19 — Cross-section view of an ESZ built inside the BN disc for CSTP

The calculation of fluid flow, electromagnetic fields and particle motions were based on the mathematical model and numerical methods described in Section 5.1.2 for aluminum LiMCA. The physical properties of magnesium melt and the dimensions of the ESZ orifice and the countersunk at the inlet of the ESZ orifice used in this study, as well as the typical operating conditions of magnesium LiMCA are listed in Table 5.2.

Figure 5.20 shows the predicted fluid streamlines. It can be seen that a large recirculation zone is generated inside the countersunk region. Considering the symmetry of the calculation domain, there is actually a toroidal type of recirculation zone, which is symmetric with respect to the central axis. The recirculation zone is generated as a result of the pressure established by the strong electromagnetic pinch force inside the orifice. This pressure becomes higher than the upstream pressure of the fluid inside the countersunk region. It seems reasonable to believe that the high background noise in the CSTP was partially induced by this recirculation zone.

Table 5.2 Physical properties of liquid magnesium and typical operating conditions of LiMCA in molten magnesium

Liquid magnesium:	
Temperature (^{0} C)	700
Density (kg/m^3)	1.577×10^3
Electrical resistivity (Ωm)	0.28×10^{-6}
Viscosity (kg/ms)	1.23×10^{-3}
Typical operating conditions:	
Orifice size D (mm)	0.3
Orifice length $L_{orifice}$ (mm)	0.3
Diameter of the opening of the countersunk D_{c-s} (mm)	13
Mean fluid velocity in the cylindrical orifice (m/s)	4.0
Electric current (Ampere)	60
Pre-amplifier gain	1000
Noise threshold set (μV)	± 15

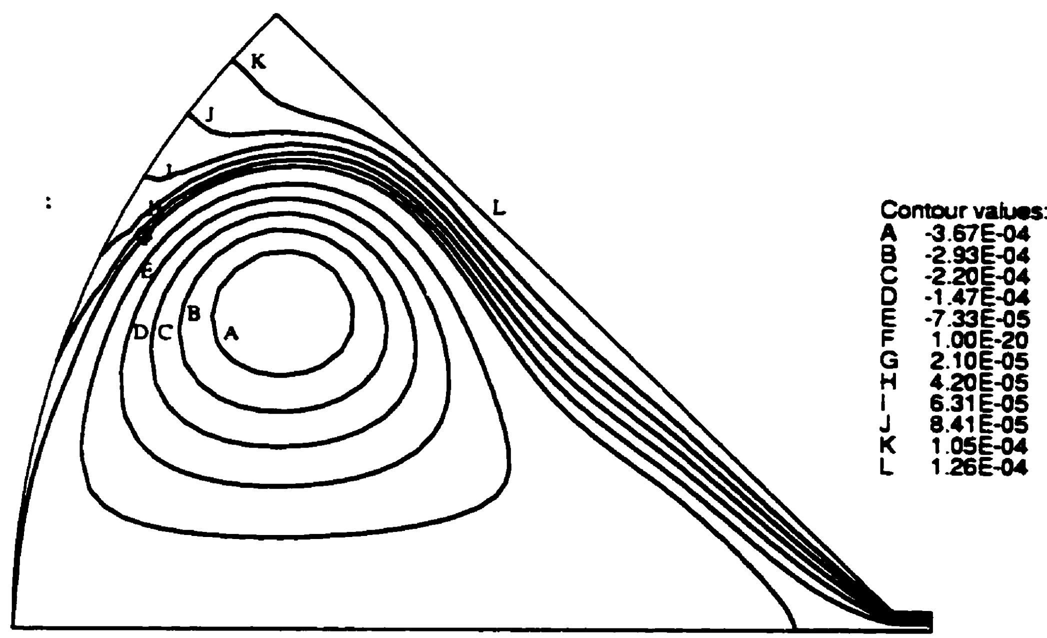

Figure 5.20 — Predicted streamlines in magnesium LiMCA under typical operating conditions.

The trajectory of a non-conductive particle flowing into the countersunk region from an entry point of $y_0/R = 2.0$ is shown in Figure 5.21. It is noted that the particle is entrained within the recirculation zone and does not even flow into the orifice. During the operation, more particles will flow into the probe, and some of them will also be entrained within the recirculation zone. It is believed that some of the small particles entrained within the recirculation zone coalesce to become larger particles. Some of the larger particles, under certain conditions, such as conditioning operations or shaking of the probe, have a chance to escape from the recirculation zone to be counted as larger particles or even block the orifice if their sizes are larger than that of the orifice. This could explain why much larger orifices are needed in practical operations.

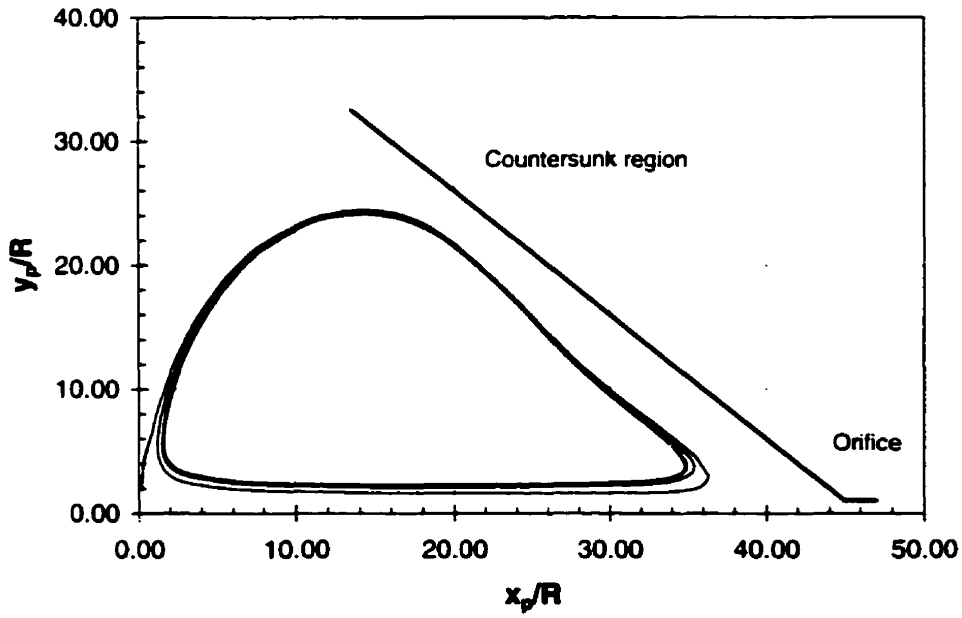

Figure 5.21 — Trajectory of a non-conductive particle flowing into magnesium LiMCA from an entry point of $y_0/R = 2.0$.

5.2.3 A New Design of the ESZ for CSTP

Based on the above discussions, a new design of the ESZ for the CSTP, which is shown in Figure 5.22, is proposed to prevent the formation of the recirculation zone at the inlet countersunk region. An important feature of this new probe is that the shape of the ESZ should be rounded, ensuring that conditioning operations take into effect. Thus, the fluid flow and the electromagnetic fields are similar to those in aluminum LiMCA.

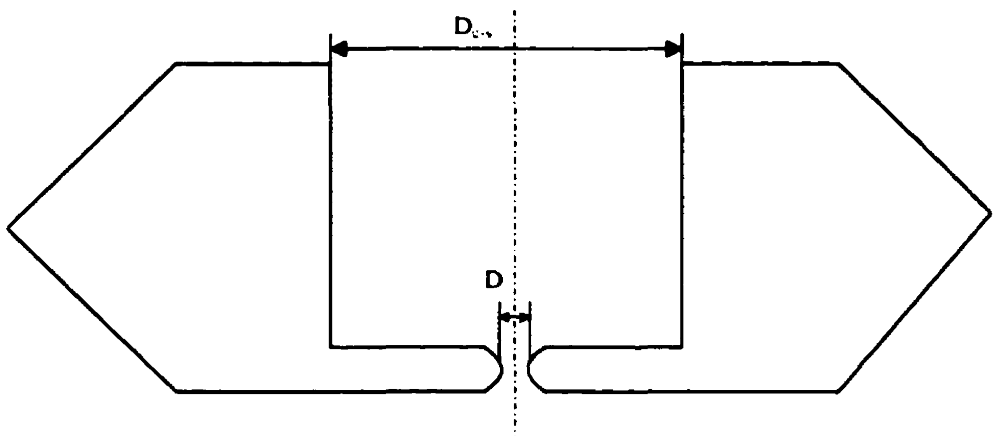

Figure 5.22 — Proposed new design of ESZ for magnesium LiMCA.

5.3 LiMCA in Molten Steel

5.3.1 Introduction

It is known that many characteristics of a steel product can be badly compromised by the presence of inclusions. Thus, properties such as ductility, toughness, drawability, machinablity, weldability, H.I.C., and fatigue strength, as well as surface characteristics such as paintability, pitting, corrosion and reflectivity, can all be critically affected by the nature, size and spatial density of such inclusions.[20]

Depending on the grades of the steel being produced, and attendant processing operations, large inclusions, typically in the range of $50\mu m$ to $200\mu m$ diameter, can be formed and enter the cast product. However, these do not usually occur with sufficient frequency to be detected using techniques such as automatic image analysis or computer-aided manual image analysis,[21] owing to the square meters of surface that would need to be sectioned and analyzed. A time consuming and materials costly method, the slime dissolution technique,[22] is routinely performed to check the existence of those inclusions by electrolytically dissolving a sufficiently large sample of steel (e.g. 10 kg) and extracting the residue.

Since the successful application of LiMCA to aluminum melts, much efforts have been devoted to the development of LiMCA probes for liquid steel. Earlier work[23] had concentrated on designing a sensor capable of continuous use based on a composite boron-nitride/silica (fused quartz) tube given that the steel is properly deoxidized. In this case, the boron nitride remained chemically stable while the quartz upper body, set out of the melt, provided the visibility needed to control successive filling and emptying operations. This design is prone to gas leak at the boron nitride/silica sealing joint, and consequently was abandoned in favor of a one-piece silica tube arrangement, supported by a graphite reinforcing inner electrode as shown schematically in Figure 5.23. This new design was demonstrated to be effective in preventing successive collapse and expansion of the fused quartz tube during filling and emptying operations. The probe being developed in Electro-Nite is based on this one-piece design, where a cylindrical ESZ is used. Although it has been successful in developing functional probes for liquid steel, sometimes the operations are troubled by the relatively high background noise, and furthermore, it is observed that the high background noise can not always be improved by conditioning operations. In the following, the fluid flow under typical operating conditions and conditioning operations are studied for steel LiMCA. A design for improving the conditioning effect is proposed.

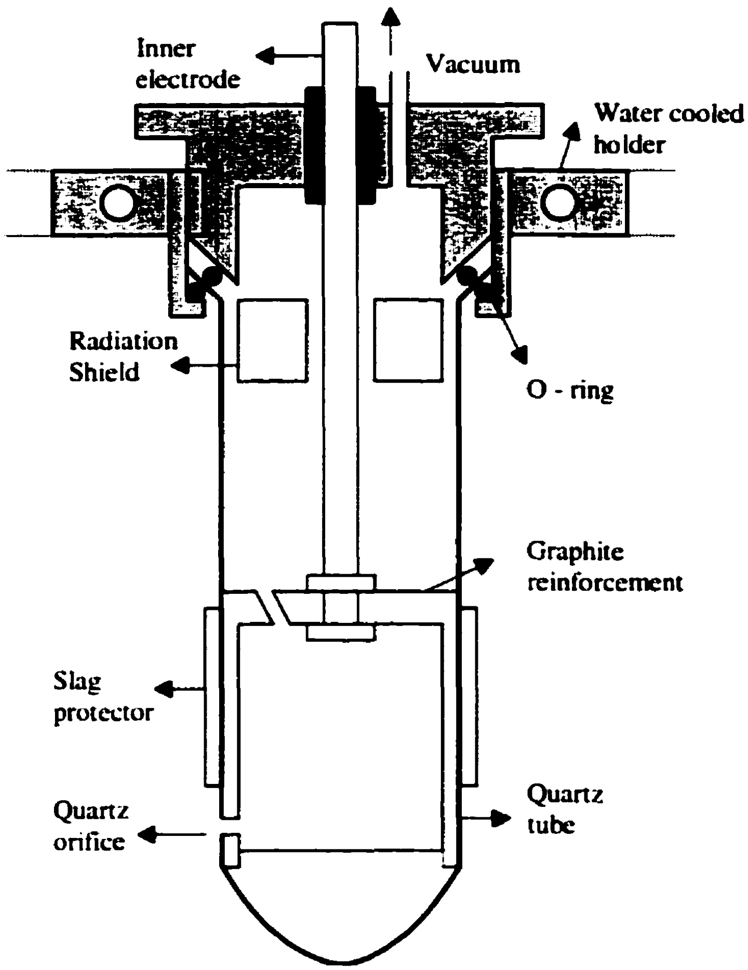

Figure 5.23 — Schematic of the quartz tube arrangement for steel LiMCA.

5.3.2 Flow Field

Physical properties of molten steel and typical operating conditions of steel LiMCA are listed in Table 5.3. Fluid flow and electromagnetic fields were studied based on the mathematical model and numerical methods

Table 5.3 Physical properties of liquid steel and typical conditions of LiMCA in molten steel

Liquid silicon-boron steel:		
Temperature (^{0} C)	1350	
Density (kg/m^3)	7.0×10^3	
Electrical resistivity (Ωm)	1.40×10^{-6}	
Viscosity (kg/ms)	7.0×10^{-3}	
Typical operating conditions:		
Orifice size (mm)		0.3
Orifice length (mm)		1.0
Electric current (Ampere)		20
Mean fluid velocity (m/s)		2.77
Pre-amplifier gain		1000
Noise threshold set (μV)		$\pm$ 15

stated in section 5.1.2. The fluid flow within the ESZ during the typical operating conditions with $I = 20A$ electric currents, and conditioning operation with $I = 200A$ electric current, are shown in Figure 5.24. It is seen that the maximum velocities are along the central axis for both cases, although the maximum velocity is lower in conditioning operation than that in typical operating condition. This is in contrast to the conditioning effect in molten aluminum, where the formed recirculation zone in the inlet region upon current surge increases dramatically the fluid velocity near the ESZ wall, removing the attached inclusions, ensuring stable and reliable operations of the LiMCA system. It can be inferred that the ineffective conditioning operation in steel LiMCA is the result of the cylindrical shape of the ESZ. A parabolic shaped ESZ, similar to that used in aluminum LiMCA, is suggested in the future development of the probe for steel LiMCA.

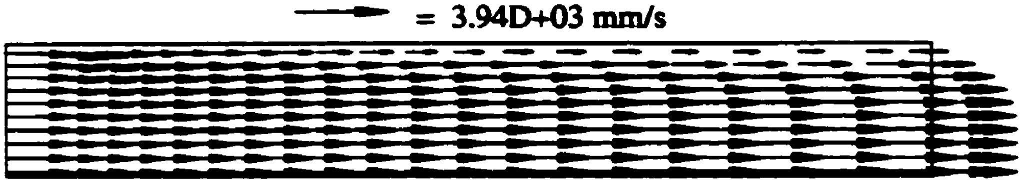

(a) $I=20A$

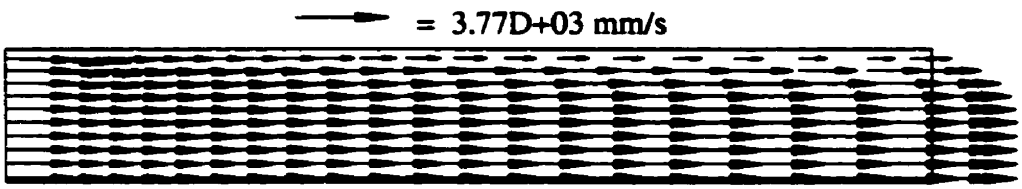

Figure 5.24 — Velocity vectors at typical operating condition (a) and conditioning operation (b).

5.4 Conclusions

Mathematical models were developed for the motion of particles in aluminum, magnesium, and steel LiMCA systems. The fluid field was obtained by solving the Navier-Stokes equations, and the trajectories of particles by equations for the motion of particles. In aluminum LiMCA system, the study of the fluid flow during the conditioning operation suggests that the dramatically increased fluid velocity near the wall helps to clear the built-up of the inclusions. The motion of particles within the parabolic shaped orifice was shown to be affected by particle conductivity, density and size. Non-conductive particles pass through the ESZ along trajectories closer to the wall, while particles that are more conductive than the molten metal closer to the central axis. Bubbles lead the fluid flow in the axial direction and travel faster than alumina particles which are denser than the fluid and lag behind the flow. Larger particles have longer transient times than smaller ones. The transient times of bubbles are shorter than those of alumina particles of the same size, and the difference of transient time is more pronounced for larger particles. The results prove from a theoretical standpoint that particles in molten aluminum are distinguishable by LiMCA system. In magnesium LiMCA system, a large recirculation zone existing in the countersunk inlet region to the cylindrical orifice under normal operation gives rise to high background noise, traps and coalesces particles and thus blocks the orifice. A rounded orifice which eliminates the recirculation zone while keeping the conditioning effect is proposed. In steel LiMCA system, the ineffective conditioning operation in the cylindrical orifice is attributed to the lack of recirculation zone upon current surge. Parabolic shaped orifice is suggested to improve the conditioning effect.

References

[1] D. Doutre and R.I.L. Guthrie: US Patent 4555662, 1985.

[2] R.I.L. Guthrie and D. Doutre: Proceedings of International Seminar on Refining and Alloying of Liquid Aluminum and Ferro-Alloys, Trondheim, Norway, 1986, pp. 146-163.

[3] W.H. Coulter: US Patent 112819, 1953.

[4] Xiaodong Shi: Upgrading Liquid Metal Cleanliness Analyzer (LiMCA) with Digital Signal Processing (DSP) Technology, Master's Thesis, McGill University, 1994.

[5] P.S. Mohanty, R.I.L. Guthrie, and J.E. Gruzleski: Light Metals, 1995, pp. 859-868.

[6] D. Doutre: The Development and Application of a Rapid Method of Evaluating Molten Metal Cleanliness, Ph.D Thesis, McGill University, 1984.

[7] G. Carayannis, F. Dallaire, X. Shi, and R.I.L. Guthrie: Symposium on Artificial Intelligence in Materials Processing Operations, Edmonton, Canada, 1992, pp. 227-244.

[8] J.C. Maxwell: A Treatise on Electricity and Magnetism, 3rd Ed., Vol. 1, Clarendon, Oxford, 1954, pp. 429.

[9] R.W. Deblois and C.P. Bean: Review of Scientific Instruments, 1970, vol. 41, pp. 909-915.

[10] A. Berlemont, P. Desjonqueres, and G. Gouesbet: Intl. J. Multiphase Flow, 1990, vol. 16, pp. 19-34.

[11] T.R. Auton, J.C.R. Hunt, and M. Prud'homme: J. Fluid Mech., 1988, vol. 83, pp. 199-218.

[12] V.M. Korovin: Magnetohydrodynamics, 1987, vol. 23, pp. 160-165.

[13] A.M. Fayon and J. Happel: AICHE Journal, 1960, vol. 6, pp. 55-58.

[14] J. Happel and H. Brenner: Low Reynolds Number Hydrodynamics, Printice-Hall, Inc., Englewood Cliffs, N.J., 1965, pp. 331.

[15] S. Housh and B. Mikuchi: Metals Handbook, 10th ed., vol. 2, 1990, pp. 496.

[16] S. Kuyucak: Ph.D Thesis, McGill University, 1991.

[17] R.I.L. Guthrie: US Patent 5789910, 1998.

[18] C. Carozza, P. Lenard, R. Sankaranayanan, and R.I.L. Guthrie: Light Metals, 1997, pp. 185-196.

[19] R.I.L. Guthrie, M. Li, and J.Y. Buyan: Proceedings of the First Israeli International Conf. on Magnesium Sci. and Tech., November 10-12, 1997, Dead Sea, Israel, pp. 81-87. (Keynote address)

[20] T. Emiard and Y. Iida: 3rd Intl. Conf. on Refining of Iron and Steel by Powder Injection, Scaninject III, Lulea, Sweden, 1983, pp. 1.1-1.31.

[21] S. Johansson: Scand. J. Metallurgy, 1990, vol. 19, pp. 79-81.

[22] Y. Yoshita and Y. Funahashi: Trans. ISIJ, 1976, vol. 16, pp. 628-635.

[23] H. Nakajima and R.I.L. Guthrie: Proc. JSPS 19th Committee Meeting, Japan, 1992, pp. 1-15.

CHAPTER 6

On the Detection, and Selective Separation of Inclusions in LiMCA Systems

The ESZ orifices of LiMCA systems widely used in aluminum industry and being developed for molten magnesium and steel have diameters of around 300 to 400 μm, corresponding to detection limits of 20 to 40 μm. However, LiMCA systems with detection limits lower than 20 μm are required to monitor small particles encountered as detrimental inclusions in steel, as intermetallic compounds in magnesium, and as grain refining additions (TiB_2) in aluminum-silicon casting alloys. One way to lower the detection limit is to reduce the orifice size, but the accompanying problem is the probability of orifice blockage by large particles within the melts. In this chapter, the model developed in Chapter 2 is modified to design new ESZ probes for molten magnesium and steel which can lower their detection limit, while resolving the problem of orifice blockage.

6.1 Introduction

The LiMCA system is based on the ESZ or Coulter Counter principle.[1,2] As shown in section 3.1, the change in resistance ΔR_{AB} caused by the introduction of a non-conducting particle into an orifice is given by:[3,4]

$$\Delta R_{AB} = \frac{4\rho_e d^3}{\pi D^4} f(d/D) \qquad (6.1)$$

where ρ_e is the electrical resistivity of the liquid, d and D are the respective diameter of the particle and the orifice, and $f(d/D)$[5] is the correction factor for the distortion of the current by the particle. By applying an electric current I, the resistive pulse voltage can be expressed as:

$$\Delta V_{AB} = \frac{4\rho_e I d^3}{\pi D^4} f(d/D) \qquad (6.2)$$

Presently, background electronic noise can be reduced to below $10\mu V$ for operations in most molten metals, allowing resistive voltage pulses above a threshold value of $20\mu V$ to be counted. Given this threshold voltage signal, together with the diameter of the orifice, D, and the electric current through the orifice, I, the minimum particle size that can be detected with a LiMCA probe is readily determined using Equation (6.2). Table 6.1 lists the typical operating conditions and detection limits for LiMCA systems operating in various molten metals. It can be seen that under normal operations, the orifice size is usually $300\mu m$, and the detection limit is around $20\mu m$.[6,7] In some circumstances, however, it is necessary to lower the detection limit. For example, when applying the LiMCA technology to analyze the effects of grain refining additions of titanium diboride (TiB_2) on aluminum-silicon casting alloy microstructures, the size of the clusters of TiB_2 can range from 1 to $50\,\mu m$.[8] In magnesium melts, the sizes of most intermetallic particles are less than $20\mu m$.[9] In plain carbon steels, alumina inclusions as small as $10\mu m$ have been reported to affect the polishability of lens moulds used for forming plastics.[10] Theoretically, lowering the particle detection limit can be realized by reducing the orifice size. However, in practice, a small orifice is more prone to blocking when there are the occasional large inclusions within the melts. Sometimes, even a $20\mu m$ detection limit is not practical[11-13] because of the need to use orifice of $400\mu m$ or even larger to allow passage of the larger inclusions.

The blockage problem has been studied and several probe designs have

Table 6.1 Operating conditions and detection limit in molten metals

	Aluminum [2]	Magnesium [6]	Silicon-boron Steel [7]
Temperature of operation (^{0}C)	700	700	1350
Electrical resistivity (Ωm)	0.25×10^{-6}	0.28×10^{-6}	1.4×10^{-6}
Electric current (A)	60	60	20
Orifice diameter (μm)	300	300	300
Pulse height detection limit (μV)	20	20	20
Particle size detection limit (μm)	20	20	16.6

been proposed for determining the number and size of particles suspended in an aqueous electrolyte medium.[14] Couter and Hagg[15] and Hagg[16] suggested that two or more tubes with different apertures be used when the particle size distribution is too wide to be covered by a single aperture. Baccarini[17] proposed a removable orifice, and Bader an expandable orifice,[18] to surmount plugging of the aperture by larger particles. IITRI patented a more sophisticated system,[19] consisting of a trumpet-shaped orifice fitted with a micromesh screen of size equal to 40% of the orifice cross-section of a downstream flow straightener.[20]

The application of an ESZ or LiMCA probe to liquid metals is quite different from that of Coulter Counter type ESZ systems for aqueous electrolytes. The hostile thermal and chemical environments make the adoption of removable or expandable orifices impractical, while the sophisticated IITRI probe is not only very expensive to build, but is also troubled by screen blockage which usually occurs after just one minute sampling under normal operating conditions.

In this chapter, a new design of probe for the LiMCA system is proposed to tackle blocking problems associated with small orifices needed for lowering particle detection limits. The mathematical model developed in Chapter 2 for describing the motion of particles in liquid metals was generalized for optimizing the probe's design. The new design allows for the separation of larger particles from smaller ones, so that ideally, only those particles which are much smaller than the orifice size, pass through the ESZ.

6.2 Basis for the Development of a Smart-Probe

The passage of a particle through an ESZ in a molten metal system is quite different from that in an aqueous electrolyte. The heavy currents ($\sim 20-60A$) in LiMCA give rise to a strong radial electromagnetic force. This force accelerates non-conducting particles towards the sidewall of the ESZ. In Chapter 2, the study on the motion of spherical particles in current-carrying liquid metals flowing through a circular pipe has confirmed the dependence of the trajectories of particles on both hydrodynamic and electric fields, particle sizes, and the physical properties of the fluid and particles. It was shown that larger size particles, or particles with lower densities, will reach the sidewall faster than smaller, heavier particles. Based on this fact, a new probe, termed a "smart-probe", containing a contoured orifice with a co-axially built cylindrical extension, is proposed. The "smart-probe" system and its working principle for the separation of particles of different sizes are shown schematically in Figure 6.1. There D and H represent the diameter of the orifice and the radius of the extension. $L_{orifice}$ and L_e represent the lengths of the orifice and of the extension, while d_1 and d_2 are the respective diameter of the smaller and larger particles. The model developed in Chapter 2 was used to determine suitable dimensions for the extension. Under certain operational conditions, particles of size d_2, a size likely to block the orifice, will reach the wall of the extension, while the smaller particles of size d_1, which we wish to count, pass through the orifice.

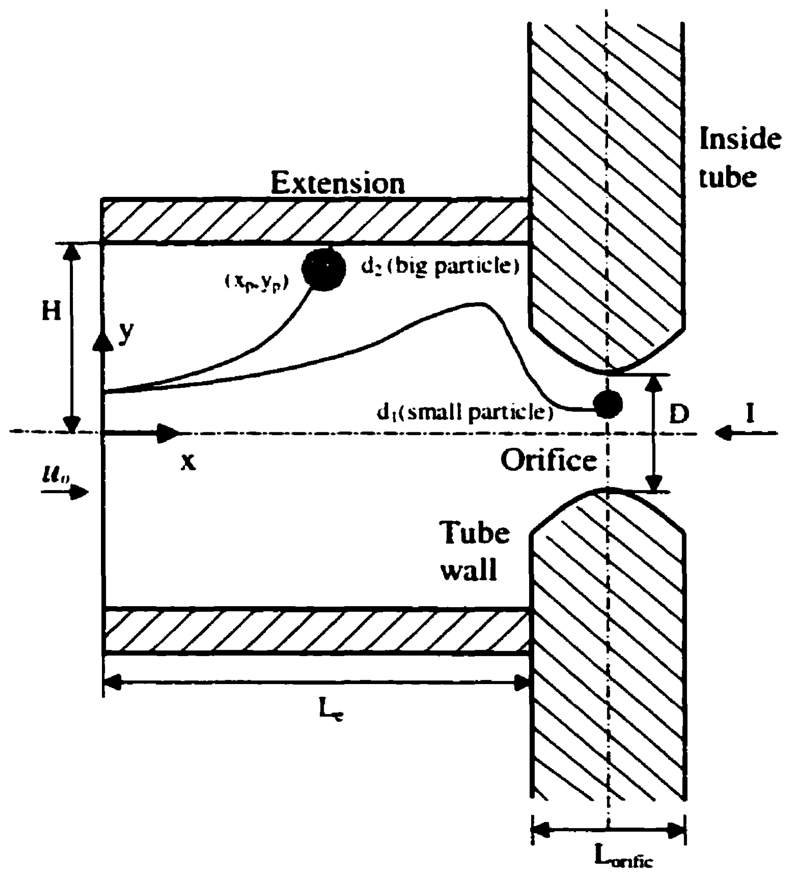

Figure 6.1 — Schematic representation of "smart-probe" and its particle separation principle.

6.3 Mathematical Model and Numerical Methods

The present study investigated the parameters of "smart-probes" for the LiMCA that can effect the separation of particles of different size or density. This was accomplished by considering the trajectories of particles entrained in a homogeneously conducting liquid metal, flowing through an orifice with a co-axially built cylindrical extension at the inlet. As shown in Figure 6.1, electric current I flows into the ESZ from inside of the sampling tube, while liquid metal from outside the extension tube. u_0 is the inlet flow velocity, which is assumed to be uniform. A two-dimensional simulation using a cylindrical coordinate system was employed since the applied electric currents are sufficiently strong as to confine any particle motion to the plane containing the mass center of the particle and the axis of the orifice. The position of the particle is designated in Figure 6.1 as (x_p, y_p), where x and y are the respective axial and radial coordinates.

6.3.1 The Flow Field

The liquid metal was taken to be incompressible, with constant properties, and the flow was considered to be laminar and steady, with a Reynolds number (Re_D) of about 1700 (Re_D is based on the diameter of the orifice under normal operating conditions of LiMCA). Given these assumptions, the problem may be stated by the continuity and Navier-Stokes equations (2.1) and (2.2), with the solution of Lorentz or electromagnetic force $\vec{F}(F_x, F_y)$ as Equations (2.3) - (2.7).

The boundary conditions for calculating the electromagnetic fields are constant electrical potential at the central cross section, i.e. the cross section in the middle of the axially symmetric orifice, uniform electric current density flowing out of the extension and zero electric current flux across the insulating wall. The boundary conditions applying to the transport equations (2.1) and (2.2) are no-slip condition on the inner walls of the extension and orifice. At the inflow boundary, the fluid velocity is assumed to be uniform, while at the outflow boundary, the exit fluid velocity gradient is taken to be zero and corrections are made in the numerical calculations to match the mass inflow rate and thereby respect continuity.

6.3.2 The Equation of Motion for Particles

As stated in Chapter 2, the trajectory of a non-conducting, rigid, spherical particle flowing within a current-carrying liquid can be described by the following equation, written in vector form:

$$\rho_p V_p \frac{d\vec{u}_p}{dt} = \frac{1}{2} C_{Dstd} \pi a^2 \rho_f \left|\vec{u} - \vec{u}_p\right| (\vec{u} - \vec{u}_p) + \frac{1}{2} \rho_f V_p \left(\frac{D\vec{u}}{Dt} - \frac{d\vec{u}_p}{dt}\right) + \rho_f V_p \frac{D\vec{u}}{Dt} + 6a^2 (\pi \mu_f \rho_f)^{1/2} \int_0^t \frac{d(\vec{u} - \vec{u}_p)/d\tau}{(t-\tau)^{1/2}} d\tau + (\rho_p - \rho_f) V_p \vec{g} - \frac{3}{4} V_p \vec{F} \tag{6.3}$$

where ρ_p and V_p are the density and volume of the particle, and $\vec{F}$ represents the electromagnetic force per unit volume of the fluid at the position of the particle.

6.3.3 Wall Effects

The presence of a solid surface in the vicinity of a moving particle will affect the drag force. In this study, the axial drag force was approximated using Equation (2.15),[21] while the wall effects in the radial direction were estimated by using the tabulated correction factor for the drag force on a solid particle moving perpendicular to a plane wall.[22]

6.3.4 Numerical Methods

A schematic representation of the computational domain and non-orthogonal, boundary-fitted grid used in this study is illustrated in Figure 6.2. Grids of variable spacing were adopted to enhance the accuracy of the calculation. The conservation equations for mass and momentum with the boundary conditions, and Equation (6.3) for the motion of particles were solved using the same method as described in Chapter 2. Δt is the time step whose value is set as 10^{-6} s when the particle flows into the extension and 10^{-8} s when the particle is near the wall or flows into the ESZ to maintain the accuracy of the calculation.

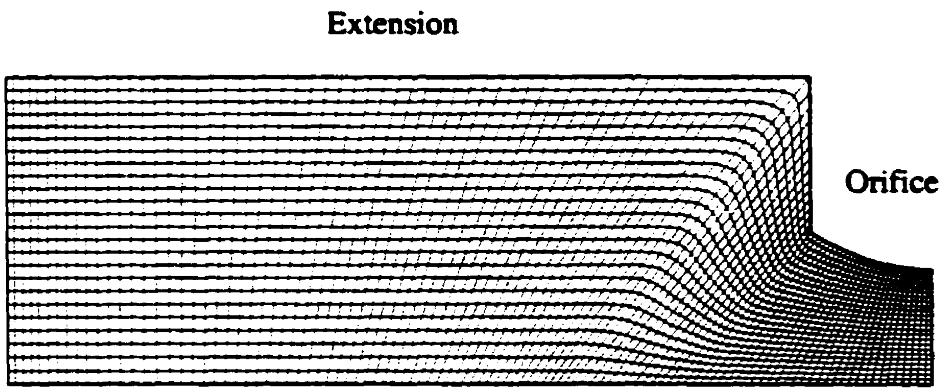

Figure 6.2 — Schematic representation of the domain and non-orthogonal, boundary-fitted grid used in the computation.

6.4 Results and Discussion

6.4.1 Particle Separation via Smart-Probes

Different from the conventional probe used in most LiMCA systems now in commercial operation, the "smart-probe" consists of a cylindrical extension built co-axially to the orifice. The extension serves to collect particles which are either large enough to potentially block the orifice or are unwanted such as micro-bubbles in aluminum melts, leaving only solid particles needing measurement, to pass through the orifice. The effectiveness of such separations within "smart-probe" depends on the nature of the fluid flow and the electromagnetic fields within the extension and orifice. Through a proper geometric combination of extension and orifice, in conjunction with suitable operating conditions, predictions suggest that the LiMCA system can provide appropriate fluid flow and electromagnetic fields for such separations.

6.4.1.1 Fluid flow and electromagnetic fields

The calculation of the fluid flow and electromagnetic fields inside a "smart-probe" for magnesium melts is based on probe dimensions, operating conditions and the physical properties of the melt listed in Table 6.2. The distributions of electrical potential, electric current density, self-induced magnetic flux density, and specific electromagnetic force within the melt, are shown in Figures 6.3(a) through 6.3(d), respectively. As can be seen from Figure 6.3(a), the isopotential along the central cross section of the orifice has its highest value, where the current flow from the inner positive electrode enters the throat of the ESZ. The electrical potential gradient is very high inside the orifice, particularly near the wall, and drops rapidly along the extension to a uniform value at around half the length of the extension. The voltage drop over the whole probe is approximately 0.10 volts. This potential distribution gives rise to the electric current density shown in Figure 6.3(b). Corresponding to the potential distribution, the current density is very high within the orifice, then decreases with increasing distance from the orifice, and eventually becomes uniform inside the extension at the point where the potential gradient starts to become uniform. The self-induced magnetic flux within the extension and orifice (Figure 6.3(c)) increases from the central axis to the wall, except in the transient region near the junction between the

Table 6.2 Probe dimensions, operating conditions and physical properties of molten magnesium used in the calculation

Dimensions of smart-probe:	
Radius of the extension (mm)	0.4
Length of the extension (mm)	1.0
Diameter of the orifice (mm)	0.3
Length of the orifice (mm)	0.3
Coefficient of the polynomial representing parabolic orifice	2.15
Operating conditions:	
Electric current (A)	60
Mean fluid velocity inside the orifice (m/s)	4.0
Physical properties of molten magnesium at 700 ^{0}C:	
Density (kg/m^3)	1.577×10^3
Viscosity (Pa s)	1.23×10^{-3}
Electrical resistivity (Ωm)	0.28×10^{-6}

orifice and the extension. In this region, the magnetic flux density increases adversely with the radial distance due to the weak axial electric current density, which contributes to the generation of this azimuthal magnetic flux density. The interaction of the electric current and its induced magnetic flux results in an electromagnetic force whose distribution is shown in Figure 6.3(d). It can be seen that the stronger electric current density and magnetic flux density within the orifice give rise to a much stronger electromagnetic force inside the orifice than inside the extension. The electromagnetic force is high near the wall, but decreases with decreasing distance from the central axis, becoming virtually and theoretically zero along the central axis. In this force field, particles suspended in a molten metal that are electrically non-conducting experience a force in the opposite direction, and are squeezed out from the liquid metal. Figure 6.4 illustrates the flow field (a) and the corresponding streamlines (b) for this "smart-probe". The flow velocity at the entrance region of the extension is quite uniform and parallel, and relatively small compared with that inside the orifice. A very small recirculation zone at the corner of the extension connecting the outside wall of the orifice is generated (as clearly shown in Figure 6.4(b)), and it is assumed that this recirculation zone would not introduce extra background noise.

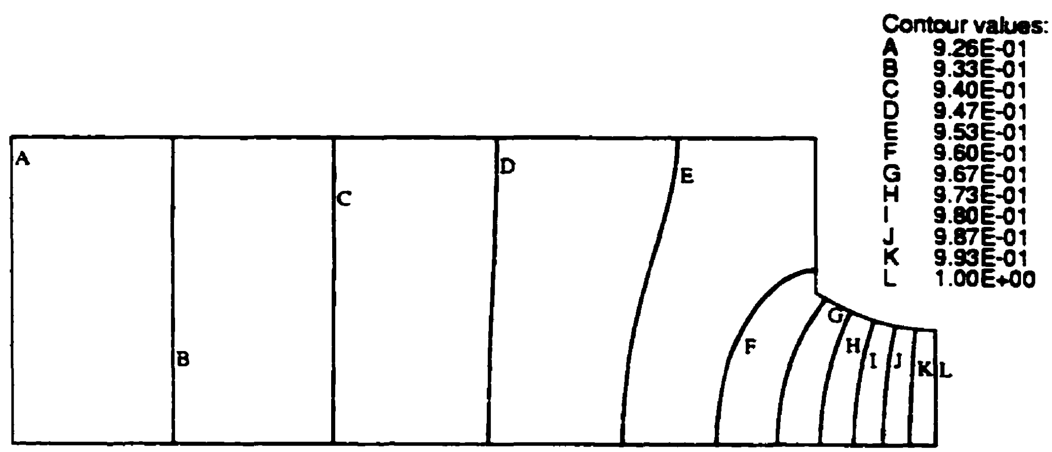

(a) Electrical potential (volt)

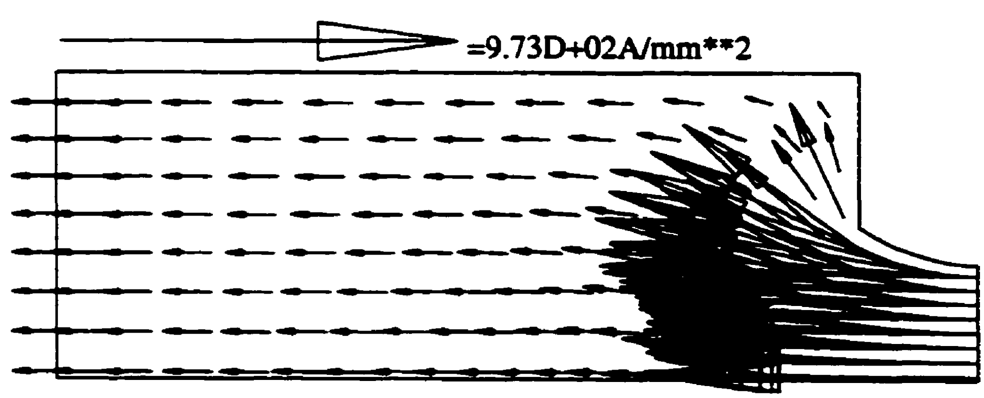

(b) Electric current density

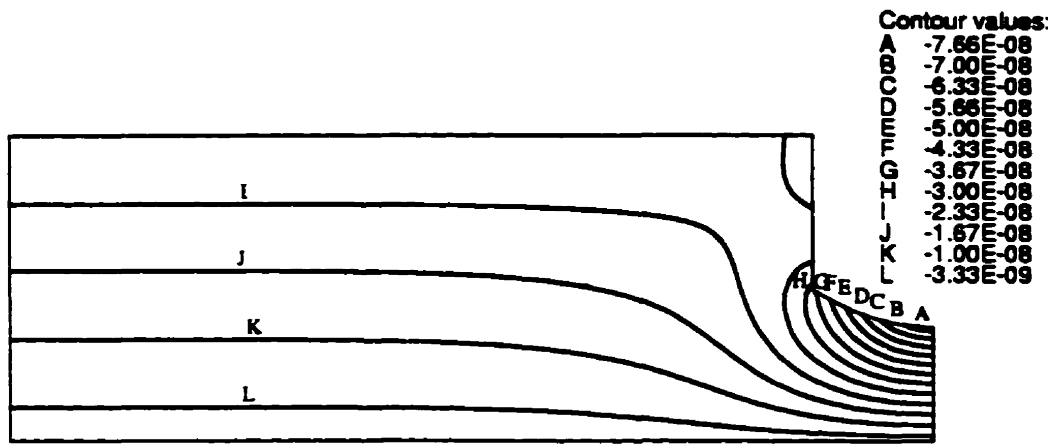

(c) Self-induced magnetic flux density (*Weber/mm*^{2})

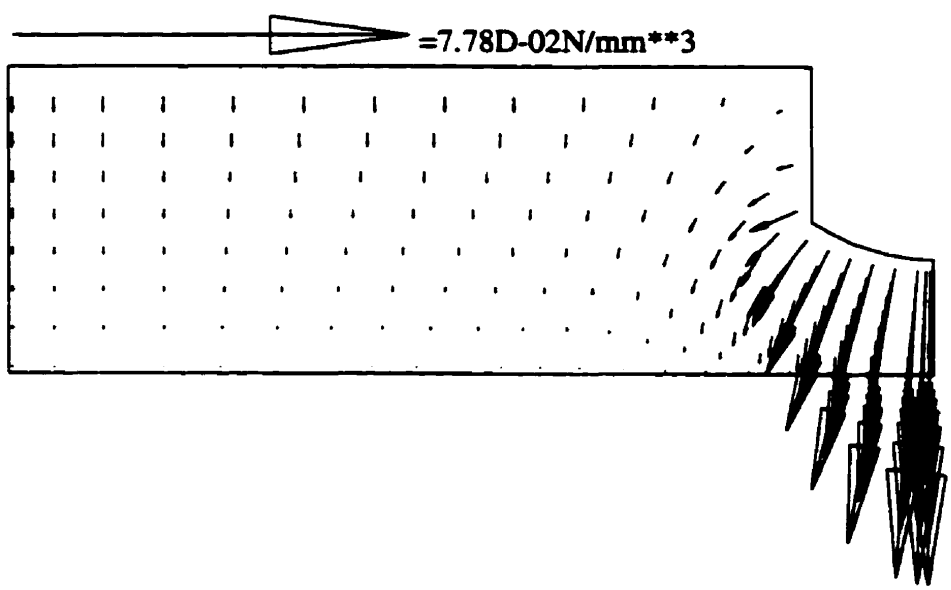

(d) Specific electromagnetic force

Figure 6.3 — Distribution of the electrical potential (a), electric current density (b), self-induced magnetic flux density (c), and specific electromagnetic force (d) for a "smart-probe" of $60A/300\mu m$, $H = 0.4\ mm$, $L_e = 1.0\ mm$, $L_{orifice} = 0.3\ mm$, $S = 2.15$, and $u_m = 4m/s$.

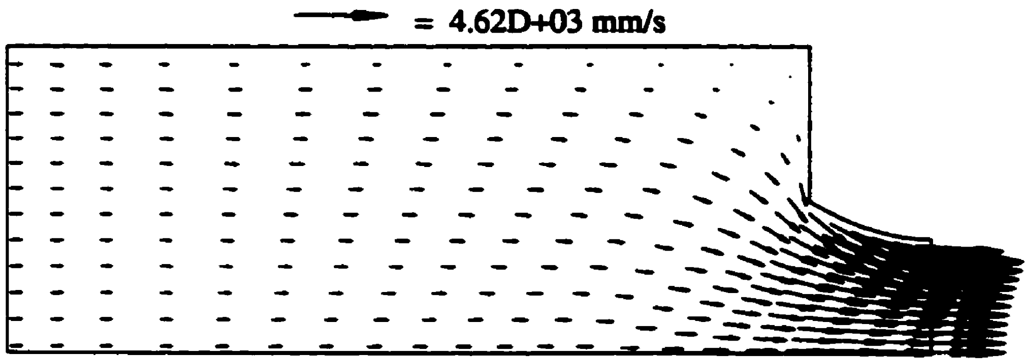

(a) Velocity vectors

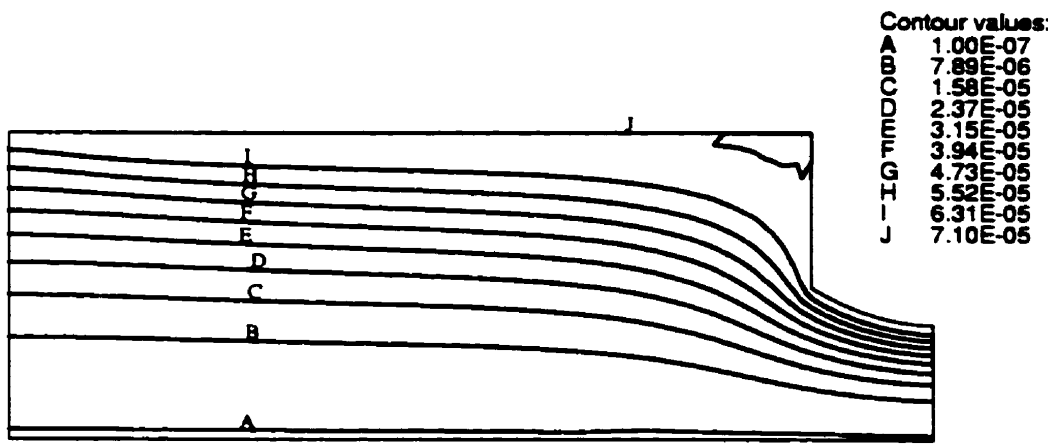

(b) Streamlines

Figure 6.4 — Predicted velocity vectors (a) and streamlines (b) for a "smart-probe" of $60A/300\mu m$, $H = 0.4mm$, $L_e = 1.0mm$, $L_{orifice} = 0.3mm$, $S = 2.15$, and $u_m = 4m/s$.

6.4.1.2 Trajectories of particles of different sizes and densities

To separate particles, they must follow different trajectories under the same fluid flow and electromagnetic fields. The study in Chapter 2 has confirmed the difference of the motion of particles of different sizes or densities flowing with current-carrying liquid metals through a cylindrical tube. The study found that larger particles reach the sidewall faster than do smaller ones, that heavier particles travel further in the axial direction before hitting the sidewall, than do those that are less dense. The predicted trajectories of particles in the fluid flow and electromagnetic fields inside the "smart-probe" are shown in Figure 6.5. As can be seen from Figure 6.5(a), the effect of particle size on the particle trajectories is tremendous. For particles flowing into the extension from two different entry positions ($y_0 = 1.0R$ and $y_0 = 1.3R$, where R is the radius of the orifice), particles of size $d = 45\mu m$ pass through the orifice, those of size $d = 120\mu m$ reach the

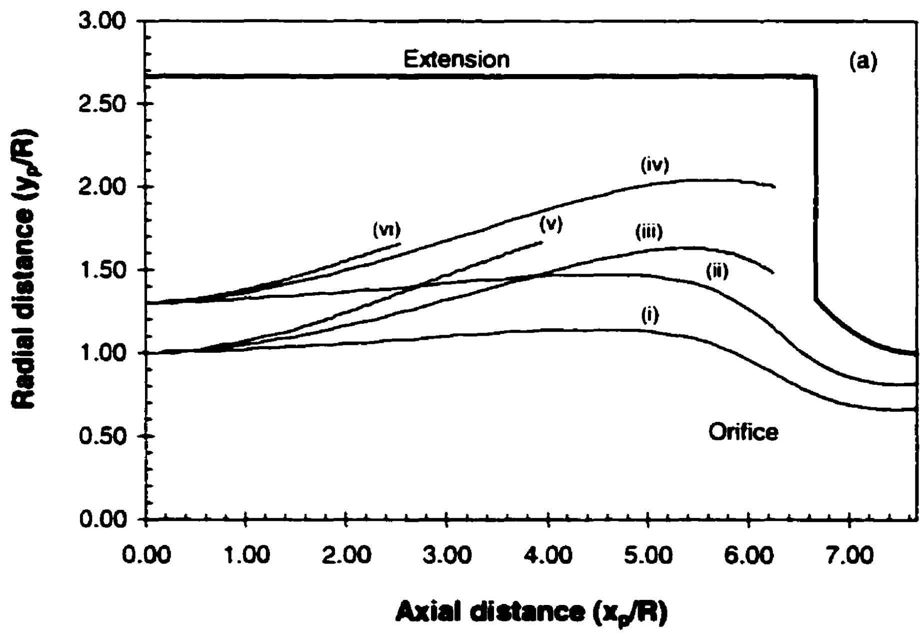

(a) Trajectories of particles of different size ($\rho_p = \rho_f$) (i) $d = 45\mu m$, $y_0 = 1.0R$; (ii) $d = 45\mu m$, $y_0 = 1.3R$; (iii) $d = 120\mu m$, $y_0 = 1.0R$; (iv) $d = 120\mu m$, $y_0 = 1.3R$; (v) $d = 300\mu m$, $y_0 = 1.0R$; (vi) $d = 300\mu m$, $y_0 = 1.3R$

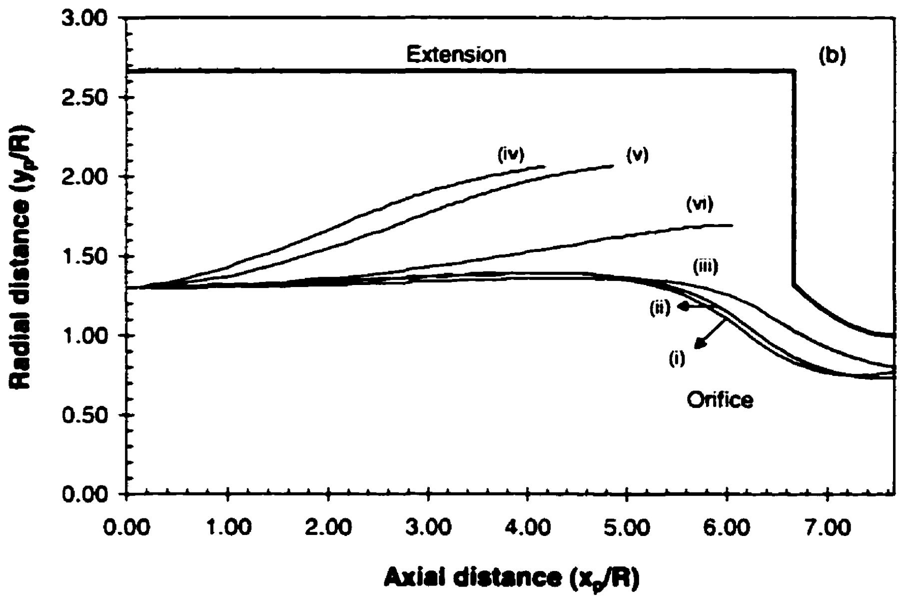

(b) Trajectories of particles of different density (i) $\rho_p = 0$, $d = 35\mu m$; (ii) $\rho_p = \rho_f$, $d = 35\mu m$; (iii) $\rho_p = 10\rho_f$, $d = 35\mu m$; (iv) $\rho_p = 0$, $d = 180\mu m$; (v) $\rho_p = \rho_f$, $d = 180\mu m$; (vi) $\rho_p = 10\rho_f$, $d = 180\mu m$

Figure 6.5 — The effect of particle size and density on the particle trajectories.

probe wall, and those of size $d = 300\mu m$ hit the sidewall of the extension. On the other hand, the effect of particle density on particle trajectories is much smaller, as can be seen from Figure 6.5(b). All particles of size $d = 35\mu m$ pass through the orifice even though their respective densities, $\rho_p = 0$, $\rho_p = \rho_f$ and $\rho_p = 10\rho_f$, are very different, while particles of size $d = 180\mu m$ all reach the wall of the tube or extension despite their different densities. Particles of $\rho_p = 0$, $\rho_p = \rho_f$ and $\rho_p = 10\rho_f$ represent bubbles, inclusions or inclusion clusters which have the same density as liquid metals, and particles which are much heavier than the molten metals, respectively. For $180\mu m$ diameter particles, it is true that heavier particles travel further in the axial direction, but they still move much faster in the radial direction than do $35\mu m$ diameter particles of zero (microbubble) density. It can also be seen from Figure 6.5(b) that $35\mu m$ diameter particles move radially towards the wall of the extension faster with density $\rho_p = 0$ than $\rho_p = \rho_f$, and much faster than $\rho_p = 10\rho_f$ under the same electromagnetic force. However, at the entrance to the orifice, strong downward acceleration of the fluid forces the particles of $\rho_p = 0$ towards the central axis of the orifice faster than neutral density particles ($\rho_p = \rho_f$), and much faster than particles ten times more dense ($\rho_p = 10\rho_f$). Further inside the orifice, the strong electromagnetic force again moves zero density particles back towards the wall of the orifice. It can be concluded from Figure 6.5, that the "smart-probe" can be used to separate differently sized particles. However, the present computations suggest that it is ineffective in separating particles of different densities, despite claims to the contrary.[23] In the following, the design parameters for the "smart-probe" will be discussed.

6.4.2 Design Parameters for Smart-Probe

Various design parameters were studied, including the electric current I / orifice size D arrangement, orifice length $L_{orifice}$, orifice shape (represented by the coefficient of the polynomial for parabolic orifice S), extension length L_e and radius H, as well as mean fluid velocity through the orifice u_m. u_m was set at $4m/s$ for most simulations, apart from a study on the effect of u_m itself.

6.4.2.1 Electric current I / orifice size D arrangement

The detection limit of LiMCA system is determined by the combination of the applied electric current I and orifice size D. In magnesium melts, $60A/300\mu m$, $40A/275\mu m$, $30A/256\mu m$, and $20A/231\mu m$ arrangements all give a detection limit of $20\mu m$ diameter particle size. In practical operations, orifice sizes greater than $400\mu m$ proved necessary to prevent the orifice blockage, increasing the detection limit up to about $30\mu m$ for an applied electric current of $60A$. To keep the inclusion detection limit to $20\mu m$, a "smart-probe" could be designed which employs a reduced orifice size, and at the same time, protects this small orifice from blocking by using the cylindrical extension to collect larger particles onto its walls before they can reach the orifice. For this purpose, the majority of particles whose sizes range from $20\mu m$ to $30\mu m$ should pass through the orifice to give an accurate measurement, while particles larger than 80 percent of the orifice size need to be collected as far as possible. The effect of the electric current I / orifice size D arrangement on the pass-through fraction of particles of different size is presented in Figure 6.6. In these calculations, particles were assumed to have the same density as the liquid magnesium. The length and radius of the extension were set at $0.5mm$ and $0.3mm$, respectively. The length of the orifice was $0.3mm$, and the coefficient of the polynomial representing the parabolic shaped orifice S was 2.15. This value was obtained by fitting the data from the micrograph of a real orifice[24] to the equation for a parabola ($y = Sx^2 + R$). One can see from Figure 6.6 that it is more effective in separating larger particles from smaller ones to increase electric current than to decrease orifice size. Thus, the pass-through fraction of particles of $30\mu m$ is lower than 60 percent for an orifice with an I/D arrangement of $60A/300\mu m$, while the corresponding value is about 75 percent for an orifice with an I/D arrangement of $30A/256\mu m$. The larger the particles, the faster they reach the extension wall, resulting in a lower pass-through fraction. When particle size increases up to $180\mu m$, the pass-through fraction becomes lower than 10 percent for all studied I/D arrangements. It is also noted

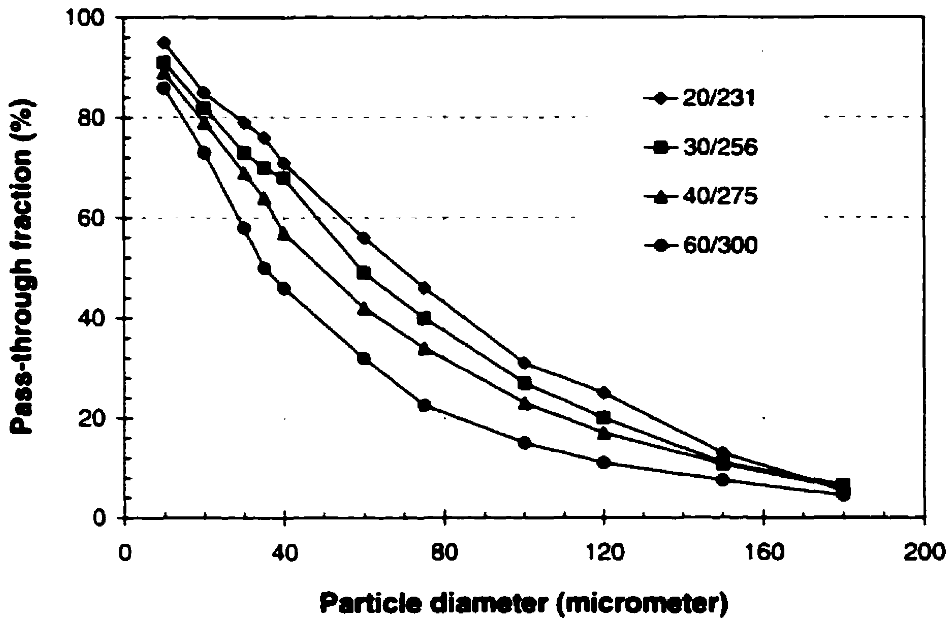

Figure 6.6 — The effect of electric current I (ampere) / orifice size D (μm) arrangement on the pass-through fraction of particles for a "smart-probe" of H = 0.3mm, L_e = 0.5mm, $L_{orifice}$ = 0.3mm, S = 2.15, and u_m = 4m/s.

that the pass-through fraction for small particles in the "smart-probe" is lower than that for conventional probes. For example, a conventional $60A/300\mu m$ orifice gives a pass-through fraction of 95 percent for particles of size $35\mu m$, while the corresponding fraction is only 50 percent for a "smart-probe" with a $60A/300\mu m$ orifice condition. This can be explained by the fact that although these particles have not been caught by the extension tube, and still have the chance to flow into the orifice, these smaller particles have also been moved out radially towards the wall of the extension as have the large particles. Therefore, more small particles flow into the orifice from near the wall rather than would be the case for a conventional probe for which the radial distribution would be uniform.

Because the size of these particles is much smaller than that of the orifice, the orifice will not be blocked. In the following studies on the effect of other design parameters of the "smart-probe", the $30A/256\mu m$ orifice condition was adopted as the standard condition.

6.4.2.2 *Orifice length $L_{orifice}$*

The effect of orifice length $L_{orifice}$ on the pass-through fraction of particles of different size is shown in Figure 6.7. The calculation was based on $H = 0.4mm$, $L_e = 0.7mm$, $S = 2.15$. As expected, the longer the orifice, the lower the pass-through fraction for particles larger than $20\mu m$. The difference between the pass-through fraction for $L_{orifice}$ = 0.5*mm* and $L_{orifice}$ = 0.6*mm* is very small, although both are 2 to 4 percent lower than that

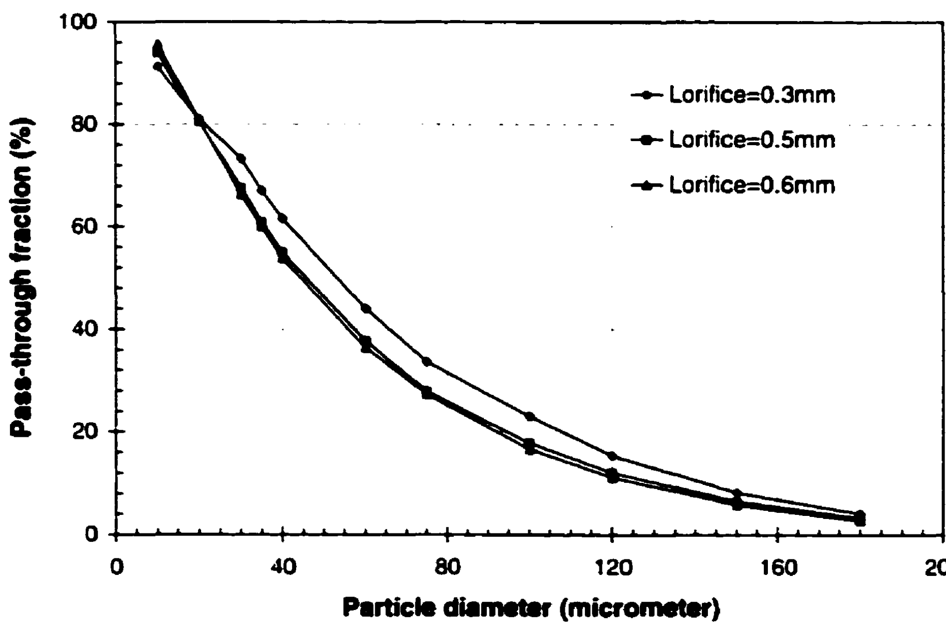

Figure 6.7 — The effect of orifice length $L_{orifice}$ on the pass-through fractions of particles for a "smart-probe" of $30A/256\mu m$, $H = 0.4mm$, $L_e = 0.7mm$, $S = 2.15$, and $u_m = 4m/s$.

for $L_{orifice}$ = $0.3mm$. On the other hand, more particles as small as $10\mu m$ pass through the orifice of length $0.6mm$ than that of length $0.5mm$, and much more than that of length $0.3mm$. This can be explained by the fact that the shorter vertical tube wall inside the extension associated with the parabolic shaped orifice of the long orifice makes it easier for these small particles to flow into the orifice.

6.4.2.3 Orifice shape S

The orifices currently used in magnesium and aluminum melts have smooth entrance and exit, however, those in molten steel are cylindrical ($S=0$). The streamlines for a "smart-probe" with cylindrical orifice are shown in Figure 6.8(a). The dimensions of the extension are $H=0.3mm$, L_e = $0.7mm$, and the orifice length is $L_{orifice}$ = $0.3mm$. It can be seen from Figure 6.8(a) that there is a recirculation zone inside the orifice, which is believed to introduce background noise during the operation of the LiMCA system. This recirculation zone, which is absent for a cylindrical orifice without extension or for a contoured orifice connected with an extension, results from the strong downward velocity at the periphery of the sharp entrance to the cylindrical orifice. The effect of orifice shape on the pass-through fraction of particles of different sizes is illustrated in Figure 6.8(b). As can be seen from Figure 6.8(b), the shape of the orifice has little effect as long as it has smooth entrance to prevent the generation of a recirculation zone inside the orifice.

6.4.2.4 Extension radius H

The effect of the radius of extension on the pass-through fraction of particles of different sizes was studied for a "smart-probe" with L_e = $0.7mm$, $L_{orifice}$ = $0.3mm$, and $S=2.15$, and the results are presented in

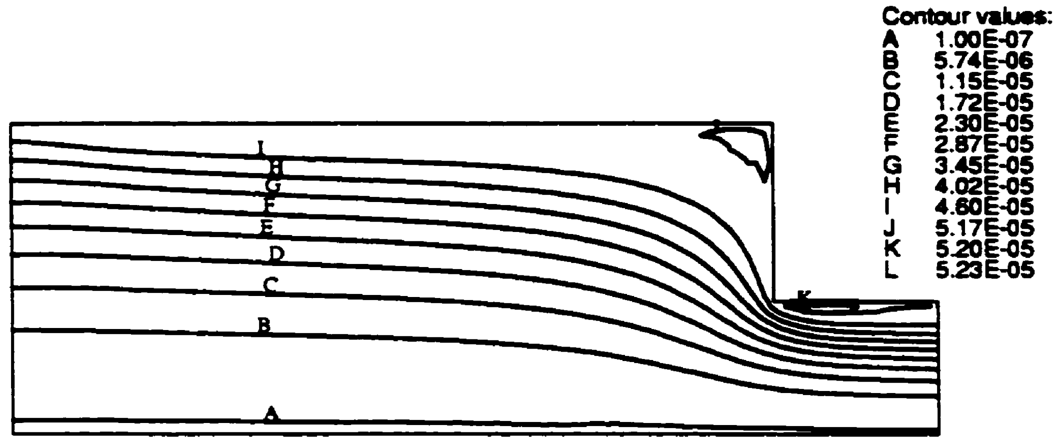

(a)

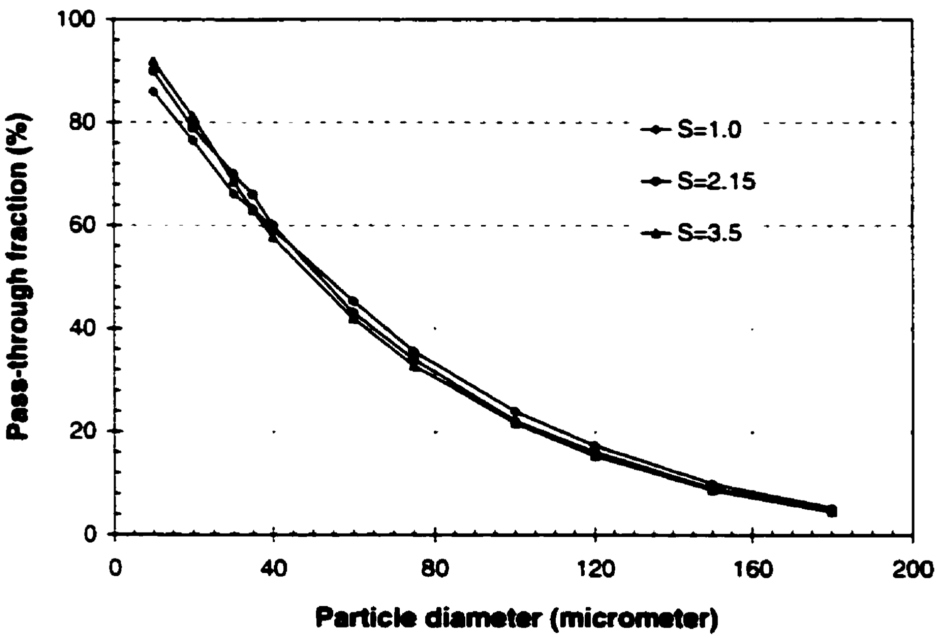

(b)

Figure 6.8 — (a) The streamlines for a "smart probe" with cylindrical orifice (S=0), (b) the effect of orifice shape on the pass-through fraction of particles for a "smart-probe" of $30A/256\mu m$, $H = 0.3mm$, $L_e = 0.7mm$, $L_{orifice} = 0.3mm$, and $u_m = 4m/s$.

Figure 6.9. Generally speaking, the pass-through fraction for particles larger than $80\mu m$ decreases as H increases, while that for particles smaller than $80\mu m$ increases with H. The reason is that the axial velocity inside the extension decreases with an increase in H, when keeping u_m constant at $4m/s$. The lower axial velocity gives larger particles a longer residence time inside the extension, resulting in more particles being collected and a lower pass-through fraction. On the other hand, as H increases, the radial velocity towards the central axis increases at the entrance to the orifice, which gives smaller particles flowing into the orifice a stronger initial radial velocity towards the axis of the orifice, and therefore an increased pass-through fraction.

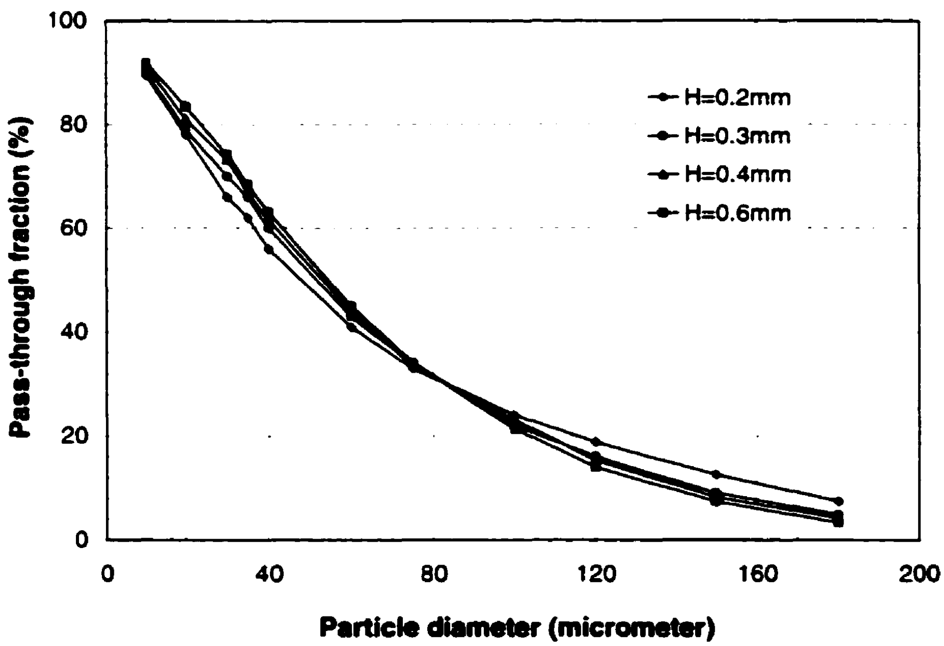

Figure 6.9 — The effect of extension radius H on the pass-through fraction of particles for a "smart-probe" of $30A/256\mu m$, $L_e = 0.7mm$, $L_{orifice} = 0.3mm$, $S = 2.15$, and $u_m = 4m/s$.

6.4.2.5 Extension length L_e

Figure 6.10 shows the effect of extension length L_e of a "smart-probe" on the pass-through fraction of particles of different sizes. The calculations were based on $H = 0.3mm$, $L_{orifice} = 0.3mm$, and $S = 2.15$. As can be seen from Figure 6.10, the pass-through fraction increases with smaller L_e. For particles of $20\mu m$, the pass-through fraction increases from 75 percent up to 82 percent as L_e decreases from $1.0mm$ to $0.5mm$. The reason for this is that the longer residence time associated with the longer extension gives particles more time to reach the wall, resulting in a lower pass-through fraction.

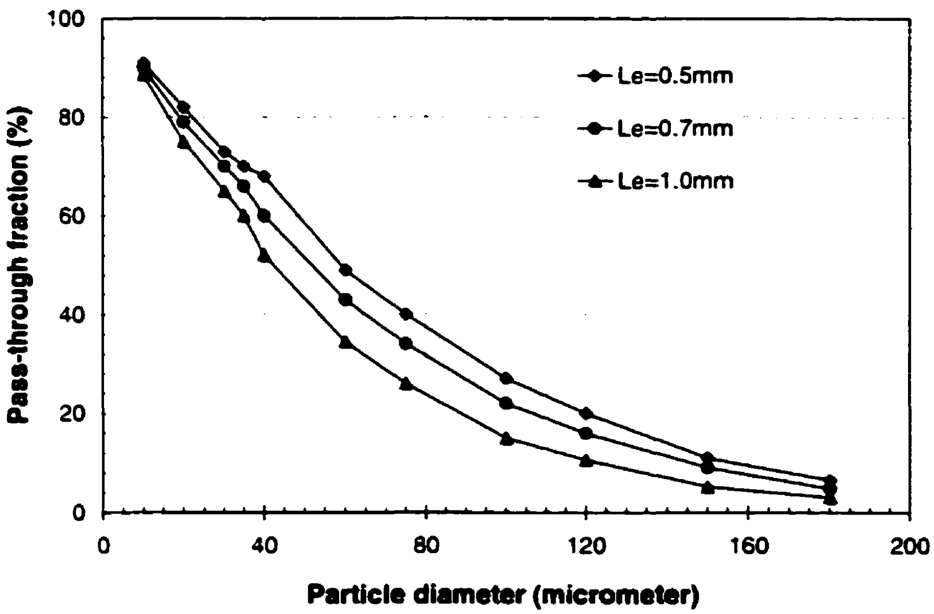

Figure 6.10 — The effect of extension length L_e on the pass-through fraction of particles for a "smart-probe" of $30A/256\mu m$, $H = 0.3mm$, $L_{orifice} = 0.3mm$, $S = 2.15$, and $u_m = 4m/s$.

6.4.2.6 Mean fluid velocity u_m flowing through the orifice

Figure 16.11 shows the predicted velocity field (Figure 6.11(a)) and streamlines (Figure 6.11(b)) for a magnesium melt flowing with a mean orifice fluid velocity of $0.5 m/s$ through a "smart-probe" of $H = 0.3mm$, L_e = $0.7mm$, $L_{orifice}$ = $0.3mm$, and $S = 2.15$. It can be seen that a large

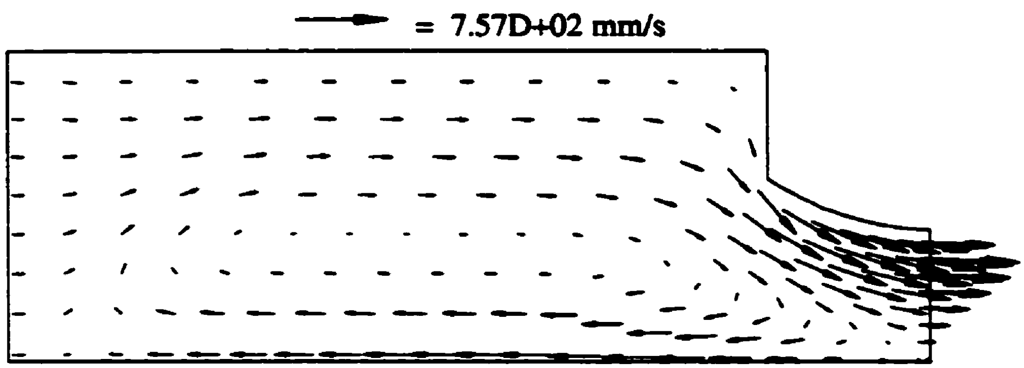

(a) Velocity vectors

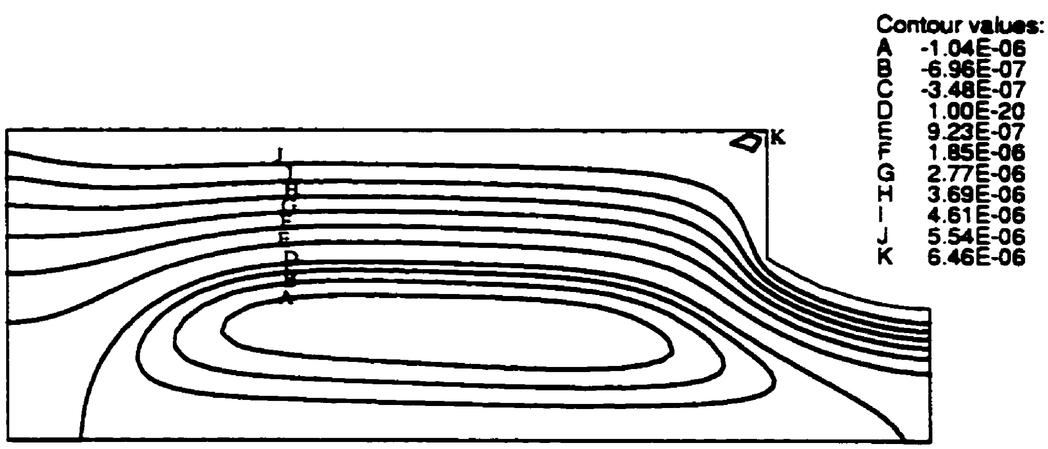

(b) Streamlines

Figure 6.11 — The predicted velocity vectors (a) and streamlines (b) for a "smart-probe" of 30A/256μm, $H = 0.3mm$, $L_e = 0.7mm$, $L_{orifice} = 0.3mm$, $S = 2.15$, and $u_m = 0.5m/s$.

recirculation zone is generated inside the extension near the entrance to the orifice. Considering the symmetry of the calculation domain, there is actually a toroidal type of recirculation zone within the extension, that is symmetric with respect to the central axis. In terms of a planar vertical cross section through the cylinder's axis, two symmetric recirculation zones are generated as a result of the pressure established by the strong electromagnetic pinch force at the center of the orifice. This pressure becomes higher than the upstream pressure of fluid inside the extension. With increase in fluid flow velocity, the pressure at the upstream end increases, so that this recirculation is finally suppressed once the negative pressure gradient is absent. This was illustrated in Figure 6.4 for $u_m = 4m/s$. For the practical application of the "smart-probe", therefore, it is necessary that the fluid flow velocity be sufficiently high to prevent the formation of the recirculation zones. The effect of the mean orifice velocity on the pass-through fraction of particles of different sizes is shown in Figure 6.12, from which it can be seen that the pass-through fraction increases as the fluid velocity increases due to the resulting shorter residence time.

6.4.3 Smart-Probes for Magnesium and Steel LiMCA

As discussed in the former sections, an orifice size of at least $400\mu m$ is found (empirically) to be needed to prevent the blockage of LiMCA system in typical magnesium melts, giving a particle detection limit of $30\mu m$ with $60A$ electric current. A "smart-probe" (denoted as SP magnesium) of $30A/256\mu m$, $H = 0.3mm$, L_e = $0.5mm$, $L_{orifice}$ = $0.3mm$, and $S = 2.15$ could reduce the detection limit to $20\mu m$. The practical operation of the LiMCA system in steel employs an electric current of 20 amperes passing through a $300\mu m$ diameter orifice. Under this condition, the particle detection limit is $16.6\mu m$. The lower detection limit can be

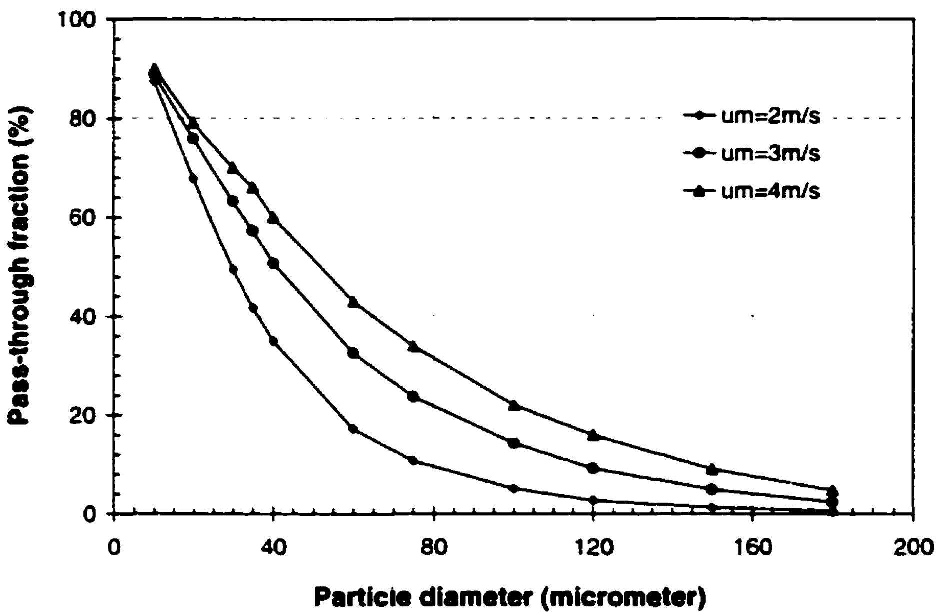

Figure 6.12 — The effect of mean fluid velocity u_m on the pass-through fraction of particles for a "smart-probe" of $30A/256\mu m$. $H = 0.3mm$. $L_e = 0.7mm$. $L_{orifice} = 0.3mm$. and $S = 2.15$.

achieved by designing a proper "smart-probe". One possible design which lowers the detection limit from $16.6\mu m$ to $10\mu m$ is a "smart-probe" (denoted as SP steel) of $20A/200\mu m$, $H = 0.2mm$, $L_e = 0.75mm$, $L_{orifice} = 0.3mm$, and $S = 2.15$. The pass-through fractions of particles of different sizes for the above "smart-probes" for magnesium and steel LiMCA systems are shown in Figure 6.13. The density and dynamic viscosity of steel used in the computation are $7\times10^3 kg/m^3$ and $5\times10^{-3} Pa\,s$, respectively. It can be seen from Figure 6.13 that the percentage of particles passing through the orifice decreases dramatically with increasing particle sizes. More than 90 percent of inclusions with sizes up to $20\mu m$ for steel "smart-probe" (SP steel) and around 75 percent of inclusions with sizes up to $30\mu m$ for magnesium "smart-probe" (SP magnesium) could successfully pass through the orifice. Less than 10 percent of inclusions of size $180\mu m$ for SP magnesium and only slightly above 2 percent of inclusions of this size for SP steel pass through the orifice. This proves that smart-probe can be used to detect small particles below the detection limit of the conventional probe. Meanwhile, it is also noted that a relative percentage of particles ranging from $30\mu m$ to $180\mu m$ were collected on the sidewalls. Therefore, to measure the melt cleanliness accurately, "smart-probe" should be used in conjunction with conventional probes to cover a wide range of particle sizes.

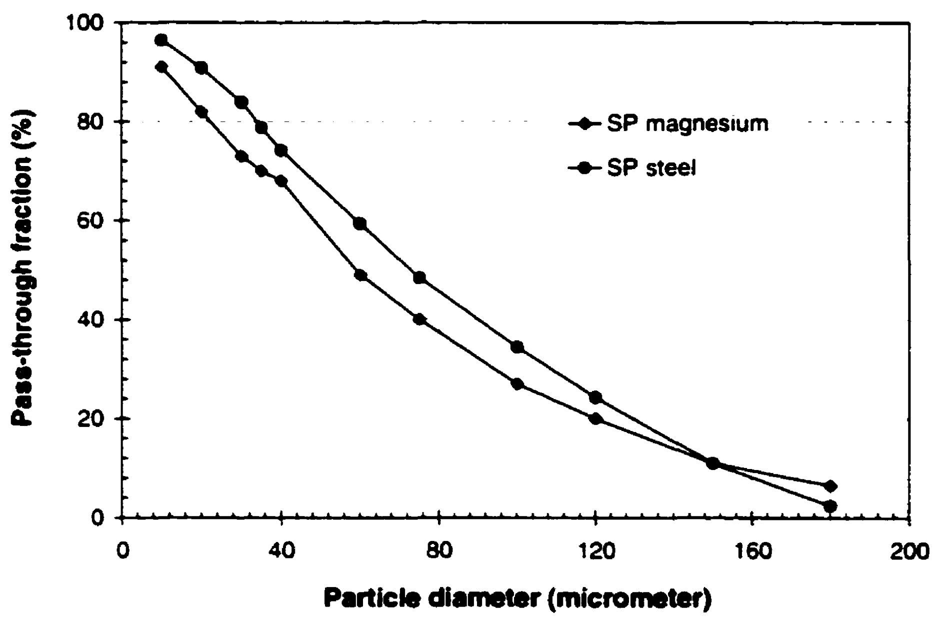

Figure 6.13 — The predicted pass-through fraction in "smart-probe" for magnesium (SP magnesium: $30A/256\mu m$, $H = 0.3mm$, $L_e = 0.5mm$, $L_{orifice} = 0.3mm$, $S = 2.15$, and $u_m = 4m/s$) and steel (SP steel: $20A/200\mu m$, $H = 0.2mm$, $L_e = 0.75mm$, $L_{orifice} = 0.3mm$, $S = 2.15$, and $u_m = 4m/s$).

6.5 Conclusions

A new design of the probe for the LiMCA system, which consists of a contoured orifice and a co-axially built cylindrical extension, has been proposed to tackle the blocking problem associated with small orifice needed for lowering the detection limit. Large particles, which have the potential to block the orifice, can be separated from smaller ones and collected onto the wall of the extension. A generalized mathematical model was developed for the motion of particles entrained in liquid metals flowing in this newly designed probe. The fluid field was obtained by solving the Navier-Stokes equations, and the trajectories of particles by equations for the motion of particles, which involve transient motion and incorporate the drag, the added mass, the fluid acceleration, the history and the electromagnetic forces on the particle. The results showed that the separation of larger from smaller particles are affected by the applied electric current, orifice size, orifice length, orifice shape, extension length and radius, as well as mean fluid velocity through the orifice. Increasing the electric current or decreasing orifice size lowers the pass-through fraction of particles of all sizes. Longer orifice gives rise to a lower pass-through fraction, and this effect diminishes as the length increases up to $0.5mm$. The shape of the orifice has little effect on the pass-through fraction of the particles, but it is critical to have a smooth entrance to the orifice to prevent the generation of recirculation zone inside the orifice. Increasing extension radius increases pass-through fraction of small particles, but decreases that of large ones. Moreover, pass-through fraction also increases with the decrease of extension length and the increase in mean fluid velocity through the orifice. The separation of particles of different density with "smart-probe" can only be achieved when the difference in density is dramatic. "Smart probes" for magnesium and steel

LiMCA are proposed for detecting particles below the detection limit of conventional probes.

References

[1] D. Doutre and R.I.L. Guthrie: US Patent 4555662, 1985.

[2] R.I.L. Guthrie and D. Doutre: Proceeding of International Seminar on Refining and Alloying of Liquid Aluminum and Ferro-Alloys, Trondheim, Norway, 1986, pp. 146-163.

[3] R.W. Deblois and C.P. Bean: Review of Scientific Instruments, 1970, vol. 41, pp. 909-915.

[4] R.W. Deblois, C.P. Bean, and R.K.A. Wesley: J. Colloid and Interface Sci., 1977, vol. 61, pp. 323-335.

[5] W.R. Smythe: Physics of Fluids, 1961, vol. 4, pp. 756-759.

[6] S. Kuyucak and R.I.L. Guthrie: 26th Annual Conf. Metallurgists, CIM, Winnipeg, August 1987, pp. 23-26.

[7] S. Kuyucak and R.I.L. Guthrie: Second Int. Symp. on the Effects and Control of Inclusions and Residuals in Steels, CIM, Toronto, August 1986, pp.17-20.

[8] C.J. Simensen and G. Berg: Aluminum, 1980, vol. 56, pp. 335-340.

[9] E.F. Emley: "Principles of Magnesium Technology", Pergamon Press, Elmsford, NY, 1966.

[10] H. Bengtsson: Swedish Symposium on Non-Metallic Inclusions in Steel, H. Nordberg and R. Sandstrom Eds, Arranged by the Uddeholm Research Foundation, Swedish Institute for Metal Research, April 27-29, 1981, pp. 450-462.

[11] X.G. Chen, R.I.L. Guthrie, and J.E. Gruzleski: Proceedings of the 4th Intl. Conf. on Molten Aluminum Processing, Sheraton World Resort, Orlando, Florida, November 12-15, 1995, pp. 15-28.

[12] C. Carozza, P. Lenard, R. Sankaranaraynanan, and R.I.L. Guthrie:

Light Metals 1997, Metaux Legers Symposium, 36th Annual Conf. of Metallurgists, Sudbury (ON), August 1997, pp. 185-196.

[13] R.I.L. Guthrie, M. Li, and J.Y. Byun: Proceedings of the First Israeli Intl. Conf. on Magnesium Sci. & Technol., Dead Sea, Israel, November 1997, pp. 81-87.

[14] W.H. Coulter: US Patent 112819, 1953.

[15] W.H. Coulter and W.R. Hogg: US Patent 3444464, 1969.

[16] W.R. Hogg: US Patent 3746977, 1973.

[17] S. Baccarini: US Patent 3638677, 1972.

[18] H. Bader: US Patent 3395344, 1968.

[19] R. Karuhn, R. Davies, and B.H. Kaye: US Patent 3739268, 1973.

[20] R. Davies, R. Karuhn, and J. Graf: Powder Technology, 1975, vol. 12, pp. 157-166.

[21] A.M. Fayon and J. Happel: AICHE Journal, 1960, vol. 6, pp. 55-58.

[22] J. Happel and H. Brenner: Low Reynolds Number Hydrodynamics, Printice-Hall, Inc., Englewood Cliffs, N.J., 1965, pp. 331.

[23] D. Doutre: US Patent 5834928, 1998.

[24] G. Carayannis, F. Dallaire, X. Shi, and R.I.L. Guthrie: Symposium on Artificial Intelligence in Materials Processing Operations, Edmonton, Canada, 1992, pp. 227-244.

CHAPTER 7

Conclusions

In this thesis, a mathematical model has been developed to describe the motion of particles in current-carrying liquid metals encountered in many electromagnetic materials processing operations. The model thus developed has been applied to study fluid flow and particle trajectories in LiMCA systems, including the water based LiMCA - APS II system, aluminum, magnesium, and steel LiMCA systems.

The model is concerned with the motion of particles in current-carrying liquid metals in a cylindrical coordinate system. The fluid flow was obtained by solving the Navier-Stokes equations, and particle trajectories by solving equations for the motion of particles which incorporate the drag, added mass, history, fluid acceleration and electromagnetic force, with correction factors for particle shape and orientation. Wall effects and flow conditions in the entrance region are considered. Dimensionless numbers Re, R_H, γ, and k are introduced to represent the fluid velocity, electric current, particle density and particle size, respectively. From this work, the following conclusions can be drawn:

- For non-conductive spherical particles flowing with current-carrying liquid metals through a cylindrical pipe, the particle trajectories are affected by the magnetic pressure number R_H, the Reynolds number Re, the blockage ratio k and the particle-fluid density ratio γ according to the relative importance of the associated force terms. In the axial direction, particles follow the fluid velocity closely, and will move further axially before reaching the wall as the fluid velocity (Re) increases. In the radial direction, the outwardly directed electromagnetic force on the particle increases with radial distance from the axis, with increasing current (R_H), and increasing size of the particle. The competition between the electromagnetic force and the radial fluid acceleration force in the entrance region results in particle movement towards the central axis before moving towards the wall for small electric current (low R_H) and directly towards the wall for large current (high R_H). The low inertia (γ) bubbles move faster towards the wall than do heavier particles. The radial velocity of the particle movement as it approaches the wall is predicted to decrease due to wall effects.

- For non-conductive spheroidal particles passing through a cylindrical ESZ orifice, the effects of particle shape and orientation on the motion of particles are taken into account by including correction factors, R^D for drag, M^A for added mass, B for history, and E^M for electromagnetic force. The movement of spheroidal particles are affected by Re, R_H, γ, k and the wall in the same way as they do for non-conductive spherical particles. Spheroidal particles with symmetric axes perpendicular to the transverse axis of the ESZ move faster towards the sidewall as the particle aspect ratio (E) increases. The dominating increase in the added mass (M^A) over the increase in the electromagnetic force (E^M) with decreasing E makes this effect much stronger for oblate ($E<1$) than for prolate ($E>1$) spheroids. The stronger drag force (R^D) on a prolate spheroid with its symmetric axis parallel to the axis of the ESZ makes it move slower towards the wall than a prolate with its axis of symmetry perpendicular to the axis of the ESZ. The effect of solid to liquid density ratio γ is stronger for a prolate traversing with its symmetric axis perpendicular rather than parallel to the axis of the ESZ due to its smaller added mass (M^A), and also stronger for prolate than for oblate spheroidal particles traversing with their symmetric axes perpendicular to the axis of the ESZ owing to the decrease in added mass (M^A) as E increases.

- For non-conductive particles flowing into a parabolic ESZ orifice with water, the motion of particles is affected by particle density and particle size. Bubbles lead the fluid flow and travel faster than latex microspheres which are slightly denser than the fluid and follow the fluid flow closely. Silica particles which are much denser than the fluid lag behind the flow and travel slower than latex microspheres, and much slower than bubbles. The relative velocity decreases with decreasing of the diameter of particles of the same density. Larger particles experience longer transit times through an ESZ than do smaller ones. The transient times of bubbles are shorter than those of latex spheres and much shorter than those of silica particles of the same size. The difference in transit times is more pronounced for larger particles, consistent with experimental measurements. These findings confirm that particle discrimination in water based LiMCA system is realizable.

- For particles flowing into a parabolic ESZ with molten aluminum, the motion of particles inside the parabolic shaped orifice is affected by particle conductivity, density and size. Non-conductive particles pass through the ESZ along trajectories closer to the wall, while particles that are more conductive than the molten metal move closer towards the central axis. Bubbles lead the fluid flow in the axial direction and travel faster than alumina particles which are denser than the fluid and lag behind the flow. Larger particles have longer transient times than do smaller ones. The transient times of bubbles are predicted to be shorter than those of alumina particles of the same size, and the difference of transient times is more pronounced for larger particles, proving that particles in molten aluminum are distinguishable in LiMCA system. The helpful "conditioning effect" discovered by the inventors of the LiMCA system for aluminum melts can be attributed to the dramatic increase in fluid velocity near the wall of the parabolic orifice upon current surge, together with a flow reversal, thereby clearing the build-up of inclusions ahead and within the ESZ.

- For non-conductive particles flowing with molten magnesium through a cylindrical ESZ orifice with a countersunk conical inlet region, a large recirculation zone is predicted to form in the countersunk region, potentially leading to higher background electrical noise and orifice blockage. A rounded ESZ probe orifice is proposed to eliminate the recirculation zone while maintaining the advantages of conditioning effect.

- For non-conductive particles flowing with molten steel through a cylindrical ESZ, the ineffective conditioning operation can be plausibly explained in terms of a little increase in fluid velocity near the wall upon current surge. A parabolic orifice, similar to that used in aluminum LiMCA operation is suggested to improve the conditioning operation.

- To lower the detection limits of LiMCA systems while preventing orifice blockage, "smart-probes" for magnesium and steel LiMCA are proposed. They consist of a contoured orifice and a co-axially built cylindrical extension. It is proposed that large particles which have the potential to block the orifice can be separated from smaller ones and collected onto the wall of this extension, allowing small particles to be measured pass through the ESZ probe.

- The applicability of LiMCA systems for monitoring molten metal cleanliness is proved theoretically based on the predicted pass-through fractions of particles through the ESZ orifice.

Statement of Originality

The author claims the following contributions to knowledge:

- Developed a mathematical model and the associated computer codes for the motion of particles in current-carrying liquid metals.
- Studied in detail the effects of particle inertia and various force terms, including drag, added mass, fluid acceleration, history and electromagnetic force, on the motion of particles.
- Studied the effects of shape and orientation on the motion of spheroidal particles in current-carrying liquid metals.
- Defined a correction factor E^M for the electromagnetic force on spheroidal particles of different shapes and orientation.
- Predicted the particle pass-through fractions, confirmed theoretically the applicability of LiMCA systems for molten metals.
- Simulated the particle motion in water-based LiMCA — APS II system, predicted the transient time and shape of signals by combing Ohmic model and the simulated particle motion, confirmed the possibility of particle discrimination.
- Simulated the motion of particles in molten aluminum LiMCA system, predicted the intrinsic difference in trajectories of conductive and non-conductive particles, proved theoretically the possibility of particle discrimination based on transient time and signal shape.
- Clarified the mechanism of conditioning operation in aluminum LiMCA.
- Identified the countersunk inlet region as a possible problem in magnesium LiMCA, proposed a new design of ESZ probe orifice.
- Explained the ineffective conditioning operation in steel LiMCA, emphasized the importance of rounded shape of ESZ probe orifice.
- Proposed a new design for lowering detection limits of molten metal LiMCA systems.

Appendix A

Schematic Configuration of DSP-based LiMCA System

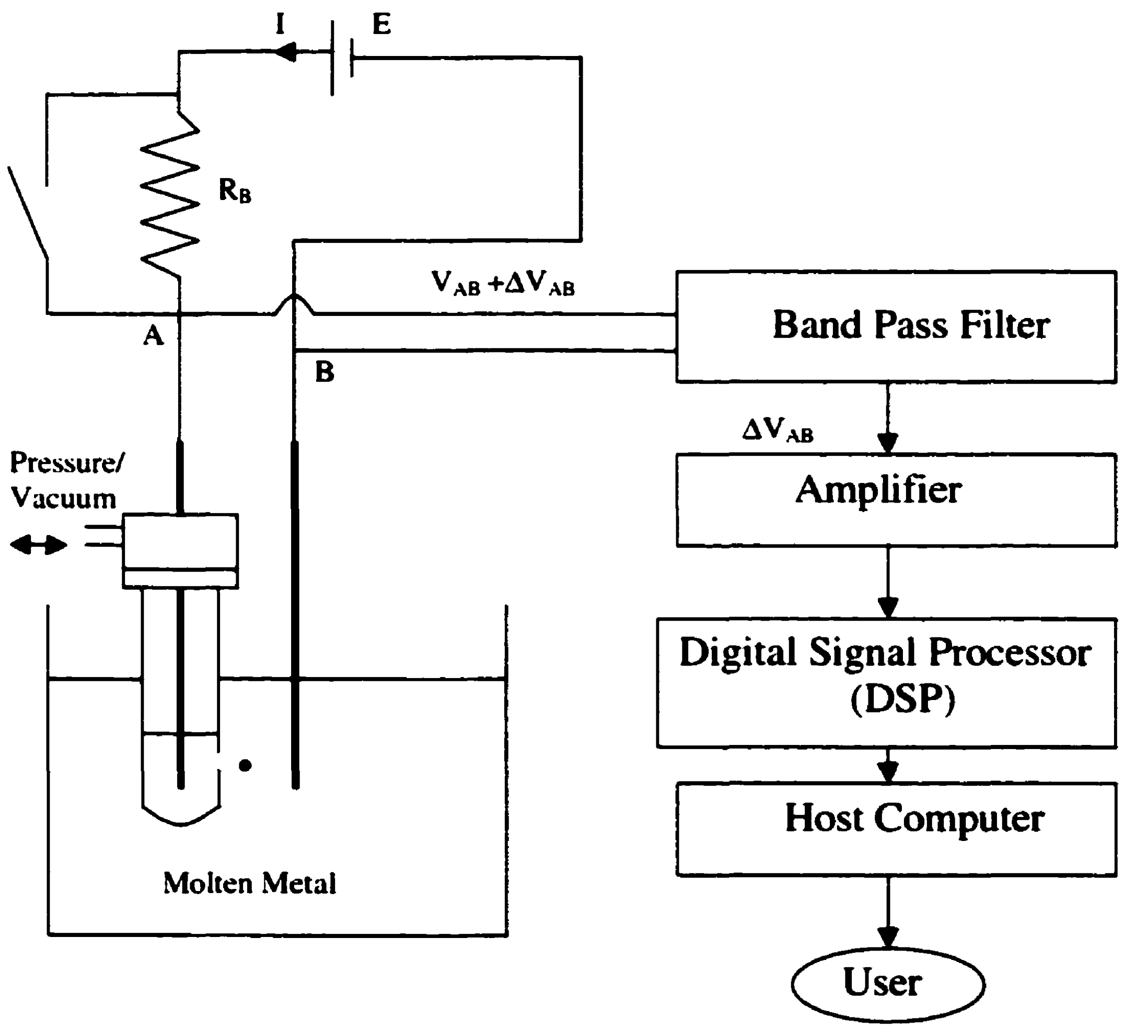

Appendix B

Mathematical Model Construction and Validation

B.1 Mathematical Model Construction

B.1.1 Assumptions

- Steady-state and laminar flow conditions.
- Liquid metal as incompressible Newtonian fluid.
- MHD approximation applicable.
- Effect of flow motion on electric current negligible.
- Constant physical properties of liquid metals, such as density, viscosity and temperature.
- Non-deformable particles, droplets and bubbles.

B.1.2 Mathematical formulations

Navier-Stokes equations:

$$\vec{\nabla} \bullet \vec{u} = 0 \tag{B.1}$$

$$\vec{u} \bullet \vec{\nabla}\vec{u} = -\frac{\vec{\nabla}p}{\rho_f} + \nu_f \nabla^2\vec{u} + \frac{1}{\rho_f}\vec{F} \tag{B.2}$$

Electromagnetic force:

$$\vec{F} = \vec{J} \times \vec{B} \tag{B.3}$$

Laplace equation for electrical potential:

$$\frac{\partial^2\varphi}{\partial x^2} + \frac{1}{y}\frac{\partial}{\partial y}(y\frac{\partial\varphi}{\partial y}) = 0 \tag{B.4}$$

Electric current density and magnetic flux density:

$$J_x = -\sigma_e \frac{\partial \varphi}{\partial x} \qquad J_y = -\sigma_e \frac{\partial \varphi}{\partial y} \tag{B.5}$$

$$B_\theta = \frac{\mu_0}{y} \int_0^y J_x \xi d\xi \tag{B.6}$$

Equation of motion of particles:

$$\begin{aligned} \rho_p V_p \frac{d\bar{u}_p}{dt} &= \frac{1}{2} C_{Dstd} \pi a^2 \rho_f \left|\bar{u} - \bar{u}_p\right| (\bar{u} - \bar{u}_p) + \frac{1}{2} \rho_f V_p \left(\frac{D\bar{u}}{Dt} - \frac{d\bar{u}_p}{dt}\right) + \rho_f V_p \frac{D\bar{u}}{Dt} \\ &+ 6a^2 (\pi \mu_f \rho_f)^{1/2} \int_0^t \frac{d(\bar{u} - \bar{u}_p)/d\tau}{(t-\tau)^{1/2}} d\tau + V_p (\rho_p - \rho_f) \bar{g} - \frac{3(1-\chi)}{4} V_p \bar{F}_e \end{aligned} \tag{B.7}$$

$$\chi = \frac{3\sigma_{e_p}}{\sigma_{e_p} + 2\sigma_e} \tag{B.8}$$

B.1.3 Boundary conditions

- Inlet: uniform normal fluid velocity and electric current density.
- Outlet: constant electrical potential and zero fluid velocity gradient.
- Wall: zero slip along and zero electric current flux across the insulating wall.
- Symmetry plane: zero normal velocity component and electric current density. zero normal gradient of velocity component parallel to the symmetry plane.

B.1.4 Initial condition of particle motion

- Particles assuming the fluid velocity at inlet.

B.1.5 Numerical procedure

The conservation equations for mass (equation (B.1)) and momentum (equation (B.2)), and Laplace equation for electrical potential (equation (B.4)) were discretized on non-orthogonal boundary fitted grids using the finite volume approach and a collocated arrangement of variables.[1,2]

The control volume and the notion used are shown in Figure B.1. Here

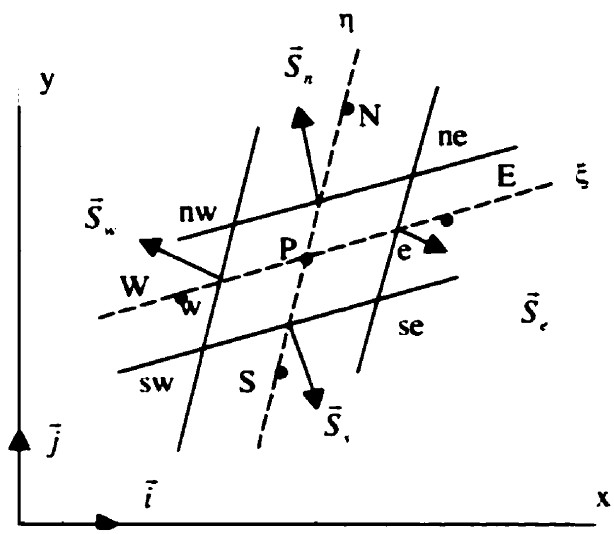

Figure B.1 — The 2D control volume and the notion.

only the discretization on "e" face will be considered, the other faces being treated in an analogous way. The mass flux can be expressed as:

$$\dot{F}_e = \rho_e (S^x u_x + S^y u_y)_e \qquad \text{(B.9)}$$

where S^x and S^y are the two components of a surface vector.

The convective flux of any transported quantity may now be evaluated as follows:

$$C_e = \dot{F}_e \phi_e \qquad \text{(B.10)}$$

where ϕ_e stands for the cell face mean value of the variable ϕ.

The diffusion flux of ϕ through the "e" cell face can be written as:

$$D_e = \Gamma_e S_e \frac{\phi_E - \phi_P}{L_{P,E}} + \Gamma_e S_e \overline{(grad\phi)_e} \bullet (\vec{n} - \vec{i}_\xi) \qquad \text{(B.11)}$$

The second term vanishes when the grid is orthogonal, and is small compared to the first term if the grid non-orthogonality is not severe, therefore, it is treated explicitly.

The source term is to be integrated over the cell volume ΔV:

$$S_P = \int_V s_P dV = (s_\phi)_P \Delta V \qquad \text{(B.12)}$$

Summarizing the fluxes through all faces of one CV results in an algebraic equation which links the value of the dependent variable at the CV center with the neighboring values:

$$A_P \phi_P = \sum_{nb} A_{nb} \phi_{nb} + S_\phi \qquad \text{nb} = \text{E, W, N, S} \qquad \text{(B.13)}$$

The coefficients A_{nb} contain contributions from the convection and diffusion fluxes as defined by equations (B.10) and (B.11). The central coefficient A_P can be expressed as:

$$A_P = \sum_{nb} A_{nb} \qquad \text{(B.14)}$$

The discretized momentum equation at CV center may be written as:

$$u_P^* = \frac{\sum_{nb} A_{nb} u_{nb}^* + Q_u^*}{A_P} + (\frac{S}{A_P})_P (P_e^* - P_w^*) \qquad \text{(B.15)}$$

where the pressure difference in the w-e direction has been taken out of the Q - term and shown explicitly. The cell face value u_e^* was obtained by linear interpolation and expressed as:

$$u_e^* = \overline{\left[\frac{\sum_{nb} A_{nb} u_{nb}^* + Q_u^*}{A_P}\right]_e} + \overline{\left(\frac{S}{A_P}\right)_e} (P_E^* - P_P^*) \qquad \text{(B.16)}$$

where the overbar denotes linear interpolation.

Velocity and pressure corrections are introduced to enforce mass conservation and linked by:

$$u_e' = -\overline{\left(\frac{S}{A_P}\right)_e} (P_E' - P_P') \qquad \text{(B.17)}$$

The continuity equation then reads:

$$F_e' + F_w' + F_s' + F_n' + S_m = 0 \qquad \text{(B.18)}$$

where $S_m = F_e^* + F_w^* + F_s^* + F_n^*$, which leads to an equation for the pressure correction which has the same form as equation (B.13). The solution procedure is the same as that for the staggered variable arrangement which has been described in detail by Patankar.[3]

Grids of variable spacing were used in this study to enhance the accuracy of the calculation, *i.e.*, a finer spacing was adopted near the wall and inflow boundary and a coarser grid further away. Central differences were used to approximate both convection and diffusion fluxes. The equations are solved sequentially using the strongly implicit procedure of Stone.[4] which is based on the ILU (Incomplete Lower and Upper Matrices)-decomposition. Pressure-velocity coupling is achieved via SIMPLE (Semi-Implicit-Method for Pressure-Linked Equations) algorithm.[3] The solution of the fluid flow equations provides the hydrodynamic conditions for the calculation of the motion of particles. The fluid velocity at the instantaneous center of the particle was obtained by bi-linear interpolation of the grid values. The equation of particle motion was solved by employing a fourth-order Runge-Kutta method.

Another numerical method[5] that has been used to study particle motion considered the particle as a moving boundary. The basic procedure of this explicit-implicit scheme is as follows:

(i) Explicit updating. At each time step t_i, the current position, velocity and force of the particle are used to predict the new position and velocity at the next time step t_{i+1}.

(ii) Re-meshing and projection. For this new position, the computational domain is remeshed, and the velocity field at t_i is projected onto the new mesh.

(iii) Navier-Stokes solution. On the new mesh, the pressure and velocity field are solved using the velocity field at t_i (after projection). The explicitly updated particle velocity serves as the boundary condition on the particle surface. Then the force and moment on the particle are computed.

(iv) Implicit updating. The velocity of the particle is re-updated implicitly using the force and moment at t_{i+1}. If the new particle velocity is different from the one obtained in (i), then go back to (iii) and solve the N-S equations using the new particle velocity as the boundary condition. This process is repeated until satisfactory convergence is reached. Then go back to (i) and advance in time.

This scheme takes into account of the interactions between the particle, fluid and wall directly. However, it is so computationally expensive that only the motion of free fall particles in stagnant flow field has been considered[5]. Therefore, it was not adopted in this study.

B.2 Mathematical Validation

The problems defined below were chosen so as to include the most important features of the complex flows involved in this study and to test for the solution methods developed in this thesis.

Case 1. Lid-driven cavity flow

Lid-driven cavity flow has long served as a standard test case for orthogonal or non-orthogonal boundary-fitted grids. The case studied here is set up by inclining the side walls of the cavity to an angle of 45°. The length of each side of the cavity L=1, fluid density $\rho_f = 1$ and lid velocity $u_L = 1$ were used in the calculations. The Reynolds number, defined using the lid velocity, u_L, and cavity length, L, was varied from 100 to 1000 by changing the viscosity from 0.01 to 0.001.

By systematically refining the grid, grid-independent solutions were obtained from 300 × 300 CV (control volume). One of the grids with 80 × 80 CV is shown in Figure B.2. Figure B.3 shows the streamlines for Re=100. It can be seen that the main vortex fills almost the whole cavity. The counter rotating vortex lies deep in the corner and is three orders of magnitude weaker. The stream function values indicate the mass flux inside the vortex. The maximum or minimum value in one vortex center defines the total mass flow across any line connecting the vortex center with the vortex boundary. For the two strongest vortices, these values, denoted as ψ_{min} (first vortex) and ψ_{max} (second vortex), were evaluated on all grids.

Figure B.4 shows the convergence of ψ_{max} and ψ_{min} towards the grid-independent values as the grid was refined.

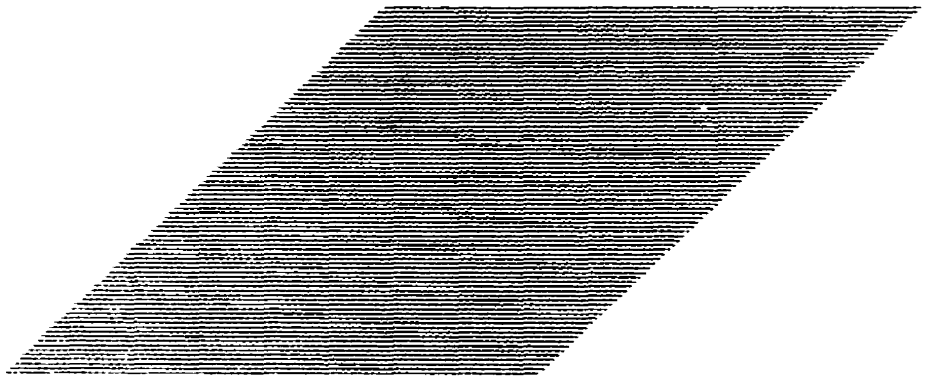

Figure B.2— Non-orthogonal, boundary-fitted grid used in lid-driven cavity flow.

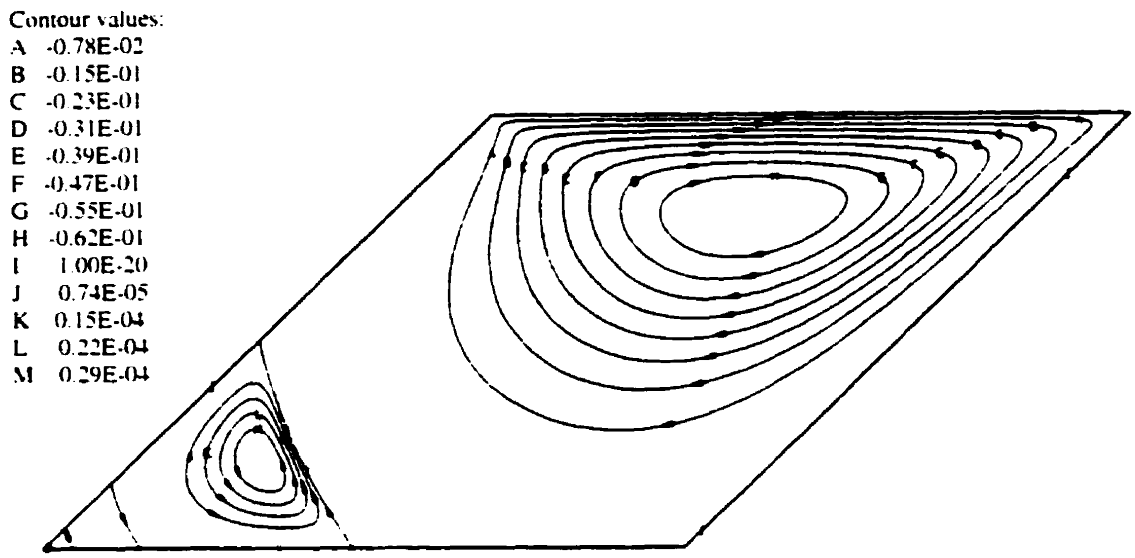

Figure B.3 — Predicted streamlines for 300 × 300 CV at Re=100.

In all the studies in thesis, tests were performed first so as to choose a grid field which was sufficiently fine to render flow field computations independent of grid size. In most cases, even finer grids were used for obtaining an accurate particle trajectory.

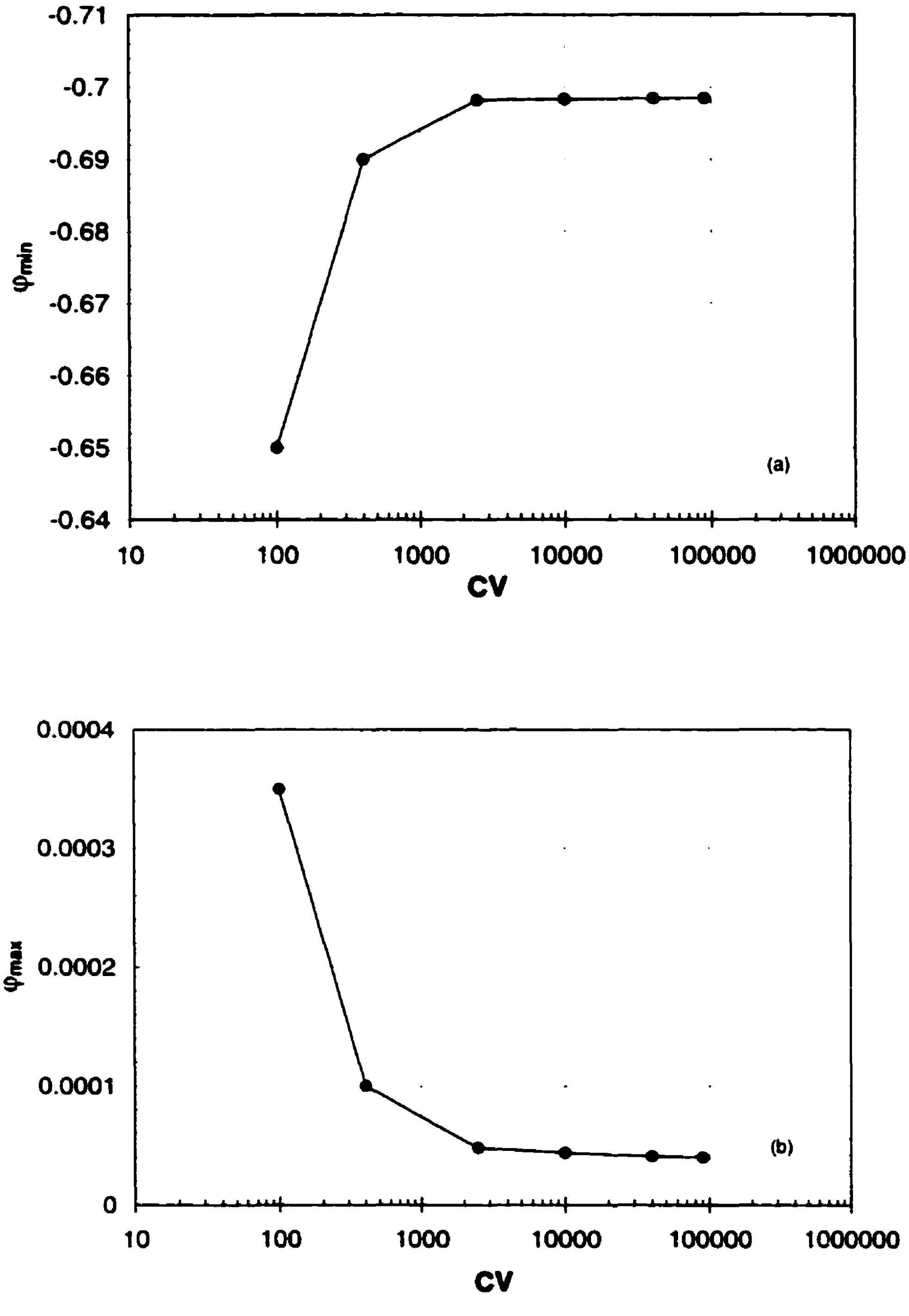

Figure B.4 — Variation of (a) minimum and (b) maximum stream function values at Re=100 as a function of control volume number.

Case 2. Laminar flow around a circular cylinder in a channel

The numerical method developed in this thesis was further tested on more complicated boundary fitted grids. The problem was described as follows.

At inlet of the channel, a parabolic velocity profile is prescribed:

$$u_x = \frac{6u_0}{L^2}[(y-y_p)L-(y-y_p)^2] \qquad u_y = 0 \qquad \text{(B.9 \& B.10)}$$

where u_0 is the mean velocity, $L = 4.1d$ is the channel height and $y_p = -2d$ is the y coordinate of the bottom wall, and the origin of the coordinate system is set at the center of the particle of diameter d. The axis of the cylinder is not on the horizontal symmetry plane of the channel so the flow is slightly asymmetric.

Steady flow at a Reynolds number of $\mathrm{Re} = 20$, based on the mean velocity in the channel and cylinder diameter, was considered. Calculations were performed on systematically refined non-orthogonal, boundary-fitted grids. One grid of 208 × 16 CV is shown in Figure B.5. The forces on the cylinder were quantities of primary interest.

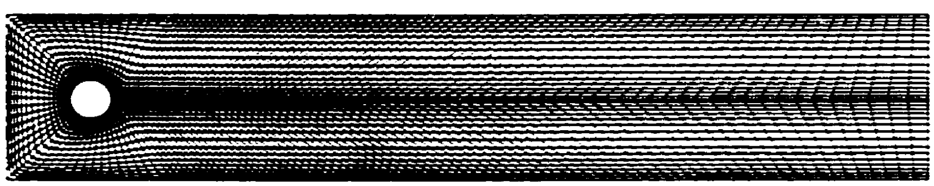

Figure B.5 — Non-orthogonal, boundary-fitted grid used in laminar flow around a circular cylinder in a channel.

If the configuration was fully symmetric, the steady flow would yield zero lift force on the cylinder. There is a small lift force due to the asymmetry, as the flow rate (and therefore the pressure) is different above and below the cylinder. The drag coefficient is defined as:

$$C_D = \frac{F_x}{\frac{1}{2}\rho u_0^2} \quad (B.11)$$

where F_x is the x component of the force exerted by the fluid on the cylinder. This force is calculated by integrating the pressure and shear force over the cylinder surface. The grid-independent solutions on the drag coefficient were obtained from 416 × 32 CV, and the results was shown in Figure B.6.

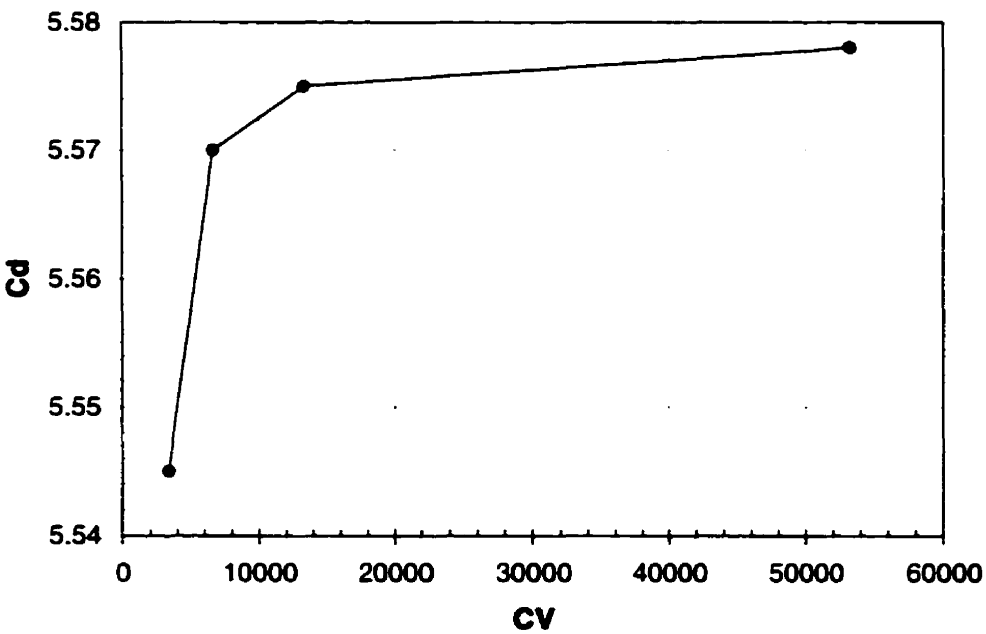

Figure B.6 — Drag coefficient for the 2D flow around a cylinder in a channel as a function of control volume number.

Case 3. Ballistics of a spherical projectile

To evaluate the numerical method developed for particle motion, comparison is made between the particle trajectories obtained from present study and previous work.

It is well known that in small-scale motions, a projectile traces out a parabola when shooting upward in a direction not perpendicular to the earth's surface. Previous studies on the motion of a projectile in a stagnant viscous fluid included added mass, gravity, buoyancy, and drag force, as well as particle inertia.[6] In this thesis, the drag coefficient C_D was estimated as follows:[7]

$$\begin{aligned}
&\mathrm{Re} < 0.01 && C_D = 3/16 + 24/\mathrm{Re} \\
&0.01 < \mathrm{Re} \le 20 && \log_{10}\left[\frac{C_D \mathrm{Re}}{24} - 1\right] = -0.881 + 0.82w - 0.05w^2 \\
& && \text{i.e., } C_D = \frac{24}{R_e}\left[1 + 0.1315\,\mathrm{Re}^{(0.82-0.05w)}\right] \qquad \text{(B.12)} \\
&20 < \mathrm{Re} \le 260 && \log_{10}\left[\frac{C_D \mathrm{Re}}{24} - 1\right] = -0.7133 + 0.6305w \\
& && \text{i.e., } C_D = \frac{24}{R_e}\left[1 + 0.1935\,\mathrm{Re}^{0.6305}\right] \\
&260 < \mathrm{Re} \le 1500 && \log_{10} C_D = 1.6435 - 1.1242w + 0.1558w^2
\end{aligned}$$

where $w = \log_{10}\mathrm{Re}$.

The trajectory of a steel ball of d=0.05m in air with an initial speed of 50m/s at an elevation angle of 30 degree was studied. The results were shown in Figure B.6 with the predictions from previous study.[6] It can be seen that the very good agreement was achieved. By neglecting the added mass, buoyancy and drag force, the predictions were compared with the analytical expression for ballistics of projectile in vacuum, and again agreement was achieved.[6]

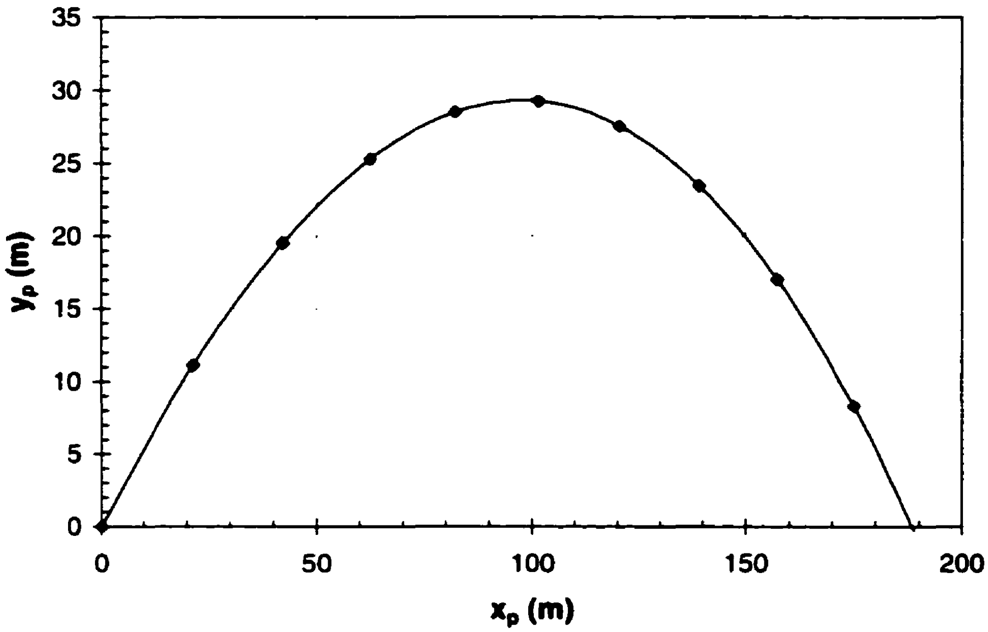

Figure B.7 — Trajectory of a steel ball in air. — this study, ◆ [6].

Case 4. Particle trajectory in an electric dust collector

A dust precipitator consists of a pair of oppositely charged plates between which dust-laden gases flow. The minimum length of precipitator is taken to be the length where the smallest particle present will reach the bottom plate just before it has a chance to be swept out of the channel. Assume that the flow between the two plates is laminar, and the particle velocity in axial direction is the same as the fluid velocity in this direction. Assume further that the Stokes drag on the sphere as well as the gravity force acting on the particle as it is accelerated in the vertical direction can be neglected. Under these assumptions, the minimum length in terms of the charge of the particle, e, the electric field strength, E, the pressure difference between the inlet and outlet, Δp, the particle mass, m_p, and the gas viscosity, μ_f, is given as:[8]

$$L_{min} = [64\Delta p^2 R^5 m_p / 225\mu_f^{\,2} eE]^{\frac{1}{4}} \qquad \text{(B.13)}$$

Assuming the values of e, E, Δp, m_p, R and μ_f are 1 in SI unit. The numerical prediction of particle's trajectory was shown in Figure B.8. Compared with the analytical result from equation (B.13), which is 0.730296743m, the predicted result is 0.730296787m. It can be seen that the good agreement was achieved.

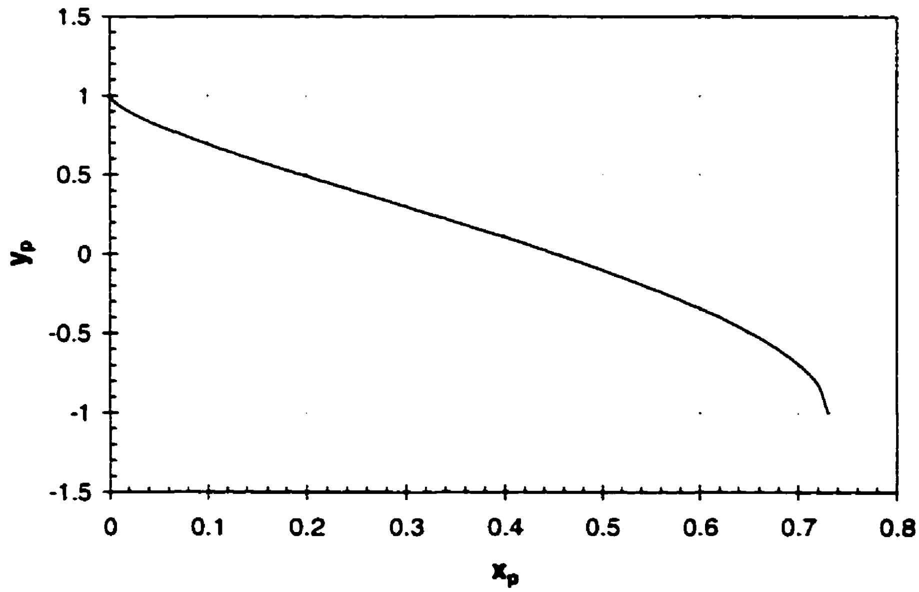

Figure B.8 — Predicted particle trajectory inside an electric dust precipitator.

References

[1] M. Peric, R. Kessler, and G. Scheuerer: Comput. Fluids, 1988,

vol. 16, pp. 389-403.

[2] I.Demirdzic and M. Peric: International Journal for Numerical Methods in Fluids, 1990, vol. 10, pp. 771-790.

[3] S.V. Patankar and D. B. Spalding: Int. J. Heat and Mass Trans., 1972, vol. 15, pp. 1787.

[4] H.L. Stone: SIAM J. Numer. Anal., 1968, vol. 5, pp. 530-558.

[5] H.H. Hu, M.J. Crochet, and D.D. Josef: Theor. Comput. Fluid Dyn., 1992, vol. 3, pp. 285-306.

[6] Chuen-Yen Chow: An Introduction to Computational Fluid Mechanics, Seminole Publishing Company, Boulder, Colorado, 1983.

[7] R. Clift, J.R. Grace, and M.E. Weber: Bubbles, Drops, and Particles, Academic Press, Inc., New York, NY, 1978, pp. 112.

[8] R.I.L. Guthrie: Engineering in Process Metallurgy, Oxford University Press, Oxford, 1989, pp. 99.